University of Zagreb

Faculty of Chemical Engineering and Technology

Sara Krivačić

SCALABLE CONTACTLESS FABRICATION OF POTENTIOMETRIC CHEMICAL SENSORS

DOCTORAL THESIS

Zagreb, 2025

University of Zagreb

Faculty of Chemical Engineering and Technology

Sara Krivačić

SCALABLE CONTACTLESS FABRICATION OF POTENTIOMETRIC CHEMICAL SENSORS

DOCTORAL DISSERTATION

Mentor:
Assoc. Prof. Petar Kassal, PhD

Zagreb, 2025

Sveučilište u Zagrebu

Fakultet kemijskog inženjerstva i tehnologije

Sara Krivačić

BESKONTAKTNA IZRADA POTENCIOMETRIJSKIH KEMIJSKIH SENZORA U VELIKIM RAZMJERIMA

DOKTORSKI RAD

Mentor:
Izv. prof. dr. sc. Petar Kassal

Zagreb, 2025

Bibliographic page

Supervisor information

Odluka o prihvaćanju teme

zahvale

ABSTRACT

SCALABLE CONTACTLESS FABRICATION OF POTENTIOMETRIC CHEMICAL SENSORS

Sara Krivačić

University of Zagreb Faculty of Chemical Engineering and Technology
Trg Marka Marulića 19, 10000 Zagreb

Solid-contact potentiometric sensors have emerged as reliable, miniaturized tools for use beyond traditional laboratories. As electronic devices, their fabrication has shifted from conventional circuit board techniques to contactless printing methods. Among these, inkjet printing and automated dispensing offer scalable, low-waste production, though technical challenges remain. In this research an inkjet-printable conductive ink based on melamine-intercalated graphene nanosheets was developed and used to fabricate ammonium-selective electrodes. To improve ion-selective membrane deposition, automated dispensing was used with optimized membrane formulations. Solid-contact reference electrode fabrication was significantly shortened by developing a unique reference membrane using photochemically reduced silver chloride. All components were evaluated for performance and stability, confirming the potential of printed potentiometric sensors.

Keywords: potentiometric sensors, solid-contact ion-selective electrode, solid-contact reference electrode, inkjet printing, automated dispensing.

Prošireni sažetak

Elektrokemijski senzori su uređaji koji pretvaraju elektrokemijsku interakciju na elektrodi u analitički korisnu informaciju. Među njima se potenciometrijski senzori ističu jednostavnošću izvedbe. Potenciometrijska ćelija sastoji se od indikatorske (ion-selektivne) i referentne elektrode koje s voltmetrom visoke ulazne impedancije zatvaraju strujni krug.

Posljednjih nekoliko desetljeća minijaturizacija te decentralizacija analitičkih protokola dobiva velik značaj, a potenciometrijski se senzori javljaju kao obećavajuće platforme za kliničke i okolišne analize. Ključna otkrića koja su omogućila minijaturizaciju i razvoj modernih potenciometrijskih senzora jesu (1) zamjena ion-selektivnih stakala s polimernim ion-selektivnim membranama temeljenim na ionoforu i ionskom izmjenjivaču, te (2) zamjena kapljevitog pretvornika s čvrstim kontaktom. Jednak razvojni smjer karakterizira i referentne elektrode. Tako je ostvarena plošna izvedba senzora čije su rane proizvodne tehnike utvrđene u proizvodnji tiskanih pločica. Međutim, pokazalo se da su one prespore, nekompatibilne s fleksibilnim podlogama te generiraju velike količine štetnog otpada.

Moderne tehnologije proizvodnje elektrokemijskih senzora – sitotisak te *injket* ispis – prikladne su za proizvodnju plošnih elektroda na fleksibilnim podlogama, što posebno proširuje obim primjene modernih elektrokemijskih senzora. Sitotisak je trenutno dominantna komercijalna proizvodna tehnologija. Međutim, kontaktna priroda ove tehnike, potreba za šablonama, niska rezolucija te velika potrošnja materijala čine ga neprikladnim za najnovije zahtjeve elektrokemijskih senzora.

Inkjet ispis – još uvijek istraživačka tehnologija u proizvodnji elektrokemijskih senzora – javlja se kao alternativa sitotisku. To je u potpunosti digitalna, beskontaktna, visoko precizna tehnologija, koja selektivno i prema potrebi deponira pikolitarske kapljice vodljive tinte na razne, često fleksibilne podloge. Tako je ostvarena visoka preciznost i niska količina otpada, što ju čini idealnom za razvoj proizvodnih protokola na visokoj skali. Međutim, izazovi ostaju u razvoju stabilnih, vodljivih tinti kompatibilnih s inkjet ispisom te

osiguravanju snažnog prianjanja tinte na podloge od interesa i pravilne naknadne obrade s ciljem formiranja električnih vodova, odnosno funkcionalnih elektrodnih slojeva.

Ova disertacija stoga ima za cilj odgovoriti na takve izazove u izradi ionsko-selektivnih i referentnih elektroda s čvrstim kontaktom korištenjem *inkjet* ispisa za kontrolirano nanošenje električnih vodova i čvrstog kontakta. Budući da je *inkjet* ispis polimernih ion-selektivnih membrana nemoguć bez prethodnog radikalnog umanjivanja masenog udjela čvrstih komponenata membranskog koktela, istraženo je automatizirano nanošenje membranskog koktela na plošne elektrode.

Razvijena je vodljiva tinta temeljena na grafenu (MGNS, melaminom interkalirane grafenske nanoplahte) za potenciometrijske senzore proizvedene *inkjet* ispisom. Grafen je odabran zbog svoje visoke vodljivosti, hidrofobnosti i velike površine, idealne za slojeve u čvrstom kontaktu koji sprječavaju stvaranje vodenog sloja. MGNS sintetizirane su ekološki prihvatljivim mehanokemijskim putem korištenjem grafita i melamina. Tinta za inkjet ispis formulirana je u zelenoj smjesi otapala (etanol, voda, etilen glikol) te je pokazala prikladna svojstva za inkjet ispis. Tinta je uspješno ispisana na fleksibilne polimerne podloge te je obrađena kombinacijom toplinskog tretmana i tretmana intenzivnom pulsirajućom svjetlošću (IPL). Izmjerena je električna vodljivost ispisanih uzoraka od 626 Ω/□, čime je potvrđena njezina prikladnost za izradu fleksibilnih senzora.

Razvijena je grafenska tinta nadalje korištena za ispis čvrstog kontakta u razvoju planarnih amonij-selektivnih elektroda (SC-ISE). Srebrni kontakti i MGNS sloj ispisani su na poliimid, potom termički i IPL obrađeni te modificirani amonij-selektivnom membranom. Uvođenje MGNS sloja smanjilo je otpor elektrode s 7,31 MΩ na 4,30 MΩ, poboljšavajući prijenos naboja. Elektrode su pokazale osjetljivost 52,0 mV dec^{-1}, donju granicu detekcije 25,1 μM i visoku selektivnost prema NH_4^+. Ispitan je učinak prepolarizacije na zanošenje potencijala. Nakon prepolarizacije zanošenje potencijala je smanjeno s –0,39 na 0,10 mV h^{-1}, a linearni raspon proširen na 10^{-6}–10^{-1} M uz donju granicu detekcije 0,88 μM. MGNS sloj značajno je smanjio zanošenje potencijala zbog vodenog sloja (s 16 na 0,22 mV h^{-1}) i osigurao stabilan EMF (RSD 0,59 %). U analizi

procjedne vode izmjerena je koncentracija amonijevih iona u skladu s referentnom metodom.

Važan dio istraživanja bila je optimizacija sastava polimerne membrane za automatiziranu proizvodnju potenciometrijskih senzora. Umjesto razrjeđivanja otopine, optimiran je omjer otapala tetrahidrofuran (THF) i cikloheksanon (CH) radi stabilnog nanošenja pomoću dozatorskog robota. Analiza topografije boje pokazala je da jednaki volumni omjer (THF:CH = 1:1) daje najujednačeniju debljinu membrane. Praćenjem impedancijskih profila u stvarnom vremenu tijekom sušenja polimerne membrane utvrđeno je da se THF-membrana suši za <1 min, CH-membrana za 23 min, a mješavina za 11,5 min, sa završnom impedancijom oko 5,6 MΩ. Time je potvrđeno da kombinacija otapala omogućuje brže i kontrolirano sušenje. Kalijeva selektivna membrana (K-ISM) izrađena u omjeru THF:CH = 1:1 automatski je nanesena na elektrode. Već jedan sloj osigurao je stabilan odziv u kliničkom rasponu koncentracija K^+, dok su dva sloja smanjila standardnu devijaciju E^0 na ±4,0 mV dec^{-1}. Cijeli proces izrade i sušenja traje manje od 30 minuta, što omogućuje brzu i pouzdanu automatiziranu proizvodnju senzora.

Razvijena je planarna referentna elektroda s čvrstim kontaktom (SC-RE) kompatibilna s izrađenim *inkjet* ispisanim senzorima. Unutar membranske matrice temeljene na poli(vinil butiralu) (PVB) formiran je Ag/AgCl par pomoću fotoredukcije intenzivnom pulsirajućom svjetlošću (IPL). IPL fotoredukcija traje 91 μs, što znatno pojednostavljuje izradu SC-RE elektroda. Optimalna energija IPL impulsa bila je 100 J pri 2000 V, čime se postigla stabilna Ag–AgCl ravnoteža bez prekomjernog stvaranja Ag nanočestica. Pripremljene membrane nanesene su na staklenu ugljičnu (GC-RM) i *inkjet* ispisanu srebrnu elektrodu (PE-RM). PE-RM je pokazala bržu stabilizaciju potencijala (3 min) i manju impedanciju, što ukazuje na bolji električni kontakt između membrane i tiskane površine. PE-RM elektrode pokazale su nisko zanošenje potencijala (–0,25 mV h^{-1}), dobru ponovljivost (ΔE^0 < 6 mV) i stabilan odziv u širokom rasponu iona i pH (2–10). U testovima s komercijalnim senzorima i redoks sustavom $[Fe(CN)_6]^{3-/4-}$, PE-RM su dale rezultate usporedive s komercijalnim referentnim elektrodama, potvrđujući njihovu pouzdanost i primjenjivost u elektrokemijskim mjerenjima.

U sklopu ovog istraživanja razvijen je skalabilan, isplativ pristup izradi potenciometrijskih senzora korištenjem *inkjet* ispisa. Električki vodljiva tinta na bazi grafenskih nanoplahta optimizirana je s naglaskom na primjenu ekološki prihvatljivih sintetskih postupaka, otapala, uzimajući u obzir stabilnost i ujednačenost. Proizvedena je fleksibilna amonij-selektivna elektroda s poboljšanim prijenosom naboja i smanjenim učinkom vodenog sloja, postižući visoku točnost u stvarnim uzorcima. Novi sustav otapala i automatizirana metoda nanošenja ion-selektivne membrane osigurali su ujednačene ionsko-selektivne membrane s brzim sušenjem. Fotokemijski pripremljena Ag/AgCl referentna membrana osigurala stabilne potencijale na svim podlogama. Ovi napredci potvrđuju izvedivost potpuno integrirane *inkjet* ispisane platforme za mjerenje, otvarajući put brzoj proizvodnji i integraciji u mikrofluidičke i nosive uređaje.

Contents

1. INTRODUCTION

World population growth, combined with global occurrences such as disease epidemics, has shifted the perception of medical diagnostics, moving it gradually from specialized laboratories to arrangements designed to be executed and understood by a large population of non-experts. Further on, extensively used smart technologies are driving the demand for adaptable tools capable of real-time, on-site monitoring and quantification of chemical species. With this, the idea of decentralisation of analytical laboratories has been proposed and further validated by growing environmental concerns that urged tracking ecologically relevant species.

Chemical information – e.g. concentration– can be investigated using chemical sensors. It originates from a specific interaction between the species of interest – an analyte – with a recognition element (receptor). A receptor is in direct spatial contact with a transducer that converts the energy carrying the sample chemical information into a useful analytical signal. The classification of chemical sensors is based on the operating principle of the transducer [1]. Relying on spontaneous electrochemical interactions between an analyte and a transducer, potentiometric electrochemical sensors are specifically interesting due to their operational simplicity, as they require only two electrodes and a voltmeter. In such a configuration, the open circuit potential of a sensor (indicator electrode) is measured against a reference electrode.

Potentiometry has been routinely used in many areas, including clinical, biomedical [2], environmental [3, 4] and industrial analyses [5], for almost fifty years. During that time, two key advances brought up to coining the idea of mass-production and miniaturisation of potentiometric sensing systems: substituting ion-selective glasses with receptor (ionophore) containing liquid polymeric membranes and the discovery and development of solid-material transducers. Compared to liquid counterparts, solid-contact transducers enabled planar layered electrode configuration that consists of an electrical lead, transducer and an ion-selective membrane. Techniques established in circuit boards

manufacturing were adopted at first, however, these were proven to be too slow, compatible with only a few substrates, and generated large amounts of toxic waste [6].

The second wave of planar electrode production was directed towards reducing material and energy consumption. The techniques originally developed for the graphics industry, namely screen printing and inkjet printing, were implemented. Comparing the two techniques, digital non-contact inkjet printing deposits material on demand, gives higher resolutions, and does not require masks or templates. Thus, inkjet printing is highly desirable when the material to be deposited is expensive or limited, and when the substrate material is stress sensitive. It is highly adaptable for research and development of novel functional ink formulations [7]. Functional ink development still presents a challenge: the ink's physical properties should be tailored to enable unique droplet generation and sufficient adhesion to the substrate. Post-production processing should be considered too, as it helps in restoring the electrical conductivity of the printed patterns [6]. Very similar to inkjet printing, automated fluid dispensing relies on pressure-driven fluid ejection from a nozzle controlled by a robot. Compared to inkjet printing, the nozzles of the dispenser have a greater diameter, enabling the ejection of more viscous liquids.

Within this context, the aim of this dissertation is to resolve challenges associated with the production of solid-contact ion-selective and reference electrodes using contactless deposition techniques, namely inkjet printing and automated dispensing. To achieve this, we first developed an inkjet printable, electrically conductive ink based on melamine-intercalated graphene nanosheets (MGNS). We explored different solvents and stabilisers to enable the jetting of isolated droplets and good adhesion of homogeneous lines on polymer substrates. We examined the number of overprints and post-print processing conditions needed for achieving electrically conductive inkjet printed patterns. Next, ammonium-selective electrodes were fabricated by printing silver nanoparticle ink as electrical leads, MGNS ink as solid-contact material, and drop-casting the polymeric membrane. By doing so, we examined the possibility of using the MGNS ink as a solid-contact layer in ammonium-selective electrodes and evaluated the analytical performance of the developed electrodes.

It is well known that inkjet printing of the ion-selective membrane is extremely challenging. To establish means of reproducible membrane deposition in the fewest steps possible, we have optimised ion-selective membrane composition for contactless deposition, without changing the membrane solute content. The membrane was dispensed onto screen-printed carbon electrodes using an automated fluid dispenser. We evaluated membrane evaporative drying by tracking the impedance changes as the solvent evaporates.

Finally, to close the potentiometric circuit, a reference membrane based on the silver / silver chloride pair produced by partial photoreduction with intense pulsed light was deposited onto different electrically conductive substrates. The stability of the electrode response was rigorously tested using different electroanalytical techniques.

The presented research was concluded to test the following hypotheses:

1. Improved analytical performance of ion-selective electrodes can be achieved using carbon nanomaterials as solid contacts in inkjet printing.
2. Optimizing the ion-selective membrane allows for contactless automated deposition and satisfactory performance.
3. A solid-contact reference electrode from photoreduced silver chloride will have stable potential across a wide concentration range.

2. STATE OF THE ART IN THE DEVELOPMENT OF SOLID-CONTACT POTENTIOMETRIC SYSTEMS

2.1. Potentiometry

A chemical sensor is a self-contained device that gives information on the concentration of a specific sample component within a system of interest. The information is an analytically useful signal delivered from a series of interactions: an analyte specifically interacts with a recognition element (receptor) confined in direct proximity to a transduction element. The transducer converts the energy carrying the chemical information about the sample into a physical quantity that an end user can interpret. The accepted classification of chemical sensors is based on the operating principle of the transducer. This classification includes: optical, electrochemical, electrical, mass sensitive, magnetic, and thermometric sensors. Electrochemical sensors transform the effect of the electrochemical interaction of an analyte with an electrode into a measurable signal. Such effects may be stimulated electrically or may result from a spontaneous interaction at the zero-current condition [1].

Operating at zero-current conditions, potentiometric electrochemical sensors are galvanic cells containing an ion-selective electrode (ISE) and a reference electrode (RE), Figure 1. The two electrodes are connected to a high-impedance milivoltmeter that ensures zero-current measurements. During a potentiometric measurement, a magnitude of potential difference between the two electrodes is measured as a function of an analyte concentration. The measured potential change is correlated to analyte concentration after electrode calibration.

Potentiometry as an analytical technique appeared at the beginning of the 20th century, after discovering pH-sensitive glasses. Although pH meters based on thin glass bulb electrodes were commercialised in the 1930s [8], the renaissance of potentiometry is closely related to the discovery of ion-binding properties of antibiotics valinomycin and nonactin in 1965 by Berton C. Pressman [9]. This discovery was followed by extensive

research and synthesis of an abundance of ionophores, resulting in receptors for more than a hundred ionic species [10]. The research and commercialisation of potentiometric analysers are closely related to clinical blood analyses, as potentiometry successfully replaced flame photometry in the 1980s, allowing traditional laboratory testing to move closer to the patient for improved patient care in the emergency, surgical, and critical care settings [11].
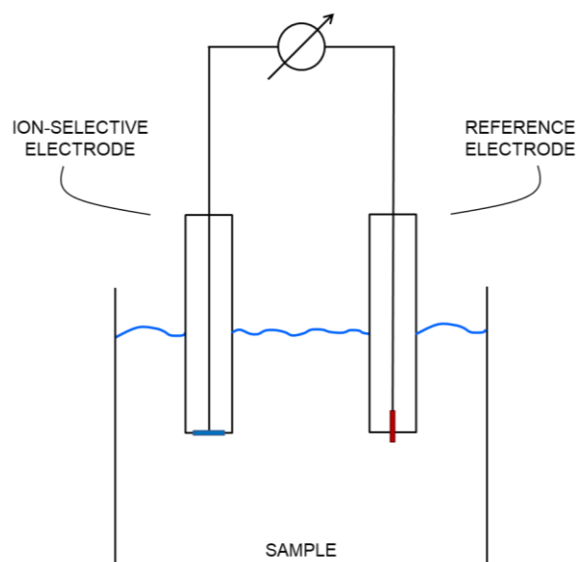
Figure 1. Schematic diagram of an electrochemical cell for potentiometric measurements.

2.1.1. *Conventional ion-selective electrode design*

The response mechanism of ion-selective electrodes stems from its' design and ion-selective membrane composition. Modern ion-selective electrodes consist of three key functional parts: ion-selective membrane, transducer and electrical lead.

Ion-selective membrane

The ion-selective membrane (ISM) is a lipophilic matrix that holds together the components responsible for a well-defined potentiometric response: an ionophore and a lipophilic ion-exchanger [12]. Historically, different kinds of ion-selective membranes have been used. Cremer's discovery that the potential of a thin glass bulb depends on the pH of the solution propelled the systematic study of the glass membrane composition to the

electrode response to different charged species. However, these first membranes with fixed ionic sites were very brittle and suffered from poor selectivities [13]. The earliest examples of polymeric membranes with mobile ionic sites were prepared as ionophore solutions in non-volatile and viscous organic water immiscible solvents infused into porous support, such as filter paper or glass frit [14].

The electrodes' mechanical stability was significantly improved after introducing polymers as ion-selective membrane matrices. The ideal polymer provides a rubberlike homogeneous medium in which membrane components can move freely, as they do in a water-immiscible solvent [12]. During the last fifty years, silicon rubber, photocured polymers of acrylic or urethane nature, and acrylic siloxane polymers have been used [15]. However, plasticised poly(vinyl chloride) (PVC) remained historically the most relevant and still most widely used [12, 14].

Typically, solvent polymeric membranes contain about 33 wt.% of PVC and 66 wt.% of plasticiser. Plasticisers are non-volatile organic liquids with relatively small molecules that, when mixed with polymers separate polymer chains and lower the polymers' glass transition temperature (T_g) below room temperature. By adding the plasticiser, the polymer turns from hard and brittle into soft and flexible. This improves the ion mobility within the membrane and lowers the membrane resistance [16]. Mostly used PVC membrane plasticisers are bis(2-ethylhexyl sebacate) (DOS) and *o*-nitrophenyl octyl ether (*o*-NPOE).

(a)   (b)
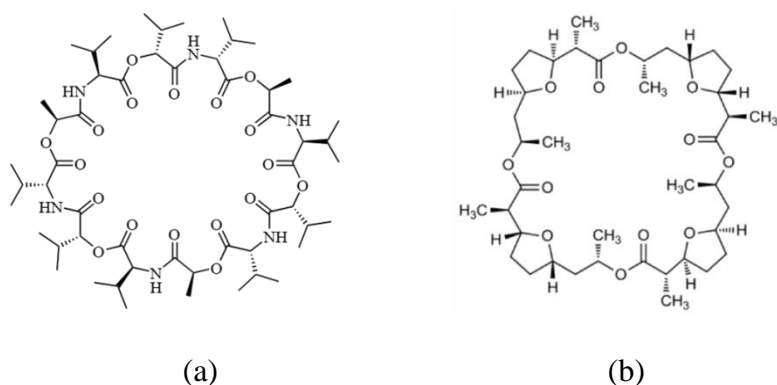
Figure 2. Chemical structure of (a) valinomycin (K^+ ionophore) and

(b) nonactin (NH_4^+ ionophore).

Lipophilic ionophores and ion exchangers are required to obtain a reliable potentiometric response. Both are used in relatively small amounts of 1–3 wt.%. An ionophore is basically a potentiometric electrochemical sensors' receptor – it selectively binds ions within the membrane. Ionophores' building blocks include alkyl chains that ensure lipophilicity needed to retain the molecule within the membrane; a polar moiety or a set of polar functional groups responsible for the target recognition; and hydrophobic regions compatible with the surrounding membrane matrix [14]. Among the first and still widely used ionophores were those of macrocyclic structure; valinomycin (high selectivity to K^+ ions) and nonactine (high selectivity to NH_4^+ ions) (Figure 2).

Ionophores are key components for achieving sensors' high selectivity: a properly functioning ionophore should bind the primary ion more strongly than the interfering ions. This binding interaction between the ionophore and analyte is expressed with the equilibrium constant, β_{IL}. The stronger the interaction with the primary ion, the more selective the electrode will be for it [17].

Most ionophores used in modern ion-selective electrodes are electrically neutral molecules in their uncomplexed form. As such, they do not render the ion-exchanging properties needed for proper ion-selective electrode functioning. Thus, in the absence of negatively charged sites within the membrane, both primary ions (e.g. cations) and anions will enter the membrane. Lipophilic ion exchangers are salts that form the counterion of the

complexed analyte ion within the membrane, thus maintaining a constant concentration of the primary ions within the membrane, and preventing the counterions from the sample from entering the membrane. For instance, a cation-selective membrane may contain the ionophore and alkali metal salt of tetraphenylborate (TPB$^-$), tetrakis[p-chlorophenyl]borate (TpClPB$^-$) or tetrakis[3,5-bis(trifluoromethyl)phenyl]borate (TFPB$^-$), with structures shown in Figure 3. Anion-selective membranes may be doped with tridodecylmethylammonium (TDMA$^+$) chloride as anion-exchanger in addition to the ionophore [18].

| (a) | (b) | (c) |
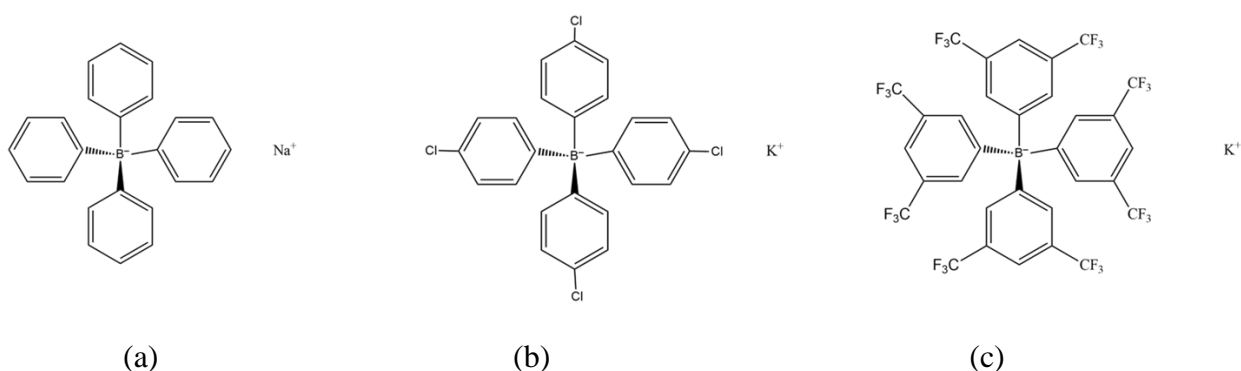
Figure 3. Chemical structure of alkali metal salt of (a) tetraphenylborate (TPB$^-$),
(b) tetrakis[p-chlorophenyl]borate (TpClPB$^-$) and
(c) tetrakis[3,5-bis(trifluoromethyl)phenyl]borate (TFPB$^-$).

Conventional (inner filling) transducer

Conventional ion-selective electrodes are relatively robust, consisting of a tubular body made from chemically and mechanically resistant polymer, with a polymeric ion-selective membrane fixed at the end of the body with suitable glue or clamping. In this electrode configuration, the ion-selective membrane is actually a separator between the sample and the inner filling solution. For a stable potentiometric response, the potential difference between the ion-selective membrane and inner filling solution must remain constant during the scope of measurement. Thus, an inner filling must contain a constant concentration of an ion to which the electrode is sensitive.

Within the membrane and internal filling, ion movement contributes to the conductivity, while the electrical contacts are electronic conductors. A reversible transduction from the ionic to electronic conductivity is achieved by using an internal reference electrode, mostly an Ag/AgCl electrode. This is a second-order metallic electrode, where ion-to-electron transduction is based on the following reversible redox reaction:

$$AgCl_{(s)} + e^- \rightleftarrows Ag_{(s)} + Cl^- \tag{1}$$

The internal reference electrode requires a defined chloride concentration to give a stable potential. This is achieved owing to the low solubility of the silver salt and by ensuring a constant concentration of Cl^- ions within the inner filling [16].

2.1.2. Conventional reference electrode design

A stable reference electrode is as equally important as a sensing electrode, as its potential stability dictates the integrity of the overall measured electromotive force. Thus, the potential of a reliable reference electrode should not drift nor change regardless of the sample composition, it should only show minimal temperature dependence without any hysteresis, it should obey the Nernst equation concerning species comprised within the reference half-cell, and it should be robust to poisoning by chemical species [19].

Reference electrodes are typically metallic electrodes of the second order, that is, a metal in contact with its low-soluble salt, immersed in a solution containing the anion forming that salt. Both the electrode and internal reference solution are contained within a reservoir and separated from the sample by a porous glass, polymeric frit, gel, membrane or capillary. Silver/silver chloride reference electrode immersed in 3 mol dm^{-3} KCl solution is probably the most frequently used in modern electroanalytical practice; it's non-toxic, simple to construct and maintain, and easy to miniaturise [20]. In cases where the reference electrolyte is chemically incompatible with the sample or may result in contamination, an intermediate salt bridge is placed between the reference electrolyte and the sample solution.

2.2. Ion-selective electrode response

There has been a lot of discussion on the response theory of solvent polymeric membrane electrodes during the last 50 years [21]. However, all the models rest on the same groundwork: the phase boundary potential model. Potentiometric electrochemical sensors measure the potential difference between two electrodes within a galvanic cell under zero-current conditions, typically represented as:

Ag | AgCl | KCl$_{(aq)}$ | LiOAc$_{(aq)}$ || sample || ISM | internal reference solution | AgCl | Ag

E_1 E_2 E_3 E_J E_M E_4 E_5

reference electrode   ion-selective electrode
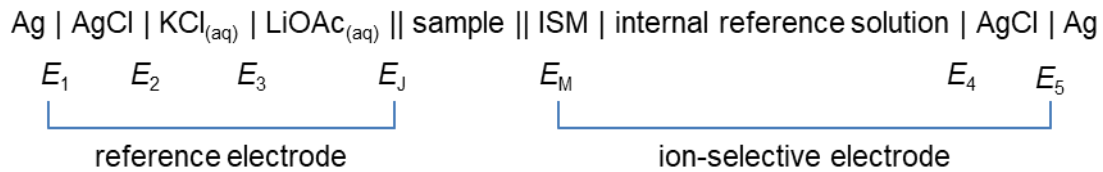
where ISM represents an ion-selective membrane and LiOAc is lithium acetate bridge electrolyte. The bridge electrolyte is not a necessary component of a reference electrode, but it plays a vital role in maintaining a stable ionic environment at the vicinity of the porous frit. In practice, lithium acetate is preferred as Li^+ and OAc^- have very similar mobilities, suggesting the smallest liquid junction potential, E_J, the potential difference generated at the phase boundary of the reference electrode's intermediate salt bridge and the sample solution. The measured electromotive force (EMF) between the two cell terminals is the sum of all phase boundary potentials across the cell:

$$EMF = \sum E_{PB} = (E_1 + E_2 + E_3 + E_4 + E_5) + E_J + E_M \tag{2}$$

Due to the electrodes' construction, potential differences E_1 to E_5 are sample independent and thus constant. The measured EMF can be described as:

$$EMF = E_{const.} + E_J + E_M \tag{3}$$

where E_J is the liquid junction potential and E_M is the membrane potential. . E_J should be kept as small as possible. Then, the only remaining phase-boundary potential that is not included in the constant term is the membrane potential:

$$EMF = E_{\text{const.}} + E_{\text{M}} \tag{4}$$

In conventional electrode design, the ISM is fixed between the inner reference electrolyte and the sample. Thus, E_{M} arises from the phase boundary potential between the inner solution and the membrane (E_{PB}), the diffusion within the membrane (E_{D}) and the phase boundary potential between the membrane and the sample (E_{PB^*}):

$$E_{\text{M}} = E_{\text{PB}} + E_{\text{D}} + E_{\text{PB}^*} \tag{5}$$

E_{PB} can be assumed constant and independent of the sample. The diffusion within the ISM becomes insignificant once an electrode is conditioned with a solution of the target ion it responds to (the electroneutrality condition). Finally, the potential of the ISM depends only on the phase boundary potential between the membrane and the sample, that is: $E_{\text{M}} = E_{\text{PB}^*}$ [12, 14, 22]. These assumptions provide the foundation for the thermodynamical considerations for the electrochemical potential at both the aqueous (sample) and organic (ISM) phase:

$$\mu(\text{aq}) = \mu^0(\text{aq}) + RT \ln a_{\text{I}}(\text{aq}) + z_{\text{I}} F \phi(\text{aq}) \tag{6}$$

$$\mu(\text{org}) = \mu^0(\text{org}) + RT \ln a_{\text{I}}(\text{org}) + z_{\text{I}} F \phi(\text{org}) \tag{7}$$

Where μ is the chemical potential (μ^0 under standard conditions), z_{I} is the charge, a_{I} the activity of the uncomplexed ion I, ϕ is the electrical potential, R, T, F are the universal gas constant, the absolute temperature and the Faraday constant. Assuming that ion transfer is fast and reversible and that the organic and aqueous phases are immiscible, the phase boundary potential for the condition of electrochemical equilibrium between the organic and aqueous phases can be expressed as:

$$E_{\text{PB}} = \Delta\phi = -\frac{\mu^0(\text{org}) - \mu^0(\text{aq})}{z_{\text{I}} F} + \frac{RT}{z_{\text{I}} F} \ln \frac{a_{\text{I}}(\text{aq})}{a_{\text{I}}(\text{org})} \tag{8}$$

11

After combining the standard chemical potentials into the ion-partition constant related to the free energy of the primary ion, k_I:

$$k_I = \exp\frac{\mu^0(\text{aq}) - \mu^0(\text{org})}{RT} \tag{9}$$

$$E_{PB} = \frac{RT}{z_I F}\ln k_I + \frac{RT}{z_I F}\ln\frac{a_I(\text{aq})}{a_I(\text{org})} \tag{10}$$

$$E_{PB} = E^0 + \frac{RT}{z_I F}\ln\frac{a_I(\text{aq})}{a_I(\text{org})} \tag{11}$$

$$E_{PB} = E^0 + \frac{2.303 \cdot RT}{z_I F}\log\frac{a_I(\text{aq})}{a_I(\text{org})} \tag{12}$$

E^0 is the standard potential that depends on the solvation energies of the ion I in the two phases. The Nernstian response to the ion I in the sample phase, that is, the optimal selectivity, can only be obtained if the term $a_I(\text{org})$ is constant. Then, the term $a_I(\text{org})$ can be included with all other sample-independent potential contributions (E^0), giving the simplified Nernst equation:

$$E_{PB} = E^0 + \frac{2.303 \cdot RT}{z_I F}\log a_I(\text{aq}) \tag{13}$$

The sample solution always contains both primary ions and their counter ions. Then, both primary ions (e.g. cations) and their counter ions (e.g. anions) will diffuse into neutral ionophore-doped ISM due to the electroneutrality condition. Selectivity towards cations (permselectivity) can be obtained by doping a membrane with a lipophilic salt of a tetraphenylborate derivative as an anionic site, whereas anion selectivity can be obtained by doping a membrane with a salt of a lipophilic tetraalkylammonium as a cationic site [22]. Typically, the amount of ion-exchanger is 50 mol% of the ionophore, assuring the excess of the free ionophore in the ISM for the analyte binding [23].

Even though both ion-selective and reference electrodes with liquid reservoirs are quite robust and easy to make, the accepted setup comes with non-negligible disadvantages. Due to the sensitivity of the inner filling solution to evaporation and leakage, they lack from restricted temperature and pressure usage. Furthermore, as the ionic strength of the sample and internal reference solution differentiates, the developed osmotic pressure results in net water transport into or out of the reference solution [24]. Thus, the reference solution should be frequently checked and replaced, which is standard laboratory practice. On the other hand, to achieve truly miniaturisable sensors that can be integrated into various architectures, often unattainable to the conventional sensors' setup, the liquid reservoir is replaced with a solid-state counterpart. In this way, sensor miniaturisation is no longer limited by the minimum reference electrolyte volume that does not evaporate during the measurement.

2.3. Solid-contact ion-selective electrodes

A primer to solid-contact ion-selective electrodes (SC-ISE) – presented in 1970 by Hirata and Date [25] and followed by Cattrall – is well-known in the electroanalytical community as a coated-wire electrode (CWE). The first CWE was obtained by directly coating a Pt-wire with a polymeric calcium-selective membrane [26]. Despite the simplicity and affordability, the CWE did not stay in use, as the electrode suffered from poor potential stability due to the 'blocked' interface between the purely electronic conductor (metal wire) and the purely ionic conductor (ISM). This interface can be described as an asymmetric capacitor having a very small interfacial contact area. Thus, CWEs easily pick up noise and suffer from large potential drifts, as they are easily polarizable and prone to the formation of a thin aqueous layer at the metal | ISM interface [24].

Solid-contact electrode configuration presents the last step in modern ion-selective (and reference) electrode development. SC-ISEs are obtained by placing an adequate solid material in direct spatial contact with an electrode material on one side and an ion-selective membrane on the other side. The solid contact is in fact a transducer that acts as a mediator

to the potential stability of the electrode, which is a prerequisite for obtaining a reliable potentiometric response. Thus, a stable potential of SC-ISE stems from [27]:

1) Stable and reversible transition from ionic to electronic conductivity

2) Ideally non-polarizable interfaces with high exchange current densities

3) Absence of side reactions parallel to the main electrode reaction.

For any ISE, the input signal is the activity of a specific ion, and the output is an electrical potential. Within the ISM, the free charge carriers are ions, however, at the membrane | electrically conducting substrate interface, the conversion of the charge carrier from ions to electrons must occur. The well-defined ion-to-electron transduction processes of SC-ISEs are related to the presence of redox or double-layer capacitance at the SC | ISM interface, which is determined by the inherent characteristics of solid-contact functional materials acting as ion-to-electron transducers.

Conductive polymers (CP) were the first materials to be introduced as the solid transducer in the early 1990s [28] and were later followed by nanostructured materials [29]. The last three decades of ISE development were marked by the introduction of many other functional materials classes, including metal nanomaterials [30], molecular redox couples [31], and metal-organic frameworks [32]. The transduction mechanism and response of SC-ISEs is explained by two key mechanisms: 1. high redox capacitance and 2. high double-layer capacitance; both schematically presented in Figure 4.
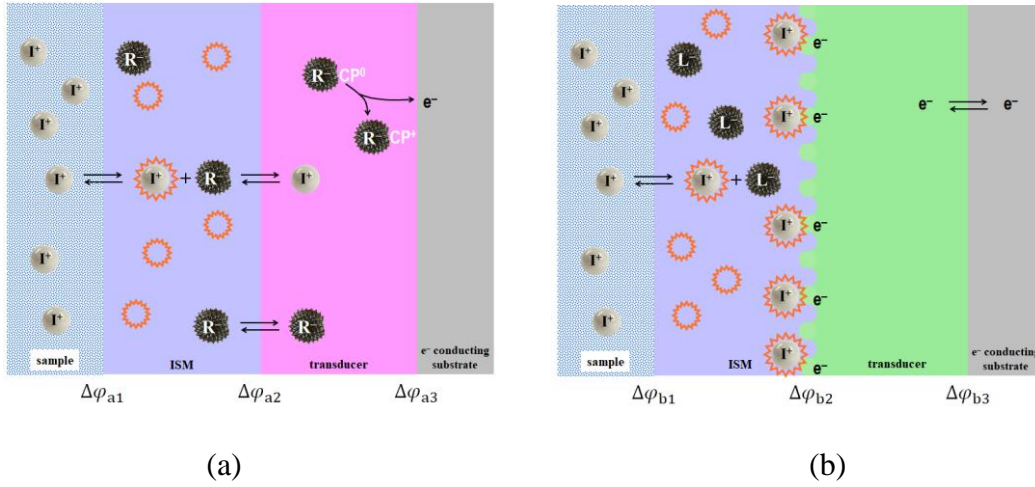
Figure 4. Schematic representation of a transduction mechanism of a solid-contact ion-selective electrode based on (a) high redox capacitance; (b) high double-layer capacitance.

2.3.1. High redox capacitance solid contact

Analogous to the signal transduction of classical ion-selective electrodes with a liquid reservoir, high redox capacitance-based ion-to-electron transduction involves the reversible redox reaction between the oxidising and reducing species. As illustrated in Figure 4(a), the response relies on the phase boundary potential model. At the ISM | solution interface the primary ion I^+ binds to an electrically neutral ionophore, L:

$$I_{(aq)} + L_{(m)} \rightleftarrows I^+L_{(m)} \tag{14}$$
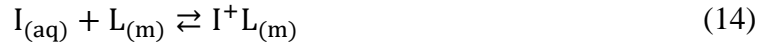
The interfacial potential at this phase boundary ($\Delta\varphi_{a1}$) is determined by the charge separation between the ISM and sample, which is related to the primary ion activity, according to equation (13). At the second phase boundary – the SC | ISM interface – φ_{a2} arises due to the distribution of I^+ and lipophilic ion-exchanger (R^-). I^+ and R^- can partition both into and from the SC causing a local redox reaction within the SC [Hu (2016)] [24]:

$$CP^+A^-_{(solid\ contact)} + I^+_{(ISM)} + e^- \rightleftarrows CP^0A^-I^+_{(solid\ contact)} \tag{15}$$

$$CP^+R^-_{(solid\ contact)} + e^- \rightleftarrows CP^0_{(solid\ contact)} + R^-_{(membrane)} \tag{16}$$

15
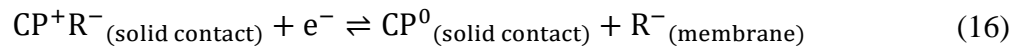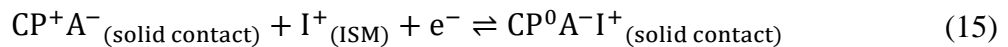
where CP denotes the conductive polymer, A^- is the doping ion of the CP, I^+ is the analyte cation, and R^- the hydrophobic counter ion (ion-exchanger). Consequently, the interfacial potential at the SC | electronic conductor interface ($\Delta\varphi_{a3}$) arises due to the electron flow to/from the electrically conductive substrate, enabling the electrical potential difference to be measured by the equipment [33]. It is assumed that both $\Delta\varphi_{a2}$ and $\Delta\varphi_{a3}$ are constant values and are actually included in the term E^0 in equation (13).

The high redox capacitance comes from redox buffering properties of materials that contribute to the electrical conductivity by mixed electronic and ionic conductivity. The potential drift at the SC | ISM interface can be related to the SC capacitance:

$$\text{potential drift} = \Delta\varphi_{a2} = \frac{\Delta E}{\Delta t} = \frac{i}{C} \tag{17}$$

For a given constant electrical current i, there will be a change in the electrode potential with time. As the current-flow through a potentiometric cell is infinitesimally small, the potential drift falls as the capacitance, C increases, buffering the potential drifts due to 'blocked' interfaces [21].

Historically most important representatives are conducting polymers. Polypyrrole, poly(3-octylthipohene), polyaniline, and poly(3,4-ethylenedioxythiophene) (PEDOT) are most often used as SC-materials [21]. Their properties can be relatively easily tailored by doping and functionalization. For example, PEDOT was functionalized with perfluorinated alkanoate side chain, which significantly increased the materials' hydrophobicity, thus reducing the possibility of water-layer formation and increasing the sensors' lifetime [34]. However, conducting polymers' redox activity can cause drift to the measured potential; polyaniline is well-known for its' pH sensitivity and it should not be used in combination with H^+ and OH^- permeable membranes [24].

Other electroactive materials that rely on high redox capacitance properties have also been investigated. Redox couples that maintain a stable and reproducible potential in environments containing oxidising or reducing impurities, or systems where small currents

are passing were investigated. Lipophilic redox-active self-assembled monolayers (SAMs) as transducers were introduced by Pretsch's group [35]. In principle, SAM-based redox mediators adhere strongly to the Au electrode through strong Au–S bonds, forming a compact lipophilic layer that supports ISM deposition and simultaneously enables signal transduction via their redox-active terminal groups. Terminating groups such as tetrathiafulvalene [36] and ferrocene [37] have been shown to significantly improve sensors' response stability. Alternative redox mediators which do not require the Au-electrode surface have been studied. Bühlmann's group reported a SC-ISE based on tetrakis(pentafluorophenyl)borate (TPFPB$^-$) salts of cobalt(II)tris(1,10-phenanthroline) ([Co(phen)$_3$]$^{2+}$) and cobalt(III)tris(1,10-phenanthroline) ([Co(phen)$_3$]$^{3+}$) [38]. These highly lipophilic salts were directly mixed into a solvent PVC-based ion-selective membrane that was drop-cast onto various electrode supports, giving electrodes of exceptional E^0 reproducibility. Michalska et al. showcased that a combination of two different compounds containing metal ions in different oxidation states, cobalt(II) porphyrin and cobalt(III) corrole can effectively stabilize the redox potential at the backside of the ISM, assuring high reproducibility of recorded potentials in time [39, 40] conductive nanomaterials

2.3.2. *High double-layer capacitance solid contact*

For transducers that do not rely on the reversible redox reaction, the signal conversion stems from charging and discharging phenomena at the SC | ISM phase boundary. Thus, this phase boundary can be regarded as an asymmetric capacitor, that is, an electrical double layer, where ions accumulate on one plane (ISM), while electrons or holes accumulate on the other plane (SC). This is schematically illustrated in Figure 4(b). Again, based on the phase boundary potential model, the potential change at the ISM | solution interface ($\Delta\varphi_{b1}$) stems from the partitioning of ion I^+ between the two phases (equation (14)), and is described by equation (13). The interfacial potential at the asymmetric capacitor ($\Delta\varphi_{b2}$) develops due to the charge attraction and relies on the charge quantity in the electrical double layer. Its' stability against drifting is defined by the capacitance value of the asymmetric capacitor and it follows the equation (15). Finally, at the electronic conductor | SC interface ($\Delta\varphi_{b3}$) arises due to the electron flow to/from the electrically

conductive substrate. The described transduction mechanism is purely capacitive, as functional materials do not exhibit redox behaviour [33].

A routine method to increase the double-layer capacitance is to increase the interfacial SC | ISM contact area without necessarily increasing the geometric projection of the solid contact [24]. This is done by utilising electrically conductive nanomaterials as SC, such as sp^2-hybridized carbon nanomaterials. Reduced graphene oxide [41], graphene [42], carbon nanotubes [43], fullerene C_{60} [44] and metal-organic frameworks [32] were shown to improve the potentiometric response stability, repeatability and reliability. These materials act as an extension to the electronically conducting electrode and do not suffer from redox side reactions, gaseous or light interferences, or thin water-layer formation.

2.3.3. Solid-contact materials characterisation

Originating from the phase-boundary response model, the measured ion-selective electrode potential stems from the phenomena happening at the ISM | sample phase boundary. All the other phase boundary-related potential drops are sample independent and are included in the standard potential value, E^0. Thus, E^0 – obtained by electrode calibration – depends on the identity of the SC material. E^0 stability and reproducibility, both of a single electrode and within the series of equally fabricated electrodes, present the ultimate goal of SC-ISE development for a large-scale production. E^0 stability and reproducibility stem from two key properties of a solid contact material: capacitance and hydrophobicity.

SC materials' hydrophobicity is crucial against unwanted thin water layer formation at the SC | ISM junction. Since the polymeric ISM uptakes water during the conditioning, a nanometre-thin aqueous layer forms at the SC | ISM junction if an ISM does not adhere well to the SC and/or the SC is not sufficiently hydrophobic. This thin aqueous layer acts as an intermediate liquid reservoir, just as in the conventional ISE setup. However, its' composition is altered upon sample changes, leading to drifting potentials [45]. Water accumulation at the backside of the ISM causes drifts – slow, non-random changes in the

measured open circuit potential (OCP) kept in a solution of constant composition and temperature [46].

Pretsch's group proposed a protocol to detect the thin water layer presence by detecting the sample-related variation of aqueous layer at the SC | ISM junction [45]. This protocol is well-known in the sensor community as the water-layer test (WLT). The theoretical potential readings of a positive and negative WLT are depicted in Figure 5.
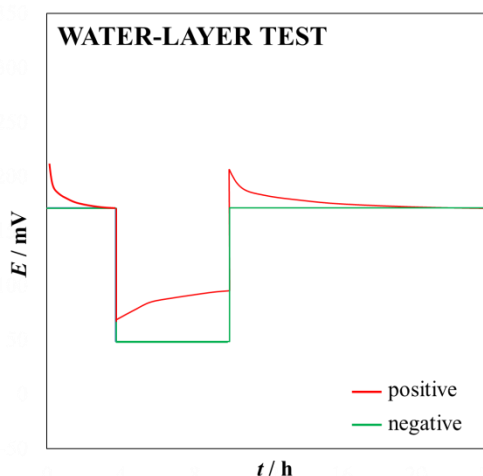
Figure 5. Theoretical potential readings of the SC-ISEs in the presence (red line) or in the absence of a thin water layer (green line) during the water layer test.

In principle, the electrode is first contacted with a primary ion solution (step 1), then the solution is replaced by an interfering ion solution (step 2) and finally, the electrode is placed back in contact with the primary ion solution (step 3). The observed response drop in step 2 is due to the preference for the primary ion. Drifts in steps 2 and 3 are the key indicators to the outcome of the WLT. A negative WLT is characterised by the fast potential stabilisation and the absence of drifts in steps 2 and 3 (see green line in Figure 5).

Positive WLT shows strong drifts in steps 2 and 3. After conditioning the electrode with primary ion solution (step 1), it is assumed that water layer of negligibly small volume contains only primary ions. In step 2, as soon as the first small amount of the discriminating ions reaches the inner membrane surface, due to the membrane selectivity, the interfering ions are expelled from the membrane, and replaced with the primary ions from the water

layer, causing the measurement of a positive drift (when discussing a cation-selective electrode). In the opposite case of exchanging the interfering ion with the primary ion (step 3) at the sample side, the change of the potential at the back of the membrane solely determines the measured drift. In particular, during step 3 at the backside of the membrane, the discriminating ions are replaced with the primary ions – this process completely determines the potential drift of the electrode. Because this process is very slow, step 3 in practice takes multiple hours recordings.

Long-term drifts are caused by Fickian diffusion of ions within the thin aqueous layer [45]. SC materials wetting properties are usually inspected by water contact angle measurements – the higher this value, the greater the SC material hydrophobicity and, ultimately better stability against water layer formation [47].

Apart from the slow ionic fluxes within the water layer, potential drifts stem from the blocked interface at the back of the ISM. In practice, all solid contacts are polarized to some extent, as a very small input current of an amplifier is imposed on the potentiometric cell during the measurement. In electrochemistry, solid interfaces are commonly illustrated using electrochemical equivalent circuits, most commonly a series of parallel resistor-capacitor elements. Applying small constant direct current perturbations to the SC-ISE influences the observed potential response in the following way:

$$E = iR_{\mathrm{t}} + \frac{it}{C_{\mathrm{L}}} \tag{18}$$

Where i is the applied electrical current, t is the time of measurement, R_{t} is the total resistance of the electrode dominated by the presence of the ISM, C_{L} is the low frequency capacitance of the electrode, that is the redox/double layer capacitance of the SC-layer. When the applied current is constant, equation (18) can be summed to equation (17) that basically shows that a large C_{L} is necessary for a satisfactory potential stability [33]. The C_{L} value is then determined from the resulting potential jump after applying a constant current of a positive and negative sign. The method is known as constant current chronopotentiometry and is a routine SC-ISE characterisation technique.

Electrochemical impedance spectroscopy (EIS) is another routinely used technique for SC-ISE characterisation, as it gives information on both low-frequency capacitance and electrode resistance [29, 48]. In EIS, a small amplitude AC voltage is superimposed on a DC voltage that is applied to the working electrode and the resulting response is obtained over a wide range of frequencies. From the obtained impedance spectra – presented as imaginary impedance versus real impedance (Nyquist plot) or impedance amplitude versus frequency of the input signal (Bodé plot) – by equivalent electrical circuit modelling one can obtain numerical values of capacitances and resistances related to different electrode elements.

2.4. Solid-contact reference electrodes

A typical solid-contact reference electrode (SC-RE) consists of an electrically conducting support, a transducer and a reference membrane. The simplest and most practical form of a SC-RE is a quasi-reference electrode: a silver/silver chloride wire or pad. However, its reliability is determined by the solubility of the thin AgCl layer and the electrodes' sensitivity to chloride and other interfering ion concentrations [49].

A true solid-state reference electrode can be constructed simply by covering the Ag/AgCl layer with a protective Cl-ion containing membrane that serves as an internal filling. A Ag/AgCl SC-RE was fabricated by smearing KCl-containing agarose gel onto a chemically chlorinated Ag-electrode surface [50]. The electrodes had shown satisfactory performance in potentiometric tests. However, the authors reported limited electrode lifetime due to agarose gel dehydration and shrinkage. Storage stability of Ag/AgCl-based SC-REs was significantly improved by depositing a commercial UV-curable paste mixed with ground KCl powder [51].

An important practical consideration in designing novel reference electrodes is ensuring their compatibility with the indicator electrodes they will be paired with. Solid-contact reference elements can be made in the same manner as SC-ISE, by layering

electronic conductors other than silver and silver chloride with a transducer element and a reference membrane. Michalska's group reported a stable and reliable SC-RE consisting of glassy electrode support, electrodeposited polypyrrole transducing layer and a poly(n-butyl acrylate)-based reference membrane doped with AgCl and KCl powder [52].

Considering the mass production, it is utterly important to define ways of simplifying electrode construction by removing unnecessary steps in the fabrication. Wang and coworkers developed a valuable strategy for a reference element applicable to Ag/AgCl pads [53]. A polyvinyl butyral (PVB) methanol solution was mixed with an excess of NaCl and deposited onto a Ag/AgCl surface. The validity and suitability of this reference element for various fully integrated sensor arrays were broadly demonstrated by many research groups [54-58]. Andrade and coworkers continued on this research and developed a reference element applicable to various non-silver conducting surfaces [59]. They added $AgNO_3$ to a NaCl-containing PVB methanol solution. Upon sonication, AgCl was formed, with NaCl in excess. This formulation was exposed to a light bulb for 10 minutes, allowing for a partial photoreduction of AgCl to Ag. Finally, the formulation was drop-cast onto glassy-carbon electrode supports and dried, forming a self-standing, reliable reference membrane.

Alternatively, reference electrodes containing ionic liquids have emerged [60]. Ionic liquids are liquid-state organic salts, composed of an organic cation and an organic anion [61]. Ionic liquids can easily be mixed within a plasticised PVC membrane and deposited onto a solid contact of choice [62]. The potential stability of ionic liquids-based reference electrodes is based on the partitioning of the ionic liquids at the membrane | solution phase boundary, that is their leakage. Because of that, ionic liquids-based reference electrodes have very short working life [63].

Typically, reference electrodes' performances are characterised by the drift measurements in solutions of different ionic composition and concentration. A drift value is typically expressed as a millivolt change per hour. When constructing a SC-RE, one must aim to minimising drifts, regardless of the sample concentration or composition.

2.5. Analytical characteristics of solid-contact potentiometric sensors

Analytical characterisation of a sensor is the last step preceding the intended use. Regardless of the transducer type, there are several analytical characteristics describing a potentiometric sensor: sensitivity and dynamic linear range, limit of detection (LOD), selectivity, stability, reproducibility, reversibility, response time, and lifetime. Different sensors can be compared based on these Figures of merit, bolding the suitability of a particular system for its intended application.

Potentiometric sensor calibration is performed by recording the open circuit potential of the potentiometric cell as a function of standard solution concentration (logarithmic concentration change). A typical calibration curve is illustrated in Figure 6. It consists of a dynamic linear range obtained by linear fitting that gives an equation with a slope equal to the sensors' sensitivity and an intercept equal to the sensors' E^0 value. The theoretical sensitivity is defined by the Nernst equation as $(2.303RT)/z_I F$, that is, $59.2/z_I$ mV dec^{-1} at 25 °C, showing that the sensitivity depends on the number of charges of an analyte.
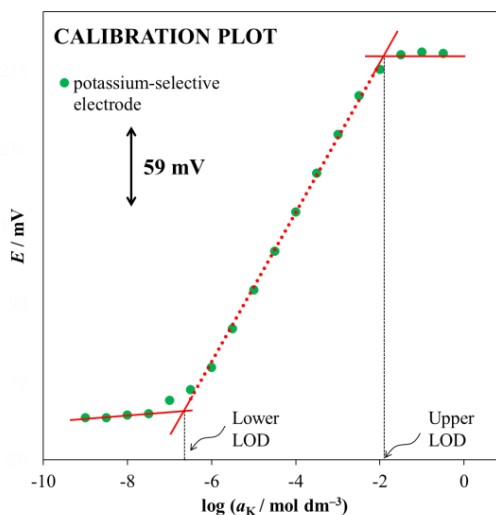

Figure 6. An example of a calibration curve of a monovalent cation selective potentiometric probe.

The linear range is defined by the lower LOD and the upper LOD. LOD is the limiting concentration above which (for lower LOD) or under which (for upper LOD) the analyte can be reliably detected. In the case of cation-selective ISEs, it was found that the lower LOD stems from cation interference, due to primary ion leaking from the ISM into the solution of very low concentration, while the upper LOD appears due to anion interference, due to the loss of permselectivity at high concentrations of charged species (and vice versa for anion-selective membranes) [64]. Thus, for potentiometry, IUPAC recommends that the upper and lower LOD are determined as the intercepts between different linear segments of the calibration curve (see Figure 6) [65].

Important information can be extracted from calibration: sensors' lifetime. It is the period within which slope, LOD and E^0 do not change to any significant extent, that is, the sensors' response is reliable.

Selectivity is unarguably the most important property of a sensor, as it determines whether a reliable measurement in the target sample is possible. It is defined as the degree of the sensors' ability to discriminate the primary ion (analyte) from any other ions present in the sample solution. Nikolskii and Eisenman have noticed that the potentiometric response to the primary ion (I) in the presence of interfering (discriminating) ions (J) deviates from the response in solely primary ions solution [66]. They have shown that a precise description of a potentiometric response in the presence of both ions I and J is in fact a Nernstian equation extended by the factor $K_{i,j}^{pot} a_j^{z_i/z_j}$:

$$E_{\text{PB}} = E^0 + \frac{RT}{z_i F} \ln \left[a_i + \sum_{j \neq i} (K_{i,j}^{pot} a_j^{z_i/z_j}) \right] \tag{19}$$

where $K_{\text{IJ}}^{\text{pot}}$ is the potentiometric selectivity coefficient, whose thermodynamic definition is given elsewhere [14]. Sensors' selectivities are usually presented in the literature as the logarithm of $K_{\text{IJ}}^{\text{pot}}$: a negative value indicates the preference to the primary ion relative to the interfering ion, a positive value indicates that the sensor is not selective to the analyte.

Two methods for calculating K_{IJ}^{pot} recommended by IUPAC are based on equation (17): separate solutions method (SSM) and fixed interference method (FIM). In SSM, the sensor is calibrated in two separate solutions: a solution containing only the primary ion, and a solution containing only the interfering ion. Then, the measured open circuit potential values at $a_I = a_J$ are used to calculate the K_{IJ}^{pot}:

$$\log K_{IJ}^{pot} = \frac{(E_J - E_I)z_I F}{2.303 RT} + \left(1 - z_I/z_J\right)\log a_I \tag{20}$$

In FIM, the potentiometric cell is calibrated in a mixed solution of ion *I* containing a constant background concentration of ion *J*. Then, K_{IJ}^{pot} is described by equation (21), where a_I equals the lower LOD [67]:

$$K_{I,J}^{pot} = \frac{a_I}{a_J^{z_I/z_J}} \tag{22}$$

There has been a lot of discussion on the accuracy of the methods for potentiometric selectivity quantification. Still, there is no explicit consensus on which methods give the truest selectivity values, as the most prevalent concerns are related to situations when $z_I \neq z_J$ [68].

Potentiometric response reversibility is determined by the presence or absence of hysteresis. According to IUPAC, hysteresis is the electrode memory that occurs as a difference in measured open circuit potential in solutions of the same primary ion concentrations, between which the sensor was exposed to a primary ion solution of different concentration. The standard deviation of the data collected in a series of measurements in solutions of the same concentration of primary ion (after removal and washing the electrodes) is called reproducibility [46].

The sensor's response time is the interval which passes between the first contact with a sample and the first moment when the open circuit potential change with time ($\Delta E/\Delta t$) reaches a limiting value that fulfils the required accuracy of the measurement [46].

It is often reported in the literature as t_{95} – a period needed to achieve 95 % of the arbitrarily chosen limit value. A concentration dependence of response time was observed: the response time is usually longer closer to the lower LOD, while in the dynamic linear range it is generally quite short. This discrepancy can be reduced by using highly efficient ion-to-electron transducers.

2.6. Scalable fabrication of potentiometric sensors

With the development of solid-contact transducers, sensors evolved into electronic devices: layered structures made of insulating substrates decorated with electrically conducting lines. Thus, fabrication technologies previously developed within the electronics industry – photolithography, chemical and physical vapour deposition, and vacuum deposition – were the first means of producing solid-contact sensing systems. Unluckily, these procedures are confined to rigid substrates only, they are expensive, slow, and wasteful [69]. Novel electronic devices are sought to be lightweight, flexible and cheap and, most importantly, mass-produced. Thus, novel materials and sensor design development is followed by a simultaneous development of suitable fabrication (and post-production) techniques.

During the last decade, screen printing and inkjet printing – techniques originally developed in the graphics industry sector – have become the state of the art in layered electrochemical sensors production [7]. As both techniques were previously well adapted for large scale production, they are known for their low cost, high throughput, reduced material wastage, and facile manufacturing processes [70].

2.6.1. Screen printing

Screen printing entered the arena of solid-state sensors production some time before inkjet printing [7] and still dominates the market of miniaturised sensors. This technique is based on forcing the ink through a screen limited by a stencil on a substrate. The mesh screen is usually made of a fine, porous mesh of fabric, silk, synthetic fibres or metal

threads [71]. The printing process consists of several steps, as schematically shown in Figure 7.

During the screen-printing process, ink is first deposited across the surface of the screen, which is aligned above a stencil positioned on the substrate. A squeegee – a blade-like rubber tool used in screen printing – is then passed across the screen under applied force. This action deflects the mesh downward into contact with the substrate, driving the ink through the permeable regions of the stencil in a controlled manner. The squeegee simultaneously imposes both vertical and horizontal (shear) stress on the ink, ensuring uniform deposition while also removing the residual ink from the screen, thereby preventing accumulation on the screen surface [72].
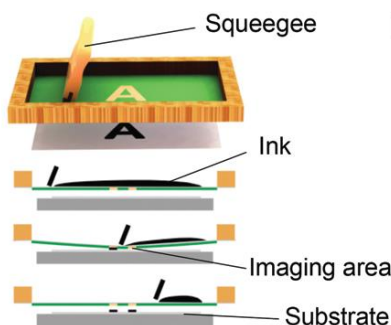

Figure 7. A schematic figure showing the principle of flat-bed screen printing.
Adapted from [71].

Screen printable inks are viscous and of thixotropic nature; their viscosity decreases with an increase in shear rate of a squeegee, facilitating shear thinning of inks and helping flow through the unblocked pores. Due to the inks' thixotropic nature, after the ink passes through the mesh onto the substrate, it becomes more viscous again, minimizing the tendency for uncontrolled spreading and contributing to precise designs [73]. Due to its working principle, screen printing requires relatively high amounts of ink and produces shapes with thicknesses in the range of a dozen to more than a hundred micrometres [74]. Such patterns are thicker than those obtained by other printing methodologies. Thus, screen printing is considered to be thick film technology [75].

The literature on screen-printed electrically conductive inks is quite saturated. Carbon-based (nano)materials [76-78] are very common, due to their low cost and excellent

electrochemical properties. Metal nanomaterials-based inks are mostly used for printing electrically conductive leads [79, 80].

Even though it is widespread, this technology comes with serious drawbacks. The first is associated with the large amounts of ink needed. Since not all the applied ink passes the stencil, there is a lot of wasted ink. Next, any modifications to the design of the printed pattern first imply the need for a new stencil design and fabrication. The mesh tends to stretch after prolonged use, contributing to batch-to-batch variation and lowering the printing quality. Finally, due to the character of the technique, the resolution of the printed patterns is restricted, posing serious drawbacks for printing complex patterns.

2.6.2. *Inkjet printing*

The idea of the selective ejection of tiny droplets of fluid onto a paper support can be traced back to 1867 when William Thomson proposed using electrostatic forces to control the release of ink drops onto paper. However, the method was commercialised sometime after, in 1951, by Siemens, after achieving programmable computer support [81].

Inkjet printing (IJP) is a non-contact materials deposition technique based on the selective break-up of liquid jets into a series of repeatable droplets, their deposition onto a substrate of choice and drying and solidification that produces a solid, continuous deposit. The printing process is contactless, as no external mechanical pressure is applied to the substrate. This prevents damage and contamination to pre-patterned components, which is the major problem in contact-printing techniques, such as screen printing [6]. Having a contactless character, IJP is highly suitable for flexible and soft substrates, but also for curved and textured surfaces. Operating at room temperature, it enables printing on substrates that usually do not withstand high temperatures.

Both the printing and droplet generation are digitally governed, enabling rapid prototype creation and reproduction. Droplets are generated by two means: continuous inkjet (CIJ) and drop-on-demand inkjet (DoD). In CIJ, a continuous stream of droplets is generated by a pressure pulse and directed by applying an electrical potential difference relative to the ground. Individual drops in the stream are steered into the gutter by charging

the deflection plates (see Figure 8a) and recycled later in the printing. A continuous character makes CIJ wasteful; another issue is the possible contamination of the ink during recycling [82]. Thus, CIJ is more common in packaging mass production, and DoD is the most suitable for research and development of functional materials deposition.
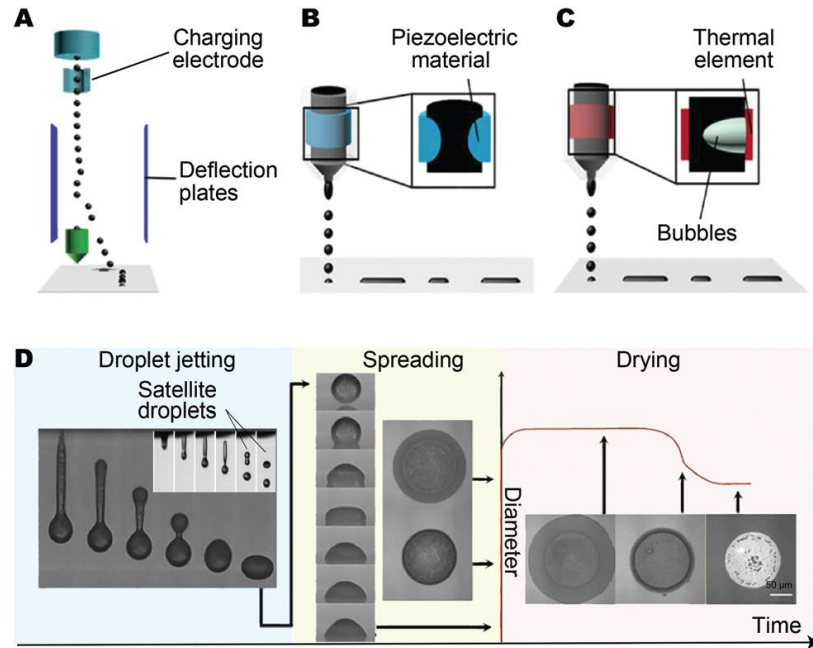

Figure 8. Inkjet printing principles: schematics of (A) CIJ, and DoD inkjet printing with (B) piezoelectric and (C) thermal head. (D) The complete inkjet printing process, showing the droplet jetting, spreading and drying stages. Adapted from [71].

Drop-on-demand inkjet printing is based on selective droplet generation, using either a thermal or piezoelectric actuator, as illustrated in Figure 8b and c. Drop positioning is achieved by locating the printer nozzle above the desired location on the substrate before the droplet ejection. In thermal DoD, an actuator (a small thin-film heater) is placed in contact with an ink container and heated to produce a vapour bubble that pushes an ink droplet through the nozzle. Thermal DoD is hence applicable only to relatively volatile inks (or inks containing a volatile component). Piezoelectric DoD is based on a pressure pulse generated by direct mechanical actuation by the voltage input. Different voltage waveforms can be superimposed on the actuator, influencing the droplet size and enabling the ejection of fluids with different physical characteristics [83, 84]. Typical print heads produce

droplets with volumes between 1 and 100 pL, which directly affects the printing resolution [85].

Ink formulation is the key step preceding the jetting process. This includes choosing an appropriate functional material particle size, solvent (mixture of solvents) and stabilisers to ensure:

      a. formation of the isolated droplets at the printer nozzle,

      b. absence of the satellite (secondary) droplets that lead to ink deposition in unwanted areas,

      c. stability against aggregation and sedimentation.

The droplet jetting behaviour cannot be predicted, but the ink's physical characteristics give a general idea about the fluid printability. The most important are the density, surface tension, and viscosity of the ink. These are conveniently combined in dimensionless numbers: Reynolds number (*Re*), Weber number (*We*) and the inverse Ohnesorge number (1/*Oh*):

$$Re = \frac{v\rho a}{\eta} \tag{23}$$

$$We = \frac{v^2 \rho a}{\gamma} \tag{24}$$

$$\frac{1}{Oh} = Z = \frac{Re}{\sqrt{We}} = \frac{\sqrt{\gamma \rho a}}{\eta} \tag{25}$$

where v is the velocity of the ejected fluid, ρ is the mass density, a is the distance of the nozzle to the support, η is the dynamic viscosity, and γ is the surface tension of the fluid. Different limiting *Z*-values have been reported, but a printable ink is generally characterised by $10 > Z > 1$. Highly viscous fluids show low *Z*-values, meaning difficulty to jet, whereas high *Z*-values indicate possible satellite droplet formation [86]. Importantly, the solvent boiling point must be considered to prevent ink evaporation that would block the nozzle. Typical fluids used for inkjet printing have a density close to 1000 kg m^{-3},

viscosity of around 20 mPa s, and surface energy below 0.1 Jm^{-2}. Drop size is related to the nozzle diameter; drops typically have diameters <100 μm. Considering the functional material particle size, 1 % of the nozzle diameter particle size is advised to avoid clogging [87].

The unique droplets of the functional ink are directed towards the substrate. Droplet deposition happens in two steps: first is the impact-driven stage lasting less than 1 μs, followed by droplet spreading. The ratio of the initial kinetic energy of the impact and the ink viscosity determines the diameter of the drop, while the surface energy at the ink/substrate defines the further spread or pinning of the drop [85]. This droplet footprint determines the resolution of the printed pattern: it depends on the interactions of the droplet with the substrate, solvent evaporation rate and the capillary flow.

Compared to conventional graphics printing, where isolated drops produce a pixelated image, in materials printing it is extremely important that drops overlap to produce patterns with continuous features, e.g. electrical conductivity. Thus, in electronic materials printing, patterns are built from the interactions between the individual droplets at the substrate.

The final step in the printing process is the evaporative drying of the printed pattern, that is, the drop solidification. Controlled drying is utterly important in functional materials printing, as it directly influences the solute distribution of a finished product. Evaporative drying is accompanied by receding the ink/substrate contact angle and solute redistribution. Solvent evaporation is the fastest at the edges of the droplets (or a pattern), especially if the droplet pins to the substrate. This is because the pattern is the thinnest at the edges, so the vapour transport is the easiest and the precipitation occurs the fastest [82]. Consequently, the solvent will flow towards the edges via capillary flow, and the solute will accumulate there, finally forming a characteristic ring-like structure, where the solute has segregated during the drying process [82]. This structure inhomogeneity, known as the coffee-ring effect (CRE), can be overcome by using a mixture of solvents characterised by significantly different surface tensions or boiling points [86, 88]. In doing so, a reverse Marangoni flow is induced by the surface tension gradient within the droplet (see Figure 9).

Due to the thermodynamic size effect, metal nanoparticles' melting point is significantly reduced compared to the bulk metals, enabling sintering at lower temperatures [86]. Among them, silver (AgNP) and gold nanoparticles (AuNP) dominate as they show superior conductivities. Thus, these materials are most used for fabricating electrical contacts and electrically conductive leads.

These inks are usually prepared by the bottom-up approach, where nanosized materials are synthesized from atomic-level precursors [89]. In principle, wet chemistry procedures rely on the chemical reduction of metallic ions originating from inorganic salts. As the reaction proceeds, the concentration of the formed metallic atoms reaches a supersaturation level and triggers the self-nucleation process – metallic atoms aggregate to form rapidly growing nanocrystals. Due to a characteristically high ratio of atoms on the surface and the interior, the nanocrystals are thermodynamically unstable and prone to aggregation [90]. Unprotected nanocrystals will continue to grow indefinitely and produce an unstable colloidal system from which large, aggregated particulates will precipitate. Stabilising agents that prevent aggregation and uncontrolled particle growth are added to the reaction mixture to prevent this. These are usually relatively bulky molecules that contain a group that binds to the metal nanoparticle on one end, and the functional group responsible for the stabilization on the other end. Different mechanisms of metallic nanoparticle stabilization using capping agents include electrostatic, steric, electro-steric and hydration mechanisms [91].

The introduced principle of inkjet printing implies picoliter-size droplet ejection. Accounting for the solvent (or solvent mixture) boiling point is one of the key factors in assuring successful printing. Volatile formulations cannot be efficiently inkjet printed because their quick evaporation causes nozzle blocking and difficult droplet formation, leading to inconsistent prints and printing failure. Considering that the typical ion-selective membrane utilises highly volatile solvent THF, inkjet printing of the polymeric membrane presents a huge challenge. Solely replacing THF with a less volatile solvent, such as cyclohexanone, does not enable stable and reproducible jetting, as the resulting fluid is too viscous for the delicate printer head geometry. Both ion-selective and reference membranes

have only been successfully inkjet printed after significantly lowering the solute membrane content. This requires dozens of overprints, bolding the material consumption, fabrication time and the cost of the overall production. This becomes a significant hurdle when transferring to a large-scale production.

Among the two state-of-the-art electrochemical sensor fabrication technologies, late bloom inkjet printing stands out due to its reduced material consumption, non-contact character, and completely digital control of the printed patterns. Compared to screen-printing, inkjet printing significantly cuts the ink consumption (and therefore costs) making it extremely valuable for highly conductive metallic inks deposition in electrical leads fabrication.
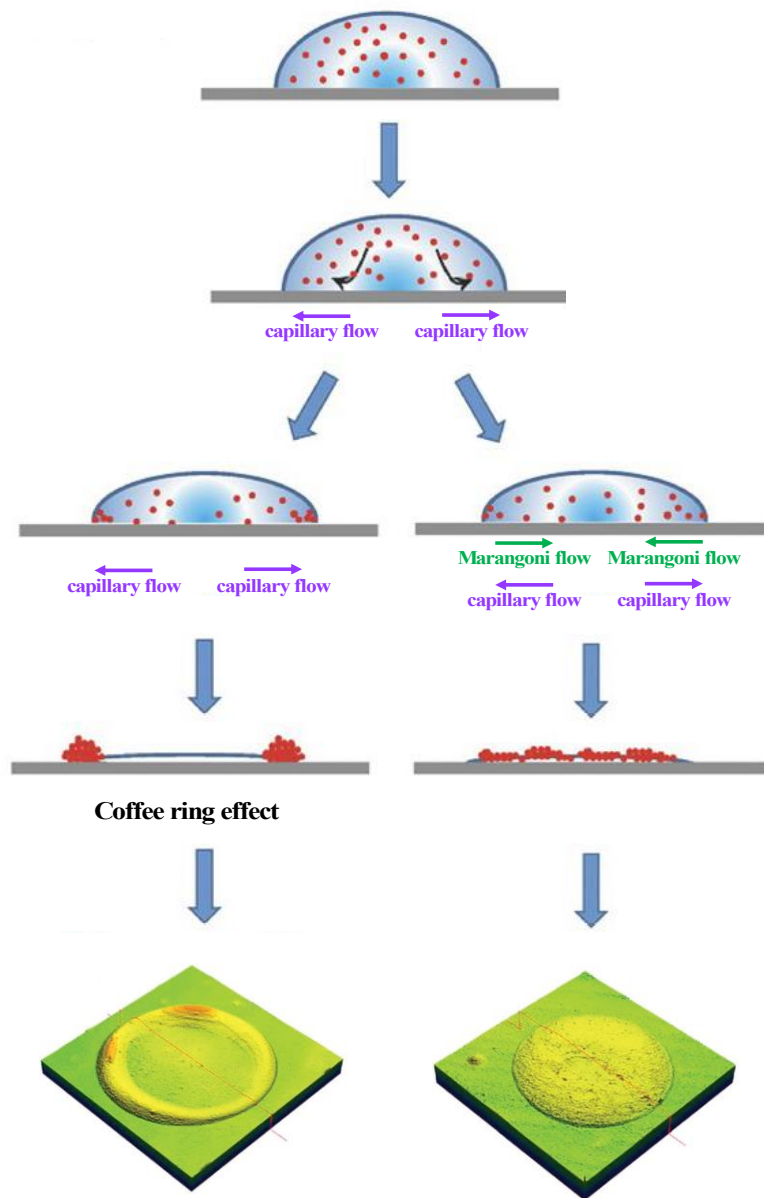
Figure 9. Schematic representation of coffee-ring effect formation.
Adapted from [92] and [93].

Table 1. The key differences between screen printing and inkjet printing in the fabrication of electrically conducting leads. Adapted from [70].

	Inkjet printing	Screen printing
Operating principle	Non-contact technique	Contact technique
	Selective, on-demand deposition of conductive ink droplets onto the substrate to form a desired pattern	Transmission of the ink through the stencil
	Droplet ejection via thermal, piezoelectric or electrostatic control	Pattern is defined via screen mesh and stencil
Advantages	Digitally controlled ink droplet deposition and location	Well-developed printing technique
	Reconfigurable pattern	High throughput
	Can print on top of prefabricated flexible circuits	High speed with control over deposition
	Less material wastage	Easily scalable to a large area
	Versatile choice of inks and substrates	
	Lower viscosity materials can be deposited	Easy alignment of the transparent mask
Drawbacks	Difficult to print viscous, membrane-like materials	Speed/throughput comparable to IJP
	Resolution is limited by the droplet size	The resolution is limited by the mesh screen (resolution > 30 μm)
	Incompatible with volatile solvents	Lower resolution
	Energy inefficient	Ink drying on the masks, resulting in deteriorated print patterns and masks
	Lower throughput	
	Nozzle clogging, misfiring	
	Coffee ring effect	Inks having higher viscosities are required to prevent bleeding and spreading out

2.6.3. *Polymeric membrane automated dispensing*

Precision fluid dispensing systems are digitally controlled and programmable robots that operate in three axes and deliver precise fluid amounts to various substrates. Their development came about as a response to the growing needs for the automatization in the electronics assembly and automotive industries, and medical devices production.

The operating principle (illustrated in Figure 10) is quite similar to inkjet printing. The dispensing fluid is contained in a syringe pump closed with a piston. A precisely controlled pressure pulse generated by a compressor presses the piston in a preprogramed manner, causing droplet generation and ejection. Compared to inkjet printing, fluid dispensers can work in a contact and a non-contact mode, enabling dots dispensing and drawing lines. Compared to inkjet printers where nozzles are constructed as tiny pinholes, fluid dispensing systems' syringes contain interchangeable needles with various diameters and sizes. Therefore, there is much more room for manoeuvring with fluids of different viscosities and droplet sizes, as well as suspensions with larger particles.
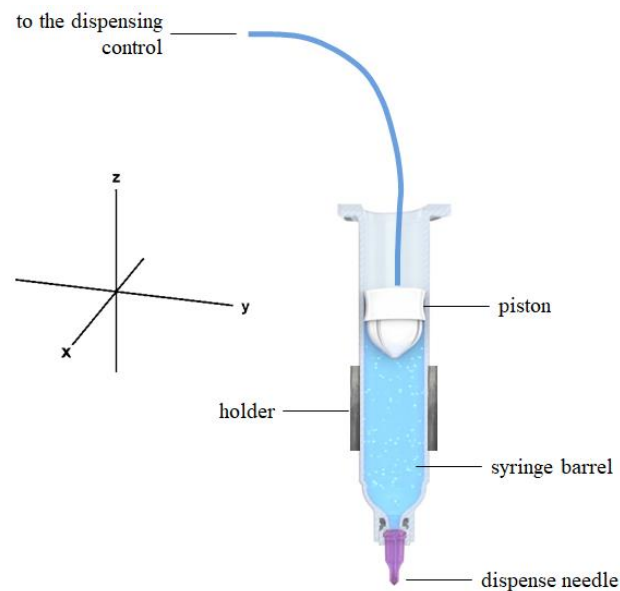

Figure 10. An illustration of the working principle of an automated fluid dispenser robot.

Precision fluid dispensing systems are unexplored in potentiometric sensor research and development, with a single report on the fabrication of solid-contact nitrate sensors, where the jetted membrane cocktail was even five times diluted compared to the widely accepted cocktail composition.

Because of the differences in printer heads and syringe barrels geometry, inkjet printing stands out as a logical means of electrical leads fabrication. On the other hand, precision fluid dispensing comes with many customizable features, including interchangeable dispensers. Precision fluid dispensing is much more appreciated in cases where fluid manipulation for the purpose of generating droplets is difficult. Owing to the various geometries and materials of the needles, it is possible to controllably and reproducibly deposit liquids that otherwise could not be deposited.

2.6.4. Post-production treatment

Along with functional material, jettable formulations often contain additives – organic molecules that separate electrically conducting (nano)particles by steric hindrances or ionic repulsions and prevent particle aggregation and sedimentation before printing. Thus, to restore the conductive paths within the printed patterns, the additives must be removed after printing. This is traditionally done by thermal decomposition, which is both time and energy consuming. Often, additives require higher temperatures for thermal decomposition than the glass transition temperature of the (plastic) substrate, which inevitably damages the substrate.

IJP coupled with an energy efficient annealing technique presents a highly convenient technological roadmap to cost-efficient and high-throughput flexible electronics production. It is not surprising that alternative (low temperature) means of annealing have been gaining popularity in the past decade. These are: chemical sintering, plasma sintering, electrical sintering, photonic sintering and microwave sintering. Particularly, photonic and microwave sintering are considered as high-throughput, due to their extremely short processing times. In principle, these methods selectively target the printed pattern, without damaging thermally sensitive substrates. Among them, a special interest was put into

photonic techniques that use various light sources for materials refinement. Using a specific wavelength which the (nano)material specifically absorbs, or manipulating irradiation conditions, enables a selective functional material treatment.

An intense pulsed light (IPL) annealing system (often referred to as Flash Lamp Annealing, FLA) consists of a xenon flash lamp, a reflector, a power supply, capacitors, and a pulse controller. The pulse controller triggers the capacitor, which delivers electrical current to the lamp within milliseconds. This causes consecutive high-intensity broad range (200 – 1200 nm) non-laser light pulses that within milliseconds irradiate the sample. The irradiation fluence can be controlled by varying pulse duration, applied voltage, and number of pulses. In that way, very selective and short-time heating at extremely high temperatures allows not only sintering but also material structural reformation [94, 95]. IPL working principle is illustrated in Figure 11.
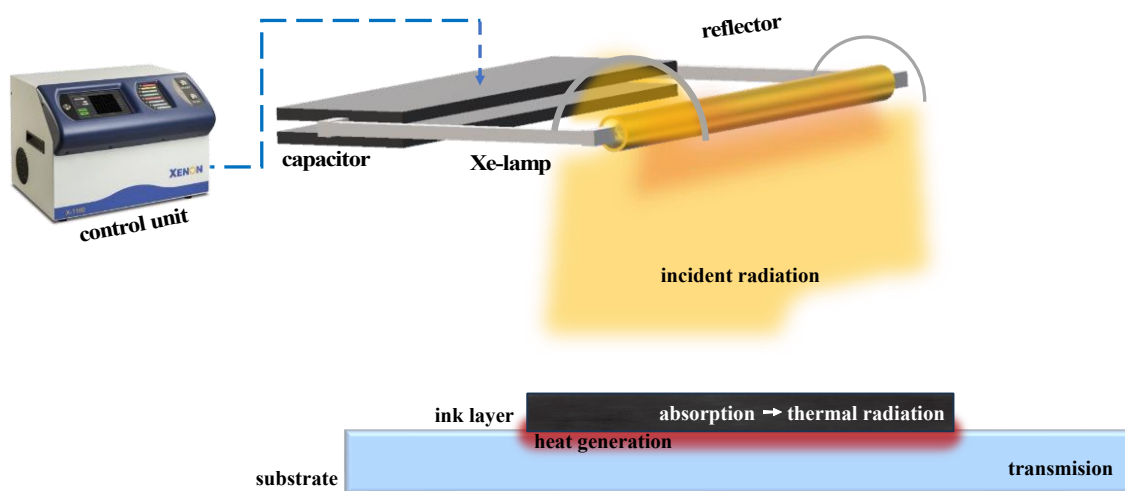
Figure 11. Working principle of IPL annealing system.

Nam et al. argued that silver microparticles, compared to nanoparticles, are significantly easier and cheaper to synthesise [96]. However to restore the electrical conductivity, due to the smaller surface-to-volume ratio microparticles generally require harsher annealing conditions. The authors have developed an IPL annealing procedure for screen-printed Ag-microparticle-based ink on flexible polyurethane substrates. The printed patterns were annealed using a single pulse of 1 s, at the lamp voltage of 450 V. The IPL

energy intensities varied at $1 - 4$ J cm^{-2}. The effect of IPL sintering on the electrical conductivity of the printed electrodes was compared to the "classical" thermal sintering (130 °C, 30 min) based on conductivity measurements using four point probe (4PP). The optimum IPL annealing energy giving the highest electrical conductivity of 60 mΩ □$^{-1}$ without damaging the stretchable electrode was 2 J cm^{-2}. Compared to thermally sintered electrodes, the electrodes annealed at the optimised IPL conditions showed superior long-range strain durability (expressed as changes in measured conductivity).

Kang et al. formulated silver nanoparticle-based ink at 50 wt.% of dry matter in diethylene glycol and inkjet printed it using a DoD piezoelectric printer onto polyimide substrate [97]. IPL annealing optimisation was carried out to find the best parameters for the lowest resistivity of the patterns. The authors varied the energy of the incident light (20 – 50 J cm^{-2}) and number of pulses. The duration of the pulses was fixed at 4 and 6 ms, with a fixed 5 ms time gap between the pulses. To fully sinter the IJP patterns, three consecutive pulses of 50 J cm^{-2} were needed. The lowest obtained average resistivity of 49 ± 3 nΩ m, was only 9 nΩ m higher than the one obtained for the thermally annealed (200 °C, 30 min) specimens, which is appropriate for printed electronics technology.

Secor et al. reported a jettable graphene dispersion, using ethyl cellulose (EC) as a stabiliser and cyclohexanol/terpineol mixture as a solvent [98]. Inks containing different amounts of EC were inkjet printed onto poly(ethylene terephthalate) (PET) substrates and annealed using IPL. It was shown that the annealing reach depends on the content of the stabiliser, indicating that EC absorbs less energy from the IPL and thus disrupts the uniform heating of the printed films. Optimising the stabiliser content and IPL parameters, the authors have significantly lowered the printed patterns sheet resistance, obtaining the minimum average sheet resistance of 26.4 ± 4.4 Ω/□ for eight IPL-annealed overprints.

2.7. Inkjet printing in potentiometric sensor construction

With the development of additive production means, as represented by screen printing and inkjet printing, electrochemical sensors commercialisation has become reality. The huge commercial success of the glucose sensing market has driven the focus to produce minimally invasive sensing devices [99]. Even though inkjet printing beats screen printing in terms of material consumption, resolution and possibilities for complex pattern design, screen printing is still state of the art in miniaturised electrochemical sensor fabrication. The key differences between the two techniques are summed in Table 1.

Inkjet printing in-line coupled with alternative processing approaches offers huge promises for large-scale sensor production. Due to their operational simplicity, potentiometric sensors can be integrated in platforms for multiplexed analyses, especially wearables and environmental analysers [4, 100]. However, there is still a lot of work to be done to truly commercialize inkjet printed solid-contact potentiometric sensing systems.

IJP potentiometric sensors construction begins with formulating a jettable ink and choosing an appropriate substrate. This is a complex process, as it must include the selection of the functional material and the formulation of a suitable functional ink. The key properties of a jettable ink include a satisfactory stability against particle aggregation, the ability for a controlled droplet generation, jetting, coalescence with the substrate, and drying to achieve a homogeneous solute spreading. The layered structure of potentiometric sensors is evident in functional materials choice and order of deposition. A metal nanoparticle ink is the first layer to be deposited directly onto the substrate. This layer functions as an electrical lead that connects the sensor to the processing unit. Next, a solid-contact layer is printed over the working electrode area, typically, carbon nanomaterials or conductive polymer-based inks are used. Such ink is formulated considering the key properties of a suitable solid-contact as discussed in **Section 2.3. Solid-contact ion-selective electrodes**. Finally, the ion-selective or reference membrane is deposited. At the moment, the deposition of an ion-selective (or reference) membrane is for the most part done by manual drop-casting for the reasons to be discussed in the later paragraphs.

Wearable sensors that collect information from the human body using sweat or interstitial fluid as a sample are usually in contact with the skin, thus a substrate of choice should align with skin and offer comfortable wearing [100]. On the other hand, environmental sensing platforms can be constructed on more rigid materials too. When considering a substrate material, one needs to take in account the thermal and chemical stability of the substrate, surface smoothness and adhesion properties, water repellency and permeability, and optical clarity. Most common substrates used in inkjet printed electrochemical sensors are flexible materials, including polymers, paper and textiles [101]. Polymer-based substrates are represented by poly(ethylene terephthalate) (PET), poly(ethylene naphtalate) (PEN) and polyimide (PI). For stretchable devices elastomers such as poly(dimethylsiloxane) (PDMS), polyurethanes and multiblock copolymer styrene–ethylene–butadiene–styrene (SEBS) are used [87].

A literature search of research papers was done in the *Web of Science* database using the keywords and title/abstract cited words containing "ion selective" OR "ion-selective" OR "potentiom*" OR "reference electrode" AND "sens*" AND "inkjet" OR "ink-jet". This search resulted in 26 research papers published between 2013 and 2025 describing ion-selective electrodes, reference electrodes or whole potentiometric systems where at least one component of the layered electrode structure was deposited by inkjet printing. Articles of interest were critically analysed to gain information about the reach of inkjet printing, that is how many layers of the layered solid-contact electrode structure were fabricated by IJP (Figure 12). This classification was broadened by reporting on type of substrate used, electrical leads and solid contact materials, analyte of interest and the key analytical parameters, and finally, the intended real application (see Tables 2 – 4).
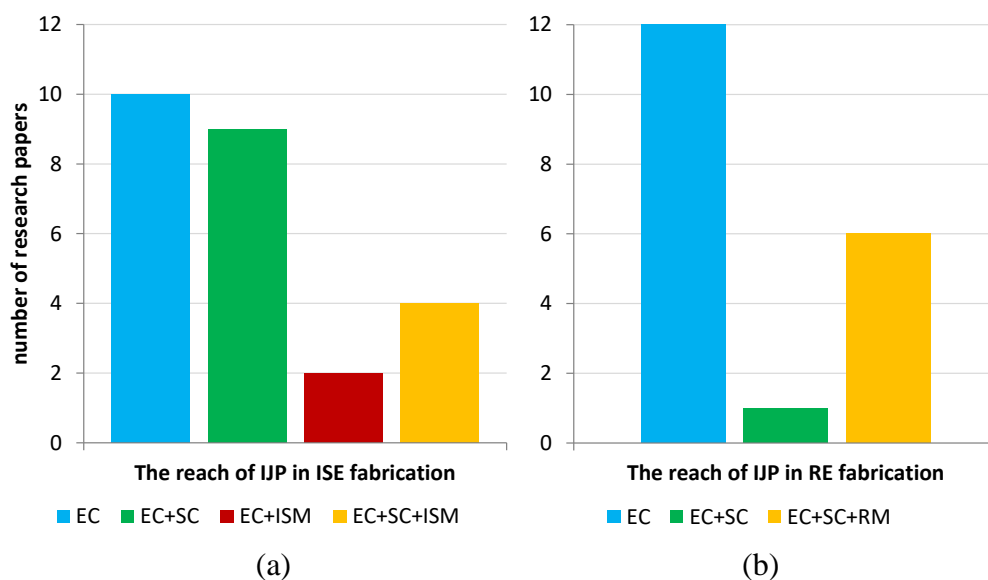
Figure 12. Radar diagrams describing the reach of inkjet printing in potentiometric sensor production; a) ion-selective electrodes, b) reference electrodes.

Figure 12 depicts the classification of relevant research papers according to the reach of inkjet printing in the fabrication of potentiometric sensors. 80 % of the found papers discuss electrode fabrication on flexible substrates, including paper and polymers (PI, PET, PEN), bolding the importance of sensor flexibility in contemporary applications.

Regarding ion-selective electrodes, the found literature was classified in four groups:

- EC – only the electrical contacts were IJP;
- EC+SC – both electrical contacts and solid contacts were IJP;
- EC+ISM – only electrical contact and ion-selective membrane were IJP;
- EC+SC+ISM – all the components of the layered electrode structure were IJP.

Evidently, electrical contacts were in all cases fabricated by the means of IJP. Diving deeper within the EC and EC+SC groups, it was found that ion-selective membrane is quite often absent in the ISE fabrication, while the transducer is obtained by the post-print processing, giving second order metallic electrodes. The found literature describes the fabrication of five such electrodes. Equally represented is the electrode design where both

the electrical contacts and the solid contacts that function as receptors were IJP as two separate layers. Four coated wire electrode designs were found, where in one case both the electrical leads and ISM were inkjet printed while in the other case, ISM was deposited manually by drop-casting Inkjet printing the electrical leads, electrodepositing the solid contact, drop-casting the ISM; or inkjet printing the separate EC and SC layers and drop-casting the ISM are the least found. Finally, four examples for fully inkjet printed electrode arrays were found.

The reach of inkjet printing in SC-RE fabrication is shown in Figure 12b. The key three categories include:

- EC – only the electrical contacts were IJP;
- EC+SC – both electrical contacts and solid contacts were IJP;
- EC+SC+ISM – all the components of the layered electrode structure were IJP.

Herein, fully inkjet printed reference electrodes dominate, with six reported electrode configurations. Pseudoreference electrode designs, where only Ag-electrical leads were IJP, and the transducer layer was formed either by a chemical or electrochemical reaction, are represented with 6 papers. A reference membrane (RM) was manually drop-cast in four different designs where the transducer layer was formed either by a chemical or electrochemical reaction. Least found were the configurations where the reference membrane was drop-cast either directly over the IJP electrical lead or over the IJP layers.

Among the search results, 6 papers described reference electrode fabrication only, 10 papers described ion-selective electrodes fabrication only, and 13 papers described the fabrication of potentiometric sensing platforms consisting of both SC-ISE and RC-RE. The relevant papers are summarised in Tables 2 – 4 and discussed in the following chapters.

Table 2. Literature review of inkjet printed potentiometric chemical sensors.

n	Substrate	EC	SC	ISM and type of deposition	Analytical parameters	Analyte	Application (if specified)	Ref
1	Glass	Ag-paste	SWCNT-COOH (IJP)	No ISM; receptor: SWCNT-COOH	DLR: 3-11 (pH); sensitivity: 48.1 mV/pH	H^+	Not specified	[102]
2	Silicon wafer	Graphene ink (IJP)	Graphene ink (IJP)	Drop-cast K-selective ISM in THF (valinomycin, KTpClPB, PVC, DOS)	DLR: $10^{-5} - 10^{-2}$ M; sensitivity: 57.2 mV dec^{-1} LOD: $10^{-5.2}$ M	K^+	Not specified	[103]
3	Paper	Ag-ink (IJP)	Graphite in PVB matrix (drop-cast or dip-coat)	Drop-cast NH_4-selective ISM in THF (NH_4-ionophore, PVC, DOS)	DLR: $10^{-5} - 10^{-1}$ M; sensitivity: 57.30 mV/dec LOD: $10^{-5.3}$ M	NH_4^+	Not specified	[104]
4	PEN	Ag-ink (IJP)	Ag/Ag_2S	No ISM; receptor: Ag/Ag_2S	DLR: $10^{-4.5} - 10^{-1.3}$ M; sensitivity: -29.4 mV dec^{-1}	S^{2-}	Sea water and river water application were presented	[105]
5	PEDOT: PSS	$Ti_3C_2T_x$ (IJP)	$Ti_3C_2T_x$ (IJP)	Drop-cast Na-selective ISM in THF (Na-ionophore, Na-TFPB, PVC, DOS)	Sensitivity in physiological Na-concentration range: 40 mV/dec	Na^+	Not specified	[106]

	EC						
6	ITO/PET	IrO_x and PDDA ink (IJP)	IrO_x (IJP)	No ISM, IrO_x is a receptor	DLR: 3-10 (pH); sensitivity: 58.4 mV/pH	H^+	Not specified	[107]
7	PET	Ag-ink (IJP)	no SC	Drop-cast NO_3-ISM in THF (TOA-bromide, DBP, PVC)	DLR: $10^{-5} - 10^{-1}$ M; sensitivity: $50 - 52$ mV/dec	NO_3^-	Not specified	[108]
8	Polyimide	Ag-ink (IJP)	no SC	Drop-cast NO_3-ISM in THF (TOAN, PVC, DBP)	DLR: $10^{-4.3} - 10^{-1}$ M; sensitivity: -56.6 mV/dec LOD: $10^{-4.5}$ M	NO_3^-	Not specified	[109]
9	Polyimide	Ag- and graphene ink (IJP)	$RuCl_3/RuO_2$ (IJP)	No ISM - RuO_2 is receptor for H^+ ions	DLR: 2-12 (pH); sensitivity: 57.9 mV/pH	H^+	the acidification of a cancer cell culture was showcased	[110]
10	Polyimide	Ag-ink (IJP)	Graphene ink (IJP)	Drop-cast NH_4-ISM (PVC, DOS, nonactin)	DLR: $10^{-6} - 10^{-1}$ M; sensitivity: 55.6 mV/dec LOD: 0.88 ± 0.17 μM	NH_4^+	Waste water analysis	Publication 2 [111]

EC – electrical contact; IJP – inkjet printed; SC – solid-contact; ISM – ion-selective membrane; SWCNT-COOH – single walled carbon nanotubes functionalised with carboxyl groups; DLR – dynamic linear range; PEN – polyethylene naphthalate; PVC – poly(vinyl chloride); LOD – lower limit of detection; PEDOT:PSS – poly(3,4-ethylenedioxythiophene):polystyrene sulfonate; TOA-bromide – tetra-*n*-octylammonium bromide; TOAN – tetraoctylammonium nitrate; DBP – dibutyl phthalate.

Table 3. Literature review of inkjet printed reference electrodes.

n	Substrate	EC	AgCl deposition method	RM and type of deposition	Analytical parameters	Ref
1	PCB	Ag-ink (IJP)	Chemical formation	no RM	SRR: 4 – 10 (pH); drift: 0.04 mV/h	[112]
2	PET, chromatrographic paper	Ag-ink (IJP)	Chemical formation	no RM	Drift < 3 mV; lifetime: 30 days	[83]
3	PET	Ag-ink (IJP)	Chemical formation	Drop-cast UV-curable ink with grind KCl powder (22.25 wt.%)	SRR: $10^{-6} – 10^{-1}$ M; Drift: <2 mV/h; Lifetime: 4 weeks	[113]
4	PET	Ag-ink (IJP)	Chemical formation	IJP RM: Cl^- saturated PVB (4 %)	SRR: 2 – 10 (pH); SRR: $10^{-6} – 10^{-2}$ M; Drift: 0.13 mV/h	[114]
5	PET	Ag-ink (IJP)	Electrochemical formation	IJP 2 wt.% agarose gel in 3 M KCl / SBS fiber-mat / EGaIn alloy	SRR: 4 – 8 (pH); SRR: $10^{-5} – 10^{-1}$ M; Drift <2 mV; Lifetime: 1 month	[115]
6	Polyimide	Ag-ink (IJP)	–	Drop-cast 10 wt.% PVB, 50 mg mL^{-1} AgNO$_3$, 50 mg mL^{-1} NaCl in methanol	SRR: $10^{-6} – 10^{-2}$ M; SRR: 2 – 10 (pH); Drift = 0.2464 mV h^{-1}	Publication 4 [116]

RM – reference membrane; SRR – stable response range; SBS – poly(styrene-block-butadiene-block-styrene; PCB – printed circuit board.

Table 4. Literature review of inkjet printed potentiometric platforms.

n	substrate	ISE	RE	analytical parameters	Analyte	Application (if specified)	ref
1	polyimide, glass	EC: Pd-ink (IJP); SC & H^+ receptor: Pd/PdO	IJP Ag-ink, AgCl chemical formation; RM (PVC, KCl, AgCl)	<u>ISE</u>: DLR: 4 – 10 (pH); sensitivity: 59 mV/dec; <u>RE</u>: drift: 2.4 mV/pH	H^+	Real water samples and milk	[117, 118]
2	paper	EC: Au-ink (IJP); SC & receptor: PANI (H^+ receptor)	Ag-ink (IJP), AgCl electrochem. formation	<u>ISE</u>: DLR: 2 – 10 (pH); sensitivity: 61 mV/dec; <u>RE</u>: drift: 4.35 mV/pH	H^+	Not specified	[119]
3	paper	EC&SC: graphene:PEDOT:PSS ink (IJP); ISM: Na-ISM, K-ISM (IJP)	Ag-ink (IJP),AgCl chemical formation; RM (IL in PVC) (IJP)	<u>Na-ISE</u>: DLR: 10^{-4} – 10^{-1} M; sensitivity: 62.5 mV/dec <u>K-ISE</u>: DLR: 10^{-4} – 10^{-1} M; sensitivity: 62.9 mV/dec	K^+, Na^+	Urine analysis	[84]
4	photo paper	EC: Au-ink (IJP); SC: PEDOT:PSS (IJP); K-ISM	EC: Au-ink (IJP); SC: PEDOT:PSS (IJP); RM (IL in PVC)	<u>ISE</u>: DLR: 10^{-5}-10^{-2} M; slope: 62.0 mV/dec <u>RE</u>: SRR: 10^{-5} – 10^{-1} M	K^+	Not specified	[120]
5	photo paper	EC: Ag-ink (IJP), Au-ink (IJP); SC: CNT ink (IJP); ISM: Na-ISM (IJP)	Ag-ink (IJP); AgCl chemical formation RM (IL in PVC) (IJP)	<u>Na-ISE</u>: DLR: 10^{-7} – 10^{-1} M; slope: 56.42 mV/dec <u>RE</u>: drift: 2.5 mV	Na^+	Urine analysis	[121]

6	PBT/PET resin	EC: carbon ink; SC-receptor: PANI ink (IJP)	EC: carbon ink; reference element: Ag/AgCl ink	ISE: DLR: 3 – 11 (pH); slope: 63 mV/dec	H^+	Artificial sweat	[122]
7	polyimide	EC: Au-ink (IJP); ISM: NO_3-ISM or NH_4-ISM containing CNT	Ag/AgCl	NO_3-ISE: DLR: 10^{-3} – 1 M; slope: –48.9 mV/dec; NH_4-ISE: DLR: $10^{-2.5}$ – 1 M; slope: 53.5 mV/dec	NO_3^-	Wastewater analysis	[123]
8	polyimide	EC: Ag-ink (IJP); SC-receptor: graphene ink (IJP)	Ag-ink (IJP); AgCl chemical formation RM (NaCl in PVB) (IJP)	H-ISE: DLR: 4 – 10 (pH); slope: 51 mV/dec	H^+	Not specified	[124]
9	polyimide	EC: Ag-ink (IJP); SC: PEDOT:PSS ink (IJP) ISM: K-ISM (IJP)	Ag-ink (IJP); AgCl chemical formation RM (IL in PVC) (IJP)	K-ISE: DLR: 0 – 2 mM; sensitivity: 59 mV/dec RE: drift: 23.1 $\mu V\ h^{-1}$	K^+	Not specified	[125]
10	polyimide	EC: Ag-ink (IJP); SC: G-PEDOT:PSS ink (IJP); ISM: K-ISM, Na-ISM (IJP)	Ag-ink (IJP); AgCl chemical formation RM (IL in PVC) (IJP)	Na-ISE, K-ISE: sensitivity > 56 mV/dec	K^+, Na^+	Not specified	[126]
11	polyimide	EC: Ag-ink (IJP) SC: Ag/AgCl; ISM: NO_3-ISE	Ag-ink (IJP); AgCl chemical formation; RM: Nafion membrane	NO_3-ISE: DLR: 10^{-6} – 10^{-2} M; slope: –56 mV/dec	NO_3^-	Soil	[127]

EC – electrical contact; PANI – polyaniline; SC-qRE – solid-state quasi-reference electrodes; IL – ionic-liquid; G-PEDOT:PSS – graphene-PEDOT:PSS; PVB – poly(vinyl butyral); PBT – polybutylene terephthalate.

2.7.1. Inkjet printing electrically conducting leads

The first layer of the potentiometric sensor's structure to be printed is the electrical contact. Metallic inks – represented by Ag- and Au-inks – are generally used for this purpose due to their superior electrical conductivity and commercial availability. For Ag-based electrical contacts, all the papers reported in Tables 2 – 4 used commercially available inks. As a rule, the discussed IJP Ag-patterns were thermally annealed at 120 – 260 °C, between 10 and 30 minutes, depending on the silver ink used.

Concerning the reports on Au-based inkjet printed electrical contacts; all the featured papers adopted a previously developed ink [119-121, 123]. This rule is not surprising, as commercially available inkjet printable gold nanoparticle-based inks tend to be very expensive.

The most referenced Au-ink used for electrical contact printing is the ink developed by Määttänen et al. [128]. Dodecanethiol-protected gold nanoparticles ink was synthesised using a water solution of $HAuCl_4 \cdot H_2O$ as a precursor, tetraoctylammonium bromide as a stabiliser, and $NaBH_4$ as a reducing agent. The obtained nanoparticles (~3 nm in diameter) were collected after solvent evaporation and redispersed in xylene (15 wt.%). This ink was inkjet printed onto paper substrates and sintered using an infrared (IR) drier. Finally, IJP gold surfaces were thiolated using 1-octadecanethiol. The printed patterns' surface topology was thoroughly characterised, while the conductivity was measured to be 1.6×10^7 S m^{-1}. The resistance values were comparable to those obtained with printed Au-pattens on glass substrates, showcasing that the remaining organic residues does not affect the electrical properties of the ink.

To reduce the number of steps in production, some authors developed jettable inks based on metals that form a second-order electrode with their oxide. For example, Qin et al. developed two palladium inks for inkjet printing electrode conductive lines [117, 118]. Both inks contained 14.8 wt.% of organoamine complex-stabilized Pd-nanoparticles, one in toluene and the other in isobutylbenzene. The inks were thoroughly characterised by viscosity and surface tension measurements. Continuous and uniform jetted ink layers were

obtained after optimising the firing voltage and cartridge temperature. The printed patterns' conductivity was restored after two-step thermolysis: in the first step, the printed Pd ink was heated to 120 °C for 1 minute to evaporate the solvent; in the second step, the temperature was increased to 200 °C to decompose the precursor and produce and immobilise a uniform Pd-layer on the substrates (as confirmed by SEM imaging and XPS spectra). The effective resistivity of a 260 nm thick Pd film was 2.9 mΩ m. The printed lines were thermally annealed at 200 °C for 48 h, during which the IJP Pd surface was converted to PdO, a receptor for H-ions. However, such harsh electrode treatment is not suitable for sensors' mass production.

He et al. were the first to demonstrate the fabrication of the ion-selective electrode by inkjet printing graphene ink that served simultaneously as the electrical and solid-contact layer [103]. Single layer graphene nanosheets were dispersed in a mixture of 85% cyclohexanone and 15 % terpineol, at the initial concentration of 3.5 mg mL^{-1}. Due to the high boiling point of both solvents, the ink had to be printed at an elevated temperature of 60 °C. The ink was filtered through a 0.45 μm syringe filter and physically characterised by the viscosity measurement (η = 10 mPa s). After adjusting the printing parameters, including the droplets speed, waveform, voltage and nominal drop-spacing, the ink was inkjet printed onto silicon wafers in 50 passes. Thermal annealing in a nitrogen atmosphere was concluded at 950 °C for 1 hour to obtain electrically conductive patterns. The electrical sheet resistance of the printed lines was lowered by several orders of magnitude from 52.8 ± 7.4 MΩ $\square^{-1}$ for unannealed patterns to 172.7 ± 33.3 Ω $\square^{-1}$ for the annealed patterns. In spite of the remarkable resistance drop, the discussed fabrication procedure is far from low energy sensors' production and unsuitable for most thermally sensitive and flexible substrates.

Girault's group [107] reported on layer-by-layer inkjet printing of flexible iridium oxide-based ink and poly(diallydimethylammonium chloride) (PDDA) ink. Iridium oxide (IrO$_x$) nanoparticles (10 nm in diameter) were prepared using K$_2$IrCl$_6$ as a precursor, tri-sodium citrate dihydrate as a stabiliser and NaOH as a reducing agent. The obtained nanoparticles were dispersed in 1:1 (v/v) water:isopropanol mixture at a 1.24 mM

concentration. PDDA ink was prepared by diluting commercially available 20 wt.% PDDA in water with isopropanol to reach the final concentration of 0.0025 wt.%. Both inks were carefully characterised by viscosity, surface tension and *zeta* potential measurements. The layer-by-layer assembly was achieved by IJP firstly the positively charged PDDA ink on the negatively charged ITO/PET substrate, solvent evaporation, and then printing the negatively charged IrO_x nanoparticle ink. Like that, five IrO_x-PDDA bilayers have been inkjet printed giving homogeneous patterns, as probed by SEM imaging. Finally, these lines were used as pH sensors without any further modification or processing.

Gianvittorio et al. reported on the simple and low-cost microfabrication of ruthenium oxide (RuO_2) thin film electrodes from Ru precursor ink at room temperature using Print-Light-Synthesis [110]. Within this fabrication protocol, an inkjet printer is directly coupled to a UV lamp, allowing for the simultaneous printing and hybrid photo-chemical/photo-thermal conversion of the IJP Ru-ink into RuO_2. The controlled deposition of variable quantities of Ru (100–200 μg_{Ru} cm^2) was achieved by optimizing Print-Light-Synthesis parameters (e.g., drops-per-inch number, ink concentration, number of inkjet printed layers and UV light intensity). The fabricated patterns did not require any further processing and were successfully used as second order metallic electrodes for pH sensing.

2.7.2. *Inkjet printing of the solid-contact transducer*

The next step in layered sensor production is the deposition of a solid contact. It was found that the majority of IJP potentiometric sensors possess a metal/metal salt-based pair solid-contact (6 research papers), which was either formed electrochemically or by thermal oxidation. However, such steps should be avoided if one aims for a high throughput sensor production. In particular, both means imply additional fabrication steps – such as washing or translating to ovens where the electrodes are subjected to temperatures that the majority of (flexible) substrates cannot withstand.

Considering the requirements for particle size, viscosity, density, surface tension and annealing parameters, a diversity of functional materials can be inkjet printed and used as a solid-contact material, as long as they possess the needed features (see Chapter 2.3.

Solid-contact ion-selective electrodes). Both high redox capacitance-based (PANI [119, 122], PEDOT:PSS [120, 125], metal/metal salt pair [105, 107, 110, 117, 118, 127]) and high double-layer capacitance-based (graphene [103, 124], carbon nanotubes [102, 121], graphite [104]) solid contact materials have been used as solid contacts.

Monsalve's group reported a fabrication protocol for a pH sensor by screen printing carbon electrical leads and inkjet printing the pH sensitive conducting polymer polyaniline [122]. Conductive polymer layers are generally formed by electrodeposition. However, considering large scale electrode fabrication one should aim for developing jettable suspensions. An environmentally friendly, aqueous suspension of PANI nanofibers stabilised with sodium dodecyl sulfate (SDS) and acrylic resins (ethyl acrylate and methyl acrylate at different wt.%) was formulated and jetted onto the screen printed electrodes. The prepared inks were characterized by viscosity, density and surface tension measurements. The stabilizer SDS was shown to have the greatest impact on the PANI ink printability, while the acrylic resins significantly improved the wear resistance – compared to electrodeposited PANI. The two means of solid contact deposition did not influence the analytical characteristics of the proposed sensors – both configurations had shown relatively large deviation of E^0 value (±65 mV for electrodeposited PANI and ±46 mV for IJP PANI resin). This was attributed to the uneven surfaces of the screen printed electrode supports – and might be improved by inkjet printing both layers.

Sjöberg et al. [120] have demonstrated that inkjet printing of poly(3,4-ethylenedioxythiophene) transducer layer with poly(styrene sulfonate) ions as counterions (PEDOT:PSS), compared to conventional electrodeposition, also does not influence the potentiometric response towards potassium model ions. The electrodes were prepared by printing Au-electrical leads over paper substrates, SC-layer deposition as described and drop-casting the potassium-selective membrane. It was shown that IJP gives smoother PEDOT:PSS layers compared to the electrodeposition. Such topographical differences were clearly reflected in the electrochemical properties of the SC-films: compared to IJP PEDOT:PSS, electrodeposited PEDOT:PSS enables faster charge transfer and ion transport. However, after the ISM deposition, no significant differences in the electrodes'

analytical characteristics were observed. Both electrode configurations were characterized by the same near-Nernstian sensitivity of 62 mV dec^{-1}, in the potassium concentration range 10^{-5} – 10^{-2} mol dm^{-3}. However, the response reproducibility expressed as the standard deviation of E^0 values was not reported.

Composite materials made from conducting polymers and carbon nanomaterials are known for their superior electrical properties compared to their "pure" components [129]. Citterio's group reported a fully inkjet printed disposable and low-cost paper-based device for potentiometric Na$^+$ or K$^+$ sensing [84]. Ag nanoparticle-based electrical leads were IJP to the paper support. Next, a composite of graphene and PEDOT:PSS (G/PEDOT:PSS) as a solid contact and potassium or sodium selective membranes were printed. The G/PEDOT:PSS composite was characterised by a faster electron transfer, compared to the control SC (IJP PEDOT:PSS). This was explained by the contribution of graphene's large surface area and high electrical conductivity to the overall charge transfer within the inkjet printed material. Finally, Na-ISM and K-ISM were inkjet printed over the SC. With PEDOT:PSS as a transducer, both electrodes have shown a sub-Nernstian sensitivity of 43.6 mV dec^{-1} for sodium and 46.1 mV dec^{-1} for potassium, both within a linear range of 10^{-4} – 10^{-1} mol dm^{-3}. With G/PEDOT:PSS as a transducer, the linear range did not change, but the sensitivity improved to 62.5 mV dec^{-1} and 62.9 mV dec^{-1} for sodium and for potassium, respectively.

2.7.3. Inkjet printing of the ion-selective membrane

The ion-selective membrane is the final layer in the solid-state potentiometric sensor construction. Regarding the materials' properties, it presents the most challenging medium for jetting. The standard membrane recipe – based on nearly 15 wt.% of the solute dissolved in a highly volatile tetrahydrofuran (THF, T_b = 66 °C) – is very difficult to IJP. Picolitre-size THF droplets are nearly impossible to generate at room temperature, as such small volumes of THF instantly evaporate and the plasticised polymer forms deposits at the printer's nozzle. This explains a scarce number of research articles discussing inkjet printing the ISM.

The conducted literature search resulted in four research papers that describe the complete fabrication of potentiometric platforms by inkjet printing [84, 121, 125, 126]. A common characteristic was found within the concerned research articles: all the reported ion-selective membrane formulations were prepared with a reduced solute content by at least a factor of 3.

First, in 2017 Citterio et al. reported on jetting sodium- and potassium-selective THF-based membrane solutions [84]. The authors successfully inkjet printed polymeric ion-selective membranes. However, a dozen overprints were needed to achieve a near-Nernstian response to the ions of interest, as the solute content of the membrane was reduced to 5 wt.%.

Next, Tsou et al. [125] demonstrated completely IJP potentiometric sensing platforms for sodium and potassium sensing. A membrane formulation containing the standard ionophore:ion-exchanger and polymer:plasticiser ratios was prepared in cyclohexanone and inkjet printed. Due to its relatively high boiling point (T_b = 155.6 C), cyclohexanone is noticeably more compatible with the jetting process.

In 2025, Citterio et al. [121] fabricated electrical leads by jetting a gold nanoparticle ink onto the photo paper. Next, carbon nanotube ink was printed as a solid transducer. This was followed by jetting a polymeric hydrogel containing lithium acetate as an intermediate layer to improve the adhesion between the ion-selective membrane and the solid contact. Finally, an ISM membrane prepared in cyclohexanone (5 wt.% solute content) was jetted over the polymeric hydrogel. In doing so, the authors showcased an innovative way of improving adhesion between the ion-selective membrane and the solid contact, lowering the water layer formation. This led to prolonged sensor lifetime, enhanced sensitivity and improved intra-electrode reproducibility.

2.7.4.   *Inkjet printing solid-contact reference electrodes*

In technical terms, the production of a reference electrode by inkjet printing is not different from the production of an ion-selective electrode. It starts with inkjet printing Ag-electrical contact lines (only a single example reports Au-electrical leads). The lack of ink

"diversity" in the found papers is quite understandable, as all the reference elements are based on the well-established Ag/AgCl pair (chemically or electrochemically formed). Concerning the fabrication process, AgCl-formation by drop-casting or jetting the chlorinating agent is more favourable, due to simplicity. However, some groups still stick to the electrochemical means of AgCl formation, as such deposit formation offers better control of the deposit morphology and thickness [119].

Merkoçi's group [83] reported a simple fabrication protocol for miniaturized, disposable, and low-cost Ag/AgCl pseudoreference electrodes using inkjet printing. First, a AgNP ink was inkjet printed on PET and chromatographic paper substrates. The ink was cured at 120 °C for 20 minutes and chemically chlorinated by immersing the IJP Ag-electrodes into a commercial bleach solution without dilution for up to 5 minutes. The formation of the AgCl layer was confirmed by a characteristic colour change, scanning electron microscopy and energy dispersive X-ray spectroscopy. Finally, the performance of the proposed solid-contact quasi-reference electrodes (SC-qRE) was evaluated by chronopotentiometry in KCl 3.0 mol dm^{-3} versus a commercial Ag/AgCl reference electrode with liquid junction and compared to an arbitrarily chosen standard (screen printed reference electrode). The authors did not report any significant difference between electrodes produced by inkjet printing and by screen printing, highlighting the reliability of the proposed SS-qRE. Long-term electrode stability during 30 days of storage in dry and dark conditions was confirmed.

Quasi-reference electrodes suffer from an inevitable problem associated with their poor stability. Due to the thinned layer of sparingly soluble AgCl, open circuit potential stability does not exceed a few minutes to a few hours range. Additionally, these SC-qRE can only be used on samples whose ionic strength is precisely controlled, and which do not contain any interference species (S^{-}, I^{-} and/or Br^{-}), to which the Ag/AgCl would react directly [130].

Solid-contact reference electrodes' robustness and stability can conveniently be preserved by using a protective membrane. Girault's group reported on a flexible SC-RE fabrication approach [113]. Ag-based conductive paths were deposited onto PET substrates

by IJP and annealed using IPL. The electrode surface was chemically chlorinated by dipping the electrode surface into a diluted hypochlorite solution. The reference membrane was prepared by adding ground KCl powder (20 wt.%) and ETH 500 salt (2.25 wt.%) into a commercial UV-curable ink that served as a membrane matrix. This membrane cocktail was drop-cast directly on Ag/AgCl electrodes. Such reference electrodes were electrochemically characterised using electrochemical impedance spectroscopy (EIS) and potentiometric measurements. The influence of the solution composition and concentration was evaluated by drift measurements in a broad concentration ($10^{-6} - 10^{-1}$ mol dm^{-3}) and pH range (3 – 11). A negligible potential change was observed for various electrolytes, indicating a high reproducibility of the fabrication process.

Moya et al. [114] developed the first fully inkjet printed solid-contact reference electrode. The electrode fabrication was concluded in four steps. First, Ag-electrical leads were IJP onto PET substrates and thermally sintered at 130 °C for 20 minutes. Next, an insulating ink was jetted to define the working electrode area. The electrode area was chemically chlorinated after printing a diluted NaClO solution. After washing the bleach, the reference membrane was jetted. The reference membrane was prepared in a carefully selected solvent mixture (40 % methanol, 30 % xylene, 15 % diacetone alcohol and 15 % butanol, all vol. %) to fit its rheological properties to be compatible with a piezoelectric printer. Poly(vinyl butyral), PVB (4 wt.%) membrane matrix and NaCl were added to the solvent mixture and inkjet printed in 1 – 20 layers over the chlorinated Ag-surface. The IJP membrane morphology was thoroughly characterised using confocal imaging and SEM microscopy. The SC-RE performances were tested by drift measurements.

Fully IJP reference electrodes are relatively scarce compared to SC-ISE. This is because these first reference membranes contain ground inorganic chloride salts, which are very likely to block the printer nozzle. Novel interesting jettable reference membrane formulations containing ionic liquids have recently been prepared. Tsou and Cheng [125] have developed jettable reference membrane formulations consisting of ionic liquid (1-dodecyl-3-methylimidazolium chloride), PVC and a plasticiser (5 wt.% solute content) in

cyclohexanone. The reference membrane solution was jetted over chemically chlorinated Ag lines on flexible polyimide substrates.

3. DISCUSSION

3.1. Preface

Solid-contact potentiometric sensors fabrication is a staged process that includes the deposition of an electrical contact, a solid contact and a receptor (ion-selective membrane). Dominating state-of-the art fabrication protocols have been adopted from the graphics industry and are represented by screen and inkjet printing. Inkjet printing holds the potential for the future large-scale and high-throughput fabrication of potentiometric sensors, particularly due to its non-contact, digital character and significantly reduced materials consumption, as compared to screen printing. Having this in mind, this research aims to bring valuable knowledge to the state-of-the-art solid-contact potentiometric sensors' research area.

Some trends have been identified in the area of inkjet printed potentiometric systems. Usually, metallic inks are printed, which are then partially coated with appropriate salts in subsequent processes – often time and energy inefficient – thus forming a second-order metal electrode. Such sensors suffer from impaired stability against interferences and metal salt dissolving. Response stability and selectivity have been significantly improved after including the ion-selective membrane in the sensors' structure.

Herein, commercially available silver ink was used for inkjet printing electrical contacts due to its exceptional electrical conductivity and cost-effectiveness. Graphene was chosen as a promising solid-contact material: the hydrophobicity in pair with excellent electrical conductivity and high double-layer capacitance make it a great candidate for a solid contact material. In particular, graphene was synthesised by a novel, environmentally friendly mechanochemical synthetic pathway; a jettable ink was formulated in environmentally friendly solvents, strongly accounting for the successful droplet formation. Both the electrical leads and solid contacts were inkjet printed onto flexible polyimide substrates and an ammonium-selective membrane was drop-cast. A potentiometric method for quantifying ammonium ions in leachate samples was developed.

Due to the fluid characteristics, liquid polymeric ion-selective membranes are scarcely deposited by inkjet printing. As a rule, the solute content is typically diluted five times in order to enable printing. In recent years, some research groups have found their own ways of improving the accuracy of the fabrication process. Herein, an automated fluid dosing robot was tested and the membrane morphology was controlled by carefully selecting the solvent mixture that promotes the Marangoni flow. In this way, the membrane was precisely and reproducibly applied, without changing the portion of dry matter.

Finally, to close the potentiometric cell, a reference membrane compatible with the inkjet printed electrical contacts was developed. Conventional SC-RE fabrication involves multiple steps – Ag contact deposition, annealing, AgCl formation, washing, and optional membrane deposition – making it relatively time-consuming. To simplify this process, a polyvinyl butyral (PVB) matrix was employed due to its compatibility with inorganic salts and ability to host a complete reference element. Remarkably, the Ag/AgCl pair within the PVB membrane was formed instantly, within 91 µs, using intense pulsed light for AgCl photoreduction. The demonstrated IPL approach significantly reduced reaction time and, consequently, fabrication time, offering a straightforward route towards commercialization.

3.2. Development of an inkjet printable, electrically conductive ink based on melamine-intercalated graphene nanosheets

The first part of the doctoral research included development of electrically conductive inks for printed electronics applications, which can be applied in IJP potentiometric sensor fabrication. In a research article in Appendix I, we aimed to explore novel, simple, scalable and green means of graphene-based ink formulations. Graphene is a great candidate for flexible electronics applications due to its outstanding electrical and mechanical properties. This has led to various production methods, all aiming to produce graphene with as few defects as possible. Liquid-phase exfoliation is the most reported large-scale production method of two-dimensional (2D) nanosheets. However, this method is quite laborious, slow, and often consumes harmful organic solvents. On the other hand,

solvent-free mechanochemical methods stand out due to their simplicity, ease of process parameter control and environmental safeness [131].

Herein, we showcased that mechanochemically synthesised graphene nanosheets can be used for an electrically conducting inkjet printable ink formulation. Graphene was chosen due to its' potential for excellent properties as a solid contact layer; it is known for its' hydrophobicity (the crucial property against unwanted thin water layer formation) and excellent electrical conductivity coupled with high surface-to-volume ratio (the key to well-defined signal transduction based on high double-layer capacitance). Graphene nanosheets were synthesised in a planetary ball mill using graphite flakes as a precursor and melamine as an exfoliating agent and stabiliser (MGNS, melamine-intercalated graphene nanosheets). An average particle height of 0.30 – 0.65 nm with a diameter of 14 nm was found, indicating single- and double-layer graphene nanosheets (see Appendix I, Figure 3). The obtained MGNS particle size satisfies the first prerequisite of a functional material to be inkjet printed, that is the particles must be small enough to successfully be jetted from the tiny printer nozzles.

The ink was formulated after dispersing the MGNS within a solvent mixture. Jettable ink production is a complex process that accounts for the filler (MGNS) stability within the solvent (that is, solvent mixture), the possibility of droplet generation, the spreading and drying of the jetted droplets on the substrate, and finally, restoring the electrical conductivity of the printed pattern. We formulated our ink, having all the above processes in mind.

Graphene is known to form stable dispersions in solvents with a similar surface energy to itself, such as N-methyl-2-pyrrolidone (NMP), N-cyclo-2-pyrrolidone, dimethylformamide (DMF), and dimethylsulfoxide (DMSO). These solvents have relatively high boiling points (> 150 °C), complicating the printing process, as the substrate platen needs to be heated for faster pattern drying. Additionally, these solvents are hazardous; hence, we did not consider using them. We have adopted a mixture of green solvents that do not impose any environmental or health concerns: ethanol (22.55 mN/m, 1.2 mPa·s), water (72 mN/m, 1.002 mPa·s), ethylene glycol (47.49 mN/m, 19.43 mPa s)

(0.50:0.45:0.05 respectively by volume). Water/ethanol mixture was used as the significant difference in the surface tension of the two solvents induces the reverse Marangoni flow of the droplet on a surface. On top of that, the employed solvents have an optimal boiling point – high enough to prevent ink evaporation in contact with air, and low enough to be rapidly dried upon pinning to the substrate surface. Stable formulations were prepared after the addition of commercially available organic stabilisers. Finally, to predict the printability of the ink, we calculated the Z-value after determining the inks' surface tension ($\gamma = 31.67$ mN m^{-1}), viscosity ($\eta = 3.26$ mPa s) and density ($\rho = 0.9373$ g mL^{-1}). The formula used for the calculation of the Z-value and the limiting values have been discussed in **Section 2.6.1. Inkjet printing**; the calculated Z-value of 7.7 indicated excellent ink capacity for droplet generation.

The hydrodynamic particle diameter and surface charge within the ink formulation were determined using dynamic light scattering (DLS) analysis and zeta-potential measurement, respectively. The DLS measurements of the MGNS ink gave an average hydrodynamic particle diameter of $d = 173.7$ nm (see Appendix I, Figure 5), indicating that MGNS particles were small enough for printing without clogging the printer head. Additionally, the measurements have shown a narrow particle size distribution, indicating the possibility of printing uniform, homogeneous layers. The determined zeta-potential of the MGNS ink was –25.7 mV, indicating that our ink was moderately stable [132].

Finally, the long-term stability of the ink formulation was assessed by collecting the UV-Vis spectra of a freshly prepared MGNS ink and during 32 days post-preparation. The reduction of the absorbance value at 512 nm was taken as the indicator of the MGNS particle sedimentation. During the first 6 hours after the ink preparation, the absorbance does not fall below 91 % of the initial value, indicating good stability for single-day printing. After more than a month of the ink storage, the initial absorbance value was regained after a minute treatment with a tip-sonicator (see Appendix I, Figure 6). This indicates that the maximum ink stability can be easily recovered and the ink reused.

The ink was inkjet printed onto PET and PI substrates in 1 – 10 overprints, dried at 55 °C and characterised by sheet resistance measurements (R_S) using a four-point probe. Up

to three overprints, the printed samples were not electrically conducting; five overprints gave $R_S = 4.27 \pm 0.87$ MΩ sq^{-1}, and 10 overprints gave $R_S = 2.0 \pm 0.9$ MΩ sq^{-1}.

To improve the electrical conductivity, we exposed the printed patterns (10 overprints) to different elevated temperatures (100, 200, 300 and 400 °C) for one hour. After thermal treatment at 400 °C, the measured sheet resistance plummeted to 44.0 ± 6.0 kΩ sq^{-1}. This resistance drop was due to the thermal decomposition of melamine (de-amonation) and Solsperse stabilisers, which led to restoring conductive pathways and increasing the printed patterns' homogeneity. SEM images taken before thermal annealing have shown large melamine crystals ($d > 10$ μm) that disrupt the electrical conductivity. After thermal annealing, more homogeneous topography was observed, which accounts for the improved conductivity. The film thickness and surface roughness were reduced after annealing, as revealed by AFM imaging. The quadratic average surface roughness parameter (R_q) decreased from 789.1 nm to 289.1 nm, typical of ink sintering and stabiliser removal. This indicates that vertical surface irregularities – including peaks and valleys – decrease, improving the inkjet printed film uniformity and consistency.

It is well-known that carbon nanomaterials-based films are great candidates for IPL annealing, as they strongly absorb in the visible part of the spectrum. Exposing the printed patterns to IPL with energies in the range 300 – 600 J (without previous thermal treatment), the sheet resistance was reduced only to around 43 % of the initial value. Increasing the IPL energy above 600 J caused a resistance increase, suggesting that the conductive film was damaged by such a strong IPL intensity (See Figure S3 in Appendix II). Compared to thermal annealing, which by its' virtue slowly heats the sample, IPL is a millisecond treatment. Given that melamine primarily decomposes through ammonia loss, we attribute the inadequacy of IPL annealing alone to melamine sublimation and the ultrafast release of ammonia, which in turn results in detachment of the graphene film from the substrate. However, after exposing the previously thermally annealed films (400 °C, 1 h) to IPL (2500 V, 700 J) we managed to significantly reduce the sheet resistance of our inkjet printed films to 5.0 ± 0.3 kΩ sq^{-1} (10 overprints) and 626 ± 106 Ω sq^{-1} (20 overprints). The obtained sheet resistance values with the number of overprints and graphene

concentration show that our ink is comparable or even better than those showcased in similar studies (see Table S2 in Appendix II). Finally, as a proof-of-concept experiment, we showcased that inkjet printed graphene traces with optimised annealing protocol can be used as a component of a printed electronic circuit, indicating the possibility of further investigation of the proposed printing protocol in more complex systems.

3.3. Development of a planar solid-contact ion-selective electrode

The developed graphene ink was next incorporated into the design of a planar ion-selective electrode and tested. The second objective of this research was to develop an inkjet printing fabrication protocol for solid-contact ion-selective electrodes and showcase their applicability in real sample analysis. State-of-the-art ion-selective electrodes are planar layered structures (see **Chapter 2.3. Solid-contact ion-selective electrodes**) with a well-defined electrical contact, solid-contact and a receptor.

The research paper in Appendix III presents a scalable and low-cost route for fabricating flexible ammonium-selective electrodes by inkjet printing silver electrical contacts and MGNS ink. Our preference for a carbon nanomaterial-based transducer over conductive polymers stems from their high specific surface area and excellent hydrophobicity. Particularly, high specific surface area paired with high electrical conductivity is a key property for high electrochemical double layer capacitance, the characteristic signal transduction of carbon-based transducers. The transducer's hydrophobicity is an important property for the stability against a thin water-layer accumulation at the SC | ISM interface, which is the most common case of the sensors' failure.

Commercially available silver ink was inkjet printed onto polyimide substrates and cured with a single IPL pulse (400 J, 2500 V). Electrodes having a working area with a diameter $d = 6$ mm were decorated by inkjet printing MGNS ink. The electrodes were annealed by a combination of thermal annealing (300 °C for 1 h) and IPL (single pulse at 2500 V and 700 J). Finally, the ammonium-selective membrane was drop-cast onto the

inkjet printed electrodes, giving an SC-ISE. The overall electrode fabrication and the demonstration of the sensors' flexibility are shown in Figure 1 of Appendix III. To determine the influence of the inkjet printed MGNS solid-contact on the electrochemical characteristics of inkjet printed sensors, we cast the ammonium-selective membrane directly onto inkjet printed Ag-leads. Thus, coated-wire electrodes were prepared for comparison.

The inkjet printed MGNS solid contact material was characterised using electrochemical impedance spectroscopy. EIS measurement was done in a three-electrode electrochemical cell consisting of a SC-ISE or CWE as a working electrode, a conventional double junction Ag/AgCl/KCl/NaNO$_3$ reference electrode and a platinum auxiliary electrode. In EIS experiments, an alternating potential is scanned from high to low frequencies, enabling the extrapolation of information related to fast processes (charge transfer) and slow processes (diffusion within the membrane), respectively. The Nyquist plot of both electrode configurations shows a typical high-frequency semicircle arising from bulk ion-selective membrane resistance (R_{bulk}) in parallel with the geometric capacitance of the membrane (C_g) [133]. R_{bulk} represents the contact resistance between the ISM and the electrode surface of the CWE, or the ISM and inkjet printed MGNS solid contact, for SC-ISE. It is obtained from the Nyquist plot as the impedance value where the semicircle touches the x-axis. As can be seen in Figure S2 in Appendix IV, by including the MGNS solid contact in the electrode structure, the R_{bulk} falls from 7.31 MΩ to 4.30 MΩ. The influence of the solid contact on the low-frequency phenomena, including the ion-to-electron transduction, was depicted as the low-frequency part of the Bodé spectra and quantified as the change of impedance modulus, |Z| [134]. Clearly, |Z| decreases after introducing the MGNS solid-contact, indicating that inkjet printed MGNS ink assists the charge transfer between the ion-selective membrane and the electrode surface.

A single electrode calibration (SC-ISE) in the concentration range of NH$_4$Cl 10^{-8} – 10^{-1} mol dm^{-3} was repeated three times (intra-reproducibility assessment). A reliable potentiometric response was obtained within c(NH$_4$Cl) = 10^{-4} – 10^{-1} mol dm^{-3}, with a sensitivity of 52.045 $\pm$ 0.525 mV dec^{-1} (R^2 = 0.9976). The lower limit of detection of 25.1

μmol dm^{-3} was calculated according to the IUPAC recommendations for potentiometric probes. Separate solutions method was used for the determination of the sensor's selectivity coefficient, $K_{NH_4^+,J}^{pot}$ for the most common interferents in biological and environmental samples, KCl, NaCl, CaCl$_2$, MgCl$_2$. All the $K_{NH_4^+,J}^{pot}$ (given in Table 1 of Appendix III) are lower than 10^{-1}, showcasing that the sensor is highly selective to its target ion.

Developing a scalable sensor production protocol, one needs to consider the reproducibility of the production process, which is defined as the response reproducibility between electrodes. The inter-electrode reproducibility is expressed as the standard deviation of the calibration curves (including the E^0, dynamic linear range and sensitivity), obtained from multiple equally prepared sensors. Additionally, the electrodes' drift during prolonged measurements should be reduced as much as possible. We have prepared a batch of SC-ISEs and evaluated the inter-electrode reproducibility by recording the potential response of three electrodes ($n = 3$) in 10 mM NH$_4$Cl for three hours (the first contact with the solution was at $t = 0$ h). The potentiometric time-trace of these electrodes is shown in Figure 3A in Appendix III. At $t = 3$ h, the measured potential range was 19 mV, and a mean drift value of -0.393 mV h^{-1}. We ascribed this non-negligible inter-electrode response discrepancy to the redox-active impurities in the MGNS solid-contact material (residual melamine and its de-amonation products).

To improve the inter-electrode response discrepancy, each electrode was chronoamperometrically polarized for 30 minutes at a potential value towards which all the electrodes were drifting ($+180$ mV). During the positive electrode prepolarization, the primary ions are pushed from the ISM/transducer boundary (the depth of the membrane) into the ISM, promoting the hydration and saturation of the ISM layer with primary ions, but preventing the incorporation of sensor primary ions into the MGNS transducer [135]. Indeed, the positive effect of the electrode prepolarization is shown both on the mid-term potential time-trace (Appendix III, Figure 3B). After prepolarization, the potential range of prepolarized electrodes was reduced to 9 mV, and a mean drift value fell to 0.103 mV h^{-1}. Positive outcome of prepolarization is best indicated in the calibration curves (see Appendix III, Figure 4). The calibration plot of unpolarized electrodes shows a super-

Nernstian response (84.52 mV/pNH$_4$; R^2 = 0.9822) in the low concentration range, 10^{-5} – 10^{-3} mol dm^{-3}, and a sub-Nernstian response in the high concentration range (36.289 mV/pNH$_4$; R^2 = 0.9996). The super-Nernstian response in the low-concentration range arises from the ion influx into the ISM, indicating the concentration gradient of the primary ions within the ISM; while the sub-Nernstian response at high NH$_4$-ion concentrations indicates that the membrane is too saturated with the primary ions.

The extension of the electrodes' dynamic linear range to 10^{-6} – 10^{-1} mol dm^{-3}, along with lowering of the lower detection limit to 0.88 $\pm$ 0.17 µmol dm^{-3} were the positive outcomes of electrode prepolarization. This is an indicator of the loss of membrane fluxes, which is necessary for an appropriate sensor functioning. Finally, the sensitivity increased to 55.594 $\pm$ 0.429 mV dec^{-1} (R^2 = 0.9856)..

Water layer tests were made with the CWE and SC-ISE. The open circuit potential was monitored during 15 hours of the electrodes' immersion; firstly, in the primary ion solution (10 mM NH$_4$Cl) for 5 hours, then with an interfering ion solution (10 mM NaCl) for two hours, and finally in the primary ion solution (10 mM NH$_4$Cl) for 8 hours (see Figure 5A in Appendix III). The CWE showed a behaviour typical of coated wire electrodes which arises from the thin water layer formation at the back of the ISM. A pronounced drift of 16.02 mV h^{-1} in an interfering ion solution was observed, and –3.98 mV h^{-1} during the second contact with the primary ion solution. The potential drifting was notably reduced after introducing the MGNS layer beneath the ISM. The measured drift in NaCl was 4.00 mV h^{-1}, and in NH$_4$Cl it plummeted to 0.22 mV h^{-1}. The prolonged measurements have shown that the MGNS solid contact significantly improves the long-term electrode stability.

Next, we tested the sensors' reversibility by performing OCP measurements upon cycling the standard solutions' concentrations between 10^{-3} and 10^{-1} mol dm^{-3} (see Figure 5B in Appendix III). The original EMF of 173 mV remained stable with 0.59 % relative standard deviation, indicating excellent reversibility and negligible hysteresis effect.

Finally, the presented fabrication protocol and detailed electrochemical and analytical characterisation were done to showcase the real sample analysis. Ammonia

nitrogen – which includes unionised ammonia, NH_3 and ammonium ion, NH_4^+ – is an indicator of water quality and natural nitrogen cycle state. Ammonia pollution from agriculture and public waste disposal presents a serious concern for human health and ecosystems welfare, as increased ammonia nitrogen causes eutrophication of water systems and air deposition causing respiratory and skin issues in humans [136]. The leachate water was taken from the leachate collector basins on the landfill site. The ammonium ion concentration within the sample was determined using a reference spectrophotometric method and the potentiometric method, using our in-house fabricated SC-ISE. For the potentiometric method, the three-point standard addition method was used. The response time of the sensor, as calculated as t_{95} was 13 seconds, making the proposed method time efficient. The method validation is presented in Table 2 in Appendix III, as a comparison of the reference and potentiometric method. Our potentiometric method resulted in ammonium ion concentration 30.61 ± 1.30 mM (n = 3), differing by less than 4% from the value obtained with the reference method. With this, we validated our fabrication approach and analytical procedure, opening the doors to on-site measurements of critical analytes.

3.4. Optimisation of ion-selective membrane composition for contactless deposition

An important part of this research was the optimisation of polymeric membrane composition that enables fast and reliable automated potentiometric sensor production. As previously stated, the most challenging part of the layered sensor construction is the automated deposition of an ion-selective membrane. The established ion-selective membrane composition is based on a plasticised poly(vinyl chloride) matrix that holds the components responsible for the sensors' analytical response (see **Section 2.1.1. Conventional ion-selective electrode design**). The membrane cocktail is usually prepared containing in total 15 wt.% of the solute in a highly volatile organic solvent, tetrahydrofuran. This composition resulted from decades of ion-selective electrode development and holds for both the theoretical and empirical knowledge. More recently,

protocols for controlled deposition of the ISM either by inkjet printing or automated dispensing have emerged. However, all the reported literature demonstrates the deposition of at least three times lower solute content compared to the common one. This in turn, calls for increasing the number of membrane overprints, slowing down the overall electrode production.

In the research article presented in Appendix V, we optimised the polymeric membrane composition for the automated production using the dispensing robot system and developed a method of tracking membrane drying. Rather than diluting the solute content of the membrane cocktail, we optimised the membrane solvent carrier composition. In addition to THF, cyclohexanone was reported as an ISM cocktail solvent, as it – due to its high boiling point – allows for better manipulation of membrane formulations [137]. Membrane cocktails prepared with different rations of cyclohexanone and THF were automatically dispensed onto photographic paper and their topography was evaluated using the colorimetric absorbance method. [138].

The 3D absorbance plots are given in Figure 2 in Appendix V. When cyclohexanone is used as a major membrane solvent, that is, at 90 and 75 vol%, a capillary flow develops during the evaporation. This is reflected in solvent flow from the centre to the edges of the droplet and accumulation of plasticised polymer particles in a characteristic ring structure. Droplets' structure homogeneity noticeably increased upon lowering the volume fraction of cyclohexanone and increasing the THF part. As the two solvents significantly differ in boiling point, viscosity and surface tension, an inward Marangoni flow is generated, opposing the capillary flow. The most uniform membrane thickness was obtained at equal volume ratios of the two membrane solvents, indicating the best solvent composition for membrane deposition using the dispenser machine.

The colorimetric absorbance method was used to determine the volume of a single spot of the membrane and the thickness of the wet and dried membranes with different solvent compositions. The volume of a single droplet was estimated to be $V \approx 0.20$ μL; the wet membranes' thicknesses were in the range $36.3 - 61.5$ μm, and dried membranes' thicknesses were in the range $11.6 - 17.2$ μm.

In tandem with fabricating the electrical leads and transducers by printing techniques, automated membrane dispensing presents the icing on the cake when considering fast and reliable sensors mass production. Fabricated sensors can be tested only when the dispensed membrane is fully dried. In practice, cast ion-selective membranes are dried overnight at room temperature. However, when considering mass production and product placement, it is beneficial to know when the membrane is fully dried and ready for testing. To investigate the effect of solvent composition on evaporative drying profiles of the ISM, we dissolved the membrane solute in three solvents: pure THF, pure cyclohexanone, and a 1:1 THF:cyclohexanone mix (indicated as THF, CH and MIX, respectively, in the rest of the text). These membranes were drop-cast onto two adjacent screen-printed electrodes. 1 μL was cast on each electrode so that the droplets connected, forming a continuous membrane and an electrical bridge between electrodes, as schematically shown in Figure 1 in Appendix V. In doing so, we prepared a two-electrode cell for accurate impedance measurements of small volume samples. Because the polymeric membrane contains volatile (THF, CH or MIX) and non-volatile components (PVC, plasticizer, valinomycin, ion-exchanger, lipophilic salt), the evaporation of volatile components rearranges membrane composition and structure, imposing the membrane impedance changes over time.

Time-resolved impedance spectroscopy was used to track evaporative membrane drying (thinning) in real time. In principle, consecutive high-frequency impedance measurements were recorded at successive time intervals, starting at the moment of membrane casting. The Bodé plot (phase angle, $-\theta$ versus frequency, f) of THF, CH and MIX membrane is shown on Figures 3A, C and E in Appendix V. Regardless of the membrane solvent, the phase angle at $t = 0$ strongly depends on the measurement frequency: starting at $f = 10^5$ Hz, phase angle approaches 90°, indicating capacitive behaviour; at one order of magnitude lower frequency, phase angle approaches 30°, a typical indicator of resistive behaviour. The capacitive behaviour at the starting frequency reflects the charge separation at the membrane / electrode interface, while the resistive behaviour at the end of each measurement stems from the bulk membrane resistance. Thus, plotting the absolute values of impedance, $|Z|$ measured at 10^4 Hz as a function of time we

obtained evaporative drying (impedance) profiles of the three membranes (see Figures 3B, D and F in Appendix V). The impedance profiles of the three membranes consist of two parts: the impedance gradient reflecting the volatile components' evaporation, and the fully dried membranes' plateau. The starting membrane impedance at the moment, $t = 0$ s was 2.09 ± 0.18 MΩ (THF) 2.65 ± 0.05 MΩ (CH), and 1.98 ± 0.83 M (mixture).

Polymeric membrane evaporative drying is explained by Fickian diffusion model and free-volume theory. In particular, the rate of diffusion of a volatile solvent (THF or CH) is determined by the free volume within the polymer matrix, which is unignorably expanded by a non-volatile liquid plasticizer, DOS. Evaporative drying profiles of both THF- and CH-based membranes were successfully described by second-order polynomial fits (see Table S1 in Appendix VI). The two profiles differ due to the extreme difference in the respective solvents' volatility. THF-based membrane completely dries within less than a minute ($|Z| = 5.14 \pm 0.27$ MΩ), while the CH-based membrane reaches the impedance plateau in 23.2 minutes ($|Z| = 5.89 \pm 0.19$ MΩ). All evaporative profiles showcase a sharp transition to the plateau, since the plasticizer present in the double amount of the polymer practically impairs the viscosity increase (which usually follows evaporative drying). Thus, the solvent transport from the bulk of the membrane to the interface with air doesn't get hindered until the last bit of solvent evaporates.

The impedance profile of the membranes prepared in the THF:CH mixture splits into two parts, each following its second order polynomial (see Table S2 in Appendix VI). The halved volume of THF evaporates almost instantly, lowering the diffusivity of the remaining cyclohexanone within the membrane and leaving the drying profile dominated by the less volatile solvent, cyclohexanone. The impedance plateau (5.60 ± 0.01 MΩ) is reached in 11.5 min, aligning with the drying time of the cyclohexanone-only system.

Potassium-selective membrane cocktail was prepared in a THF:CH mixture. The K-ISM was automatically dispensed onto screen printed carbon electrode arrays in one, two, three, four and five spots' repetitions (each spot having estimated $V \approx 0.20$ µL). The dried membrane thickness of a single spot, $h = 16 \pm 1$ µm was estimated using absorbance measurements. After examining that the membranes dispensed on the neighbouring

electrodes do not overlap, the electrode arrays were embodied in a flow cell and calibrated in standard solutions of KCl. Figure 4 in Appendix V shows the calibration plots obtained with devices modified with different numbers of membrane spots. A single spot of the K-ISM was enough to obtain an adequate potentiometric response within a clinically relevant potassium concentration range. The standard deviation of E^0 values improved from ±15.183 mV dec^{-1} for a single spot to ±4.024 mV dec^{-1} already for two spots of the K-ISM. With this, full electrode preparation, including the membrane drying can be done in less than 30 minutes. SSM was carried out in clinically relevant interferents, including Na$^+$, Ca^{2+} and Mg^{2+}, indicating good selectivity towards K$^+$ ions (see Figure S4 in Appendix VI).

3.5.   Development of a planar solid-contact reference electrode

The final objective of this thesis was to develop a planar solid-contact reference electrode, to be paired with the developed printed ISEs. In practice, SC-RE fabrication is a multi-step process which includes Ag-electrical contact deposition, annealing, chemical (or electrochemical) chlorination, washing, and an optional reference (protective) membrane deposition. Due to its processability and compatibility with inorganic salts, polyvinyl butyral (PVB) is sometimes used as a matrix for preparing a protective Cl$^-$ saturated reference element of a SC-RE, as discussed in Chapter 2.4. Solid-contact reference electrodes. Additionally, it is possible to construct a complete reference element within a PVB membrane and deposit it onto an electrically conductive material (not necessarily an Ag-based material) [59]. This significantly simplifies SC-RE fabrication, which is something one should aim for when considering the commercialisation possibilities.

The research paper in Appendix VII explores the possibility of a unique reference membrane preparation by using IPL and its application to inkjet-printed electrodes. The Ag/AgCl pair within the PVB matrix was formed instantly, within 91 µs of exposure to IPL as a light source for the photoreduction of AgCl. In particular, 250 mg of NaCl and 250 mg of AgNO$_3$ were added to a 10 wt.% methanol solution of PVB (5 mL) and bath sonicated in dark conditions for 30 minutes, during which a white suspension of AgCl was formed, with

NaCl crystals in excess. Following this, the obtained suspension was subjected to a single IPL flashlight pulse, as the applicability of IPL for (metal oxide) reduction has previously been demonstrated [139]. Figure 2 in Appendix VII shows the reference membrane color change as the IPL light gets stronger: the higher the intensity, the darker the membrane becomes, due to formed Ag nanoparticle growth. We have confirmed the silver nanoparticle (AgNP) formation by detecting its characteristic peak at 410 nm (see Figure S1 in Appendix VIII).

The reference membrane flashed at different intensities was drop-cast onto a glassy carbon electrode, dried and subjected to the OCP measurements in KCl solutions within 10^{-4} to 10^{-2} mol dm^{-3} concentration range. Treating the membrane with high intensity light pulses (energies > 200 J) pushes the degree of AgCl reduction to Ag^0, giving the membranes with an excess of AgNPs. Such electrodes gave high response slopes, indicating a response to Cl$^-$ ions. Using utterly gentle IPL energies of 100 J at 2000 V, we were able to significantly reduce the electrode response to Cl$^-$ ions. This is because at such small light intensities only a part of AgCl was reduced to Ag^0, giving Ag–AgCl clusters, which are responsible for the characteristic reference electrode behaviour [59].

The reference membrane (100 J, 2000 V) was drop-cast onto glassy carbon and inkjet printed Ag-electrode, giving GC–RM and PE–RM, respectively. Before detailed potentiometric characterisation, we examined the effect of conditioning time on the impedance changes of the prepared electrodes. The initial reference potential stabilisation during conditioning in 3 mol dm^{-3} KCl is shown in Figure 3 in Appendix VII. Both GC–RM and PE–RM show a pronounced potential drift upon the first contact with the conditioning solution. The potential response of the two electrodes fully stabilises already within 3 minutes for PE–RM, and 40 minutes for GC–RM.

To better understand the differences between the two electrodes, before and every hour during conditioning, the electrodes were moved to 0.1 mol dm^{-3} and EIS spectra were recorded. EIS spectra of the two electrode types are shown in Figure 4 in Appendix VII. EIS spectra of GC–RM prominently changed during the first hour of electrode conditioning. At $t = 0$ h, the Nyquist plot forms a semicircle impedance arc typical of

materials with high charge-transfer resistance. One hour into conditioning, the impedance spectra are composed of two parts. At high frequencies, a small semicircle reflects the charge transfer resistance that recedes as the conditioning advances. The low frequency part of the spectra is dominated by a straight line with a slope that increases as the contact with the electrolyte increases. This is a characteristic of ion diffusion through the membrane; the steeper the line, the faster the ion transport [140]. Worth noting is that the spectra dominated by the low frequency line indicates a system where the ion diffusion is a limiting process. The most prominent change in the EIS response of GC–RM is between $t = 0$ h and $t = 1$ h; this follows the potential trace during the conditioning. At $t > 1$ h, the potential stabilises, and the impedance changes are minute. The low frequency capacitance of the conditioned electrode was calculated to be 44.92 µF.

The described evolution of the impedance spectra follows the working mechanism of the developed reference membrane. In detail, the reference membrane consists of a PVB matrix saturated with Ag–AgCl clusters and an excess of NaCl. Ag–AgCl clusters are the heaviest membrane component. As the cast membrane dries on the electrode surface, Ag–AgCl clusters fall to the electrode surface; spreading there, they form a continuous coverage, governing the ion-to-electron transduction process. At the same time, the excess of NaCl provides a constant internal chloride concentration responsible for the reference electrodes' potential stability. During conditioning, the PVB matrix undergoes structural changes, as indicated by the promoted ion diffusion within the membrane. As the membrane is fully wetted, the slow diffusion of ions between the membrane bulk and the surrounding solution maintains a steady ion exchange without significant depletion of internal electrolytes, ensuring potential stability over time.

As shown in Figure 3B in Appendix VII, the potential-time trace of the PE–RM stabilised notably faster compared to the GC–RM. Likewise, the impedance values (see Figure 4B in Appendix VII) were three orders of magnitude smaller already within the first contact with the electrolyte. The impedance spectra of PE–RM practically lack the low frequency semicircle and are dominated by a straight line, showcasing the same trend of increasing slope as the conditioning continues. The low frequency capacitance of the

conditioned electrode (related to the diffusion processes) was calculated to be 690 μF. Since both the inkjet printed and rod electrode were decorated with the same membrane, similar morphological changes resulting from ion uptake are expected. Both electrodes showed EIS spectra typical of diffusion-controlled processes, but at significantly different impedance and low-frequency capacitance values. The improved conductivity observed in PE–RM suggests better electrical contact between the PVB membrane and the inkjet-printed Ag electrode, likely due to its rougher surface and greater microscopic area compared to the smooth GC electrode, as shown in SEM images (see Figure S2 in Appendix VIII).

GC–RM and PE–RM were subjected to drift measurements in 10^{-2} mol dm^{-3} KCl during 8 hours. The results of the test are shown in Appendix VIII, Figure S3. Throughout the test, PE–RM kept a stable response with a low drift value of -0.2464 mV h^{-1}. On the contrary, GC–RM response deteriorated after two hours of immersion, indicating an electrode failure. We performed a leakage study with GC–RM (see Figure S4 in Appendix VIII) to resolve whether this failure stems from Cl^{-} leakage from the reference membrane. The leakage test was carried out in deionised water by the conductivity measurements during 4 hours of the electrode immersion. Apart from the initial increase in conductivity upon immersion (probably dissolution of surface NaCl), no significant changes or trends were observed during the measurement, indicating that the PVB matrix sufficiently holds the membrane components. Instead, we attributed the GC–RM failure to partial delamination of the reference membrane from the smooth glassy carbon electrode surface. Indeed, even though both PE and GC-electrode show similar adhesion parameters with the RM (see Table S1 in Appendix VIII), the RM adhered much stronger to the rough Ag-IJP surface due to the interlocking with Ag-grains.

We measured the response stability tests for both GC–RM and PE–RM in several salts, including KCl, NaCl, $CaCl_2$ and $NaNO_3$. The response plots and slope values are given in Figure 5 and Table 1 of Appendix VII, respectively. Both electrode designs gave slope values < 4 mV dec^{-1}, indicating sufficient response stability in the broad ion concentration range ($10^{-6} - 10^{-2}$ mol dm^{-3}). The inter-electrode reproducibility of E^0 value

for PE–RM ($n = 3$) in all tested electrolytes was less than 5.63 mV. Finally, the electrode response to pH changes was absent in the $2 – 10$ pH window (see Figure 6 in Appendix VII).

Finally, two proof-of-concept experiments were performed to showcase the applicability of the proposed reference electrodes in conventional electrochemical experiments. First, we calibrated a commercial sodium selective electrode using GC–RM or PE–RM as a reference electrode. As can be seen from the respective calibration lines (Figure 7A, Appendix VII), regardless of the reference electrode, a response slope higher than 55.57 mV dec^{-1} in the dynamic linear range from 10^{-4} to 10^{-2} mol dm^{-3} was obtained. Next, a reversible electron transfer reaction of $[Fe(CN)_6]^{3-/4-}$ on a polished glassy carbon electrode was recorded in a three-electrode cell using either PE–RM or a commercial reference electrode and an auxiliary platinum electrode. The obtained cyclic voltammograms were analysed by comparing peak-to-peak separation potential (ΔE_p), giving the difference for the two measurements smaller than 3 % RSD. The measured current peak values, I_p, of the investigated redox system were used to calculate the geometric surface area (A) of the working electrode using the Randles-Ševčik equation. The relative standard deviation of A for the two systems was less than 7 %, indicating the suitability of our electrodes for the different electroanalytical techniques.

4. CONCLUSIONS

This doctoral research was conducted in the context of current trends in the electrochemical sensor community, specifically focusing on the construction of – potentiometric sensors. Nowadays, the reported potentiometric sensors have achieved fantastic characteristics. However, only a few of these innovations ever see practical application beyond the labs in which they originated. Certainly, there is a challenge yet to be solved: developing a suitable mass production method and tailoring the functional material properties to make it suitable for such. Connecting the dots, we have adopted inkjet printing as a fabrication technique of choice, as the process is exceptionally adaptable, cost-efficient and sustainable, and put forward the research objectives around it.

The first objective of this research was to develop inkjet printable electrically conductive ink based on carbon nanomaterials to be used as a solid transducer in a layered potentiometric sensor structure. As the carbon nanomaterial of choice, graphene nanosheets were quickly and inexpensively mechanochemically derived and successfully dispersed in a combination of green solvents, specifically accounting for droplet formation and printed pattern uniformity. The proposed MGNS ink was thoroughly characterized by density, surface tension, viscosity and absorbance measurements. 6 hours short-term stability was sufficient for the overall printing process and was easily restored after a month resting by a short treatment with a tip-sonicator. We successfully printed our ink onto polyimide and PET substrates. We have shown that solely photonic annealing was not applicable for restoring the printed patterns' electrical conductivity, as the lightning-fast removal of ammonia leads to the removal of the graphene film from the substrate. However, with an optimised combination of thermal and photonic annealing, we managed to lower the sheet resistance to $626 \pm 106 \ \Omega \ \text{sq}^{-1}$ for 20 overprints, indicating a great potential for further use in potentiometric sensors.

An ammonium-selective solid-state electrode fabrication protocol was developed, relying on inkjet printing silver electrical lines and our optimized MGNS ink printing and annealing protocol. With this, the hypothesis – that improved analytical performance of ion-selective electrodes can be achieved using carbon nanomaterials as inkjet printed solid

contact – was tested. EIS experiments have shown that inkjet printed MGNS layer sandwiched between an inkjet printed Ag-electrode contact and an ammonium-selective membrane improves the charge transport, facilitating the electrochemical double layer-based ion-to-electron signal transduction. Moreover, due to the inherent hydrophobicity of graphene-based nanomaterials, the detrimental occurrence of a thin water layer was significantly reduced. We validated the external electrode polarization as a means of improving the inter-electrode reproducibility; the standard deviation of E^0 was improved to 5.1 mV, making it comparable to the reported literature. Our electrodes have shown a wide linear operating range of $10^{-6} – 10^{-1}$ mol dm^{-3} and a lower limit of detection of 0.88 ± 0.17 µmol dm^{-3}. The proposed sensors were successfully used in ammonium ion determination from real samples, such as artificial urine and leachate water, giving errors smaller than 4 %. The proposed fabrication protocol is very promising, as the inkjet printed electrical and solid contacts can be further modified by depositing polymeric membranes with receptors for various other ions. Finally, an automated method for a rather viscous and volatile polymeric membrane cocktail is sought.

A worthy contribution of this research was the development and optimization of an ion-selective membrane solvent carrier that does not compromise the well-established membrane solute content. Using the automated fluid dispensing machine, a controlled and repeatable deposition of homogeneous membrane films was achieved. The deposited membrane homogeneity was visualized using an innovative colorimetric absorbance method. A mixture of THF and cyclohexanone at equal volume ratios gave membranes with the highest degree of uniformity, without coffee-ring structures. In addition to that, we proposed a novel protocol of tracking ion-selective membrane evaporative drying by performing time-resolved high-frequency impedance measurements. Comparing the drying profiles of membrane cocktails prepared in pure solvents, THF or cyclohexanone, with a proposed solvent mixture, we have concluded that THF evaporates first, and is followed by cyclohexanone evaporation, resulting in a membrane drying profile governed by the least volatile solvent. The utility of impedance-based tracking of membrane drying lies in the ability of this method to pinpoint the exact moment of reaching the completely dried ion-selective membrane. Thus, the mixed solvent membrane was completely dried after 11.5

minutes, highlighting the rapid character of the proposed production protocol. The membrane cocktails with optimized solvent composition were robotically deposited onto screen printed carbon electrode arrays. A single spot of a potassium-selective membrane ($V = 0.20$ µL) was enough to achieve the desired potentiometric response.

The final hypothesis of this research was to prepare a unique reference membrane based on the Ag/AgCl pair, applicable to different electrically conductive substrates. The membrane cocktail was prepared using poly(vinyl butyral) as a membrane matrix and $AgNO_3$ and NaCl as a source of Ag^+ and Cl^- ions, respectively. Herein, we tested whether we could induce a photochemical reduction of the fromed AgCl to Ag^0 using extremely short-time light pulses from the IPL system. Indeed, Ag–AgCl clusters responsible for the reference electrode potential stability were obtained after 91 µs treatment with IPL, as confirmed by UV-Vis and OCP measurements, which significantly reduces the time needed for the photochemical reaction exhibited in the literature. A thorough analysis of surface changes at the RM–electrolyte interface during conditioning using EIS was presented, bolding a more reliable electrical contact for an Ag-inkjet printed electrode | RM system, compared to a glassy-carbon rod electrode | RM system. These findings were confirmed by mid-term stability tests in KCl where the glassy carbon-based RM exhibited drift after 2 h, while the inkjet-printed variant showed enhanced stability with only –0.2464 mV drift over 8 h. Regardless of the conducting substrate, the electrodes maintained potential stability within ±4 mV over a tenfold increase in concentration for various salts (KCl, NaCl, $CaCl_2$, $NaNO_3$). Electrochemical characterization confirmed the applicability of inkjet-printed electrodes in both potentiometric and amperometric setups. These findings support a simplified, scalable protocol for rapid production of electrochemical sensor platforms.

To sum up, this thesis presents valuable practical research that deals with all the important criteria to be considered when designing sensing platform fabrication protocols. All of the proposed research hypotheses were successfully confirmed and the research objectives were achieved. The presented research is just a snippet of the ongoing work, and it is about to be followed by the development of an overall unique potentiometric sensing platform that includes the deposition of electrical leads and solid contacts by inkjet printing

and the ion-selective and reference membranes by automated dispensing. With this, printed sensor integration into microfluidic devices and wearable devices will be enabled.

5. LIST OF ABBREVIATIONS, ACRONYMS, AND SYMBOLS

a – the distance of the printer nozzle to the substrate

a_I – ion activity

A – geometric surface area

AFM – atomic force microscopy

AgNP – silver nanoparticles

AuNP – gold nanoparticles

β_{IL} – ion–ionophore equilibrium constant

C – redox capacitance

CIJ – continuous inkjet

C_L – low-frequency capacitance

CP – conductive polymer

CRE – coffee ring effect

CWE – coated-wire electrode

ΔE_p – peak-to-peak separation potential

$\Delta\varphi$ – phase-boundary potential difference

DLS – dynamic light scattering

DMF – dimethylformamide

DMSO – dimethylsulfoxide

DoD – drop-on-demand

DOS – bis(2-ethylhexyl sebacate)

E^0 – standard electrode potential

E_D – the diffusion within the ion-selective membrane

EIS – electrochemical impedance spectroscopy

E_J – liquid junction potential

E_M – membrane potential

E_{PB} – phase boundary potential

η – dynamic viscosity

ε – molar extinction coefficient

η – dynamic viscosity

F – Faraday constant

f – frequency

ϕ – electrical potential

FIM – fixed interference method

FLA – flash-light annealing

γ – surface tension

GC–RM – glassy carbon electrode modified with a reference membrane

GO – graphene oxide

i – electrical current

IJP – inkjet printed

I_P − peak current

IPL – intensive pulsed light

IR – infrared

ISE – ion-selective electrode

ISM – ion-selective membrane

k_I – ion partition constant

K_IJ^pot – potentiometric coefficient of selectivity

LOD – limit of detection

MGNS – melamine-intercalated graphene nanosheets

μ – chemical potential

μ^0 – standard chemical potential

NMP – N-methyl-2-pyrrolidone

o-NPOE – o-nitrophenyl octyl ether

ν – fluid velocity

OCP – open-circuit potential

Oh – Ohnesorge number

PDMS – poly(dimethylsiloxane)

PE–RM – inkjet printed electrode modified with a reference membrane

PEDOT:PSS – poly(3,4-ethylenedioxythiophene):polystyrene sulfonate

PEN – polyethylene naphthalate

PET – poly(ethylene terephthalate)

PI – polyimide

PVB – poly(vinyl butyral)

PVC – polyvinyl chloride

RE – reference electrode

Re – Reynolds number

RM – reference membrane

ρ – mass density

R_T – total resistance

SC-ISE – solid-contact ion-selective electrode

SC-qRE – solid-contact quasi-reference electrode

SC-RE – solid-contact reference electrode

SEBS – styrene–ethylene–butadiene–styrene

SEM – scanning electron microscopy

SSM – separate solutions method

t – time

T – thermodynamic temperature

t_{95} – response time

T_g – glass transition temperature

THF – tetrahydrofuran

$-\theta$ – phase angle

V – volume

We – Webber's number

WLT – water-layer test

Z – impedance

z_I – charge of ion I

6. BIBLIOGRAPHY

1.   A. Hulanicki, S. Glab, F. Ingman, Chemical sensors: Definitions and classification, Pure Appl. Chem. 63 (1991) 1247-1250.

2.   F. Arduini, L. Micheli, D. Moscone, G. Palleschi, S. Piermarini, F. Ricci, G. Volpe, Electrochemical biosensors based on nanomodified screen-printed electrodes: Recent applications in clinical analysis, Trends Anal. Chem. 79 (2016) 114-126.

3.   G. Lisak, Reliable environmental trace heavy metal analysis with potentiometric ion sensors - reality or a distant dream, Environ. Pollut. 289 (2021) 117882.

4.   M. Cuartero, G. A. Crespo, All-solid-state potentiometric sensors: A new wave for in situ aquatic research, Curr. Opin. Electrochem. 10 (2018) 98-106.

5.   M. M. Elhassan, A. M. Mahmoud, M. A. Hegazy, S. Mowaka, J. G. Bell, New trends in potentiometric sensors: From design to clinical and biomedical applications, Talanta 287 (2025) 127623.

6.   N. C. Raut, K. Al-Shamery, Inkjet printing metals on flexible materials for plastic and paper electronics, J. Mater. Chem. C. 6 (2018) 1618-1641.

7.   A. Moya, G. Gabriel, R. Villa, F. J. del Campo, Inkjet-printed electrochemical sensors, Curr. Opin. Electrochem. 3 (2017) 29-39.

8.   W. G. Hines, R. de Levie, The early development of electronic pH meters, J. Chem. Educ. 87 (2010) 1143-1153.

9.   B. C. Pressman, Induced active transport of ions in mitochondria, PNAS 53 (1965) 1076-1083.

10.   P. Buhlmann, E. Pretsch, E. Bakker, Carrier-based ion-selective electrodes and bulk optodes. 2. Ionophores for potentiometric and optical sensors, Chem. Rev. 98 (1998) 1593-1687.

11.   C. C. Young, Evolution of blood chemistry analyzers based on ion selective electrodes, J. Chem. Educ. 74 (1997) 177-182.

12.   P. Bühlmann, L. D. Chen, Ion-selective electrodes with ionophore-doped sensing membranes. In supramolecular chemistry, Wiley, USA, 2012.

13.   G. J. Moody, Mechanistic studies of ion-selective electrodes, J. Biomed. Eng. 7 (1985) 183-195.

14.   E. Bakker, P. Buhlmann, E. Pretsch, Carrier-based ion-selective electrodes and bulk optodes. 1. General characteristics, Chem. Rev. 97 (1997) 3083-3132.

15.   I. Pechenkina, K. Mikhelson, Materials for the ionophore-based membranes for ion-selective electrodes: Problems and achievements (review paper), Russ. J. Electrochem. 51 (2015) 93-102.

16.   K. N. Mikhelson, Ion-selective electrodes, Springer Berlin Heidelberg, Berlin, Heidelberg, 2013.

17. E. Bakker, M. Willer, M. Lerchi, K. Seiler, E. Pretsch, Determination of complex-formation constants of neutral cation-selective ionophores in solvent polymeric membranes, Anal. Chem. 66 (1994) 516-521.

18. E. Bakker, E. Pretsch, Lipophilicity of tetraphenylborate derivatives as anionic sites in neutral carrier-based solvent polymeric membranes and lifetime of corresponding ion-selective electrochemical and optical sensors, Anal. Chim. Acta 309 (1995) 7-17.

19. B. K. Troudt, C. R. Rousseau, X. I. N. Dong, E. L. Anderson, P. Bühlmann, Recent progress in the development of improved reference electrodes for electrochemistry, Anal. Sci. 38 (2022) 71-83.

20. P. Spitzer, S. Wunderli, K. Maksymiuk, A. Michalska, A. Kisiel, Z. Galus, G. Tauber, Handbook of reference electrodes, Springer Berlin Heidelberg, Berlin, Heidelberg, 2013.

21. J. Bobacka, A. Ivaska, A. Lewenstam, Potentiometric ion sensors, Chem. Rev. 108 (2008) 329-351.

22. S. Amemiya, Handbook of electrochemistry, Elsevier, Amsterdam, 2007.

23. K. Maksymiuk, E. Stelmach, A. Michalska, Unintended changes of ion-selective membranes composition-origin and effect on analytical performance, Membranes 10 (2020) 266-280.

24. J. B. Hu, A. Stein, P. Bühlmann, Rational design of all-solid-state ion-selective electrodes and reference electrodes, Trends Anal. Chem. 76 (2016) 102-114.

25. H. Hirata, K. Dato, Copper(II) sulphide-impregnated silicone rubber membranes as selective electrodes for copper(II) ions, Talanta 17 (1970) 883-887.

26. R. W. Cattrall, H. Freiser, Coated wire ion-selective electrodes, Anal. Chem. 43 (1971) 1905-1906.

27. B. P. Nikolskii, E. A. Materova, Ion-selective electrode reviews, Elsevier, the Netherlands, 1985.

28. A. Cadogan, Z. Gao, A. Lewenstam, A. Ivaska, D. Diamond, All-solid-state sodium-selective electrode based on a calixarene ionophore in a poly(vinyl chloride) membrane with a polypyrrole solid contact, Anal. Chem. 64 (1992) 2496-2501.

29. G. A. Crespo, S. Macho, J. Bobacka, F. X. Rius, Transduction mechanism of carbon nanotubes in solid-contact ion-selective electrodes, Anal. Chem. 81 (2009) 676-681.

30. E. Jaworska, M. Wójcik, A. Kisiel, J. Mieczkowski, A. Michalska, Gold nanoparticles solid contact for ion-selective electrodes of highly stable potential readings, Talanta 85 (2011) 1986-1989.

31. X. U. Zou, X. V. Zhen, J. H. Cheong, P. Bühlmann, Calibration-free ionophore-based ion-selective electrodes with a Co(II)/Co(III) redox couple-based solid contact, Anal. Chem. 86 (2014) 8687-8692.

32. L. Mendecki, K. A. Mirica, Conductive metal–organic frameworks as ion-to-electron transducers in potentiometric sensors, ACS Appl. Mater. Interfaces 10 (2018) 19248-19257.

33. Y. Z. Shao, Y. B. Ying, J. F. Ping, Recent advances in solid-contact ion-selective electrodes: Functional materials, transduction mechanisms, and development trends, Chem. Soc. Rew. 49 (2020) 4405-4465.

34. S. Papp, M. Bojtár, R. E. Gyurcsányi, T. Lindfors, Potential reproducibility of potassium-selective electrodes having perfluorinated alkanoate side chain functionalized poly(3,4-ethylenedioxytiophene) as a hydrophobic solid contact, Anal. Chem. 91 (2019) 9111-9118.

35. M. Fibbioli, K. Bandyopadhyay, S. G. Liu, L. Echegoyen, O. Enger, F. Diederich, P. Bühlmann, E. Pretsch, Redox-active self-assembled monolayers as novel solid contacts for ion-selective electrodes, Chem. Commun. (2000) 339-340.

36. M. Fibbioli, K. Bandyopadhyay, S. G. Liu, L. Echegoyen, O. Enger, F. Diederich, D. Gingery, P. Bühlmann, H. Persson, U. W. Suter, E. Pretsch, Redox-active self-assembled monolayers for solid-contact polymeric membrane ion-selective electrodes, Chem. Mater. 14 (2002) 1721-1729.

37. E. Grygołowicz-Pawlak, K. Wyglądacz, S. Sęk, R. Bilewicz, Z. Brzózka, E. Malinowska, Studies on ferrocene organothiol monolayer as an intermediate phase of potentiometric sensors with gold inner contact, Sens. Actuators B Chem. 111-112 (2005) 310-316.

38. X. U. Zou, J. H. Cheong, B. J. Taitt, P. Bühlmann, Solid contact ion-selective electrodes with a well-controlled Co(II)/Co(III) redox buffer layer, Anal. Chem. 85 (2013) 9350-9355.

39. E. Jaworska, M. L. Naitana, E. Stelmach, G. Pomarico, M. Wojciechowski, E. Bulska, K. Maksymiuk, R. Paolesse, A. Michalska, Introducing cobalt(II) porphyrin/cobalt(III) corrole containing transducers for improved potential reproducibility and performance of all-solid-state ion-selective electrodes, Anal. Chem. 89 (2017) 7107-7114.

40. E. Jaworska, G. Pomarico, B. B. Berna, K. Maksymiuk, R. Paolesse, A. Michalska, All-solid-state paper based potentiometric potassium sensors containing cobalt(II) porphyrin/cobalt(III) corrole in the transducer layer, Sens. Actuators B Chem. 277 (2018) 306-311.

41. J. Ping, Y. Wang, Y. Ying, J. Wu, Application of electrochemically reduced graphene oxide on screen-printed ion-selective electrode, Anal. Chem. 84 (2012) 3473-3479.

42. H. J. Park, J. M. Jeong, J. H. Yoon, S. G. Son, Y. K. Kim, D. H. Kim, K. G. Lee, B. G. Choi, Preparation of ultrathin defect-free graphene sheets from graphite via fluidic delamination for solid-contact ion-to-electron transducers in potentiometric sensors, J. Colloid Interface Sci. 560 (2020) 817-824.

43. S. Papp, J. Kozma, T. Lindfors, R. E. Gyurcsányi, Lipophilic multi-walled carbon nanotube-based solid contact potassium ion-selective electrodes with reproducible standard potentials. A comparative study, Electroanalysis 32 (2020) 867-873.

44. M. Fouskaki, N. Chaniotakis, Fullerene-based electrochemical buffer layer for ion-selective electrodes, Analyst 133 (2008) 1072-1075.

45. M. Fibbioli, W. E. Morf, M. Badertscher, N. F. de Rooij, E. Pretsch, Potential drifts of solid-contacted ion-selective electrodes due to zero-current ion fluxes through the sensor membrane, Electroanalysis 12 (2000) 1286-1292.

46. R. P. Buck, E. Lindner, Recommendations for nomenclature of ionselective electrodes (IUPAC recommendations 1994), Pure Appl. Chem. 66 (1994) 2527-2536.

47. N. Lenar, R. Piech, B. Paczosa-Bator, Candle soot-smoked electrodes as a natural superhydrophobic material for potentiometric sensors, Talanta 285 (2025) 127389.

48. J. Bobacka, Potential stability of all-solid-state ion-selective electrodes using conducting polymers as ion-to-electron transducers, Anal. Chem. 71 (1999) 4932-4937.

49. M. W. Shinwari, D. Zhitomirsky, I. A. Deen, P. R. Selvaganapathy, M. J. Deen, D. Landheer, Microfabricated reference electrodes and their biosensing applications, Sensors 10 (2010) 1679-1715.

50. W. Y. Liao, T. C. Chou, Fabrication of a planar-form screen-printed solid electrolyte modified Ag/AgCl reference electrode for application in a potentiometric biosensor, Anal. Chem. 78 (2006) 4219-4223.

51. Ł. Tymecki, E. Zwierkowska, R. Koncki, Screen-printed reference electrodes for potentiometric measurements, Anal. Chim. Acta 526 (2004) 3-11.

52. A. Kisiel, A. Michalska, K. Maksymiuk, E. A. H. Hall, All-solid-state reference electrodes with poly(n-butyl acrylate) based membranes, Electroanalysis 20 (2008) 318-323.

53. T. Guinovart, A. J. Bandodkar, J. R. Windmiller, F. J. Andrade, J. Wang, A potentiometric tattoo sensor for monitoring ammonium in sweat, Analyst 138 (2013) 7031-7038.

54. W. Gao, S. Emaminejad, H. Y. Y. Nyein, S. Challa, K. Chen, A. Peck, H. M. Fahad, H. Ota, H. Shiraki, D. Kiriya, D. H. Lien, G. A. Brooks, R. W. Davis, A. Javey, Fully integrated wearable sensor arrays for multiplexed in situ perspiration analysis, Nature 529 (2016) 509-514.

55. M. Parrilla, J. Ferré, T. Guinovart, F. J. Andrade, Wearable potentiometric sensors based on commercial carbon fibres for monitoring sodium in sweat, Electroanalysis 28 (2016) 1267-1275.

56. Q. Li, W. Tang, Y. Su, Y. Huang, S. Peng, B. Zhuo, S. Qiu, L. Ding, Y. Li, X. Guo, Stable thin-film reference electrode on plastic substrate for all-solid-state ion-sensitive field-effect transistor sensing system, IEEE Electron Device Lett. 38 (2017) 1469-1472.

57. S. Søpstad, K. Imenes, E Johannessen, A,, Chloride and pH determination on a wireless, flexible electrochemical sensor platform, IEEE Sens. J. 20 (2020) 599-609.

58. S. C. Park, H. J. Jeong, M. Heo, J. H. Shin, J. H. Ahn, Carbon nanotube-based ion-sensitive field-effect transistors with an on-chip reference electrode toward wearable sodium sensing, ACS Appl. Electron. Mater. 3 (2021) 2580-2588.

59. T. Guinovart, G. A. Crespo, F. X. Rius, F. J. Andrade, A reference electrode based on polyvinyl butyral (PVB) polymer for decentralized chemical measurements, Anal. Chim. Acta 821 (2014) 72-80.

60. T. Kakiuchi, T. Yoshimatsu, N. Nishi, New class of Ag/AgCl electrodes based on hydrophobic ionic liquid saturated with AgCl, Anal. Chem. 79 (2007) 7187-7191.

61. C. Coll, R. H. Labrador, R. M. Mañez, J. Soto, F. Sancenón, M. J. Seguí, E. Sanchez, Ionic liquids promote selective responses towards the highly hydrophilic anion sulfate in PVC membrane ion-selective electrodes, Chem. Commun. (2005) 3033.

62. R. Mamińska, A. Dybko, W. Wróblewski, All-solid-state miniaturised planar reference electrodes based on ionic liquids, Sens. Actuators B Chem. 115 (2006) 552-557.

63. N. Tiuftiakov, E. Zdrachek, E. Bakker, Ion-exchange and lipophilicity limitations of ionic liquid reference electrodes, Sens. Actuators B Chem. 407 (2024) 135474.

64. E. Bakker, A. Xu, E. Pretsch, Optimum composition of neutral carrier based pH electrodes, Anal. Chim. Acta 295 (1994) 253-262.

65. G. G. Guilbault, Recommendations for publishing manuscripts on ion-selective electrodes, Pure Appl. Chem. 53 (1981) 1907-1912.

66. W. Zhang, A. Fakler, C. Demuth, U. E. Spichiger, Comparison of different methods for determining the selectivity coefficient using a magnesium-selective electrode, Anal. Chim. Acta 375 (1998) 211-222.

67. Y. Umezawa, P. Bühlmann, K. Umezawa, K. Tohda, S. Amemiya, Potentiometric selectivity coefficients of ion-selective electrodes. Part I. Inorganic cations (technical report), 72 (2000) 1851-2082.

68. E. Bakker, R. K. Meruva, E. Pretsch, M. E. Meyerhoff, Selectivity of polymer membrane-based ion-selective electrodes: Self-consistent model describing the potentiometric response in mixed ion solutions of different charge, Anal. Chem. 66 (1994) 3021-3030.

69. A. Kamyshny, S. Magdassi, Conductive nanomaterials for printed electronics, Small 10 (2014) 3515-3535.

70. X. Du, S. P. Wankhede, S. Prasad, A. Shehri, J. Morse, N. Lakal, A review of inkjet printing technology for personalized-healthcare wearable devices, J. Mater. Chem. C. 10 (2022) 14091-14115.

71. G. Hu, J. Kang, L. W. T. Ng, X. Zhu, R. C. T. Howe, C. G. Jones, M. C. Hersam, T. Hasan, Functional inks and printing of two-dimensional materials, Chem. Soc. Rew. 47 (2018) 3265-3300.

72. T. Tuomaala, H. Määttä, T. Tuhkala, N. Torniainen, R. Valasma, M. Nissinen, Practical guide to screen-printing in printed electronics, Oulu University of Applied Sciences, Finland, 2025.

73. R. R. Suresh, M. Lakshmanakumar, J. B. B. Arockia Jayalatha, K. S. Rajan, S. Sethuraman, U. M. Krishnan, J. B. B. Rayappan, Fabrication of screen-printed electrodes: Opportunities and challenges, J. Mater. Sci. 56 (2021) 8951-9006.

74. M. R. Somalu, A. Muchtar, W. R. W. Daud, N. P. Brandon, Screen-printing inks for the fabrication of solid oxide fuel cell films: A review, Renew. Sustain. Energy Rev. 75 (2017) 426-439.

75. J. P. Metters, R. O. Kadara, C. E. Banks, New directions in screen printed electroanalytical sensors: An overview of recent developments, Analyst 136 (2011) 1067-1076.

76. H. Wei, J. J. Sun, Yu Xie, C. G. Lin, Y. M. Wang, W. H. Yin, G. N. Chen, Enhanced electrochemical performance at screen-printed carbon electrodes by a new pretreating procedure, Anal. Chim. Acta 588 (2007) 297-303.

77. L. Liu, Z. Shen, X. Zhang, H. Ma, Highly conductive graphene/carbon black screen printing inks for flexible electronics, J. Colloid Interface Sci. 582 (2021) 12-21.

78. W. J. Hyun, E. B. Secor, M. C. Hersam, C. D. Frisbie, L. F. Francis, High-resolution patterning of graphene by screen printing with a silicon stencil for highly flexible printed electronics, Adv. Mater. 27 (2015) 109-115.

79. S. Laschi, I. Palchetti, M. Mascini, Gold-based screen-printed sensor for detection of trace lead, Sens. Actuators B Chem. 114 (2006) 460-465.

80. R. Venkata Krishna Rao, K. Venkata Abhinav, P. S. Karthik, S. P. Singh, Conductive silver inks and their applications in printed and flexible electronics, RSC Adv. 5 (2015) 77760-77790.

81. C. Williams, Ink-jet printers go beyond paper, Phys. World 19 (2006) 24-29.

82. B. Derby, Inkjet printing of functional and structural materials: Fluid property requirements, feature stability, and resolution, Annu. Rev. Mater. Res. 40 (2010) 395-414.

83. E. T. S. G. da Silva, S. Miserere, L. T. Kubota, A. Merkoçi, Simple on-plastic/paper inkjet-printed solid-state Ag/AgCl pseudoreference electrode, Anal. Chem. 86 (2014) 10531-10534.

84. N. Ruecha, O. Chailapakul, K. Suzuki, D. Citterio, Fully inkjet-printed paper-based potentiometric ion-sensing devices, Anal. Chem. 89 (2017) 10608-10616.

85. G. Cummins, M. P. Y. Desmulliez, Inkjet printing of conductive materials: A review, Circuit World 38 (2012) 193-213.

86. L. Nayak, S. Mohanty, S. K. Nayak, A. Ramadoss, A review on inkjet printing of nanoparticle inks for flexible electronics, J. Mater. Chem. C. 7 (2019) 8771-8795.

87. A. Kamyshny, S. Magdassi, Conductive nanomaterials for 2D and 3D printed flexible electronics, Chem. Soc. Rew. 48 (2019) 1712-1740.

88. R. D. Deegan, O. Bakajin, T. F. Dupont, G. Huber, S. R. Nagel, T. A. Witten, Capillary flow as the cause of ring stains from dried liquid drops, Nature 389 (1997) 827-829.

89. Q. Huang, Y. Zhu, Printing conductive nanomaterials for flexible and stretchable electronics: A review of materials, processes, and applications, Adv. Mater. Technol. 4 (2019) 1800546.

90. A. L. Nogueira, R. A. F. Machado, A. Z. de Souza, F. Martinello, C. V. Franco, G. B. Dutra, Synthesis and characterization of silver nanoparticles produced with a bifunctional stabilizing agent, Ind. Eng. Chem. Res. 53 (2014) 3426-3434.

91. D. V. Goia, E. Matijević, Preparation of monodispersed metal particles, New J. Chem. 22 (1998) 1203-1215.

92. K. N. Al-Milaji, R. R. Secondo, T. N. Ng, N. Kinsey, H. Zhao, Interfacial self-assembly of colloidal nanoparticles in dual-droplet inkjet printing, Adv. Mater. Interfaces 5 (2018) 1701561.

93. D. Kim, S. Jeong, B. K. Park, J. Moon, Direct writing of silver conductive patterns: Improvement of film morphology and conductance by controlling solvent compositions, Appl. Phys. Lett. 89 (2006) 264101-264105.

94. S. Wünscher, R. Abbel, J. Perelaer, U. S. Schubert, Progress of alternative sintering approaches of inkjet-printed metal inks and their application for manufacturing of flexible electronic devices, J. Mater. Chem. C. 2 (2014) 10232-10261.

95. H. S. Lim, S. J. Kim, H. W. Jang, J. A. Lim, Intense pulsed light for split-second structural development of nanomaterials, J. Mater. Chem. C. 5 (2017) 7142-7160.

96. H. J. Nam, S. Y. Kang, J. Y. Park, S. H. Choa, Intense pulse light sintering of an ag microparticle-based, highly stretchable, and conductive electrode, Microelectron. Eng. 215 (2019) 111012.

97.   J. S. Kang, J. Ryu, H. S. Kim, H. T. Hahn, Sintering of inkjet-printed silver nanoparticles at room temperature using intense pulsed light, J. Electron. Mater. 40 (2011) 2268-2277.

98.   E. B. Secor, B. Y. Ahn, T. Z. Gao, J. A. Lewis, M. C. Hersam, Rapid and versatile photonic annealing of graphene inks for flexible printed electronics, Adv. Mater. 27 (2015) 6683-6688.

99.   J. Kim, A. S. Campbell, B. E. F. de Ávila, J. Wang, Wearable biosensors for healthcare monitoring, Nat. Biotechnol. 37 (2019) 389-406.

100.   W. Gao, H. Ota, D. Kiriya, K. Takei, A. Javey, Flexible electronics toward wearable sensing, Acc. Chem. Res. 52 (2019) 523-533.

101.   M. Hassan, G. Abbas, N. Li, A. Afzal, Z. Haider, S. Ahmed, X. Xu, C. Pan, Z. Peng, Significance of flexible substrates for wearable and implantable devices: Recent advances and perspectives, Adv. Mater. Technol. 7 (2022) 2100773.

102.   Y. Qin, H. J. Kwon, A. Subrahmanyam, M. M. R. Howlader, P. R. Selvaganapathy, A. Adronov, M. J. Deen, Inkjet-printed bifunctional carbon nanotubes for pH sensing, Mater. Lett. 176 (2016) 68-70.

103.   Q. He, S. R. Das, N. T. Garland, D. Jing, J. A. Hondred, A. A. Cargill, S. Ding, C. Karunakaran, J. C. Claussen, Enabling inkjet printed graphene for ion selective electrodes with postprint thermal annealing, ACS Appl. Mater. Interfaces. 9 (2017) 12719-12727.

104.   I. Ivanišević, S. Milardović, A. Ressler, P. Kassal, Fabrication of an all-solid-state ammonium paper electrode using a graphite-polyvinyl butyral transducer layer, Chemosensors 9 (2021) 333-349.

105.   R. Pol, A. Moya, G. Gabriel, D. Gabriel, F. Céspedes, M. Baeza, Inkjet-printed sulfide-selective electrode, Anal. Chem. 89 (2017) 12231-12236.

106.   A. Saleh, S. Wustoni, E. Bihar, J. K. El-Demellawi, Y. Zhang, A. Hama, V. Druet, A. Yudhanto, G. Lubineau, H. N. Alshareef, S. Inal, Inkjet-printed $Ti_3C_2T_x$ mxene electrodes for multimodal cutaneous biosensing, J. Phys Mater. 3 (2020) 044004.

107.   M. Jović, J. C. Hidalgo-Acosta, A. Lesch, V. Costa Bassetto, E. Smirnov, F. Cortés-Salazar, H. H. Girault, Large-scale layer-by-layer inkjet printing of flexible iridium-oxide based ph sensors, J. Electroanal. Chem. 819 (2018) 384-390.

108.   H. Jiang, W. Yu, J. F. Waimin, N. Glassmaker, N. Raghunathan, X. Jiang, B. Ziaie, R. Rahimi, Inkjet-printed solid-state potentiometric nitrate ion selective electrodes for agricultural application, IEEE SENSORS (2019) 1-4.

109.   L. K. Lin, J. T. Tsai, S. Díaz-Amaya, M. R. Oduncu, Y. Zhang, P. Y. Huang, C. Ostos, J. P. Schmelzel, R. Mohammadrahimi, P. Xu, A. M. Ulloa Gomez, S. N. Shuvo, N. Raghunathan, X. Zhang, A. Wei, D. Bahr, D. Peroulis, L. A. Stanciu, Antidelaminating, thermally stable, and cost-effective flexible kapton platforms for nitrate sensors, mercury aptasensors, protein sensors, and p-type organic thin-film transistors, ACS Appl. Mater. Interfaces. 13 (2021) 11369-11384.

110.   S. Gianvittorio, M. Malferrari, H. Pick, S. Rapino, A. Lesch, Print-light-synthesis of ruthenium oxide thin film electrodes for electrochemical sensing applications, Bioelectrochemistry 163 (2025) 108909.

111. S. Krivačić, Ž. Boček, M. Zubak, V. Kojić, P. Kassal, Flexible ammonium ion-selective electrode based on inkjet-printed graphene solid contact, Talanta 279 (2024) 126614.

112. S. Papamatthaiou, U. Zupancic, C. Kalha, A. Regoutz, P. Estrela, D. Moschou, Ultra stable, inkjet-printed pseudo reference electrodes for lab-on-chip integrated electrochemical biosensors, Sci. Rep. 10 (2020) 17152.

113. A. Bananezhad, M. Jović, L. F. Villalobos, K. V. Agrawal, M. R. Ganjali, H. H. Girault, Large-scale fabrication of flexible solid-state reference electrodes, J. Electroanal. Chem. 847 (2019) 113241.

114. A. Moya, R. Pol, A. Martínez-Cuadrado, R. Villa, G. Gabriel, M. Baeza, Stable full-inkjet-printed solid-state Ag/AgCl reference electrode, Anal. Chem. 91 (2019) 15539-15546.

115. X. Lu, M. Zhang, L. Wang, G. Liu, Liquid metal fiber mat as a highly stable solid-state junction for inkjet-printed flexible reference electrodes, Anal. Chem. 94 (2022) 6728-6735.

116. S. Krivačić, M. Zubak, D. Vrsaljko, P. Kassal, Application of intense pulsed light in the development of poly(vinyl butyral)-based all-solid-state Ag/AgCl reference electrodes, Electroanalysis 36 (2024) e202300368.

117. Y. Qin, A. U. Alam, M. M. R. Howlader, N. X. Hu, M. J. Deen, Inkjet printing of a highly loaded palladium ink for integrated, low-cost pH sensors, Adv. Funct. Mater. 26 (2016) 4923-4933.

118. Y. Qin, A. U. Alam, s. Pan, M. M. R. Howlader, R. Ghosh, N. X. Hu, H. Jin, S. Dong, C. H. Chen, M. J. Deen, Integrated water quality monitoring system with pH, free chlorine, and temperature sensors, Sens. Actuators B Chem. 255 (2018) 781-790.

119. A. Määttänen, U. Vanamo, P. Ihalainen, P. Pulkkinen, H. Tenhu, J. Bobacka, J. Peltonen, A low-cost paper-based inkjet-printed platform for electrochemical analyses, Sens. Actuators B Chem. 177 (2013) 153-162.

120. P. Sjöberg, A. Määttänen, U. Vanamo, M. Novell, P. Ihalainen, F. J. Andrade, J. Bobacka, J. Peltonen, Paper-based potentiometric ion sensors constructed on ink-jet printed gold electrodes, Sens. Actuators B Chem. 224 (2016) 325-332.

121. K. Teekayupak, P. Preechakasedkit, N. Chuaypen, T. Dissayabutra, P. A. Lieberzeit, O. Chailapakul, N. Ruecha, D. Citterio, Polymeric hydrogel integrated paper-based potentiometric ion-sensing device for the determination of sodium ions in human urine, Analyst 150 (2025) 841-850.

122. E. Bilbao, S. Kapadia, V. Riechert, J. Amalvy, F. N. Molinari, M. M. Escobar, R. R. Baumann, L. N. Monsalve, Functional aqueous-based polyaniline inkjet inks for fully printed high-performance pH-sensitive electrodes, Sens. Actuators B Chem. 346 (2021) 130558.

123. Y. Huang, T. Wang, Z. Xu, E. Hughes, F. Qian, M. Lee, Y. Fan, Y. Lei, C. Brückner, B. Li, Real-time in situ monitoring of nitrogen dynamics in wastewater treatment processes using wireless, solid-state, and ion-selective membrane sensors, Environ. Sci. Technol. 53 (2019) 3140-3148.

124. T. Pandhi, C. Cornwell, K. Fujimoto, P. Barnes, J. Cox, H. Xiong, P. H. Davis, H. Subbaraman, J. E. Koehne, D. Estrada, Fully inkjet-printed multilayered graphene-based

flexible electrodes for repeatable electrochemical response, RSC Adv. 10 (2020) 38205-38219.

125. K. L. Tsou, Y. T. Cheng, A miniaturization scheme of flexible inkjet-printed Ag/AgCl(s) reference electrodes using the ionic liquid (IL)-typed PVC membrane with the addition of graphene for electrochemical sensing applications, Sensors and Actuators Reports 5 (2023) 100145.

126. K. L. Tsou, Y. T. Cheng, Miniaturized inkjet-printed flexible ion-selective sensing electrodes with the addition of graphene in PVC layer for fast response real-time monitoring applications, Talanta 275 (2024) 126107.

127. K. Y. Chen, A. Biswas, S. Cai, J. Huang, J. Andrews, Inkjet printed potentiometric sensors for nitrate detection directly in soil enabled by a hydrophilic passivation layer, Adv. Mater. Technol. 9 (2024) 2301140.

128. A. Määttänen, P. Ihalainen, P. Pulkkinen, S. Wang, H. Tenhu, J. Peltonen, Inkjet-printed gold electrodes on paper: Characterization and functionalization, ACS Appl. Mater. Interfaces 4 (2012) 955-964.

129. M. Baibarac, P. Gómez-Romero, Nanocomposites based on conducting polymers and carbon nanotubes: From fancy materials to functional applications, J. Nanosci. Nanotechnol. 6 (2006) 289-302.

130. T. Matsumoto, A. Ohashi, N. Ito, Development of a micro-planar Ag/AgCl quasi-reference electrode with long-term stability for an amperometric glucose sensor, Anal. Chim. Acta 462 (2002) 253-259.

131. J. L. Do, T. Friščić, Mechanochemistry: A force of synthesis, ACS Cent. Sci. 3 (2017) 13-19.

132. S. Bhattacharjee, DLS and Zeta potential – what they are and what they are not?, JCR 235 (2016) 337-351.

133. G. A. Crespo, S. Macho, F. X. Rius, Ion-selective electrodes using carbon nanotubes as ion-to-electron transducers, Anal. Chem. 80 (2008) 1316-1322.

134. U. Mattinen, S. Rabiej, A. Lewenstam, J. Bobacka, Impedance study of the ion-to-electron transduction process for carbon cloth as solid-contact material in potentiometric ion sensors, Electrochim. Acta 56 (2011) 10683-10687.

135. A. Michalska, Optimizing the analytical performance and construction of ion-selective electrodes with conducting polymer-based ion-to-electron transducers, Anal. Bioanal. Chem. 384 (2006) 391-406.

136. K. E. Wyer, D. B. Kelleghan, V. Blanes-Vidal, G. Schauberger, T. P. Curran, Ammonia emissions from agriculture and their contribution to fine particulate matter: A review of implications for human health, J. Environ. Manage. 323 (2022) 116285.

137. M. Rostampour, B. Bailey, C. Autrey, K. Ferrer, B. Vantoorenburg, P. K. Patel, P. Calvo-Marzal, K. Y. Chumbimuni-Torres, Single-step integration of poly(3-octylthiophene) and single-walled carbon nanotubes for highly reproducible paper-based ion-selective electrodes, Anal. Chem. 93 (2021) 1271-1276.

138. Y. Soda, K. J. Robinson, T. J. Cherubini, E. Bakker, Colorimetric absorbance mapping and quantitation on paper-based analytical devices, Lab Chip 20 (2020) 1441-1448.

139. Y. R. Jang, S. J. Joo, J. H. Chu, H. J. Uhm, J. W. Park, C. H. Ryu, M. H. Yu, H. S. Kim, A review on intense pulsed light sintering technologies for conductive electrodes in printed electronics, IJPEM-GT 8 (2021) 327-363.

140. J. Sun, Q. Wang, G. Luo, W. Meng, M. Cao, Y. Li, M. D. Masterman-Smith, H. Yang, X. Sun, M. F. Lang, A novel flexible Ag/AgCl quasi-reference electrode based on silver nanowires toward ultracomfortable electrophysiology and sensitive electrochemical glucose detection, JMR&T 9 (2020) 13425-13433.

7. APPENDICES

7.1. Appendix I – Manuscript of Publication 1

Conductive inks based on melamine intercalated graphene nanosheets for inkjet printed flexible electronics

Magdalena Kralj[1,*], Sara Krivačić[2,*], Irena Ivanišević[2], Marko Zubak[2], Antonio Supina[3], Marijan Marciuš[4], Ivan Halasz[1] and Petar Kassal[2]

[1] Division of Physical Chemistry, Ruđer Bošković Institute, Bijenička cesta 54, 10000 Zagreb, Croatia

[2] Faculty of Chemical Engineering and Technology, University of Zagreb, Trg Marka Marulića 19, 10000 Zagreb, Croatia

[3] Institute of Physics, Bijenička cesta 46, 10000 Zagreb, Croatia

[4] Division of Materials Chemistry, Ruđer Bošković Institute, Bijenička cesta 54, 10000 Zagreb, Croatia

Author contribution:

* M.K. and **S.K.** contributed equally as the first authors

M.K and **S.K**: formal analysis, investigation, methodology, writing – original draft; **I.I.**: formal analysis, investigation, writing – review and editing; **M.Z.**: formal analysis, investigation; **A.S.**: formal analysis, investigation; **M.M.**: formal analysis, investigation; **I.H.**: funding acquisition, supervision, resources, writing – review and editing; **P.K.**: conceptualization, funding acquisition, methodology, project administration, resources, supervision, writing – review and editing.

This paper is published in an open access journal (https://doi.org/10.3390/nano12172936)

Conductive Inks Based on Melamine Intercalated Graphene Nanosheets for Inkjet Printed Flexible Electronics

Magdalena Kralj [1,†], Sara Krivačić [2,†], Irena Ivanišević [2], Marko Zubak [2], Antonio Supina [3], Marijan Marciuš [4], Ivan Halasz [1] and Petar Kassal [2,*]

[1] Division of Physical Chemistry, Ruđer Bošković Institute, Bijenička cesta 54, 10000 Zagreb, Croatia
[2] Faculty of Chemical Engineering and Technology, University of Zagreb, Marulićev trg 19, 10000 Zagreb, Croatia
[3] Institute of Physics, Bijenička cesta 46, 10000 Zagreb, Croatia
[4] Division of Materials Chemistry, Ruđer Bošković Institute, Bijenička cesta 54, 10000 Zagreb, Croatia
* Correspondence: pkassal@fkit.hr
† These authors contributed equally to this work.

Abstract: With the growing number of flexible electronics applications, environmentally benign ways of mass-producing graphene electronics are sought. In this study, we present a scalable mechanochemical route for the exfoliation of graphite in a planetary ball mill with melamine to form melamine-intercalated graphene nanosheets (M-GNS). M-GNS morphology was evaluated, revealing small particles, down to 14 nm in diameter and 0.4 nm thick. The M-GNS were used as a functional material in the formulation of an inkjet-printable conductive ink, based on green solvents: water, ethanol, and ethylene glycol. The ink satisfied restrictions regarding stability and nanoparticle size; in addition, it was successfully inkjet printed on plastic sheets. Thermal and photonic post-print processing were evaluated as a means of reducing the electrical resistance of the printed features. Minimal sheet resistance values (5 kΩ/sq for 10 printed layers and 626 Ω/sq for 20 printed layers) were obtained on polyimide sheets, after thermal annealing for 1 h at 400 °C and a subsequent single intense pulsed light flash. Lastly, a proof-of-concept simple flexible printed circuit consisting of a battery-powered LED was realized. The demonstrated approach presents an environmentally friendly alternative to mass-producing graphene-based printed flexible electronics.

Keywords: mechanochemistry; graphene nanosheets; conductive ink; inkjet printing; printed electronics

1. Introduction

Flexible electronic devices manufactured by printing techniques on various substrates, such as paper, polymers, and textiles, have recently gained tremendous attention [1,2]. Unlike traditional silicon-based production techniques—often described as costly and complicated—printing offers faster, simpler, as well as environmentally and economically beneficial production possibilities [3,4]. Numerous examples include printed electronic circuits [5], displays [6], radio frequency identification tags (RFIDs) [7], thin-film transistors (TFTs) [8], and sensors [9]. Among different printing techniques, inkjet printing offers several advantages in the publishing and graphics industries [10]. This noncontact additive manufacturing technique is based on the selective ejection of individual drops of a liquid material (ink) from the nozzle upon thermal or pressure pulse [11]; this makes it easily adaptable for mass production. The arrival of inkjet printing outside the scope of classical application came with the development of nanoparticle-based inks with functional properties, especially electrical conductivity [2,12].

Printable inks are based upon a careful selection of the ink components, including the functional material and (a combination of) solvents and stabilizers [13]. Metal

nanoparticles [14–16], conductive polymers [17,18], and carbon nanomaterials [19–21] are the most used functional components in electrically conductive inks. When formulating inks, rheological properties must be carefully tailored to ensure proper jetting. In the case of nanoparticle-based inks, additional restrictions regarding nanoparticle size and ink stability are imposed; these all prevent nozzle clogging.

Even though metal nanoparticles—due to their excellent conductivity—are among the most commonly used materials, a growing interest is being devoted to carbon (nano)materials [22]. Inkjet-printed carbon nanomaterials have therefore been used in the development of flexible and wearable electronics [23,24], sensors [25,26], and film heaters [27]. Considering its intriguing and unique physicochemical properties, such as large surface area, exceptional thermal stability, excellent electrical conductivity, high electron mobility, superior mechanical strength, flexibility, and undemanding chemical functionalization, graphene has attracted attention as a promising functional material in the production of flexible electronic components [28]. To achieve greater concentration in an ink, without the reaggregation of the (nano)particles of the functional material, a suitable solvent based on adequate solubility parameters should be selected; and/or a stabilizing agent should be employed [29,30]. Common solvents for carbon (nano)material-based inks, such as N-methyl-2-pyrrolidone (NMP), N-cyclo-2-pyrrolidone, dimethylformamide (DMF), and dimethylsulfoxide (DMSO), are either expensive, chemically harsh, toxic, and/or difficult to remove post-printing due to their high boiling points [30,31]; thus, their use is not recommended [31–33]. However, environmentally compatible solvents often require the additional use of stabilizers, such as polymers and surfactants. For example, graphene suspensions in cyclohexanone and terpineol have been stabilized with ethyl-cellulose [34,35]; in water [36] and ethylene glycol [37] with the stabilizing agent sodium dodecyl sulfate (SDS) [38]; and in ethanol, ethanediol, propanetriol, and deionized water along with sodium carboxymethyl cellulose (CMC) [39].

Different synthetic routes toward graphene have been thoroughly investigated since its discovery. These include the two main approaches: the top-down (TD) approach and the bottom-up (BU) approach [28,32,40,41]. BU approaches, based on the nucleation of a carbon precursor, are generally expensive and time-consuming. On the other hand, in the TD approach, carbonaceous materials (such as graphite) are cut into nano-sized particles by physicochemical processes, which pave the road to the mass production of graphene. TD approaches include the famous Hummers' method and liquid-phase exfoliation (LPE) of graphite [42–44]. Yet, these have major limitations, such as the need for harmful and complex pretreatments, high energy consumption, low yields, agglomeration tendency, low-stability in polar solvents, high precursor costs, or the need for special equipment [41,45].

Clearly, a facile, sustainable, reproducible, and low-cost route for the large-scale preparation of graphene nanosheets (GNS) with minimal surface defects is required to satisfy the growing industry requirements. For this reason, methods of mechanochemistry have become attractive as they often provide quick and quantitative reactions of solids, even on a large scale, while according with the principles of Green Chemistry [46]. There are numerous examples of mechanochemical synthesis and modification of monodisperse nanoparticle systems in a solvent-free environment [47–49]. As recently demonstrated, graphite can be exfoliated through non-covalent interactions with melamine (1,3,5-Triazine-2,4,6-triamine) in a ball milling process under solid, i.e., dry conditions [50]; this is in contrast to the exfoliation of graphite with melamine in aqueous media [51–54].

We present here a facile, scalable, and green method for the development of inkjet printable conductive graphene-based inks. We have adopted a mechanochemical route for the exfoliation of graphite with melamine to form melamine-intercalated graphene nanosheets (M-GNS). The M-GNS were used as the conductive material in the formulation of an inkjet printable ink, with the aid of polymeric dispersants in green solvents (water, ethanol, ethylene glycol). The electrical properties of the printed features were evaluated and post-print processing optimized, to yield flexible printed electronic circuits.

2. Materials and Methods

2.1. Materials

Graphite flakes (G) having particle sizes 200–300 µm were purchased from Graphenea, San Sebastian, Spain and melamine from Alfa Aesar, Kandel, Germany. Ethanol (absolute) and 2-propanol were obtained from Gram-Mol, Zagreb, Croatia, ethylene glycol from Sigma-Aldrich, St. Louis, MO, USA, and terpineol (mixture of isomers) from Alfa Aesar, Kandel, Germany. All the chemicals were of analytical grade and were used as received. Melamine intercalated graphene nanosheets (M-GNS, 1–2 sheets) were obtained by a mechanochemical route and can be used without additional purification. Aqueous solutions were prepared with deionized water (Millipore Milli-Q, specific conductivity 0.059 µS cm^{-1}). Commercial polymeric stabilizing agents Solsperse 12000S and Solsperse 20000 were supplied by Lubrizol, Wickliffe, OH, USA. Surface mount light-emitting diodes for the proof of concept experiment were from Kingbright Electronic Co, New Taipei City, Taiwan; they were glued to the printed conducting traces using a conductive glue, Wire Glue, Anders Products, Melrose, MA, USA.

2.2. Mechanochemical Synthesis of Melamine-Intercalated Graphene Nanosheets (M-GNS)

Single- and double-layer melamine-intercalated graphene nanosheets (M-GNS) were obtained by neat grinding in a ball to powder ratio $m_b{:}m_p$ = 1:12.7. The process was performed at room temperature using a planetary ball mill PULVERISETTE 6 operating at 500 rpm, in a 50 mL stainless steel jar equipped with 12 stainless steel balls (m = 4 g; d = 10 mm). Graphite flakes (m = 0.5 g), melamine (m = 2.5 g), and dry ice (m = 0.8 g) were milled in a mass ratio m(G):m(I):m(M) = 1:1.6:5 for 48 h in periods of 1 h milling, followed by 10 min of resting. The product was a black free-flowing powder that could be easily collected from the jar using a spatula.

2.3. Preparation of M-GNS Inks

M-GNS inks were prepared by dispersing the powdered product in various solvents using a Sonopuls Serie 2000.2 tip-sonicator, with the addition of Solsperse stabilizers. The sonication was performed for 15 min at 25% amplitude of the initial power of 70 W. The physical properties of the as-prepared formulations, including viscosity and surface tension, were measured with a micro-Ostwald viscosimeter 516 13/Ic, SI Analytics GmbH, (Mainz, Germany) and KRÜSS K6 tensiometer (Hamburg, Germany), respectively. All the measurements were performed at room temperature (23 ± 2 °C).

2.4. Inkjet Printing of M-GNS Inks and Post-Printing Processing

Inkjet printing was performed using a Fujifilm Dimatix DMP-2850 (Tokyo, Japan) drop-on-demand printer, which utilizes 16 nozzles with a diameter of 21 µm and a nominal drop volume of 10 pL. The experimental printing parameters were optimized to achieve continuous conductive features of the deposited ink on the selected substrates: PI (Kapton, DuPont, Wilmington, NC, USA, d = 25 µm); and clear PET (Melinex 505, DuPont, Wilmington, NC, USA, d = 125 µm). The printed patterns for characterization were 8 mm × 8 mm squares designed in Dimatix Drop Manager Software 3.0, Fujifilm, Tokyo, Japan.

To improve electrical conductivity, the printed squares were processed both thermally and photothermally using intense pulsed light (IPL). For thermal processing, the specimens were placed in a furnace (Demiterm, Estherm d.o.o., Sveta Nedelja, Croatia) at different temperatures for 1 h. For IPL processing, the jetted patterns were set approximately 1 cm from the flash lamp (Xenon, Wilmington, NC, USA, LH-912) of a Xenon X-1100 IPL system. A series of experiments were performed to find the optimal energy at 2500 V.

2.5. Characterization

Powder X-ray diffraction data were collected on a   Aeris bench-top diffractometer, Panalytical, Almelo, Netherlands, with Ni-filtered CuKα radiation obtained from an X-ray tube operating at 7.5 mA and 40 kV, in the 2θ range of 5–70° (step size of 0.027166°, 7.65 s per step). Thermogravimetric measurements were performed with a Shimadzu, Kyoto, Japan, DTG-60H analyzer at a heating rate of 10 °C min^{-1} from room temperature to 1000 °C in a stream of nitrogen, for bulk M-GNS samples and the prepared ink; and from room temperature to 1000 °C in a stream of oxygen for the polymeric stabilizers. Scanning electron microscopy (SEM) imaging was performed on a Jeol, Tokyo, Japan, JSM-7000F field emission scanning electron microscope, operating at 10 kV; while energy-dispersive X-ray spectroscopy (EDX) analysis was performed on an Oxford Instruments, Abingdon, UK, INCA 350 spectrometer coupled with the FE-SEM. Atomic force micros-copy (AFM) micrographs were obtained by NanoWizard 4 ULTRA AFM, Bruker, Biller-ica, MA, USA in AC mode. Samples for AFM were prepared by diluting the stock solu-tions to a given concentration of 10^{-3} mg/mL and spin coating on a freshly exfoliated mica substrate before drying at 70 or 150 °C in a Biobase Bov-30V Lab high-temperature vac-uum oven for 2 h. Fourier-transform infrared attenuated total reflectance (FTIR-ATR) spectra in KBr tablets were recorded on a PerkinElmer, Waltham, MA, USA, Spec-trumTwo L1600400 spectrometer equipped with a diamond cell in the range of 4000–450 cm^{-1} with a resolution of 8 cm^{-1}. UV–Vis spectroscopy of the conductive ink was per-formed with a Shimadzu, Kyoto, Japan, UV-1280 UV–Vis spectrometer. The absorption spectra were recorded in the range 320–800 nm after diluting to 1:100 to assure a mean-ingful absorbance range. Particle size distribution (PSD) was determined using a Zetasizer Ultra (Malvern Panalytical, Malvern, UK) based on a He-Ne laser (λ = 632.8 nm) and a thermostated sample cell. The sample dilution was φ = 1:33, accounting for the graphene refractive index of 1.957. Before measurement, the sample was equilibrated for 120 s at 25 °C ± 0.1 °C. The intensity of the scattered light was converted into contribution per number of particles within the measured sample volume. Zeta-potential measurements of the M-GNS ink formulation were carried out using the aforementioned instrument and the same thermostated sample cell. The ZS Xplorer v1.00, Malvern Panalytical, Malvern, UK soft-ware was used for data analysis. The sheet resistance of the printed samples was meas-ured before and after both thermal and IPL processing using a four-point probe (Ossilla, UK).

3. Results and Discussion

3.1. Synthesis and Characterization of Melamine-Intercalated Graphene Nanosheets

For the synthesis of the conducting nanoparticles, we adopted melamine-induced ex-foliation in a planetary ball-mill that produces melamine intercalated single and two-lay-ered graphene nanosheets (M-GNS). The role of melamine is to aid the exfoliation of graphite by noncovalent interactions, and prevent re-aggregation of the graphene sheets into a graphitic structure. Melamine has an aromatic core that interacts with the π-system of graphene; however, multiple melamine molecules can form extended 2D networks via hydrogen bonding, and this improves the exfoliation and stabilization of GNS [50]. The synthesized M-GNS were thoroughly characterized to determine their composition, mor-phology, and thermal properties. The Fourier-transform infrared attenuated total reflec-tance (FTIR-ATR) spectrum of M-GNS exhibits bands characteristic of melamine, while the absence of any additional bands demonstrates that the sample was pure (Figure 1).

Scanning electron microscopy (SEM) was used to evaluate the formation, size distri-bution, and morphology of the M-GNS; while EDX analysis provided additional infor-mation about the elemental composition of the sample. Figure 2 shows the morphology and elemental structure of the raw M-GNS sample. It is noticeable that melamine, after undergoing a grinding process, is present in the sample (evidenced by the significant

nitrogen amount). A wide particle size distribution is also observed. The morphology corresponds to previously examined mechanochemically treated carbon materials [55].
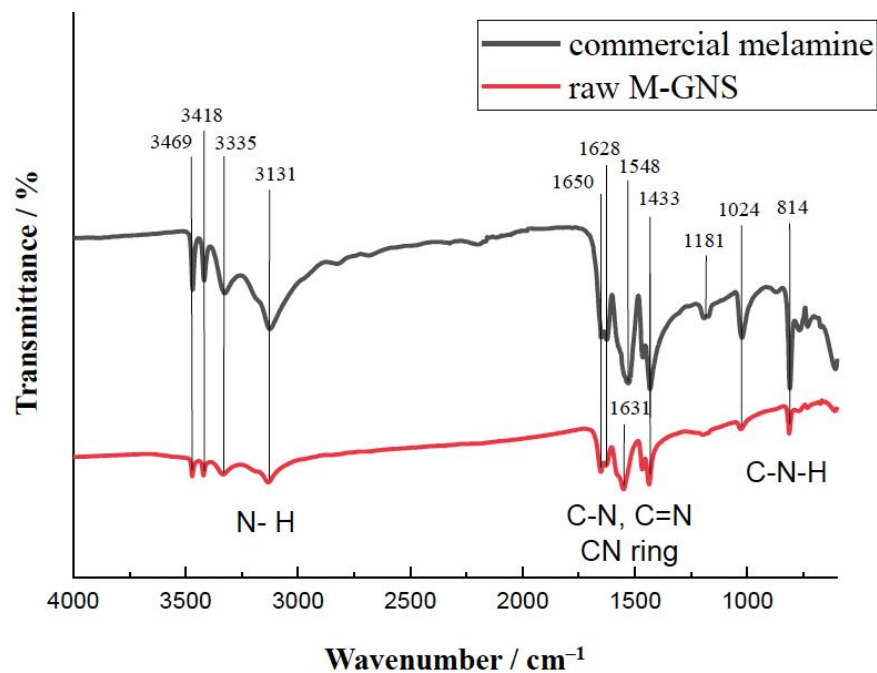

Figure 1. Fourier-transform infrared (FTIR) spectra for the raw sample of melamine-intercalated graphene nanosheets (M-GNS).
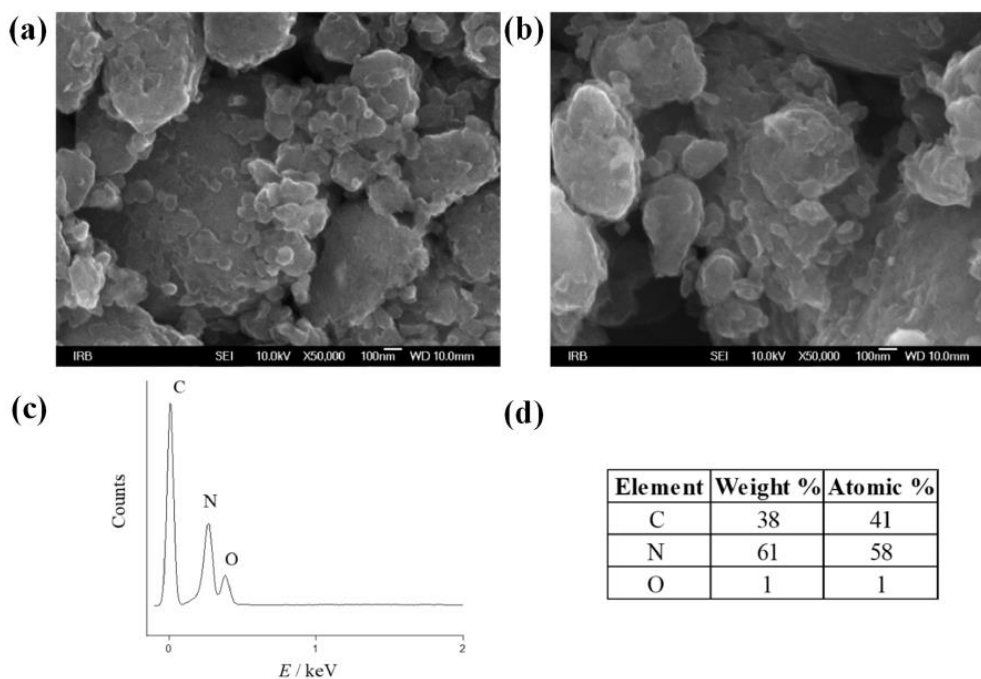

Element	Weight %	Atomic %
C	38	41
N	61	58
O	1	1

Figure 2. (**a,b**) Scanning electron microscopy (SEM) images and (**c,d**) energy-dispersive X-ray (EDX) spectra of the raw M-GNS.

Topological and morphological studies via atomic force microscopy (AFM) were conducted primarily to visualize the surface structure of the M-GNS and height profiles with and without melamine present in the sample. The AFM image (Figure 3a) shows melamine layers with a lateral dimension of 200 nm. On the other hand, after thermal annealing at 130 °C in a vacuum oven, the larger melamine flakes were removed by sublimation and only smaller graphene nanosheets remained (Figure 3b,c). The average diameter of the GNS was determined to be around 14 nm. AFM height measurements revealed an average height of 0.3–0.65 nm corresponding to single- and double-layer GNS.
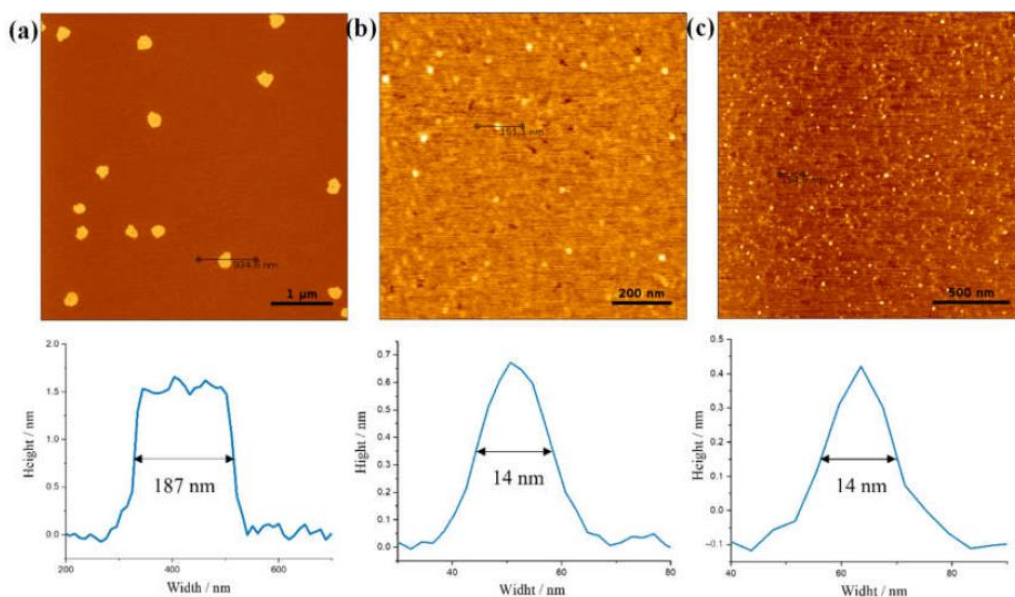
Figure 3. Atomic force microscopy (AFM) images and cross-section analysis of the M-GNS dispersed in a mixture of ethanol:water:EG = 0.50:0.45:0.05. The sample was spin-coated on freshly cleaved mica substrates and was dried in a vacuum oven for 2 h at (**a**) 70 °C and (**b,c**) 130 °C.

The prepared M-GNS were heated from room temperature to 1000 °C to determine their thermal stability. It has been reported that melamine decomposition takes place in three stages, undergoing progressive endothermic condensation during heating; with the release of ammonia and forms products, such as melam, melem, and melon [56]. Products of thermal decomposition of melamine are thermally more stable than melamine. Finally, graphitic carbon nitride, g-C_3N_4 is produced under further heating [57,58].

As expected, a typical differential weight loss in several regions was observed (Figure 4). The first stage covered the regions of maximum weight loss corresponding to the characteristic mass loss at the range of 300–400 °C. This is associated with melamine condensation to melam (a short-lived intermediate) and further condensation to melem [57]. At higher temperatures (around 400–600 °C), the condensation reaction slowly progresses; at first, it yields melon and then, graphitic carbon nitride [59,60]. Finally, thermal decomposition of graphitic carbon nitride takes place in the range of 600–750 °C [61]; whereas additional changes in weight loss were not observed, proving good thermal stability of GNS. The residual mass of GNS amounts to 18.6%, which is in good agreement with the initial mass ratio of graphite to melamine during the mechanochemical exfoliation.
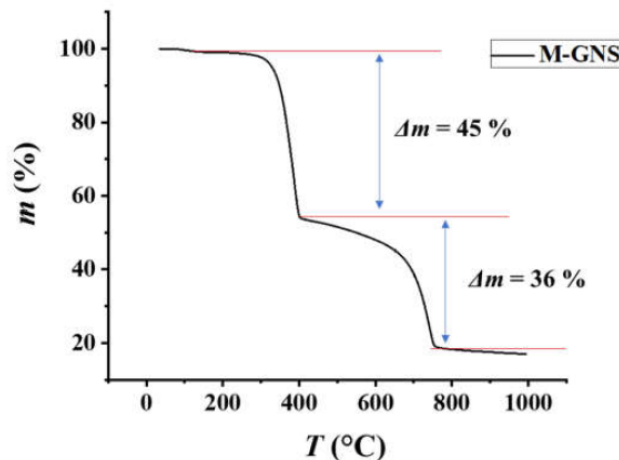
Figure 4. Thermogravimetric analysis (TGA) curve showing the mass loss profile of M-GNS.

3.2. Preparation and Characterization of M-GNS Inks

The M-GNS were dispersed in green solvents using an ultrasonic probe to form conductive inks for inkjet printing. We focused on less harmful polar solvents (water and alcohols) and aimed to formulate an ink compatible with substrates commonly used in printed electronics—PET and PI. Graphene is known to form stable dispersions in solvents with a similar surface energy to itself [62]. When adopting solvents of incompatible surface energy, there is a requirement for stabilizers that adsorb to graphene nanosheets during the homogenization step [36]. In this way, the stability of the ink is improved and the shelf life is significantly extended. Commercially available Solsperse polymeric hyperdispersants—steric stabilizers with anchor groups optimized for strong adsorption to the particle surface—were used for this purpose. We evaluated the stability of the M-GNS in several solvents and their mixtures (see Supplementary Materials, Figure S1). Ultimately, the selected composition of the ink was 2 mg/mL of the M-GNS dispersed in a solvent mixture consisting of ethanol:water:ethylene glycol = 0.50:0.45:0.05 by volume; with the addition of 0.36 mg/mL of Solsperse 20,000 and 0.04 mg/mL of Solsperse 12000S stabilizers. The prepared ink is shown in Figure 5a. This composition demonstrated good wetting of PET and PI substrates, with no observable coffee ring effect after drying.

The bottleneck of a piezoelectric drop-on-demand inkjet process is the development of stable, single droplets without the formation of satellite (secondary) droplets [63]. This can be achieved by tuning the inks composition and its physical properties, including viscosity, density, and surface tension. The droplet formation behavior is often characterized by Z, a dimensionless inverse Ohnesorge (*Oh*) number [11,64], $Z = \sqrt{\gamma \rho a}/\eta$; where ρ, η, γ, and a are the density, dynamic viscosity, surface tension, and dimensional parameter of the printer, respectively. Low Z-values (<4) indicate possible difficulties in fluid ejection due to the high viscosity, whereas a higher Z-value (>13) suggests the formation of satellite droplets or, at least, uncontrollable ink leakage [2]. The requirements for inkjet printable fluids include low viscosity (4–30 mPa s) and relatively high surface tension (around ~35 mN m^{-1}) [11]. Our ink formulation had a measured Z-value of 7.7, indicating excellent suitability for jetting.

The second major requirement of nanoparticle-based inks is nanoparticle size and suspension stability. A maximum nanoparticle size of about 200–500 nm (1% of the nozzle diameter) is generally suggested, along with the necessary stability against aggregation and sedimentation [12]. Failure to meet either of these requirements can cause the clogging of printer nozzles. Dynamic light scattering (DLS) analysis was performed to

determine the particle size distribution of the fabricated M-GNS ink based on the number of scattering particles, Figure 5b.
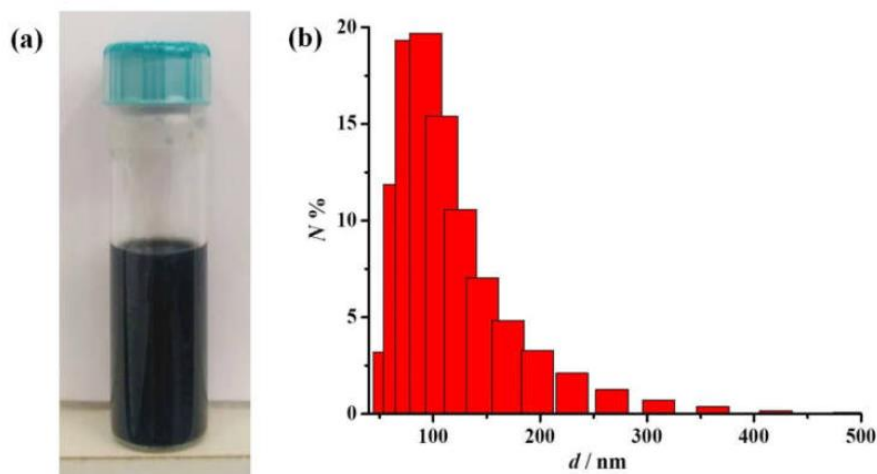
Figure 5. (a) The M-GNS ink after 24 h at rest after preparation; and (b) a histogram of the prepared M-GNS ink from Dynamic light scattering (DLS) measurements, recorded in an aqueous medium with a sample dilution of $\varphi = 1{:}33$.

The histogram in Figure 5b shows that the sample contains particles of different sizes, resulting in an average hydrodynamic particle diameter of $d = 173.7$ nm; this corresponds to the size of melamine sheets observed in the AFM measurements (Figure 3a) and indicates that the nanoparticles are small enough for printing without clogging. The stability of the conductive inks was evaluated using zeta-potential measurements. Particle dispersions with zeta-potential values of ±20–30 mV are generally assumed to be moderately stable [65]. The measured ζ-potential of the M-GNS ink was –25.7 mV, indicating moderate stability of the prepared graphene particles in the solution phase [66]. The stability of real systems is determined by the relationship between attractive van der Waals forces (information that is not detectable with ζ-potential measurements) and electrostatic repulsive forces between particles (provided by the zeta-potential). Accounting for that, dispersions with a lower absolute zeta-potential than that generally acknowledged should not be discarded in terms of colloidal stability [67].

The long-term stability of the ink was additionally evaluated by optical absorption spectroscopy. We collected UV–Vis spectra of freshly prepared ink and compared it to those taken up to 32 days post-formation. Graphene has an absorbance maximum at ~270 nm [68–70]; however, this part of the spectrum is affected by absorption of the Solsperse 20000 stabilizer. Solsperse 12000S, on the other hand, has very strong absorbance in the visible part of the spectrum (Figure S2); while its lowest absorbance is at $\lambda = 514$ nm. Therefore, 514 nm was chosen as the wavelength for monitoring graphene absorbance reduction as a function of ink instability over time, Figure 6. As can be seen from Figure 6b, sedimentation is strongest within the first 6 h. However, the absorbance at 514 nm does not fall below 91% of the initial value; this indicates good short-term stability for single-day printing. In the following days, the absorbance decreases more slowly; it reaches a minimum at 66% of the initial value after 32 days. On the 34th day of the ink storage, we tip-sonicated the ink for 1 min (25% amplitude) and regained the initial absorbance value (100%). This indicates that although the ink shows moderate stability over prolonged periods, the maximum stability can be recovered after only one minute of ultrasonication.
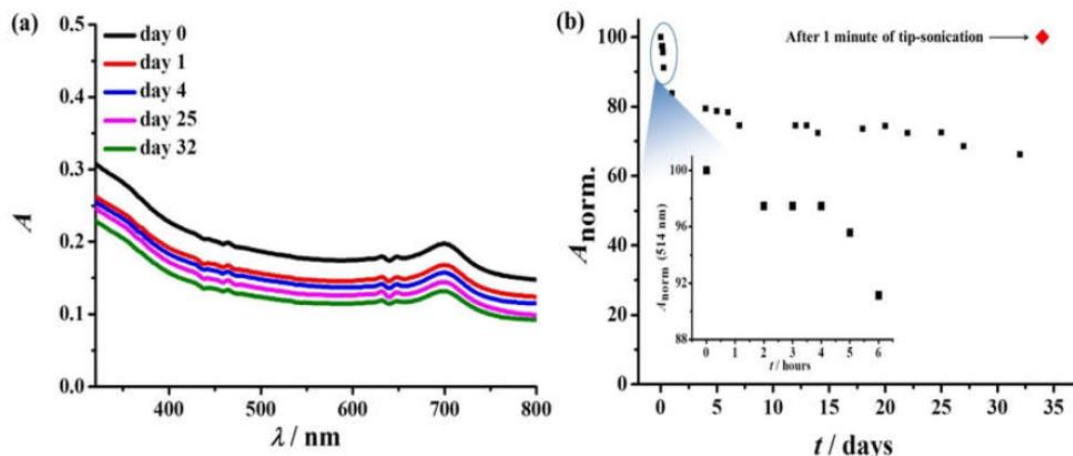
Figure 6. (a) A comparison of UV–Vis spectra recorded immediately after ink preparation (**day 0**), and **1, 4, 25** and **32 days** post-preparation (dilution: 100 x); (b) the normalized view of the absorption at 514 nm (dilution: 100×); (b) **inset** sedimentation of the ink within the first six hours after ink preparation.

3.3. Inkjet Printing and Post-Printing Processing

The printing process starts with optimizing the printing parameters, which include the following: waveform, applied voltage, drop spacing, jetting frequency, cartridge height, number of printed layers, cartridge temperature, and platen temperature. The printing was performed at a moderate temperature of 55 °C and low jetting frequency. The other optimized printing parameters are shown in Table S1. For characterization, 8 × 8 mm squares were printed on polyethylene terephthalate (PET) and polyimide (PI) sheets; this is due to these substrates being commonly used in printed electronics [12,71]. Multiple layers of the conductive ink were printed (Figure 7), which is a practical way of increasing conductivity. The printed samples were characterized by sheet resistance measurements (R_s) with a four-point probe. The printed films were not electrically conductive up to three layers. At five layers, the measured sheet resistance was 4.27 ± 0.87 MΩ/sq (SD) and further decreased with additional layers. Nevertheless, such high sheet resistances are inadequate for most printed electronics applications; moreover, increasing the number of printed layers becomes pointless beyond a certain number of layers, since this greatly increases printing duration. Conductivity is instead commonly increased by removal of non-conducting ink components, usually by thermal post-print processing [72].

We exposed the printed squares to thermal annealing in order to improve the electrical conductivity via the removal of melamine and polymeric stabilizers. As presented in Figure 4, most of the melamine thermally decomposes at temperatures of up to 400 °C. The polymeric stabilizer Solsperse 20000 decomposes at somewhat lower temperatures (Figure S4); while Solsperse 12000S is more stable, but present in minuscule amounts. Therefore, the printed squares on PI were processed for 1 h at different temperatures, up to 400 °C (Figure 7b). The sheet resistance decreased gradually with temperature from the initial value of around 2.0 ± 0.9 MΩ/sq (SD), down to 44 ± 6 kΩ/sq (SD) at 400 °C. The thermal processing also benefited the homogeneity of the printed features, as evidenced by the decreasing standard deviations of measured sheet resistances.
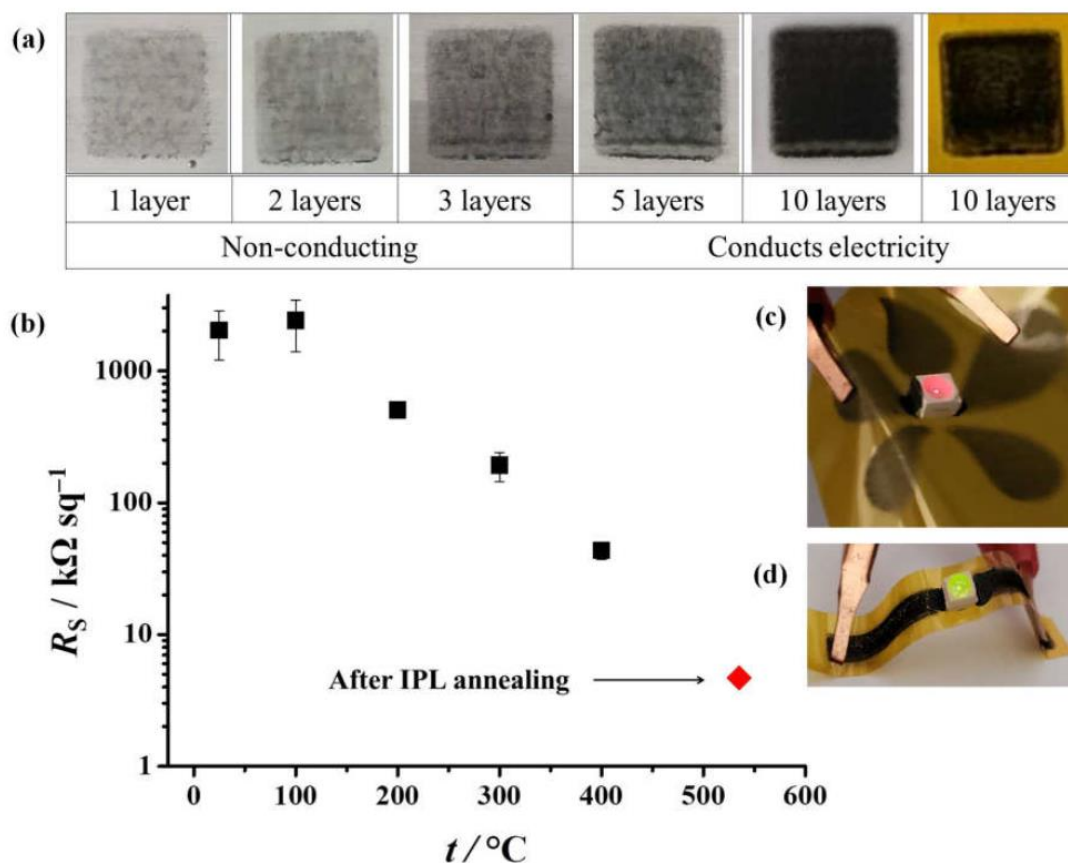
Figure 7. (a) The different number of printing passes of the conductive ink on a PET and PI substrate; (b) the sheet resistance of printed squares on PI, after thermal annealing at different temperatures. Error bars represent one standard deviation ($n = 6$); red diamond indicates the sheet resistance value after intense pulsed light (IPL) annealing at the energy of 700 J; examples of flexible printed electronics using 10 layers (c) and 20 layers (d) of the M-GNS ink.

To gain better insight into the morphology and topology of the printed features, SEM and AFM analysis were performed before and after thermal annealing at 400 °C (Figure 8). The surface morphology of the printed pattern before annealing is rough and inhomogeneous. We observed large melamine crystals (larger than 10 μm in diameter), which disrupt the electrical conductivity (Figure 8a). The SEM picture of the printed pattern after thermal annealing confirms a significant enhancement of the film quality and removal of melamine crystals due to thermal decomposition (Figure 8d,e). Accordingly, AFM measurements revealed a decrease in film thickness after annealing, along with a decrease in surface roughness (Figure 8c,f). The surface roughness parameter R_a (average) decreased from 580.6 nm to 216.0 nm, while the R_q (quadratic average) decreased from 789.1 nm to 289.1 nm.

103
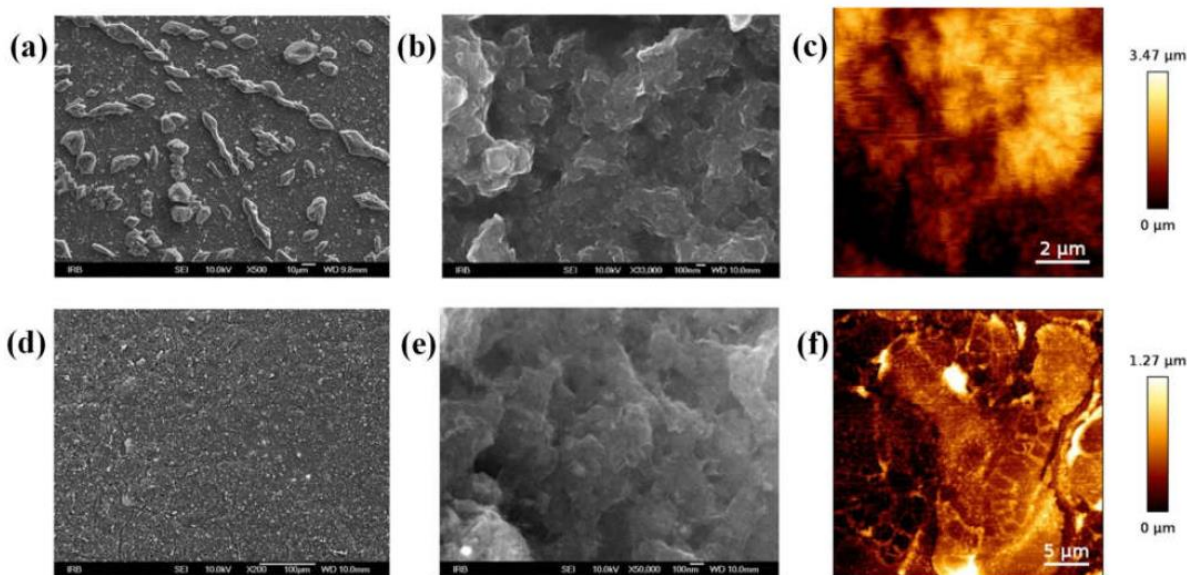
Figure 8. SEM (under different magnification) and AFM images of the M-GNS film on a PI substrate: (**a**–**c**) before annealing; and (**d**–**f**) after annealing at 400 °C.

In addition to thermal processing, we evaluated intense pulsed light (IPL) as a way of photothermal processing. IPL uses very short high-energy pulses of visible light; it thereby diminishes the thermal stress on the sensitive polymeric substrate, which makes it highly compatible with printed flexible electronics [73]. Graphene-based materials are great candidates for IPL annealing due to their high absorption coefficient in the visible part of the spectrum [74,75]. Nevertheless, the sheet resistance of printed squares was reduced only to around 43% of the initial value after exposure to 600 J (Figure S5). A further increase in IPL energy caused an increase in resistance, suggesting that the conductive film was damaged during the annealing process. This can be attributed to the formation of gaseous products (ammonia) of melamine decomposition [58] in very short time intervals, leading to the removal of graphene from the substrate. Therefore, IPL in itself is not an optimal processing technology for this kind of conducting ink containing melamine. However, we exposed the previously thermally annealed samples (at 400 °C) to IPL energies of 700 J. This combined processing procedure resulted in the lowest sheet resistances of only 5.0 ± 0.3 kΩ/sq (SD) for 10 printed layers (shown in Figure 7b) and 626 ± 106 Ω/sq (SD) for 20 printed layers. As can be seen from Table S2, the measured sheet resistances are comparable to, or better than, those obtained in similar studies and for a comparable number of printing passes. While printed metal nanoparticle inks can yield the lowest sheet resistances, in some cases less than 1 Ω/sq [12], in the case of graphene inks, sheet resistances are usually larger than 1 kΩ/sq for a single digit number of printed layers. Increasing the number of printing passes reduces the sheet resistance below the value of 1 kΩ/sq, which is usually observed at 20 passes or more (Table S2). Such resistivities are sufficient for different printed electronics applications [23]. Finally, as a proof-of-concept experiment, we constructed simple flexible LED circuits; we constructed the circuits by printing 10 and 20 layers of the conductive ink on PI, either as plain 2 mm wide conducting traces or in the shape of our institution logo (Figure 7c,d). The printed traces were annealed in the same way as previously optimized, by combining thermal and IPL processing. The attached surface mount LEDs were successfully powered from a single 9 V battery.

4. Conclusions

We described here a novel mechanochemical synthesis of melamine-intercalated graphene nanosheets; we suggest it as a potential approach for large-scale preparation of graphene, which would comply with the basic principles of green chemistry. The prepared M-GNS were used as a functional material for the formulation of a stable graphene-based ink, suitable for inkjet printing. The printing process was optimized to generate electrically conductive patterns on flexible PET and PI substrates. A combination of thermal and photonic (IPL) annealing reduced the electrical resistance of the printed patterns by three orders of magnitude. The presented procedure is both scalable and environmentally friendly; in addition, it represents a starting point in the development of graphene-based printed flexible electronics.

References

1. Raut, N.C.; Al-Shamery, K. Inkjet printing metals on flexible materials for plastic and paper electronics. *J. Mater. Chem. C* **2018**, *6*, 1618–1641. https://doi.org/10.1039/c7tc04804a.
2. Nayak, L.; Mohanty, S.; Nayak, S.K.; Ramadoss, A. A review on inkjet printing of nanoparticle inks for flexible electronics. *J. Mater. Chem. C* **2019**, *7*, 8771–8795. https://doi.org/10.1039/c9tc01630a.
3. Wu, W. Inorganic nanomaterials for printed electronics: A review. *Nanoscale* **2017**, *9*, 7342–7372. https://doi.org/10.1039/c7nr01604b.
4. Khan, Y.; Thielens, A.; Muin, S.; Ting, J.; Baumbauer, C.; Arias, A.C. A New Frontier of Printed Electronics: Flexible Hybrid Electronics. *Adv. Mater.* **2020**, *32*, 1905279. https://doi.org/10.1002/adma.201905279.
5. Huang, L.; Huang, Y.; Liang, J.; Wan, X.; Chen, Y. Graphene-based conducting inks for direct inkjet printing of flexible conductive patterns and their applications in electric circuits and chemical sensors. *Nano Res.* **2011**, *4*, 675–684. https://doi.org/10.1007/s12274-011-0123-z.
6. Pietsch, M.; Schlisske, S.; Held, M.; Strobel, N.; Wieczorek, A.; Hernandez-Sosa, G. Biodegradable inkjet-printed electrochromic display for sustainable short-lifecycle electronics. *J. Mater. Chem. C* **2020**, *8*, 16716–16724. https://doi.org/10.1039/d0tc04627b.
7. Ali, Z.; Perret, E.; Barbot, N.; Siragusa, R.; Hely, D.; Bernier, M.; Garet, F. Authentication Using Metallic Inkjet-Printed Chipless RFID Tags. *IEEE Trans. Antennas Propag.* **2020**, *68*, 4137–4142. https://doi.org/10.1109/tap.2019.2948740.

8. Baby, T.T.; Rommel, M.; von Seggern, F.; Friederich, P.; Reitz, C.; Dehm, S.; Kübel, C.; Wenzel, W.; Hahn, H.; Dasgupta, S. Sub-50 nm Channel Vertical Field-Effect Transistors using Conventional Ink-Jet Printing. *Adv. Mater.* **2017**, *29*, 1603858. https://doi.org/10.1002/adma.201603858.

9. Ivanisevic, I.; Milardović, S.; Ressler, A.; Kassal, P. Fabrication of an All-Solid-State Ammonium Paper Electrode Using a Graphite-Polyvinyl Butyral Transducer Layer. *Chemosensors* **2021**, *9*, 333. https://doi.org/10.3390/chemosensors9120333.

10. Cummins, G.; Desmulliez, M.P.Y. Inkjet printing of conductive materials: A review. *Circuit World* **2012**, *38*, 193–213. https://doi.org/10.1108/03056121211280413.

11. Derby, B. Inkjet Printing of Functional and Structural Materials: Fluid Property Requirements, Feature Stability, and Resolution. In *Annual Review of Materials Research*; Clarke, D.R., Ruhle, M., Zok, F., Eds., 2010; pp. 395–414, Volume 40.

12. Kamyshny, A.; Magdassi, S. Conductive nanomaterials for 2D and 3D printed flexible electronics. *Chem. Soc. Rev.* **2019**, *48*, 1712–1740. https://doi.org/10.1039/c8cs00738a.

13. Kamyshny, A.; Magdassi, S. Conductive Nanomaterials for Printed Electronics. *Small* **2014**, *10*, 3515–3535. https://doi.org/10.1002/smll.201303000.

14. Zea, M.; Moya, A.; Fritsch, M.; Ramon, E.; Villa, R.; Gabriel, G. Enhanced Performance Stability of Iridium Oxide-Based pH Sensors Fabricated on Rough Inkjet-Printed Platinum. *Acs Appl. Mater. Interfaces* **2019**, *11*, 15160–15169. https://doi.org/10.1021/acsami.9b03085.

15. Sjoberg, P.; Määttänen, A.; Vanamo, U.; Novell, M.; Ihalainen, P.; Andrade, F.J.; Bobacka, J.; Peltonen, J. Paper-based potentiometric ion sensors constructed on ink-jet printed gold electrodes. *Sens. Actuators B-Chem.* **2016**, *224*, 325–332. https://doi.org/10.1016/j.snb.2015.10.051.

16. Milardovic, S.; Ivanišević, I.; Rogina, A.; Kassal, P. Synthesis and Electrochemical Characterization of AgNP Ink Suitable for Inkjet Printing. *Int. J. Electrochem. Sci.* **2018**, *13*, 11136–11149. https://doi.org/10.20964/2018.11.87.

17. Park, J.; Yoon, H.; Kim, G.; Lee, B.; Lee, S.; Jeong, S.; Kim, T.; Seo, J.; Chung, S.; Hong, Y. Highly Customizable All Solution-Processed Polymer Light Emitting Diodes with Inkjet Printed Ag and Transfer Printed Conductive Polymer Electrodes. *Adv. Funct. Mater.* **2019**, *29*, 1902412. https://doi.org/10.1002/adfm.201902412.

18. Kulkarni, M.V.; Apte, S.K.; Naik, S.D.; Ambekar, J.; Kale, B. Ink-jet printed conducting polyaniline based flexible humidity sensor. *Sens. Actuators B-Chem.* **2013**, *178*, 140–143. https://doi.org/10.1016/j.snb.2012.12.046.

19. Gbaguidi, A.; Madiyar, F.; Kim, D.; Namilae, S. Multifunctional inkjet printed sensors for MMOD impact detection. *Smart Mater. Struct.* **2020**, *29*, 085052. https://doi.org/10.1088/1361-665X/ab98eb.

20. Tortorich, R.P.; Song, E.; Choi, J.W. Inkjet-Printed Carbon Nanotube Electrodes with Low Sheet Resistance for Electrochemical Sensor Applications. *J. Electrochem. Soc.* **2014**, *161*, B3044–B3048. https://doi.org/10.1149/2.008402jes.

21. Vasiljevic, D.Z.; Mansouri, A.; Anzi, L.; Sordan, R.; Stojanovic, G.M. Performance Analysis of Flexible Ink-Jet Printed Humidity Sensors Based on Graphene Oxide. *IEEE Sens. J.* **2018**, *18*, 4378–4383. https://doi.org/10.1109/jsen.2018.2823696.

22. Huang, Q.J.; Zhu, Y. Printing Conductive Nanomaterials for Flexible and Stretchable Electronics: A Review of Materials, Processes, and Applications. *Adv. Mater. Technol.* **2019**, *4*, 1800546. https://doi.org/10.1002/admt.201800546.

23. Htwe, Y.Z.N.; Mariatti, M. Printed graphene and hybrid conductive inks for flexible, stretchable, and wearable electronics: Progress, opportunities, and challenges. *J. Sci. Adv. Mater. Devices* **2022**, *7*, 100435. https://doi.org/10.1016/j.jsamd.2022.100435.

24. Htwe, Y.Z.N.; Mariatti, M. Surfactant-assisted water-based graphene conductive inks for flexible electronic applications. *J. Taiwan Inst. Chem. Eng.* **2021**, *125*, 402–412. https://doi.org/10.1016/j.jtice.2021.06.022.

25. Maribou, K.; Gil, W.; Al Ghaferi, A.; Saadat, I.; Alhammadi, K.; Khair, A.M.; Younes, H. Assessing the Stability of Inkjet-Printed Carbon Nanotube for Brine Sensing Applications. *J. Nanosci. Nanotechnol.* **2020**, *20*, 7644–7652. https://doi.org/10.1166/jnn.2020.18614.

26. Jelbuldina, M.; Younes, H.; Saadat, I.; Tizani, L.; Sofela, S.; Al Ghaferi, A. Fabrication and design of CNTs inkjet-printed based micro FET sensor for sodium chloride scale detection in oil field. *Sens. Actuators A Phys.* **2017**, *263*, 349–356. https://doi.org/10.1016/j.sna.2017.06.035.

27. Xu, L.; Wang, H.; Wu, Y.; Wang, Z.; Wu, L.; Zheng, L. A one-step approach to green and scalable production of graphene inks for printed flexible film heaters. *Mater. Chem. Front.* **2021**, *5*, 1895–1905. https://doi.org/10.1039/D0QM00803F.

28. Agudosi, E.S.; Abdullah, E.C.; Numan, A.; Mubarak, N.M.; Khalid, M.; Omar, N. A Review of the Graphene Synthesis Routes and its Applications in Electrochemical Energy Storage. *Crit. Rev. Solid State Mater. Sci.* **2020**, *45*, 339–377. https://doi.org/10.1080/10408436.2019.1632793.

29. Wang, C.Y.; Xia, K.; Wang, H.; Liang, X.; Yin, Z.; Zhang, Y. Advanced Carbon for Flexible and Wearable Electronics. *Adv. Mater.* **2019**, *31*, 1801072. https://doi.org/10.1002/adma.201801072.

30. Backes, C.; Higgins, T.M.; Kelly, A.; Boland, C.; Harvey, A.; Hanlon, D.; Coleman, J.N. Guidelines for Exfoliation, Characterization and Processing of Layered Materials Produced by Liquid Exfoliation. *Chem. Mater.* **2017**, *29*, 243–255. https://doi.org/10.1021/acs.chemmater.6b03335.

31. Capasso, A.; Castillo, A.D.R.; Sun, H.; Ansaldo, A.; Pellegrini, V.; Bonaccorso, F. Ink-jet printing of graphene for flexible electronics: An environmentally-friendly approach. *Solid State Commun.* **2015**, *224*, 53–63. https://doi.org/10.1016/j.ssc.2015.08.011.

32. Backes, C.; Abdelkader, A.M.; Alonso, C.; Andrieux-Ledier, A.; Arenal, R.; Azpeitia, J.; Balakrishnan, N.; Banszerus, L.; Barjon, J.; Bartali, R.; et al. Production and processing of graphene and related materials. *2D Mater.* **2020**, *7*, 022001. https://doi.org/10.1088/2053-1583/ab1e0a.

33. Kamarudin, S.F.; Mustapha, M.; Kim, J.K. Green Strategies to Printed Sensors for Healthcare Applications. *Polym. Rev.* **2021**, *61*, 116–156. https://doi.org/10.1080/15583724.2020.1729180.

34. He, Q.; Das, S.R.; Garland, N.T.; Jing, D.; Hondred, J.A.; Cargill, A.A.; Ding, S.; Karunakaran, C.; Claussen, J.C. Enabling Inkjet Printed Graphene for Ion Selective Electrodes with Postprint Thermal Annealing. *Acs Appl. Mater. Interfaces* **2017**, *9*, 12719–12727. https://doi.org/10.1021/acsami.7b00092.

35. Pandhi, T.; Cornwell, C.; Fujimoto, K.; Barnes, P.; Cox, J.; Xiong, H.; Davis, P.H.; Subbaraman, H.; Koehne, J.E.; Estrada, D. Fully inkjet-printed multilayered graphene-based flexible electrodes for repeatable electrochemical response. *Rsc Adv.* **2020**, *10*, 38205–38219. https://doi.org/10.1039/d0ra04786d.

36. Parvez, K.; Worsley, R.; Alieva, A.; Felten, A.; Casiraghi, C. Water-based and inkjet printable inks made by electrochemically exfoliated graphene. *Carbon* **2019**, *149*, 213–221. https://doi.org/10.1016/j.carbon.2019.04.047.

37. Majee, S.; Song, M.; Zhang, S.-L.; Zhang, Z.-B. Scalable inkjet printing of shear-exfoliated graphene transparent conductive films. *Carbon* **2016**, *102*, 51–57. https://doi.org/10.1016/j.carbon.2016.02.013.

38. Kudr, J.; Zhao, L.; Nguyen, E.P.; Arola, H.; Nevanen, T.K.; Adam, V.; Zitka, O.; Merkoçi, A. Inkjet-printed electrochemically reduced graphene oxide microelectrode as a platform for HT-2 mycotoxin immunoenzymatic biosensing. *Biosens. Bioelectron.* **2020**, *156*, 112109. https://doi.org/10.1016/j.bios.2020.112109.

39. Ji, A.; Chen, Y.; Wang, X.; Xu, C. Inkjet printed flexible electronics on paper substrate with reduced graphene oxide/carbon black ink. *J. Mater. Sci.-Mater. Electron.* **2018**, *29*, 13032–13042. https://doi.org/10.1007/s10854-018-9425-1.

40. Kumar, N.; Salehiyan, R.; Chauke, V.; Botlhoko, O.J.; Setshedi, K.; Scriba, M.; Masukume, M.; Ray, S.S. Top-down synthesis of graphene: A comprehensive review. *Flatchem* **2021**, *27*, 100224. https://doi.org/10.1016/j.flatc.2021.100224.

41. Kang, S.; Jeong, Y.K.; Jung, K.H.; Son, Y.; Choi, S.-C.; An, G.S.; Han, H.; Kim, K.M. Simple preparation of graphene quantum dots with controllable surface states from graphite. *RSC Adv.* **2019**, *9*, 38447–38453. https://doi.org/10.1039/c9ra07555k.

42. Hummers, W.S.; Offeman, R.E. Preparation of Graphitic Oxide. *J. Am. Chem. Soc.* **1958**, *80*, 1339–1339. https://doi.org/10.1021/ja01539a017.

43. Munuera, J.; Britnell, L.; Santoro, C.; Cuéllar-Franca, R.; Casiraghi, C. A review on sustainable production of graphene and related life cycle assessment. *2D Mater.* **2022**, *9*, 012002. https://doi.org/10.1088/2053-1583/ac3f23.

44. Bonaccorso, F.; Lombardo, A.; Hasan, T.; Sun, Z.; Colombo, L.; Ferrari, A.C. Production and processing of graphene and 2d crystals. *Mater. Today* **2012**, *15*, 564–589. https://doi.org/10.1016/s1369-7021(13)70014-2.

45. Yan, Y.X.; Nashath, F.Z.; Chen, S.; Manickam, S.; Lim, S.S.; Zhao, H.; Lester, E.; Wu, T.; Pang, C.H. Synthesis of graphene: Potential carbon precursors and approaches. *Nanotechnol. Rev.* **2020**, *9*, 1284–1314. https://doi.org/10.1515/ntrev-2020-0100.

46. Do, J.L.; Friscic, T. Mechanochemistry: A Force of Synthesis. *Acs Cent. Sci.* **2017**, *3*, 13–19. https://doi.org/10.1021/acscentsci.6b00277.

47. Chang, D.W.; Choi, H.-J.; Jeon, I.-Y.; Seo, J.-M.; Dai, L.; Baek, J.-B. Solvent-free mechanochemical reduction of graphene oxide. *Carbon* **2014**, *77*, 501–507. https://doi.org/10.1016/j.carbon.2014.05.055.

48. Jeon, I.Y.; Shin, Y.-R.; Sohn, G.-J.; Choi, H.-J.; Bae, S.-Y.; Mahmood, J.; Jung, S.-M.; Seo, J.-M.; Kim, M.-J.; Chang, D.W.; et al. Edge-carboxylated graphene nanosheets via ball milling. *Proc. Natl. Acad. Sci. USA* **2012**, *109*, 5588–5593. https://doi.org/10.1073/pnas.1116897109,.

49. Yan, L.; Lin, M.; Zeng, C.; Chen, Z.; Zhang, S.; Zhao, X.; Wu, A.; Wang, Y.; Dai, L.; Qu, J.; et al. Electroactive and biocompatible hydroxyl-functionalized graphene by ball milling. *J. Mater. Chem.* **2012**, *22*, 8367–8371. https://doi.org/10.1039/c2jm30961k.

50. Leon, V.; Rodriguez, A.M.; Prieto, P.; Prato, M.; Vázquez, E. Exfoliation of Graphite with Triazine Derivatives under Ball-Milling Conditions: Preparation of Few-Layer Graphene via Selective Noncovalent Interactions. *Acs Nano* **2014**, *8*, 563–571. https://doi.org/10.1021/nn405148t.

51. Chen, C.H.; Yang, S.-W.; Chuang, M.-C.; Woon, W.-Y.; Su, C.-Y. Towards the continuous production of high crystallinity graphene via electrochemical exfoliation with molecular in situ encapsulation. *Nanoscale* **2015**, *7*, 15362–15373. https://doi.org/10.1039/C5NR03669K.

52. Ma, H.; Shen, Z. Exfoliation of graphene nanosheets in aqueous media. *Ceram. Int.* **2020**, *5*, 1895–1905. https://doi.org/10.1016/j.ceramint.2020.05.314.

53. Shi, G.; Araby, S.; Gibson, C.T.; Meng, Q.; Zhu, S.; Ma, J. Graphene Platelets and Their Polymer Composites: Fabrication, Structure, Properties, and Applications. *Adv. Funct. Mater.* **2018**, *28*, 1706705. https://doi.org/10.1002/adfm.201706705.

54. Samoechip, W.; Pattananuwat, P.; Potiyaraj, P. Synthesis of Graphene Functionalized Melamine and its Application for Supercapacitor Electrode. *Key Eng. Mater.* **2018**, *773*, 128–132. https://doi.org/10.4028/www.scientific.net/KEM.773.128.

55. Deng, M.J.; Cao, X.; Guo, L.; Cao, H.; Wen, Z.; Mao, C.; Zuo, K.; Chen, X.; Yu, X.; Yuan, W. Graphene quantum dots: Efficient mechanosynthesis, white-light and broad linear excitation-dependent photoluminescence and growth inhibition of bladder cancer cells. *Dalton Trans.* **2020**, *49*, 2308–2316. https://doi.org/10.1039/c9dt04575a.

56. Wirnhier, E.; Mesch, M.B.; Senker, J.; Schnick, W. Formation and Characterization of Melam, Melam Hydrate, and a Melam-Melem Adduct. *Chem.-A Eur. J.* **2013**, *19*, 2041–2049. https://doi.org/10.1002/chem.201203340.

57. Lotsch, B.V.; Schnick, W. New Light on an Old Story: Formation of Melam during Thermal Condensation of Melamine. *Chem.-A Eur. J.* **2007**, *13*, 4956–4968. https://doi.org/10.1002/chem.200601291.

58. Liu, X.; Hao, J.W.; Gaan, S. Recent studies on the decomposition and strategies of smoke and toxicity suppression for polyurethane based materials. *Rsc Adv.* **2016**, *6*, 74742–74756. https://doi.org/10.1039/c6ra14345h.

59. Costa, L.; Camino, G. Thermal behaviour of melamine. *J. Therm. Anal.* **1988**, *34*, 423–429. https://doi.org/10.1007/BF01913181.

107

60. May, H. Pyrolysis of melamine. *J. Appl. Chem.* **1959**, *9*, 340–344. https://doi.org/10.1002/jctb.5010090608.

61. Fang, L.; Ohfuji, H.; Shinmei, T.; Irifune, T. Experimental study on the stability of graphitic C3N4 under high pressure and high temperature. *Diam. Relat. Mater.* **2011**, *20*, 819–825. https://doi.org/10.1016/j.diamond.2011.03.034.

62. Hernandez, Y.; Nicolosi, V.; Lotya, M.; Blighe, F.M.; Sun, Z.; De, S.; McGovern, I.T.; Holland, B.; Byrne, M.; Gun'Ko, Y.K.; et al. High-yield production of graphene by liquid-phase exfoliation of graphite. *Nat. Nanotechnol.* **2008**, *3*, 563–568. https://doi.org/10.1038/nnano.2008.215.

63. Hu, G.H.; Kang, J.; Ng, L.W.T.; Zhu, X.; Howe, R.C.T.; Jones, C.G.; Hersam, M.C.; Hasan, T. Functional inks and printing of two-dimensional materials. *Chem. Soc. Rev.* **2018**, *47*, 3265–3300. https://doi.org/10.1039/c8cs00084k.

64. Li, D.D.; Lai, W.-Y.; Zhang, Y.-Z.; Huang, W. Printable Transparent Conductive Films for Flexible Electronics. *Adv. Mater.* **2018**, *30*, 1704738. https://doi.org/10.1002/adma.201704738.

65. Bhattacharjee, S. DLS and zeta potential—What they are and what they are not? *J. Control. Release* **2016**, *235*, 337–351. https://doi.org/10.1016/j.jconrel.2016.06.017.

66. Krishnamoorthy, K.; Veerapandian, M.; Yun, K.; Kim, S.-J. The Chemical and structural analysis of graphene oxide with different degrees of oxidation. *Carbon* **2013**, *53*, 38–49. https://doi.org/10.1016/j.carbon.2012.10.013.

67. Lyklema, J.; van Leeuwen, H.P.; Minor, M. DLVO-theory, a dynamic re-interpretation. *Adv. Colloid Interface Sci.* **1999**, *83*, 33–69. https://doi.org/10.1016/s0001-8686(99)00011-1.

68. Backes, C.; Paton, K.R.; Hanlon, D.; Yuan, S.; Katsnelson, M.I.; Houston, J.; Smith, R.J.; McCloskey, D.; Donegan, J.F.; Coleman, J.N. Spectroscopic metrics allow in situ measurement of mean size and thickness of liquid-exfoliated few-layer graphene nanosheets. *Nanoscale* **2016**, *8*, 4311–4323. https://doi.org/10.1039/C5NR08047A.

69. Lotya, M.; Hernandez, Y.; King, P.J.; Smith, R.J.; Nicolosi, V.; Karlsson, L.S.; Blighe, F.M.; De, S.; Wang, Z.; McGovern, I.T.; et al. Liquid Phase Production of Graphene by Exfoliation of Graphite in Surfactant/Water Solutions. *J. Am. Chem. Soc.* **2009**, *131*, 3611–3620. https://doi.org/10.1021/ja807449u.

70. Tiwari, S.K.; Huczko, A.; Oraon, R.; De Adhikari, A.; Nayak, G.C. Facile electrochemical synthesis of few layered graphene from discharged battery electrode and its application for energy storage. *Arab. J. Chem.* **2017**, *10*, 556–565. https://doi.org/10.1016/j.arabjc.2015.08.016.

71. Zang, D.Y.; Tarafdar, S.; Tarasevich, Y.Y.; Choudhury, M.D.; Dutta, T. Evaporation of a Droplet: From physics to applications. *Phys. Rep.-Rev. Sect. Phys. Lett.* **2019**, *804*, 1–56. https://doi.org/10.1016/j.physrep.2019.01.008.

72. Ivanisevic, I.; Kassal, P.; Milinković, A.; Rogina, A.; Milardović, S. Combined Chemical and Thermal Sintering for High Conductivity Inkjet-printed Silver Nanoink on Flexible Substrates. *Chem. Biochem. Eng. Q.* **2019**, *33*, 377–384. https://doi.org/10.15255/cabeq.2019.1585.

73. Wunscher, S.; Abbel, R.; Perelaer, J.; Schubert, U.S. Progress of alternative sintering approaches of inkjet-printed metal inks and their application for manufacturing of flexible electronic devices. *J. Mater. Chem. C* **2014**, *2*, 10232–10261. https://doi.org/10.1039/c4tc01820f.

74. Arapov, K.; Jaakkola, K.; Ermolov, V.; Bex, G.; Rubingh, E.; Haque, S.; Sandberg, H.; Abbel, R.; De With, G.; Friedrich, H.H. Graphene screen-printed radio-frequency identification devices on flexible substrates. *Phys. Status Solidi-Rapid Res. Lett.* **2016**, *10*, 812–818. https://doi.org/10.1002/pssr.201600330.

75. Secor, E.B.; Gao, T.Z.; Dos Santos, M.H.; Wallace, S.G.; Putz, K.W.; Hersam, M.C. Combustion-Assisted Photonic Annealing of Printable Graphene Inks via Exothermic Binders. *Acs Appl. Mater. Interfaces* **2017**, *9*, 29418–29423. https://doi.org/10.1021/acsami.7b07189.

76. Secor, E.B.; Ahn, B.Y.; Gao, T.Z.; Lewis, J.A.; Hersam, M.C. Rapid and Versatile Photonic annealing of Graphene Inks for Flexible Printed Electronics. *Adv. Mat.* **2015**, *27*, 6683. https://doi.org/10.1002/adma.201502866.

77. Sui, Y.K.; Hess-Dunning, A.; Wei, P.; Pentzer, E.; Sankaran, R.M.; Zorman, C.A. Electrically Conductive, Reduced Graphene Oxide Structures Fabricated by Inkjet Printing and Low Temperature Plasma Reduction. *Adv. Mat. Tech.* **2019**, *4*, 1900834. https://doi.org/10.1002/admt.201900834.

78. Pei, L.M.; Li, Y.F. Rapid and efficient intense pulsed light reduction of graphene oxide inks for flexible printed electronics. *RSC Adv.*, **2017**, *7*, 51711–51720. https://doi.org/10.1039/C7RA10416B.

79. McManus, D.; Vranic, S.; Withers, F.; Sanchez-Romaguera, V.; Macucci, M.; Yang, H.; Sorrentino, R.; Parvez, K.; Son, S.-K.; Iannaccone, G.; et al. Water-based and biocompatible 2D crystal inks for all-inkjet-printed heterostructures. *Nature Nanotech.* **2017**, *12*, 343–350. https://doi.org/10.1038/nnano.2016.281.

80. Romagnoli, M.; Lassinantti Gualtieri, M.; Cannio, M.; Barbieri, F.; Giovanardi, R. Preparation of an aqueous graphitic ink for thermal drop-on-demand inkjet printing. *Mat. Chem. Phys.* **2016**, *182*, 263–271. https://doi.org/10.1016/j.matchemphys.2016.07.031.

7.2. Appendix II – Supplementary information for Publication 1

Supplementary information for the publication:

Conductive Inks Based on Melamine Intercalated Graphene Nanosheets for Inkjet Printed Flexible Electronics

Magdalena Kralj[1,*], Sara Krivačić[2,*], Irena Ivanišević[2], Marko Zubak[2], Antonio Supina[3], Marijan Marciuš[4], Ivan Halasz[1] and Petar Kassal[2]

[1] Division of Physical Chemistry, Ruđer Bošković Institute, Bijenička cesta 54, 10000 Zagreb, Croatia

[2] Faculty of Chemical Engineering and Technology, University of Zagreb, Trg Marka Marulića 19, 10000 Zagreb, Croatia

[3] Institute of Physics, Bijenička cesta 46, 10000 Zagreb, Croatia

[4] Division of Materials Chemistry, Ruđer Bošković Institute, Bijenička cesta 54, 10000 Zagreb, Croatia

S1. Preparation and Characterization of M–GNS Inks

Stability of the M-GNS was tested in several solvents: redistilled water (with and without stabilizers), ethanol (96 wt.%) (with and without stabilizers), terpineol (without stabilizers), as well as their mixtures. The stability of such formulations was visually examined. As shown in Figure S1., the stability against the reaggregation and particle setting is very low for pure water and terpineol without stabilizers. The selected Solsperse stabilizers can be used with polar (e.g. water and alcohol) solvents and they were not soluble in terpineol so all formulations with terpineol were discarded. Generally, stability of the ink formulation decreased upon a decrease in the used solvent polarity. While purely water-based inks with stabilizers are stable, their surface tension is too high for successful printing and wetting of the substrate. On the other hand, purely ethanol-based inks evaporate during printing (due to their low boiling points) which caused nozzle clogging and print failure. Ultimately, a formulation consisting of EtOH:H$_2$O:EG = 0.50:0.45:0.05 by volume was selected based on the ink stability and rheological properties. The droplet formation behavior can be roughly predicted by the dimensionless parameter Z, which is defined in the main text. The determined physical properties of the printed M-GNS ink include: surface tension, γ = 31.67 mN/m; viscosity, η = 3.26 mPa s; and density, ρ = 0.9373 g/mL. Thus, the calculated Z-value corresponds to 7.7. Absorbance spectra of different ink components are given in Figure S2.
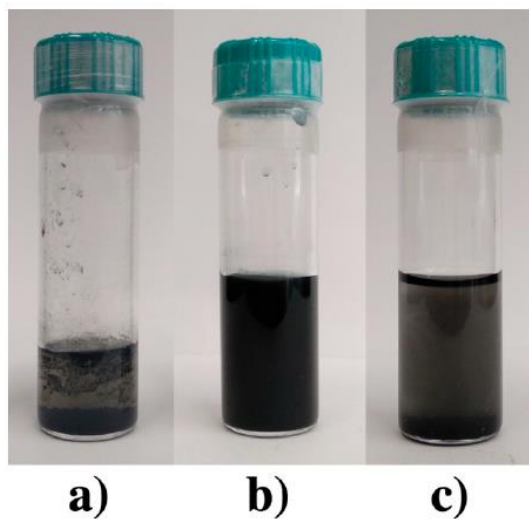
Figure S1. a) Water-based formulation without stabilizers (γ(MGNs) = 3 mg/mL), 6 days after preparation; **b)** water-based formulation with stabilizers (γ(MGNs) = 3 mg/mL), 7 days after preparation; **c)** terpineol-based formulation without stabilizers (γ(MGNs) = 1 mg/mL), 5 days after preparation.
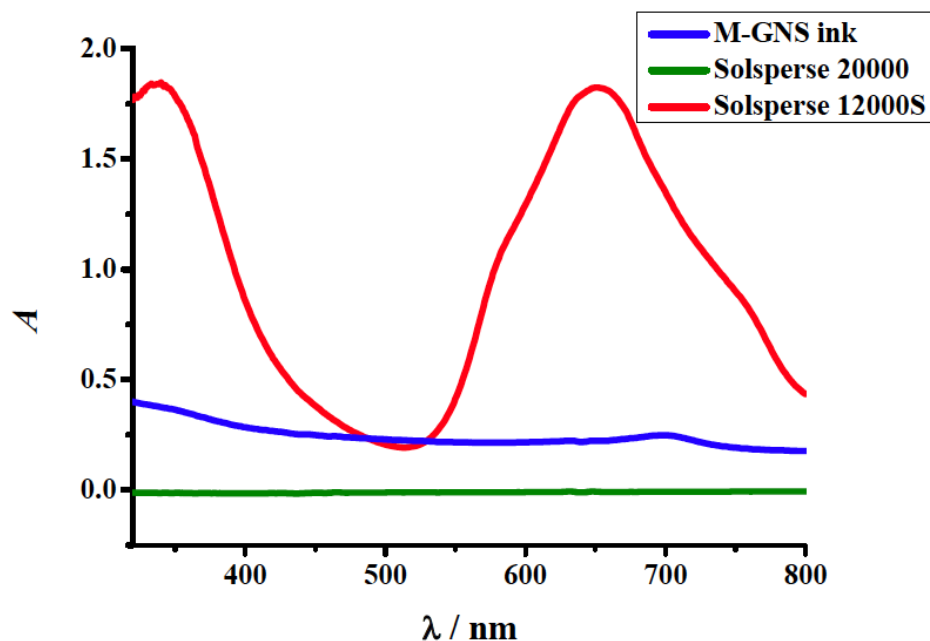
Figure S2. Absorption spectra of stabilizers and ink formulation. Both stabilizers were measured at the concentration as in M–GNS ink; the ink formulation was diluted 100 times.

S2. Inkjet Printing and Post–Print Processing

By determining an appropriate waveform and voltage, the jetting of a low viscosity ink was successfully performed. The printing resolution, determined by the drop spacing (DS), is governed by the overlapping of drops on the substrate. The DS optimization aims to enable just enough overlap to form the conductive lines, i.e. to avoid severe overlapping that could cause merging of the droplets, slower evaporation of the solvent, and consequently, the appearance of the coffee ring effect [1] and inhomogeneous deposits. The ethanol-water-EG based ink is suitable for low energy consuming processes firstly, due to its low viscosity, cartridge heating is completely unnecessary, and secondly, the ink's relatively low boiling point minimizes the prerequisite for high temperature platen heating. All printing parameters are given in Table S1. Unsuccessful printing of an IPA : H_2O based formulation, which did not show adequate wetting of the substrate is shown in Figure S3, for reference.

Table S1. The optimized printing parameters of M-GNS ink on the PET and PI substrates.

Voltage	9 V
Frequency	10 kHz
DS	5 µm
Cartridge height	1 mm
Cartridge temperature	32.5 °C
Platen temperature	55 °C
Number of overprints	10
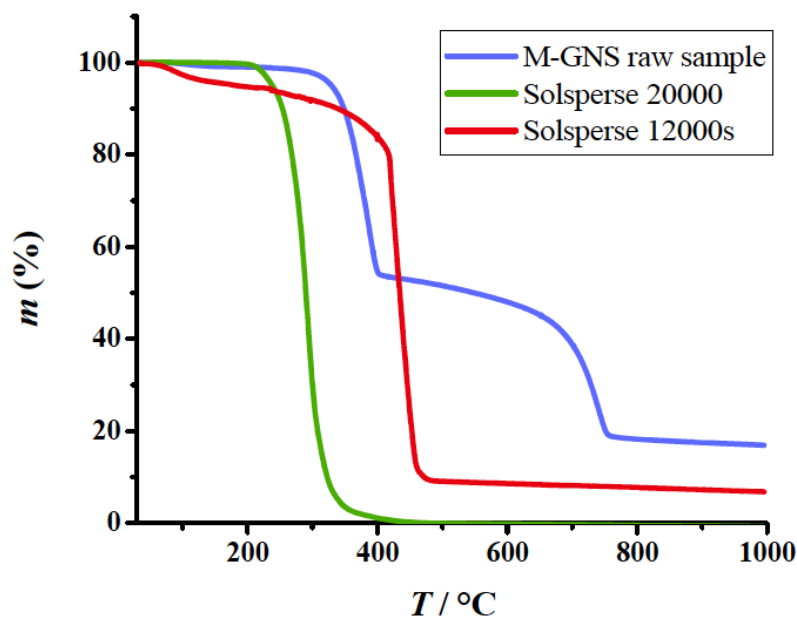
Figure S4. Thermogravimetric analysis (TGA) curve showing the mass loss profile of M-GNS (blue), and hyperdispersants Solsperse 20,000 (green) and Solsperse 12,000S (red).

Complete thermal decomposition of Solsperse 20,000 was observed in the range 180–450 °C. In addition, SOLSPERSE 12,000S decomposition also takes place in two stages. The first stage of the decomposition takes place from room temperature to 180 °C and is associated with moisture removal, mainly associated with evaporation of water content that is present in SOLSPERSE 12,000S. The second stage was observed in the temperature range 180–490 °C, corresponding to the complete decomposition of the stabilizing agent.
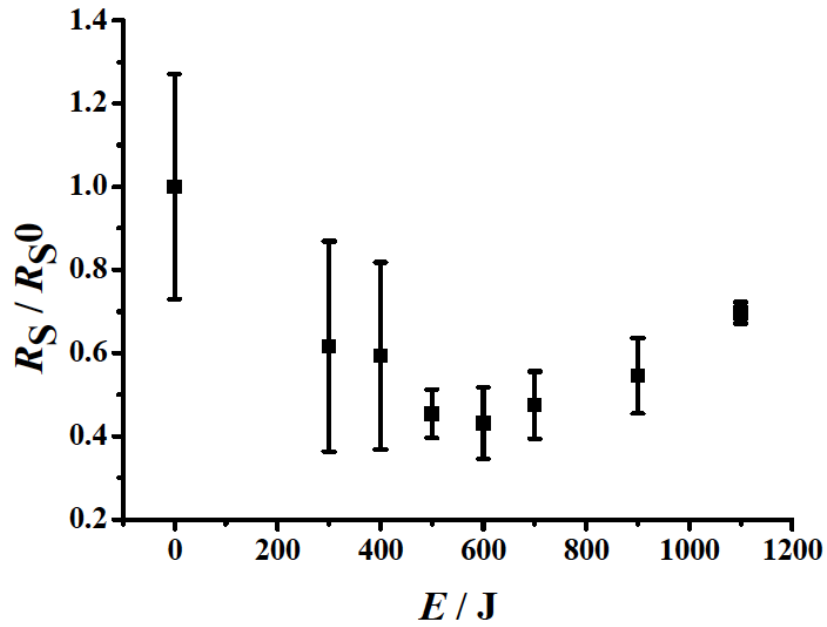
Figure S5. The normalized sheet resistance of printed 8 × 8 mm squares upon irradiation by IPL of different energies at 2500 V lamp voltage. Error bars represent one standard deviation ($n = 6$).

Table S2. An overview of relevant literature in the period from 2015 up to date. GO, Graphene oxide; RGO, Reduced graphene oxide; CB, Carbon black; M-GNS, Melamine-intercalated graphene nanosheets; MLG, Multilayered graphene; EG, Ethylene glycol; EtOH, Ethanol; D-H2O, Deionized water; NMP, N-Methyl-2-pyrrolidone; PG, Propylene glycol; IPA, Isopropyl alcohol, MEG, mono-ethylene glycol; PET, Poly(ethylene terephtalat); PI, Polyimide.

Ref.	Nanomaterial	Concentration of Nanomaterial	Solvent	Number of Layers	Substrate	Processing	Resistance
[39]	RGO and CB	4.31 mg/mL	EtOH, ethanediol, propanetriol, D-H2O	4	glossy photo paper	thermal annealing at 100 °C, for 30 min	20 kΩ/□
[31]	graphene	3.32 mg/mL	NMP	6	PET	not specified	173 kΩ/□
[76]	graphene	20 mg/mL	85% cyclohexanone; 15% terpineol	8	PET foils	IPL	25 Ω/□
[37]	graphene	3.2 mg/mL	EG	10	plastic foil	thermal annealing ~ 350 ºC for 150 min	260 Ω/□
[77]	GO	5 mg/mL	H2O:EG = 1:1	10	photo paper	plasma treatment for 120 min	2 kΩ/□
this work	**M-GNS**	**2 mg/mL**	EtOH:H2O:EG = 50:45:5	**10**	**PI**	**thermal annealing and IPL**	**5 kΩ/□**
[31]	graphene	0.62 mg/mL	EtOH:H2O = 1:1	12	PET	not specified	75 kΩ/□
this work	**M-GNS**	**2 mg/mL**		**20**	**PI**		**726.01 Ω/□**

113

			EtOH:H$_2$O:EG = 50:45:5			thermal annealing and IPL	
[78]	GO	4 mg/mL	D-H$_2$O:EtOH:EG = 1:1:1	20	PET	IPL	760.4 Ω/□
[35]	MLG	3.5 mg mL^{-1}	85% cyclohexanone; 15% terpineol	25	PI sheets	thermal annealing at 250 and 350 °C	1.60 kΩ/sq
[35]	MLG	3.5 mg mL^{-1}	85% cyclohexanone; 15% terpineol	30	PI sheets	thermal annealing at 250 and 350 °C	0.89 kΩ/sq
[79]	graphene	3 mg/mL	H$_2$O:PG=10:1	40	paper	thermal annealing	1 kΩ/□
[36]	graphene	2.25 mg mL^{-1}	H$_2$O	50	PEL paper	vacuum thermal annealing at 100 °C	1.2 ± 0.2 kΩ/sq
[80]	graphene	0.3 mg/mL	D-H$_2$O, IPA, MEG	60	photo paper	250 °C, 9 h	266.67 Ω/□

References

31 Capasso, A.; Castillo, A.D.R.; Sun, H.; Ansaldo, A.; Pellegrini, V.; Bonaccorso, F. Ink-jet printing of graphene for flexible electronics: An environmentally-friendly approach. *Solid State Commun.* **2015**, *224*, 53–63. https://doi.org/10.1016/j.ssc.2015.08.011.

35 Pandhi, T.; Cornwell, C.; Fujimoto, K.; Barnes, P.; Cox, J.; Xiong, H.; Davis, P.H.; Subbaraman, H.; Koehne, J.E.; Estrada, D. Fully inkjet-printed multilayered graphene-based flexible electrodes for repeatable electrochemical response. *Rsc Adv.* **2020**, *10*, 38205–38219. https://doi.org/10.1039/d0ra04786d.

36 Parvez, K.; Worsley, R.; Alieva, A.; Felten, A.; Casiraghi, C. Water-based and inkjet printable inks made by electrochemically exfoliated graphene. *Carbon* **2019**, *149*, 213–221. https://doi.org/10.1016/j.carbon.2019.04.047.

37 Majee, S.; Song, M.; Zhang, S.-L.; Zhang, Z.-B. Scalable inkjet printing of shear-exfoliated graphene transparent conductive films. *Carbon* **2016**, *102*, 51–57. https://doi.org/10.1016/j.carbon.2016.02.013.

39 Ji, A.; Chen, Y.; Wang, X.; Xu, C. Inkjet printed flexible electronics on paper substrate with reduced graphene oxide/carbon black ink. *J. Mater. Sci.-Mater. Electron.* **2018**, *29*, 13032–13042. https://doi.org/10.1007/s10854-018-9425-1.

76 Secor, E.B.; Ahn, B.Y.; Gao, T.Z.; Lewis, J.A.; Hersam, M.C. Rapid and Versatile Photonic annealing of Graphene Inks for Flexible Printed Electronics. *Adv. Mat.* **2015**, *27*, 6683. https://doi.org/10.1002/adma.201502866

77 Sui, Y.K.; Hess-Dunning, A.; Wei, P.; Pentzer, E.; Sankaran, R.M.; Zorman, C.A. Electrically Conductive, Reduced Graphene Oxide Structures Fabricated by Inkjet Printing and Low Temperature Plasma Reduction. *Adv. Mat. Tech.* **2019**, *4*, 1900834. https://doi.org/10.1002/admt.201900834.

78 Pei, L.M.; Li, Y.F. Rapid and efficient intense pulsed light reduction of graphene oxide inks for flexible printed electronics. *RSC Adv.*, **2017**, *7*, 51711–51720. https://doi.org/10.1039/C7RA10416B

79 McManus, D.; Vranic, S.; Withers, F.; Sanchez-Romaguera, V.; Macucci, M.; Yang, H.; Sorrentino, R.; Parvez, K. Son, S.-K.; Iannaccone, G.; et al. Water-based and biocompatible 2D crystal inks for all-inkjet-printed heterostructures. *Nature Nanotech.* **2017**, *12*, 343–350. https://doi.org/10.1038/nnano.2016.281.

80 Romagnoli, M.; Lassinantti Gualtieri, M.; Cannio, M.; Barbieri, F.; Giovanardi, R. Preparation of an aqueous graphitic ink for thermal drop-on-demand inkjet printing. *Mat. Chem. Phys.* **2016**, *182*, 263–271. https://doi.org/10.1016/j.matchemphys.2016.07.031.

7.3. Appendix III – Manuscript of Publication 2

Flexible ammonium ion-selective electrode based on inkjet-printed graphene solid contact

Sara Krivačić[1], Željka Boček[1], Marko Zubak[1], Vedran Kojić[2,3] and Petar Kassal[1]

[1]   Faculty of Chemical Engineering and Technology, University of Zagreb, Trg Marka Marulića 19, 10000 Zagreb, Croatia

[2]   Ruđer Bošković Institute, Bijenička cesta 54, 10000 Zagreb, Croatia

[3]   HIS d.o.o., Donja Višnjica 61D, 42255, Donja Višnjica, Croatia

Author contribution:

S.K: formal analysis, investigation, methodology, validation, writing – original draft; **Ž.B.**: formal analysis, investigation, writing – original draft; **M.Z.**: formal analysis, investigation; **V.K.**: resources, investigation, validation; **P.K.**: conceptualization, funding acquisition, methodology, project administration, supervision, writing – review and editing.

Flexible ammonium ion-selective electrode based on inkjet-printed graphene solid contact

Sara Krivačić [a], Željka Boček [a], Marko Zubak [a], Vedran Kojić [b,c], Petar Kassal [a,*]

[a] *University of Zagreb, Faculty of Chemical Engineering & Technology, Trg Marka Marulića 19, 10000, Zagreb, Croatia*
[b] *Ruđer Bošković Institute, Bijenička cesta 54, 10000, Zagreb, Croatia*
[c] *HIS d.o.o., Donja Višnjica 61D, 42255, Donja Višnjica, Croatia*

ARTICLE INFO

ABSTRACT

Miniaturization and mass-production of potentiometric sensor systems is paving the way towards distributed environmental sensing, on-body measurements and industrial process monitoring. Inkjet printing is gaining popularity as a highly adaptable and scalable production technique. Presented here is a scalable and low-cost route for flexible solid-contact ammonium ion-selective electrode fabrication by inkjet printing. Utilization of inkjet-printed melamine-intercalated graphene nanosheets as the solid-contact material significantly improved charge transport, while evading the detrimental water-layer formation. External polarization was investigated as a means of improving the inter-electrode reproducibility: the standard deviations of E^0 values were reduced after electrode polarization, the linear region of the response was extended to the range 10^{-1}–10^{-6} M of NH_4Cl and LODs reduced to 0.88 ± 0.17 μM. Finally, we have shown that the electrodes are adequate for measurements in a complex real sample: ammonium concentration was determined in landfill leachate water, with less than 4 % deviation from the reference method.

1. Introduction

Recent advances in open circuit potentiometry are driven by the requirements of emerging on-site analyses for clinical, environmental, and industrial process purposes [1]. Replacing the traditionally used internal solution-based transducers with solid-contact materials solved the inconveniences regarding the internal solution: changes in its composition, concentration and volume, limited transport, and scope of application of such electrodes. Thus, the ongoing trends in potentiometric sensor development were enabled [2]. Equally to the liquid counterpart, stable and reversible ion-to-electron transduction establishes the stability and credibility of the response of solid-contact ion-selective electrodes (SC-ISEs). This is achieved by good adhesion of the solid-contact material between the ion-selective membrane and electrically conducting material.

A broad range of solid-contact materials is available for implementation as the transducing layer in SC-ISEs, and these provide reversible ion-to-electron transduction (and thus a stable response) via different mechanisms [3]. Popular conducting polymer-based solid contacts are most often deposited on an electrically conducting substrate by electrodeposition, a step that complicates mass-fabrication intentions

[4]. On the other hand, carbon nanomaterials have recently attracted increasing interest as solid contacts in ion-selective electrodes, due to their high specific surface area and hydrophobic character [5]. Additionally, unlike conductive polymers, signal transduction is not affected by pH conditions [6], light, and the presence of oxygen and CO_2 [7]. Carbon nanomaterials are generally produced by liquid-phase exfoliation [8], making them compatible with a wide spectrum of additive electrode production techniques [9]. Among these materials, graphene stands out due to its excellent processability [10].

The Solid-contact electrode design enabled both miniaturization and mass production. To reduce the costs of production, printing techniques have emerged from the traditional environment of the graphics industry [11]. Among these, drop-on-demand inkjet printing presents the most promising solution for low-material consumption and mass production of electrochemical sensors [12]. Inkjet printing is a digitally controlled, contactless material deposition technology based on piezoelectrically or thermally driven ejection of picolitre drops of ink [13]. Compared to screen-printing, which currently dominates the arena of production of commercially available electrochemical sensors, inkjet printing produces higher resolution patterns on flexible and fragile substrates with less waste [14]. Maskless and digitally controlled, it is well-adopted for

---

device prototyping since the determined design can be easily altered in between the printing sessions.

Despite the convincing advantages, the scarcity of commercially available inkjet-printed electrochemical sensors is caused by the challenges in ink formulation. Being the bottleneck of the inkjet printing process, ink formulation is governed by considering the compatibility of the ink's physical properties with the print head requirements [15]. The fluid characteristics that must be considered are the formulation's viscosity, density, surface tension, and the size of the suspended nanoparticles of the functional material [16]. Finally, the ink-substrate interactions govern the quality of the printed pattern. These include the prevention of particle sedimentation at the edges of the printed pattern, e.g., coffee-ring effect [17], and adhesion of the ink to the substrate, which is crucial for sensor flexibility. As a final step, post-printing processing with the aim of solvents and stabilizers removal is necessary. Traditionally employed thermal annealing is not suitable for temperature-sensitive polymeric and paper substrates, and novel processing means are being sought [18]. Among these low-temperature sintering approaches, intense pulsed light (IPL) annealing is a photo-thermal technique that uses very short high-energy pulses of visible light. Thereby, it diminishes the thermal stress on the sensitive polymeric substrate, making it highly compatible with printed flexible electronics [19].

Although inkjet-printable inks based on graphene [20–22] and carbon nanotubes [23–26] have been presented, inkjet printing (especially of carbon nanomaterials) has been scarcely used in the development of SC-ISEs. Nitrate-selective electrodes were prepared by drop-casting the ion-selective membrane (ISM) on inkjet-printed gold [27] or silver [28] electrodes on flexible polymeric substrates. Iridium oxide nanoparticle-based ink was formulated and inkjet printed on a PET substrate giving flexible pH sensors based on reversible redox process on the electrode surface [29]. In another example, potentiometric pH sensors were prepared by inkjet printing a gold nanoparticle ink and electropolymerizing PEDOT–GOx films [30]. Potassium-selective electrodes were prepared by inkjet printing gold nanoparticle and PEDOT:PSS ink on paper substrates and drop-casting the ISM [31]. Regarding carbon nanomaterials as the solid contact, potentiometric potassium determination was also enabled by inkjet printing graphene ink on silicon wafers and drop-casting the K-ISM [32]. The authors have shown that thermal annealing at a profoundly high temperature of 950 °C gives electrodes with the best features in terms of electrical conductivity and electrochemical sensing performances. However, this approach is not applicable to heat-sensitive flexible substrates. A fully inkjet printed paper device with potassium and sodium selective electrodes was fabricated by printing graphene-PEDOT:PSS composite ink and ISMs [33]. The composite ink was prepared by adding the graphene nanopowder into a commercially available PEDOT:PSS aqueous solution. It was shown that the addition of graphene to the PEDOT:PSS ink presents a good strategy for avoiding the accumulation of water at the interface with the ion-selective membrane, provides high-surface area and improved conductivity, compared to pure PEDOT:PSS. However, the authors did not compare the properties of the composite formulation with a purely graphene-based formulation.

Chemically, ammonia in water consists of two species: ammonium ion (NH_4^+) and associated ammonia (NH_3). The total concentration of the two species is denoted as total ammonia nitrogen (TAN) [34]. Naturally occurring ammonia, formed by diazotrophic microbes, the decomposition of dead organisms in the aquatic and terrestrial environments, and as a part of fish metabolism, is present in relatively low concentrations and hence not harmful. However, ammonia pollution from agriculture and municipal waste discharges causes acidification and eutrophication of ecosystems, thus strongly violating natural biodiversity [35]. The determination of TAN in water is a vital parameter in aquatic environment monitoring and many methods have been developed and routinely used [36]. Among them, spectrophotometric, fluorometric and electrochemical methods are most used.

With the advances in the mass production of miniaturized potentiometric sensors, decentralized, on-site determination of TAN could become a reality [37]. Proving that, there is already a few examples of all-solid-state ammonium-selective electrodes, as shown in Table S1 of the Supplementary material. In light of this, we present here the route for solid-contact ammonium-selective electrode production by inkjet printing. As the solid contact, we have inkjet printed a melamine-intercalated graphene nanosheet functional ink to develop low-cost flexible ion-selective electrodes.

2. Materials and methods

Chemicals. Throughout this work, two silver inks for inkjet printing were used: JS-B25HV, purchased from NovaCentrix, USA, and DM-SIJ-3201, obtained from Dycotec, UK. Graphite flakes with 200–300 μm particle sizes were purchased from Graphenea, Spain, and melamine from Alfa Aesar, Germany. Solsperse stabilizers, Solsperse 20 000 and Solsperse 12 000S were obtained from Lubrizol, USA. Ammonium ionophore I (nonactin, 95.0 wt%, HPLC grade), bis(2-ethylhexyl) sebacate (DOS), tetrahydrofuran (THF, 99.5 % wt), and ethylene-glycol were purchased from Sigma Aldrich, Switzerland. High-molar mass poly (vinyl chloride) (PVC) was obtained from Fluka, Switzerland. Ammonium chloride, potassium chloride, sodium chloride, calcium chloride, sodium dihydrogen phosphate dihydrate, oxalic acid dihydrate, sodium sulphate, uric acid and urea, all pro-analysis grade, were purchased from Kemika, Croatia. Disodium phosphate was purchased from Acros Organics, USA. Ethanol, 99.98 %, pro-analysis grade was purchased from GramMol, Croatia. Potassium chloride was obtained from Alkaloid, North Macedonia. All solutions were prepared using double distilled deionized water (conductivity 0.060 μS cm, MiliQ, Millipore, USA).

MGNS ink preparation. Melamine-intercalated graphene (MGNS) ink was prepared according to our previous work [38]. Briefly, 2 mg mL^{-1} of single- and double-layer melamine intercalated graphene nanosheets (M-GNS) obtained by neat grinding of graphite flakes in a ball mill were dispersed using a Sonopuls Serie 2000.2 tip-sonicator in a mixture of ethanol: water: ethylene glycol = 0.50: 0.45: 0.05 by volume; with the addition of 0.36 mg mL^{-1} of Solsperse 20 000 and 0.04 mg mL^{-1} of Solsperse 12 000S stabilizers. Prior to printing, the ink was homogenized for 60 s using Sonopuls Serie 2000.2 tip sonicator.

Inkjet printing of flexible electrodes and solid contact. The electrode layout was designed in CorelDRAW software. Electrical contacts were produced by inkjet printing silver ink using a Gateway inkjet printer (China) with Epson XP600 printhead, on polyimide substrates, $t = 0.075$ mm (Kapton HN, DuPont, USA). The silver ink was dried overnight at room temperature and cured with a single pulse light at 400 J and 2500 V using XENON X1100, XENON Corporation, USA intense pulsed light (IPL). The circular working area of the electrodes, $d = 6$ mm, was constructed by inkjet printing the MGNS ink either in 50 (for results presented in Section 3.3.) or 100 layers (for all other results). The electrodes were thermally annealed at 300 °C for 1 h. Finally, the electrodes were photonically treated using IPL with a single pulse of initial voltage 2500 V and energy 700 J [38].

Morphological characterization. Morphology and elemental composition of the surface were investigated using field emission gun scanning electron microscope (FEG-SEM) JEOL model 7000F (Japan) operating at 5 or 10 kV. FEG-SEM is equipped with energy dispersive X-ray analyser (Oxford Instruments EDS/INCA 350, Japan) attached to the microscope which was used for Energy-Dispersive X-ray Spectroscopy. Spectra were recorded at 15 kV accelerating voltage. Secondary electrons detector was used for material analysis, combined with EDS obtained at the chosen area of the sample.

Ammonium ion-selective electrode preparation. The ammonium ion-selective membrane for the functionalization of the inkjet-printed solid-contact electrodes was prepared in 3 mL of THF by weighing 1 % ionophore nonactin, 32.5 % PVC and 66.5 % DOS, a total of 299.2 mg. Four aliquots (30.0 μL) of the membrane cocktail were drop-cast by

117

pipette on the working electrode area (limited to 6 mm diameter with a polypropylene ring) and left to dry overnight. The prepared electrodes were designated as SC-ISE. To determine the influence of MGNS solid contact on the electrochemical characteristics of the inkjet-printed electrodes, the ammonium-selective membrane was drop-cast in the same manner directly onto the inkjet-printed silver electrical lines (DM-SIJ-3201 ink), making the coated-wire electrode configuration (CWE). Before electrochemical characterization, the electrodes were conditioned in a 10 mM primary ion solution for 3 h.

Electroanalytical characterization. All the electroanalytical measurements were performed at room temperature. Potentiometric measurements were done with a Lawson EMF6 Interface potentiometer (Lawson Labs, Inc., Philadelphia, USA) in a two-electrode electrochemical setup, using SC-ISE or CWE as working electrode, and conventional double junction Ag|AgCl|3 M KCl|0.2 M NaNO$_3$ reference electrode. The analytical characteristics of the developed SC-ISEs for ammonium sensing in deionized water were carefully examined by performing the calibration tests in the NH$_4$Cl solutions within the concentration range 10^{-8}–10^{-1} mol dm^{-3}. Interference tests were performed utilizing the separate solutions method (SSM). Briefly, the developed electrodes were calibrated in the following salt solutions, within the above-mentioned concentration range; KCl, NaCl, CaCl$_2$, and MgCl$_2$. Finally, a water-layer test (WLT) was performed: the electrodes were first kept in 10 mM NH4Cl solution for 5 h, then in 10 mM NaCl for 2 h, and finally returned to 10 mM NH4Cl for an additional 8 h. For the estimation of redox buffer.

The effect of redox interferents was investigated by recording the open circuit potential in NH$_4^+$ solutions having a constant concentration of 10 mM and 1 mM hexacyanoferrate (II/III) redox couple at different Ox/Red ratios (1:9, 1:1 and 9:1).

Electrochemical impedance spectroscopy (EIS) measurements were performed using PalmSens4 potentiostat (PalmSens, Houten, the Netherlands) coupled to a personal computer. The EIS measurements were done in 0.1 M NH$_4$Cl solution, in a three-electrode electrochemical cell, with either the CWE or SC-ISE as working, Ag|AgCl|3 M KCl|0.2 M NaNO3 reference, and Pt auxiliary electrode, at the open circuit potential within the frequency range 100 kHz–10 mHz using 10 mV potential amplitude.

Ammonium sensing in real samples. The composition of artificial urine sample was slightly modified from Ref. [39]. Namely, it was prepared by dissolving the following salts in 100 mL of deionized water: 0.1700 g Na$_2$SO$_4$, 0.0250 g C$_5$H$_4$N$_4$O$_3$, 0.0720 g Na$_3$C$_6$H$_5$O$_7$ • 2H$_2$O, 1.5000 g CH$_4$N$_2$O, 0.2308 g KCl, 0.1756 g NaCl, 0.0185 g CaCl$_2$, 0.1266 g NH$_4$Cl, 0.0035 g C$_2$H$_2$O$_4$ • 2H$_2$O, 0.0021 g KOH, 0.1082 g MgSO$_4$ • 7H$_2$O, 0.2912 g NaH$_2$PO$_4$ • 2H$_2$O, and 0.0831 g Na$_2$HPO$_4$ • 2H$_2$O. Ammonium sensing was performed by direct potentiometry.

The leachate water was taken from the leachate collector basins on the landfill site. For the reference method, the leachate sample was mixed and diluted with demineralized water at a ratio of 4 mL of leachate with 50 mL of water and stirred for 30 min 200 μL of the diluted sample was placed in a cuvette of the test kit (HACH LANGE LCK 303 ammonia test, concentration range 2.5–60 mg dm^{-3} NH$_4$–N), mixed and left to react for 15 min. This was performed three times. Each cuvette was analysed on the DR 1900 HACH LANGE spectrophotometer to determine the ammonium ion concentration after dilution, after which the initial concentration of ammonia ion concentration in leachate was calculated. The ammonium-selective SC-ISE was tested with the same leachate samples. The ammonium-selective inkjet-printed electrodes were calibrated in NH$_4$Cl standard solutions, and the three-point standard addition method was used for the determination of c(NH$_4$). A 10 mL leachate sample was diluted 1:10 in phosphate buffer, pH = 5, prepared by mixing 0.067 mol dm^{-3} of sodium dihydrogen phosphate dihydrate and 0.067 mol dm^{-3} of disodium hydrogenphosphate. A 10 mL aliquot of the diluted sample was placed in a beaker with SC-ISE and the potential was measured. Then, 100 μL of 1 M NH$_4$Cl standard solution was added to the sample and the potential was measured. This

final step was repeated three times to calculate the ammonium ion concentration. The detection in the real sample was performed with 3 different SC-ISEs.

3. Results and discussion

3.1. Flexible SC-ISE fabrication by inkjet printing

Despite the many advantages of inkjet printing – it is a fast, scalable, low-cost, environmentally friendly technique in the production of electrochemical sensing systems [12] – inkjet printed electrochemical sensors remain underdeveloped due to challenges associated with functional ink formulation. Developing the ink for inkjet printing should be tailored to the requirements of the printhead, to enable ejection of single droplets from the printhead nozzle in a controlled manner. The fluid characteristics that must be considered are the formulation's viscosity, density, surface tension, and the size of the suspended nanoparticles of the functional material [13,15]. Herein, we investigated the possibility of incorporating our previously developed graphene-based functional ink (MGNS-ink [38]) in the architecture of solid-contact ion-selective electrodes. Based on the determined fluid characteristics ($\eta = 3.26$ mPa s, $\gamma = 31.67$ mN m^{-1}, $\rho = 0.9373$ g mL^{-1}), the MGNS-ink was found to be compatible with the printhead and was successfully inkjet printed on top of previously inkjet-printed silver lines. The complete electrode production process adopted in this work is schematically shown in Fig. 1A.

Before functionalizing the electrodes with an ion-selective membrane, processing of the inkjet-printed patterns was performed by the combination of thermal annealing and intense pulsed light (IPL). This was done to remove the additives that were initially included in the ink composition (for the purpose of prolonging the stability of the functional material against agglomeration) and to increase the conductivity of the printed MGNS solid contacts. It was shown that IPL is very effective in processing of graphene-based materials due to their high absorption coefficient in the visible part of the spectrum [38,40,41]. The electrode morphology upon inkjet printing and the combination of annealing was characterized by SEM measurements. Fig. S1 shows the boundary of the Ag-conducting line and graphene ink overprint. Uniform distribution of the graphene solid contact over the silver electrode is visible from the low magnification image and EDX analysis. The higher magnification image (Fig. S1C) of the printed graphene nanosheets shows a thin lamellar structure and features on the 100 nm scale.

The final step in the production of the electrodes was their functionalization with an ion-selective membrane. Due to our printhead's compatibility with relatively low viscosity inks, the ammonium-selective membrane was drop-cast on top of IJP solid contacts by pipette.

3.2. Electrochemical impedance spectroscopy

EIS measurements give insight into the resistance changes of the inkjet-printed silver electrodes (CWE) upon the introduction of an MGNS solid-contact material. The impedance spectra of both electrode configurations show a typical high-frequency semi-circle resulting from bulk ion-selective membrane resistance (R_{bulk}) linked to the contact resistance between the electrode surface and ion-selective membrane [42]. As depicted in Fig. S2A, incorporation of the MGNS layer lowers the R_{bulk} from 7.31 MΩ for a CWE to 4.30 MΩ for a SC-ISE. The low-frequency part of the EIS spectra depicts the ion-to-electron transduction processes. Herein, the low-frequency component is depicted as Bode spectra (Fig. S2B), where it is clearly shown that the low-frequency impedance modulus, $|Z|$ decreases with the introduction of the MGNS layer [43,44]. The observed changes indicate that the introduction of the MGNS solid contact facilitates charge transfer between the ion-selective membrane and the electrode surface, making our inkjet printed MGNS ink a reliable solid contact for SC-ISEs [42,45,46].
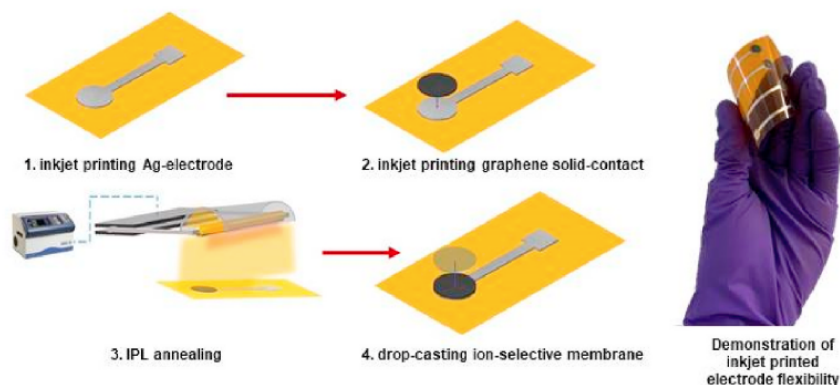
Fig. 1. (A) The schematic representation of IJP-based fabrication steps for the flexible solid-contact ion-selective electrode production; (B) the demonstration of the flexibility of the inkjet printed electrodes.

3.3. Potentiometric response and selectivity

A single solid-contact ammonium-selective electrode was calibrated using open circuit potentiometry (OCP). Fig. 2 depicts the measured potential versus a ten-fold increase in the activity of the ammonium ions, where the sensitivity of the electrode is reported as the slope of the linear portion of the calibration curve. The average slope value of the three repeated measurements with one SC-ISE, within a linear concentration range of 10^{-4}–10^{-1} M, is 52.045 ± 0.525 mV dec^{-1} ($R^2 = 0.9976$). This is slightly lower than the ideal sensitivity of 59.2 mV dec^{-1} ($t = 25$ °C) for monovalent cation sensing. Such a sub-Nernstian response is often seen in practice, due to the intrinsic properties of the ISM affected by the optimization conditions, membrane materials, ionophores, and conditioning settings [3]. The lower detection limit (LOD) was calculated by the intersection of two slopes, giving the value of 25.1 μM. The determined sensing range and sensitivity of our SC-ISE are comparable to those found in the literature for ammonium-selective electrodes with graphene-based solid contacts [47–49].

Selectivity coefficients against several cationic interferents were calculated using the separate solutions method (SSM) [50,51]. The calibration curves of each interfering ions are given in the Supplementary, Fig. S3. Table 1 gives the results of SSM performed with the proposed electrodes and compared with the literature values for other ammonium-selective electrodes. The calculated selectivity coefficients are all lower than 10^{-1}, indicating high selectivity of the employed ionophore.
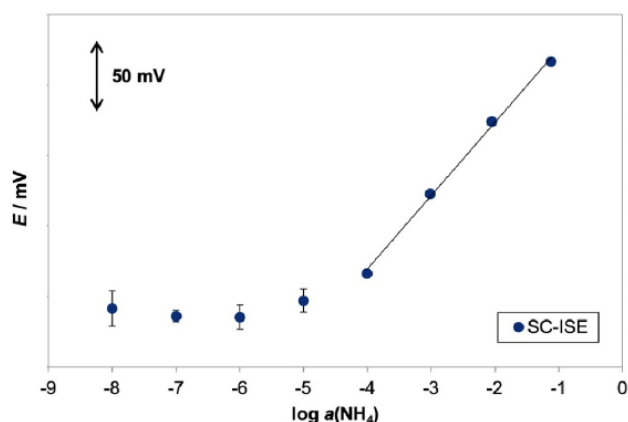
Table 1
Experimentally obtained selectivity values for this work and literature-found values for nonactin-based polymeric membranes.

$\log K^{pot}_{NH_4^+, J}$	This work	[52]	[53]	[54]	[49]
KCl	−1.03	−0.86	−0.68	−0.88	−1.8
NaCl	−2.85	−1.83	−2.28	−2.89	−2.9
CaCl$_2$	−3.93	−3.21	−2.59	−4.80	/
MgCl$_2$	−3.63	−3.78	−3.78	−5.50	/

3.4. Inter-electrode reproducibility

The emerging large-scale production protocols of single-use ion-selective electrodes have coined demands for "calibration-free" measures, which implies that only a few of the entire batches of the produced electrodes are calibrated. This requires exceptional inter-electrode reproducibility. The accepted figures of merit are reproducibility of the E^0 and slope values of the linear region of the calibration curve (expressed with their respective standard deviations), along with EMF drift which should be reduced during the expected duration of the measurement [3,55–57]. A batch of SC-ISEs was prepared and the inter-electrode potential reproducibility of three different electrodes was probed by potentiometric measurements in 10 mM NH$_4$Cl. Fig. 3A shows the initial conditioning of the three equally produced electrodes from the same batch. The potential range of the three electrodes after 3 h of conditioning was 19 mV (S.D. = 9.8 mV, $n = 3$), with a mean drift value of −0.393 mV/h.

In an attempt to improve these values, we externally polarized the SC-ISEs to 180 mV for 30 min. This prepolarization potential was chosen as the approximate potential value towards which the three electrodes were drifting [58]. It has been shown that differences between the E^0 values of the entire electrode batch can be annulated by carefully adjusting the ratio of the oxidized and reduced form of the redox active solid contact material through the application of external potential or current perturbation, and short-circuiting electrodes [58–61]. In addition to conductive polymers, this was recently conducted for TEMPO-functionalized multi-walled carbon nanotubes and highly hydrophobic TEMPO-functionalized EDOT [62,63]. During the active electrode polarization, primary ions are pushed through the bulk of the ISM and contact the solid-contact material. While this incorporation of primary ions helps in charging and discharging of conductive polymer-based solid-contact materials [4,61], enhancing the overall reproducibility parameters in carbon-based nanomaterials without well-defined redox active species is made possible owing to redox active impurities within the material [56] – in this case residual melamine and its condensation products.
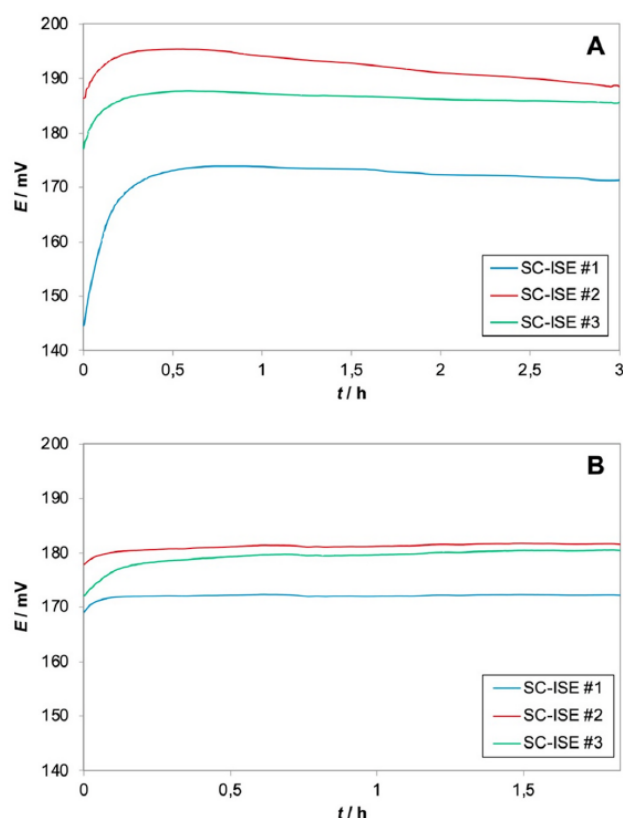

Fig. 2. Calibration curve for three repeated measurements with one ammonium-selective SC-ISE (50 overprints of MGNS ink).

Fig. 3. (A) The initial OCP measurement of MGNS-based NH$_4$-ISEs in 10 mM NH$_4$Cl and (B) after external polarization at 180 mV for 30 min in 10 mM NH$_4$Cl.

Fig. 4. The comparison between calibration curves obtained for $n = 3$ electrodes before (A) and after (B) applying the external polarization.

The positive effect of external polarization on the inter-electrode reproducibility and mid-term EMF stability can be seen in Fig. 3B: the potential range of the three electrodes was lowered to 9 mV (S.D. = 5.1 mV, $n = 3$), with a mean drift value of 0.103 mV/h.

Another positive outcome of external polarization on inter-electrode reproducibility can be clearly seen on calibration plots, Fig. 4. Unpolarized electrodes have very low linearity ($R^2 = 0.9432$), and an inflection point in the response is observed between low concentrations (10^{-5} to 10^{-3}) and high concentrations (10^{-3} to 10^{-1}) of the primary ion. In the low-concentration range, a super-Nernstian response (84.52 mV/pNH$_4$; $R^2 = 0.9822$) is observed, indicating a discrepancy between ion activities in the bulk of the membrane and at the phase boundary between the ISM and solution, i.e. the ongoing uptake of primary ions into the membrane phase [64,65]. At high concentrations of the primary ion, the membrane is highly saturated, and ion leakage tends to occur, causing the high-concentration sub-Nernstian response (36.289 mV/pNH$_4$; $R^2 = 0.9996$) [66].

It was previously stated that the undesired ion leakage can be reduced or eliminated by electrode polarization [67]. Indeed, after polarization, the SC-ISEs dynamic range was extended and can be expressed by a single linear equation with a slope of 55.594 ± 0.429 mV/pNH$_4$ ($R^2 = 0.9856$). The standard deviation of E^0 values for repeated measurements ($n = 3$) was significantly lowered from 23.97 mV for non-polarized SC-ISEs to 9.78 mV for externally polarized electrodes. These values can be further improved by incorporation of small molecule redox buffers, which is highly compatible with mass fabrication by inkjet printing. The widening of the electrodes' dynamic range from 10^{-1}–10^{-5} M to 10^{-1}–10^{-6} M, along with LOD lowered to 0.88 ± 0.17 µM further confirm the utility of external polarization on the analytical parameters of the developed electrodes. The obtained
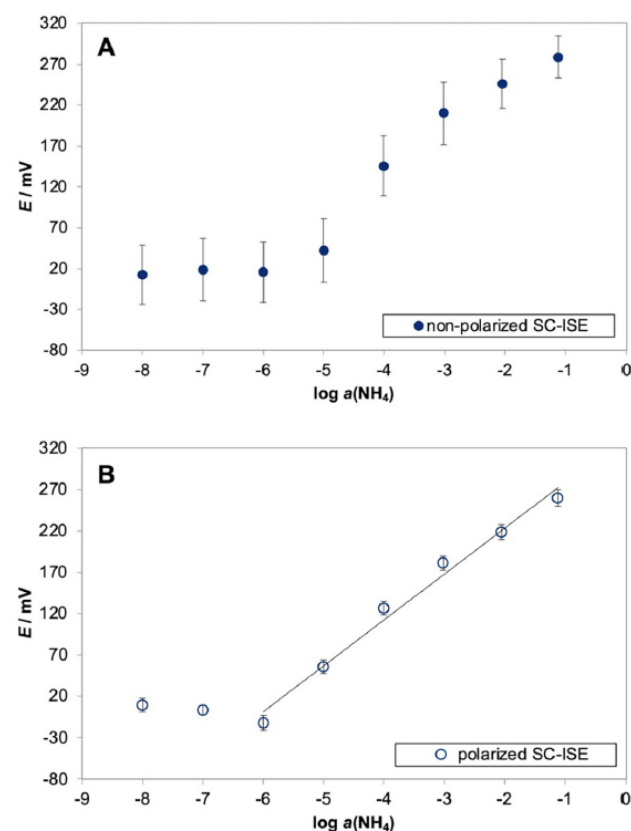
analytical parameters of the polarized inkjet printed SC-ISEs, are comparable or better than many similar carbon-based ammonium ion sensors found in the literature (Table S1).

3.5. Stability and reversibility

Another key factor in assessing the EMF stability of solid-contact ion-selective electrodes is investigating the possibility of formation of a thin aqueous layer between the electrically conducting substrate and ion-selective membrane [68]. The water layer can develop upon prolonged contact of the electrode with the aqueous sample, if the solid contact material is not sufficiently hydrophobic. It thus presents an undesirable process that disrupts the well-defined ion-to-electron transduction between the SC and ISM and introduces parallel processes that cause drifts to the measured EMF [55].

Herein, the response of SC-ISE and CWE was compared during prolonged measurements: the electrodes were firstly immersed in primary ion solution (NH$_4$Cl), then in interfering ion solution (NaCl) and finally again in NH$_4$Cl (all 10 mM aqueous solutions). As shown in Fig. 5A, both CWE and SC-ISE stabilize within the first 2 h of OCP measurement. Replacing the primary ion solution with the interfering ion, a sudden change in the measured OCP for both the electrodes reflects the selectivity towards ammonium ions. The OCP of a CWE measured in the interfering ion solution shows a pronounced positive drift of 16.02 mV/h. Replacing the solution back to the primary ion, a negative drift of −3.98 mV/h is observed. This behaviour clearly reflects the formation of a thin aqueous layer between the ISM and inkjet printed silver contact, as is common for coated wire electrodes [2]. Upon introducing the MGNS solid contact, the potential drift in both the interfering ion and primary solutions is largely reduced and we can assume no water layer is
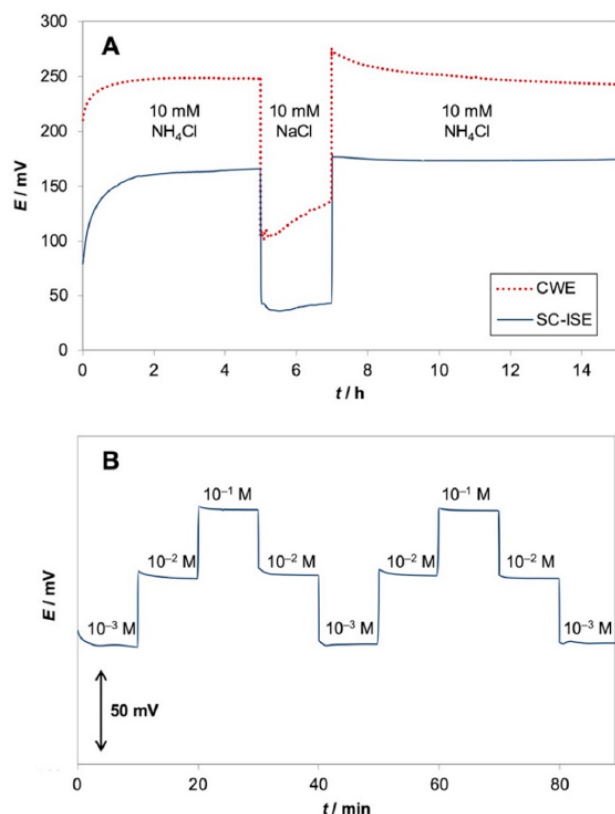
Fig. 5. (A) The comparison of water layer test on inkjet printed ammonium-selective electrode without (CWE) and with (SC-ISE) the MGNS-solid contact; (B) reversibility test with ammonium MGNS-ISE within 10^{-3} to 10^{-1} M range of NH$_4$Cl.

formed due to the MGNS hydrophobicity.

Maintaining the sensor signal stability and reversibility is an important request for the application in real environmental samples, where the ion concentrations often tend to fluctuate, especially during the prolonged measurements. Hence, the reversibility carry-over tests were performed by continuously monitoring OCP while repetitively cycling the concentration of standard solutions between 10^{-1} and 10^{-3} M. As seen in Fig. 5B, concluding the carry-over tests with 10^{-3} M NH$_4^+$ solution, the original EMF of 173 mV remained stable with 0.59 % relative standard deviation, indicating excellent reversibility and negligible hysteresis effect.

Another factor that could influence the stability of a sensor in real environment is the effect of the sample redox interferents. Fig. S4 shows the influence of the redox interferents on the EMF stability of the ammonium electrode. The potential was measured in a mixture of potassium ferricyanide and ferrocyanide, both at 1 mM in molar ratios 1:1, 1:9 and 9:1.). We found there is a negligible effect of the change in ferri-: ferro-ratios on the ISE potential (less than 1 mV for a 9 × change in ratio).

3.6. Ammonium sensing in real samples

A final proof-of-concept examination was to determine the validity of our sensors for ammonium-ion concentration measurements in real samples. Urine is an extremely valuable diagnostic biofluid, as it contains many clinically relevant ions and metabolites, among others ammonium. For the proof-of-concept testing, we adopted the artificial urine composition from Sarigul et al. [39]. Fully conditioned electrodes were first calibrated in a narrow concentration range (Fig. S5) and then

used for ammonium detection by direct potentiometry. The measured ammonium concentration in the artificial urine sample was 22.36 mM, giving an error of 4.0 % to the known concentration of ammonium ions in the sample.

Next, we determined the validity of our sensors for ammonium-ion concentration measurements in landfill leachate water. Fully conditioned electrodes were first calibrated (Fig. 6A) and then used for ammonium detection in buffered samples by the three-point standard addition method. The potential of the electrodes was measured before and after adding 100 μL of a standard solution (1 M NH4Cl) to the sample (Fig. 6B). The response time for the first addition, calculated as the time needed for the sensor to reach 95 % of the total signal (t_{95}), was 13 s, making the proposed analytical protocol remarkably time efficient.

Table 2 gives the comparison of the results of the ammonium ion determination with three inkjet-printed SC-ISEs and the results of the reference spectrophotometric analysis. The determined ammonium ion concentration with the standard addition method was 30.61 ± 1.30 mM ($n = 3$), deviating from the value determined with the reference method less than 4 %. Thus, we demonstrated that the described fabrication methodology along with the developed analytical procedure are comparable to the traditionally used technique.

4. Conclusion

In this work, we have successfully inkjet printed a graphene-based solid contact over flexible inkjet printed silver electrodes and determined its influence on the electrochemical characteristics of the produced sensors. Based on the EIS experiments, we have proven that incorporating the MGNS ink between silver conductive lines and the ion-selective membrane facilitates the charge transport and significantly
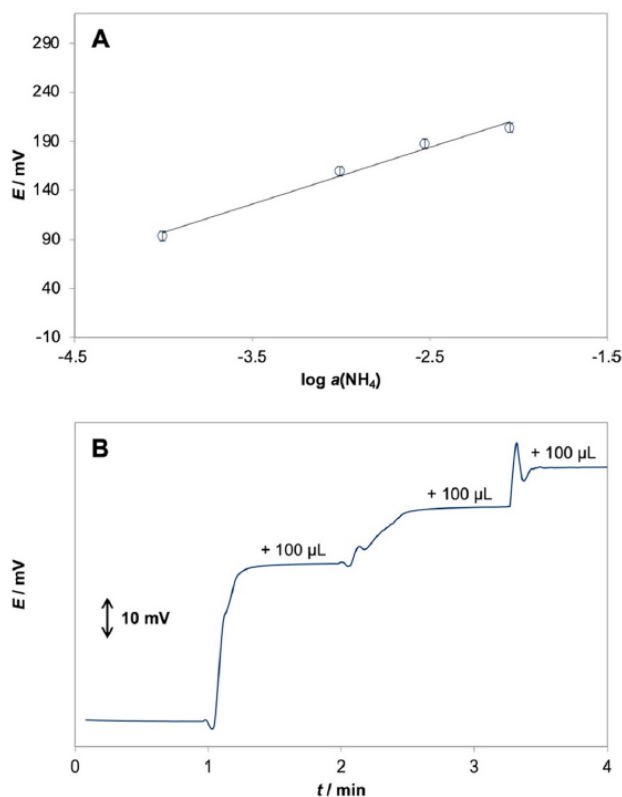

Fig. 6. (A) Potentiometric calibration curve of the MGNS-ISE-based ammonium sensor measured in standard solutions, and (B) the potential trace in the real sample upon the three consecutive standard additions of 100 μL of 1 M NH$_4$Cl.

Table 2
The results of the validation test in the real sample obtained by herein described NH_4-SC-ISEs ($n = 3$) and evaluated by reference spectrophotometric method.

Concentration of NH_4^+/mM		*% error*
Inkjet printed SC-ISE ($n = 3$)	Cuvette test ($n = 3$)	
30.61 ± 1.30	31.88 ± 0.54	3.98

lowers the occurrence of the detrimental water layer formation. By applying an external potential, we have significantly improved the inter-electrode reproducibility: the standard deviations of E^0 values were reduced from 9.8 mV for non-polarized electrodes to 5.1 mV for polarized electrodes, while the linear region of the fabricated SC-ISEs was extended from 10^{-1}–10^{-5} M to 10^{-1}–10^{-6} M and LODs improved to 0.88 ± 0.17 µM (polarized electrodes). Finally, we have shown that our electrodes are competent for measurements in real samples, such as ammonium determination from artificial urine (by direct potentiometry) and a very complex sample of leachate water, with errors less than 4 %. By functionalizing the proposed inkjet printed solid-contact electrodes with ion-selective membranes containing different ionophores, the proposed production protocol could enable mass fabrication of a wide range of flexible potentiometric sensors. Future work will include inkjet printing of ion-selective membranes, either by using printheads compatible with higher viscosities or exploring alternative ion-selective membrane compositions.

CRediT authorship contribution statement

Sara Krivačić: Methodology, Investigation, Formal analysis, Validation, Writing – original draft. **Željka Boček:** Investigation, Formal analysis, Writing – original draft. **Marko Zubak:** Investigation, Formal analysis. **Vedran Kojić:** Resources, Investigation, Validation. **Petar Kassal:** Conceptualization, Methodology, Writing – review & editing, Supervision, Funding acquisition, Project administration.

Declaration of competing interest

The authors declare that they have no known competing financial interests or personal relationships that could have appeared to influence the work reported in this paper.

Data availability

Data will be made available on request.

Appendix A. Supplementary data

Supplementary data to this article can be found online at https://doi.org/10.1016/j.talanta.2024.126614.

References

[1] M. Parrilla, M. Cuartero, G.A. Crespo, Wearable potentiometric ion sensors, Trac. Trends Anal. Chem. 110 (2019) 303–320, https://doi.org/10.1016/j.trac.2018.11.024.
[2] E. Lindner, R.E. Gyurcsányi, Quality control criteria for solid-contact, solvent polymeric membrane ion-selective electrodes, J. Solid State Electrochem. 13 (1) (2009) 51–68, https://doi.org/10.1007/s10008-008-0608-1.
[3] Y.Z. Shao, Y.B. Ying, J.F. Ping, Recent advances in solid-contact ion-selective electrodes: functional materials, transduction mechanisms, and development trends, Chem. Soc. Rev. 49 (13) (2020) 4405–4465, https://doi.org/10.1039/c9cs00587k.
[4] A. Michalska, Optimizing the analytical performance and construction of ion-selective electrodes with conducting polymer-based ion-to-electron transducers, Anal. Bioanal. Chem. 384 (2) (2006) 391–406, https://doi.org/10.1007/s00216-005-0132-4.
[5] C.Y. Wang, K.L. Xia, H.M. Wang, X.P. Liang, Z. Yin, Y.Y. Zhang, Advanced carbon for flexible and wearable electronics, Adv. Mater. 31 (9) (2019) https://doi.org/10.1002/adma.201801072.
[6] T. Lindfors, A. Ivaska, pH sensitivity of polyaniline and its substituted derivatives, J. Electroanal. Chem. 531 (1) (2002) 43–52, https://doi.org/10.1016/s0022-0728(02)01005-7.
[7] C. Bieg, K. Fuchsberger, M. Stelzle, Introduction to polymer-based solid-contact ion-selective electrodes-basic concepts, practical considerations, and current research topics, Anal. Bioanal. Chem. 409 (1) (2017) 45–61, https://doi.org/10.1007/s00216-016-9945-6.
[8] M. Yi, Z.G. Shen, A review on mechanical exfoliation for the scalable production of graphene, J. Mater. Chem. A 3 (22) (2015) 11700–11715, https://doi.org/10.1039/c5ta00252d.
[9] C. Backes, A.M. Abdelkader, C. Alonso, A. Andrieux-Ledier, R. Arenal, et al., Production and processing of graphene and related materials, 2D Mater. 7 (2) (2020), https://doi.org/10.1088/2053-1583/ab1e0a.
[10] J. Fernandes, S.S. Nemala, G. De Bellis, A. Capasso, Green solvents for the liquid phase exfoliation production of graphene: the promising case of cyrene, Front. Chem. 10 (2022), https://doi.org/10.3389/fchem.2022.878799.
[11] G. Cummins, M.P.Y. Desmulliez, Inkjet printing of conductive materials: a review, Circ. World 38 (4) (2012) 193–213, https://doi.org/10.1108/03056121211280413.
[12] A. Moya, G. Gabriel, R. Villa, F.J. del Campo, Inkjet-printed electrochemical sensors, Curr. Opin. Electrochem. 3 (1) (2017) 29–39, https://doi.org/10.1016/j.coelec.2017.05.003.
[13] B. Derby, Inkjet printing of functional and structural materials: fluid property requirements, feature stability, and resolution, in: D.R. Clarke, M. Ruhle, F. Zok (Eds.), Annual Review of Materials Research, vol. 40, 2010, pp. 395–414.
[14] G.H. Hu, J. Kang, L.W.T. Ng, X.X. Zhu, R.C.T. Howe, C.G. Jones, M.C. Hersam, T. Hasan, Functional inks and printing of two-dimensional materials, Chem. Soc. Rev. 47 (9) (2018) 3265–3300, https://doi.org/10.1039/c8cs00084k.
[15] L. Nayak, S. Mohanty, S.K. Nayak, A. Ramadoss, A review on inkjet printing of nanoparticle inks for flexible electronics, J. Mater. Chem. C 7 (29) (2019) 8771–8795, https://doi.org/10.1039/c9tc01630a.
[16] N.C. Raut, K. Al-Shamery, Inkjet printing metals on flexible materials for plastic and paper electronics, J. Mater. Chem. C 6 (7) (2018) 1618–1641, https://doi.org/10.1039/c7tc04804a.
[17] E. Dimitriou, N. Michailidis, Printable conductive inks used for the fabrication of electronics: an overview, Nanotechnology 32 (50) (2021), https://doi.org/10.1088/1361-6528/abefff.
[18] S. Wünscher, R. Abbel, J. Perelaer, U.S. Schubert, Progress of alternative sintering approaches of inkjet-printed metal inks and their application for manufacturing of flexible electronic devices, J. Mater. Chem. C 2 (48) (2014) 10232–10261, https://doi.org/10.1039/c4tc01820f.
[19] H.S. Lim, S.J. Kim, H.W. Jang, J.A. Lim, Intense pulsed light for split-second structural development of nanomaterials, J. Mater. Chem. C 5 (29) (2017) 7142–7160, https://doi.org/10.1039/c7tc01848g.
[20] A. Capasso, A.E.D. Castillo, H. Sun, A. Ansaldo, V. Pellegrini, F. Bonaccorso, Ink-jet printing of graphene for flexible electronics: an environmentally-friendly approach, Solid State Commun. 224 (2015) 53–63, https://doi.org/10.1016/j.ssc.2015.08.011.
[21] Y.Z.N. Htwe, M. Mariatti, Surfactant-assisted water-based graphene conductive inks for flexible electronic applications, J. Taiwan Inst. Chem. Eng. 125 (2021) 402–412, https://doi.org/10.1016/j.jtice.2021.06.022.
[22] Y.Z.N. Htwe, M. Mariatti, Printed graphene and hybrid conductive inks for flexible, stretchable, and wearable electronics: progress, opportunities, and challenges, Journal of Science-Advanced Materials and Devices 7 (2) (2022), https://doi.org/10.1016/j.jsamd.2022.100435.
[23] A. Shimoni, S. Azoubel, S. Magdassi, Inkjet printing of flexible high-performance carbon nanotube transparent conductive films by "coffee ring effect", Nanoscale 6 (19) (2014) 11084–11089, https://doi.org/10.1039/c4nr02133a.
[24] D. Mitra, T. Zubkova, C. Gerlach, O. Kanoun, D. Miesel, H. Lang, R.R. Baumann, Inkjet printing and intense pulsed light sintering of multiwall carbon nanotubes for sensor applications, J. Imag. Sci. Technol. 62 (4) (2018), https://doi.org/10.2352/J.ImagingSci.Technol.2018.62.4.040409.
[25] O.S. Kwon, H. Kim, H. Ko, J. Lee, B. Lee, C.H. Jung, J.H. Choi, K. Shin, Fabrication and characterization of inkjet-printed carbon nanotube electrode patterns on paper, Carbon 58 (2013) 116–127, https://doi.org/10.1016/j.carbon.2013.02.039.
[26] K. Kordás, T. Mustonen, G. Tóth, H. Jantunen, M. Lajunen, et al., Inkjet printing of electrically conductive patterns of carbon nanotubes, Small 2 (8–9) (2006) 1021–1025, https://doi.org/10.1002/smll.200600061.
[27] C.L. Baumbauer, P.J. Goodrich, M.E. Payne, T. Anthony, C. Beckstoffer, A. Toor, W. Silver, A.C. Arias, Printed potentiometric nitrate sensors for use in soil, Sensors 22 (11) (2022), https://doi.org/10.3390/s22114095.
[28] H. Jiang, W. Yu, J.F. Waimin, N. Glassmaker, N. Raghunathan, X. Jiang, B. Ziaie, R. Rahimi, Inkjet-printed solid-state potentiometric nitrate ion selective electrodes for agricultural application, in: 2019 IEEE SENSORS, IEEE, 2019.
[29] M. Jovic, J.C. Hidalgo-Acosta, A. Lesch, V.C. Bassetto, E. Smirnov, F. Cortés-Salazar, H.H. Girault, Large-scale layer-by-layer inkjet printing of flexible iridium-oxide based pH sensors, J. Electroanal. Chem. 819 (2018) 384–390, https://doi.org/10.1016/j.jelechem.2017.11.032.

[30] A. Määttänen, U. Vanamo, P. Ihalainen, P. Pulkkinen, H. Tenhu, J. Bobacka, J. Peltonen, A low-cost paper-based inkjet-printed platform for electrochemical analyses, Sensor. Actuator. B Chem. 177 (2013) 153–162, https://doi.org/10.1016/j.snb.2012.10.113.

[31] P. Sjöberg, A. Määttänen, U. Vanamo, M. Novell, P. Ihalainen, F.J. Andrade, J. Bobacka, J. Peltonen, Paper-based potentiometric ion sensors constructed on ink-jet printed gold electrodes, Sensor. Actuator. B Chem. 224 (2016) 325–332, https://doi.org/10.1016/j.snb.2015.10.051.

[32] Q. He, S.R. Das, N.T. Garland, D.P. Jing, J.A. Hondred, A.A. Cargill, S.W. Ding, C. Karunakaran, J.C. Claussen, Enabling inkjet printed graphene for ion selective electrodes with postprint thermal annealing, ACS Appl. Mater. Interfaces 9 (14) (2017) 12719–12727, https://doi.org/10.1021/acsami.7b00092.

[33] N. Ruecha, O. Chailapakul, K. Suzuki, D. Citterio, Fully inkjet-printed paper-based potentiometric ion-sensing devices, Anal. Chem. 89 (19) (2017) 10608–10616, https://doi.org/10.1021/acs.analchem.7b03177.

[34] J.N. Galloway, The global nitrogen cycle: changes and consequences, Environ. Pollut. 102 (1998) 15–24, https://doi.org/10.1016/s0269-7491(98)80010-9.

[35] K.E. Wyer, D.B. Kelleghan, V. Blanes-Vidal, G. Schauberger, T.P. Curran, Ammonia emissions from agriculture and their contribution to fine particulate matter: a review of implications for human health, J. Environ. Manag. 323 (2022), https://doi.org/10.1016/j.jenvman.2022.116285.

[36] K.N. Lin, Y. Zhu, Y.B. Zhang, H. Lin, Determination of ammonia nitrogen in natural waters: recent advances and applications, Trends in Environmental Analytical Chemistry 24 (2019), https://doi.org/10.1016/j.teac.2019.e00073.

[37] M. Cuartero, N. Colozza, B.M. Fernández-Pérez, G.A. Crespo, Why ammonium detection is particularly challenging but insightful with ionophore-based potentiometric sensors - an overview of the progress in the last 20 years, Analyst 145 (9) (2020) 3188–3210, https://doi.org/10.1039/d0an00327a.

[38] M. Kralj, S. Krivacic, I. Ivanisevic, M. Zubak, A. Supina, M. Marcius, I. Halasz, P. Kassal, Conductive inks based on melamine intercalated graphene nanosheets for inkjet printed flexible electronics, Nanomaterials 12 (17) (2022), https://doi.org/10.3390/nano12172936.

[39] N. Sarigul, F. Korkmaz, I. Kurultak, A new artificial urine protocol to better imitate human urine, Sci. Rep. 9 (2019) 9–20159, https://doi.org/10.1038/s41598-019-56693-4.

[40] K. Arapov, K. Jaakkola, V. Ermolov, G. Bex, E. Rubingh, et al., Graphene screen-printed radio-frequency identification devices on flexible substrates, Phys. Status Solidi Rapid Res. Lett. 10 (11) (2016) 812–818, https://doi.org/10.1002/pssr.201600330.

[41] E.B. Secor, T.Z. Gao, M.H. Dos Santos, S.G. Wallace, K.W. Putz, M.C. Hersam, Combustion-Assisted photonic annealing of printable graphene inks via exothermic binders, ACS Appl. Mater. Interfaces 9 (35) (2017) 29418–29423, https://doi.org/10.1021/acsami.7b07189.

[42] Y.L. Liu, Y.Z. Liu, Z. Meng, Y. Qin, D.C. Jiang, K. Xi, P. Wang, Thiol-functionalized reduced graphene oxide as self-assembled ion-to-electron transducer for durable solid-contact ion-selective electrodes, Talanta 208 (2020), https://doi.org/10.1016/j.talanta.2019.120374.

[43] J. Bobacka, Potential stability of all-solid-state ion-selective electrodes using conducting polymers as ion-to-electron transducers, Anal. Chem. 71 (21) (1999) 4932–4937, https://doi.org/10.1021/ac990497z.

[44] U. Mattinen, S. Rabiej, A. Lewenstam, J. Bobacka, Impedance study of the ion-to-electron transduction process for carbon cloth as solid-contact material in potentiometric ion sensors, Electrochim. Acta 56 (28) (2011) 10683–10687, https://doi.org/10.1016/j.electacta.2011.07.082.

[45] J.F. Ping, Y.X. Wang, J. Wu, Y.B. Ying, Development of an all-solid-state potassium ion-selective electrode using graphene as the solid-contact transducer, Electrochem. Commun. 13 (12) (2011) 1529–1532, https://doi.org/10.1016/j.elecom.2011.10.018.

[46] V. Mazzaracchio, A. Serani, L. Fiore, D. Moscone, F. Arduini, All-solid state ion-selective carbon black-modified printed electrode for sodium detection in sweat, Electrochim. Acta 394 (2021), https://doi.org/10.1016/j.electacta.2021.139050.

[47] N.T. Garland, E.S. McLamore, N.D. Cavallaro, D. Mendivelso-Perez, E.A. Smith, D.P. Jing, J.C. Claussen, Flexible laser-induced graphene for nitrogen sensing in soil, ACS Appl. Mater. Interfaces 10 (45) (2018) 39124–39133, https://doi.org/10.1021/acsami.8b10991.

[48] I.S. Kucherenko, D. Sanborn, B.L. Chen, N. Garland, M. Serhan, E. Forzani, C. Gomes, J.C. Claussen, Ion-selective sensors based on laser-induced graphene for evaluating human hydration levels using urine samples, Advanced Materials Technologies 5 (6) (2020), https://doi.org/10.1002/admt.201901037.

[49] T. Guinovart, A.J. Bandodkar, J.R. Windmiller, F.J. Andrade, J. Wang, A potentiometric tattoo sensor for monitoring ammonium in sweat, Analyst 138 (22) (2013) 7031–7038, https://doi.org/10.1039/c3an01672b.

[50] E. Bakker, Determination of improved selectivity coefficients of polymer membrane ion-selective electrodes by conditioning with a discriminated ion, J. Electrochem. Soc. 143 (4) (1996) L83–L85, https://doi.org/10.1149/1.1836608.

[51] E. Bakker, E. Pretsch, P. Bühlmann, Selectivity of potentiometric ion sensors, Anal. Chem. 72 (6) (2000) 1127–1133, https://doi.org/10.1021/ac991146n.

[52] I. Ivanisevic, S. Milardovic, A. Ressler, P. Kassal, Fabrication of an all-solid-state ammonium paper electrode using a graphite-polyvinyl butyral transducer layer, Chemosensors 9 (12) (2021), https://doi.org/10.3390/chemosensors9120333.

[53] Y. Umezawa, P. Bühlmann, K. Umezawa, K. Tohda, S. Amemiya, Potentiometric selectivity coefficients of ion-selective electrodes Part I.: inorganic cations -: (Technical report), Pure Appl. Chem. 72 (10) (2000) 1851–2082, https://doi.org/10.1351/pac200072101851.

[54] R. Athavale, I. Kokorite, C. Dinkel, E. Bakker, B. Wehrli, G.A. Crespo, A. Brand, In situ ammonium profiling using solid-contact ion-selective electrodes in eutrophic lakes, Anal. Chem. 87 (24) (2015) 11990–11997, https://doi.org/10.1021/acs.analchem.5b02424.

[55] Y.H. Cheong, L.Y. Ge, G. Lisak, Highly reproducible solid contact ion selective electrodes: emerging opportunities for potentiometry - a review, Anal. Chim. Acta 1162 (2021), https://doi.org/10.1016/j.aca.2021.338304.

[56] J.B. Hu, A. Stein, P. Bühlmann, Rational design of all-solid-state ion-selective electrodes and reference electrodes, Trac. Trends Anal. Chem. 76 (2016) 102–114, https://doi.org/10.1016/j.trac.2015.11.004.

[57] C.R. Rousseau, P. Bühlmann, Calibration-free potentiometric sensing with solid-contact ion-selective electrodes, Trac. Trends Anal. Chem. 140 (2021), https://doi.org/10.1016/j.trac.2021.116277.

[58] S. Papp, J. Kozma, T. Lindfors, R.E. Gyurcsányi, Lipophilic multi-walled carbon nanotube-based solid contact potassium ion-selective electrodes with reproducible standard potentials. A comparative study, Electroanalysis 32 (2020) 867–873, https://doi.org/10.1002/elan.202000045.

[59] U. Vanamo, J. Bobacka, Instrument-free control of the standard potential of potentiometric solid-contact ion-selective electrodes by short-circuiting with a conventional reference electrode, Anal. Chem. 86 (21) (2014) 10540–10545, https://doi.org/10.1021/ac501464s.

[60] I. Ivanko, T. Lindfors, R. Emanuelsson, M. Sjödin, Conjugated redox polymer with poly(3,4-ethylenedioxythiophene) backbone and hydroquinone pendant groups as the solid contact in potassium-selective electrodes, Sensor. Actuator. B Chem. 329 (2021), https://doi.org/10.1016/j.snb.2020.129231.

[61] A. Michalska, Improvement of analytical characteristic of calcium selective electrode with conducting polymer contact. The role of conducting polymer spontaneous charge transfer processes and their galvanostatic compensation, Electroanalysis 17 (5–6) (2005) 400–407, https://doi.org/10.1002/elan.200403173.

[62] J. Kozma, S. Tapp, R.E. Gyurcsányi, TEMPO-functionalized carbon nanotubes for solid-contact ion-selective electrodes with largely improved potential reproducibility and stability, Anal. Chem. (2022), https://doi.org/10.1021/acs.analchem.2c00395.

[63] J. Kozma, S. Papp, R.E. Gyurcsanyi, Highly hydrophobic TEMPO-functionalized conducting copolymers for solid-contact ion-selective electrodes, Bioelectrochemistry 150 (2023), https://doi.org/10.1016/j.bioelechem.2022.108352.

[64] E. Bakker, Determination of unbiased selectivity coefficients of neutral carrier-based cation-selective electrodes, Anal. Chem. 69 (6) (1997) 1061–1069, https://doi.org/10.1021/ac960891m.

[65] E. Bakker, P. Bühlmann, E. Pretsch, The phase-boundary potential model, Talanta 63 (1) (2004) 3–20, https://doi.org/10.1016/j.talanta.2003.10.006.

[66] A. Ariri, S. Alva, D.S. Khaerudini, A.S.A. Aziz, Fabrication of lead ion selective electrodes (Pb-ISE) based on poly methyl-methacrylate-Co-butyl acrylate (MB28) thin film photo-polymers and pencil graphite electrodes (PGEs), Port. Electrochim. Acta 40 (4) (2022) 305–323, https://doi.org/10.4152/pea.2022400405.

[67] K. Maksymiuk, Chemical reactivity of polypyrrole and its relevance to polypyrrole based electrochemical sensors, Electroanalysis 18 (16) (2006) 1537–1551, https://doi.org/10.1002/elan.200603573.

[68] M. Fibbioli, W.E. Morf, M. Badertscher, N.F. de Rooij, E. Pretsch, Potential drifts of solid-contacted ion-selective electrodes due to zero-current ion fluxes through the sensor membrane, Electroanalysis 12 (16) (2000) 1286–1292, https://doi.org/10.1002/1521-4109(200011)12:16<1286::Aid-elan1286>3.0.Co;2-q.

7.4. Appendix IV – Supplementary information for Publication 2

Supplementary information for the publication:

Flexible ammonium ion-selective electrode based on inkjet-printed graphene solid contact

Sara Krivačić[1], Željka Boček[1], Marko Zubak[1], Vedran Kojić[2,3] and Petar Kassal[1]

[1]   Faculty of Chemical Engineering and Technology, University of Zagreb, Trg Marka Marulića 19, 10000 Zagreb, Croatia

[2]   Ruđer Bošković Institute, Bijenička cesta 54, 10000 Zagreb, Croatia

[3]   HIS d.o.o., Donja Višnjica 61D, 42255, Donja Višnjica, Croatia

Flexible ammonium ion-selective electrode based on inkjet-printed graphene solid contact

Supplementary Information

Sara Krivačić[a], Željka Boček[a], Marko Zubak[a], Vedran Kojić[b, c], Petar Kassal[a,*]

[a] University of Zagreb, Faculty of Chemical Engineering & Technology, Trg Marka Marulića 19, 10000 Zagreb, Croatia
[b] Ruđer Bošković Institute, Bijenička cesta 54, 10000 Zagreb, Croatia
[c] HIS d.o.o., Donja Višnjica 61D, 42255 Donja Višnjica, Croatia
*e-mail: pkassal@fkit.unizg.hr

Table S1. Literature review with examples of all-solid-state ammonium ion-selective electrodes.

Ref.	Substrate material	Solid-contact material	Slope / mV dec^{-1}	Linear range / M	Limit of detection / µM	use
[1]	Polyimide	Laser-induced graphene	51.7	10^{-5}–10^{-1}	28.2	soil
[2]	polyimide	Laser-induced graphene	51.0	10^{-4}–0.15	30.0	urine
[3]	acetate sheet etched with aluminium oxide	Graphite	53.5	10^{-4}–10^{-1}	6.0	Natural water
[4]	paper	Graphite	57.3	10^{-5}–10^{-1}	4.8	/
[5]	temporary transfer tattoo paper	Carbon	58.7	10^{-4}–10^{-1}	12.6	Sweat
[6]	paper	CNT	56.4	10^{-5}–10^{-1}	7.2	/
[7]	Glassy	AuNP-rGO	56.94	10^{-5}–10^{-2}	3.8	Lake water

	carbon disc electrode	composite				
[8]	PET	PEDOT:PSS	61.9	10^{-3}–10^{-1}	0.57	Natural water
[9]	Graphite paste (disc electrode)	Ppy	58.0	10^{-5}–10^{-1}	1.00	soil
[10]	Glassy carbon disc electrode	POT	59.5	10^{-6}–10^{-4}	0.32	seawater
[11]	Glassy carbon disc electrode	PANI	58.1	10^{-5}–10^{-1}	1.17	Wastewater
[12]	Silver wire	PANI	56.59	10^{-4}–10^{-1}	1.58	Wastewater
This work	Inkjet printed silver electrode	Melamine-intercalated graphene nanosheets	55.6	10^{-6}–10^{-1}	0.88	Wastewater
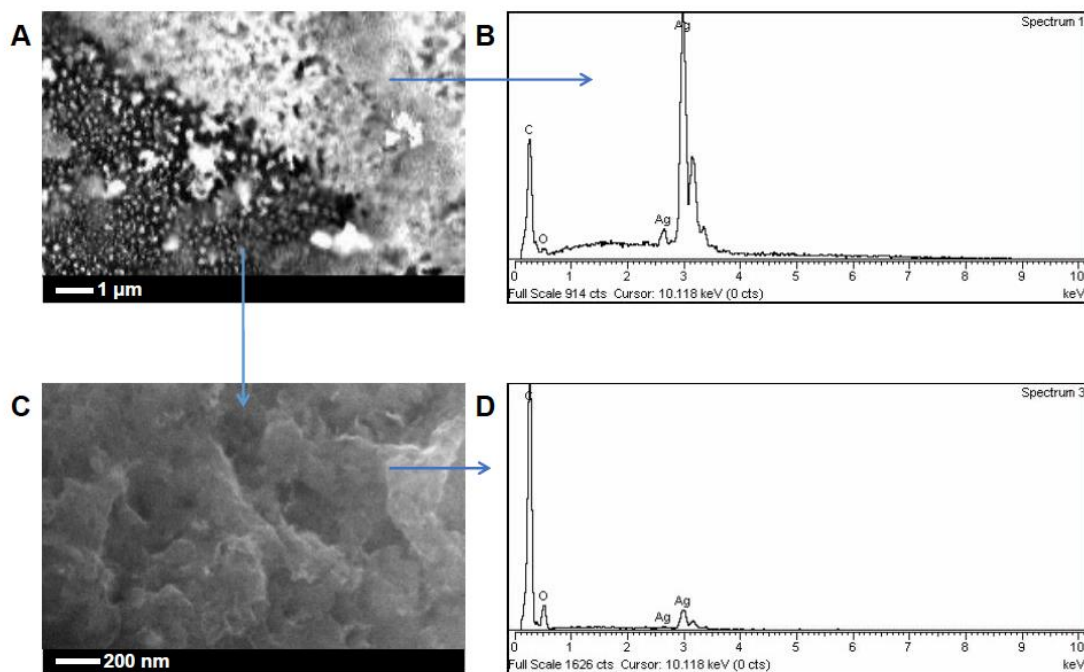
Fig. S1. The SEM micrographs of inkjet printed and annealed electrode. **(A)** Ag-surface with graphene ink overprint; **(B)** Elemental structure of Ag conducting line; **(C)** the magnification of graphene overprint from figure S1(A), and its corresponding elemental structure **(D)**.
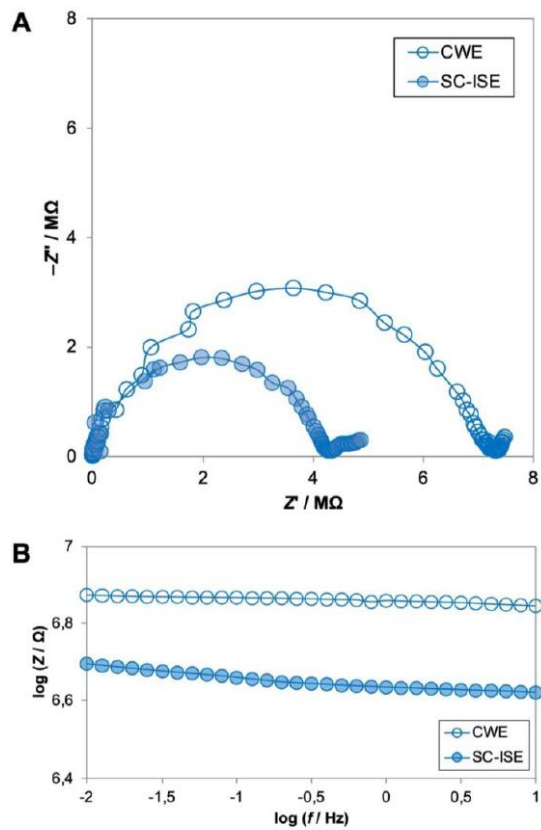
Fig. S2. (A) The Nyquist and **(B)** Bode impedance plots of NH4-SC-ISE with (filled circles) and without (empty circles) MGNS solid contact.
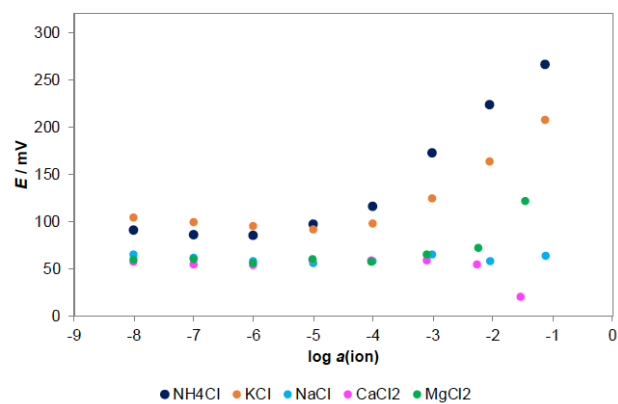
Fig. S3. The calibration curves of the interfering ions recorded with an ammonium-selective electrode using the separate solutions method.
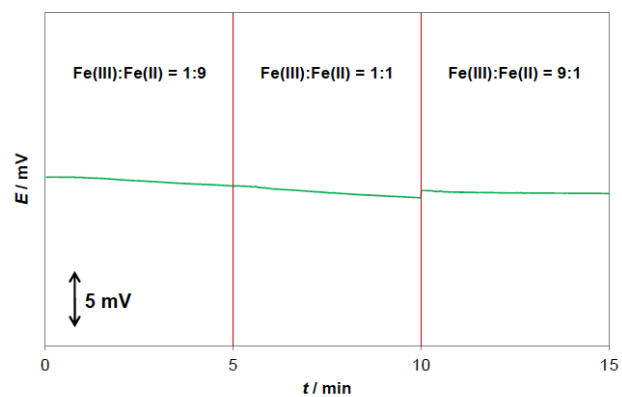
Fig. S4. The electrode response to 10 mM NH4Cl in a presence of 1 mM redox buffer.
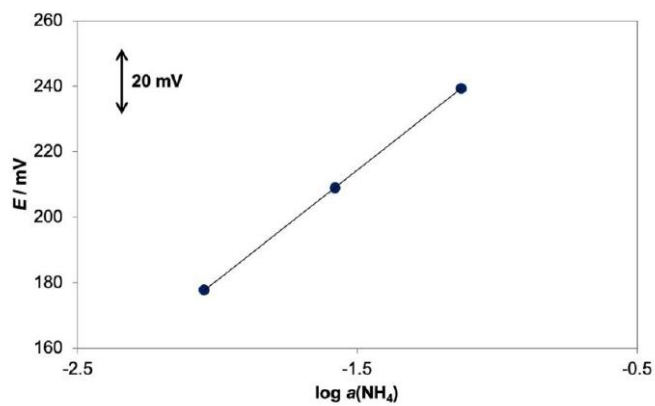
Fig. S5. The calibration plot of inkjet printed electrode in a narrow concentration range of NH$_4$Cl.

1. N.T. Garland, E.S. McLamore, N.D. Cavallaro, D. Mendivelso-Perez, E.A. Smith, D.P. Jing,J.C. Claussen, *Flexible Laser-Induced Graphene for Nitrogen Sensing in Soil.* Acs Applied Materials & Interfaces, 2018. 10(45): p. 39124-39133. DOI: 10.1021/acsami.8b10991.

2. I.S. Kucherenko, D. Sanborn, B.L. Chen, N. Garland, M. Serhan, E. Forzani, C. Gomes,J.C. Claussen, *Ion-Selective Sensors Based on Laser-Induced Graphene for Evaluating Human Hydration Levels Using Urine Samples.* Advanced Materials Technologies, 2020. 5(6). DOI: 10.1002/admt.201901037.

3. T. Fayose, L. Mendecki, S. Ullah,A. Radu, *Single strip solid contact ion selective electrodes on a pencil-drawn electrode substrate.* Analytical Methods, 2017. 9(7): p. 1213-1220. DOI: 10.1039/c6ay02860h.

4. I. Ivanisevic, S. Milardovic, A. Ressler,P. Kassal, *Fabrication of an All-Solid-State Ammonium Paper Electrode Using a Graphite-Polyvinyl Butyral Transducer Layer.* Chemosensors, 2021. 9(12). DOI: 10.3390/chemosensors9120333.

5. T. Guinovart, A.J. Bandodkar, J.R. Windmiller, F.J. Andrade,J. Wang, *A potentiometric tattoo sensor for monitoring ammonium in sweat.* Analyst, 2013. 138(22): p. 7031-7038. DOI: 10.1039/c3an01672b.

6. M. Novell, M. Parrilla, G.A. Crespo, F.X. Rius,F.J. Andrade, *Paper-Based Ion-Selective Potentiometric Sensors.* Analytical Chemistry, 2012. 84(11): p. 4695-4702. DOI: 10.1021/ac202979j.

7. L.D. Nguyen, C.M. Dang,T.C.D. Doan, *Highly stable ammonium ion-selective electrodes based on one-pot synthesized gold nanoparticle-reduced graphene oxide as ion-to-electron transducers.* Microchemical Journal, 2023. 190. DOI: 10.1016/j.microc.2023.108717.

8. A. Benoudjit, M.F. Abd-Wahab,W.W.A.W. Salim, *Fabrication of an All-Solid-State Ammonium Ion–Selective Electrode by a Two-Step Process Using Cyclic Voltammetry*, in *The 1st International Electronic Conference on Biosensors*. 2020, MDPI.

9. J. Schwarz, K. Trommer,M. Mertig, *Solid-Contact Ion-Selective Electrodes Based on Graphite Paste for Potentiometric Nitrate and Ammonium Determinations.* American Journal of Analytical Chemistry, 2018. 09(12): p. 591-601. DOI: 10.4236/ajac.2018.912043.

10. L. Ding, J. Ding, B. Ding,W. Qin, *Solid-contact Potentiometric Sensor for the Determination of Total Ammonia Nitrogen in Seawater.* International Journal of Electrochemical Science, 2017. 12(4): p. 3296-3308. DOI: 10.20964/2017.04.01.

11. Y.Z. Bao, J.B. Yan, J. Hu,J. Li, *Superhydrophobic polyaniline solid contact for potential stability improvement of NH_4^+-selective electrode.* Sensors and Actuators B-Chemical, 2023. 390. DOI: 10.1016/j.snb.2023.133997.

12. Y. Huang, J. Li, T. Yin, J. Jia, Q. Ding, H. Zheng, C.-T.A. Chen,Y. Ye, *A novel all-solid-state ammonium electrode with polyaniline and copolymer of aniline/2,5-dimethoxyaniline as transducers.* Journal of Electroanalytical Chemistry, 2015. 741: p. 87-92. DOI: 10.1016/j.jelechem.2014.12.041.

7.5. Appendix V – Manuscript of Publication 3

Towards mass-production of ion-selective electrodes by spotting: Optimization of membrane composition and real-time tracking of membrane drying

Sara Krivačić[1,2], Ayian Speck[2], Petar Kassal[1], Eric Bakker[2]

[1] Faculty of Chemical Engineering and Technology, University of Zagreb, Trg Marka Marulića 19, 10000 Zagreb, Croatia

[2] Department of Inorganic and Analytical Chemistry, University of Geneva, Quai Ernest-Ansermet 30, 1221 Genève, Switzerland

Towards mass-production of ion-selective electrodes by spotting: Optimization of membrane composition and real-time tracking of membrane drying

Sara Krivačić [a,b], Ayian Speck [a], Petar Kassal [b,*], Eric Bakker [a,*]

[a] *Department of Inorganic and Anal. Chem., University of Geneva, Quai Ernest-Ansermet 30, Genève 1221, Switzerland*
[b] *University of Zagreb, Faculty of Chemical Engineering and Technology, Trg Marka Marulića 19, Zagreb HR-10000, Croatia*

ARTICLE INFO

ABSTRACT

Solid-contact ion-selective electrodes present tools for rapid assessment of charged species within a vast number of samples. Commercially available point-of-care electrochemical sensing systems are most often produced by screen-printing. However, this method is not applicable to polymeric membrane deposition, due to the mismatch of the membrane physical characteristics to those intended for screen printing. Herein, an industrial automated dispensing machine was used for fast and controlled deposition of small volumes of ion-selective membrane. Compared to the previously published literature, the dry solute membrane content was not altered. Rather, we optimized the solvents for the ISM preparation, thus significantly lowering the required overall number of membrane deposition steps. It was shown that dry membrane uniformity strongly depends on the solvent carrier system, with the best uniformity for the membrane prepared in a solvent mixture consisting of equal volumes of THF and cyclohexanone. The volume of a single membrane deposit (spot) was estimated based on colorimetric absorbance measurements to be 0.20 μL. Already with a single spot of the ion-selective membrane, an adequate potentiometric response to potassium ions was obtained, supporting the efficiency of the production technique. Evaporative membrane drying was investigated for the first time using time-resolved impedance spectroscopy, giving useful information on the influence of the solvent composition to the characteristics of the evaporative time profiles. With this approach, the overall production and drying of the described devices takes less than 30 min.

1. Introduction

The operational and instrumental simplicity of electrochemical sensors [1] and a plethora of available ionophores for membrane electrodes [2,3] allow ion sensing platforms to be applied in complex matrices such as environmental [4] and biological samples [5]. In the past few years, the original electrode design of polymeric membrane potentiometric sensors has been reshaped: the inner liquid filling solution separating the ion-selective membrane (ISM) from the inner reference element was replaced with a solid-contact material [6], typically a conducting polymer [7] or a large surface area capacitive material [8]. Such a solid-state electrode configuration is a key design improvement for sensor miniaturization.

A recent flurry of publications aimed towards fast, simple and inexpensive potentiometric sensing platforms [9–14] is paving the way towards widespread sensor distribution. Such systems are often designed for single use that require no maintenance. Thus, achieving excellent inter-electrode reproducibility, often limited by the stability of the phase boundary potential between the ISM and underlying solid substrate [15], has become the key for the realization of truly "ready-to-use" and often disposable electrochemical sensing platforms.

Developing scalable, automated fabrication approaches should help bring about widespread ready-to-use sensors. Traditionally used fabrication procedures, such as photolithography [16] or chemical vapour deposition [17] are complicated, expensive and incompatible with soft and thin substrates such as paper or polymers. On the other hand, printing techniques originally developed within the scope of the graphics industry, e.g. screen printing and inkjet printing, have already entered the realm of commercial electrode production. These methods owe their outstanding reproducibility to the fact that the electrodes are
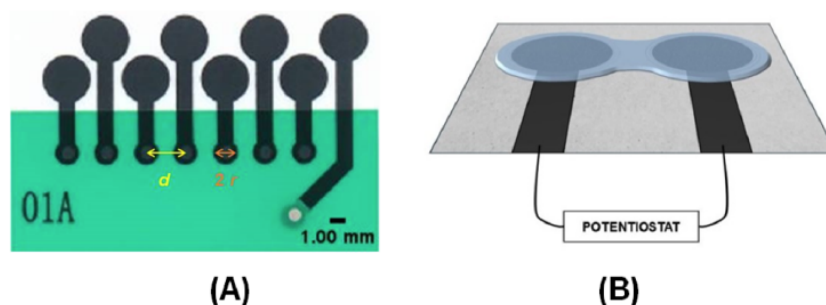
133

Fig. 1. **(A)** A photograph of screen-printed electrode arrays; **(B)** the schematic representation of electrode setup for the time-resolved impedance measurements.

produced in a predefined quantity from the same functional material contained within an ink [18]. As opposed to screen printing, which is a contact printing technique, digitally controlled inkjet printing deposits picoliter droplets of functional ink onto a substrate in a non-contact, high-precision manner, making it applicable for curved or fragile substrates. However, such small droplet volumes tend to instantly evaporate at the printer nozzle if the solvent mixture is not properly chosen [19].

Both screen printing and inkjet printing have already been used in the fabrication of potentiometric sensing systems [14,20–25]. Yet, the deposition of membrane material by inkjet printing has not been made possible without drastically altering the amount of polymeric matrix by dilution, thus requiring a large number of overprints that significantly slows down the fabrication process [14]. The controlled deposition of small volumes of polymeric solutions using high-precision automated dispensing machines may instead be integrated into the electrode production line. Dong's group reported on the fabrication of all-solid-state miniature sensors designed for long-term use in the continuous monitoring of soil nitrate. Both solid-contact material and ion-selective membrane were deposited via an automated fluid dispensing robot [26]. However, the dispensed membrane cocktail – containing poly (vinyl chloride) (PVC) as the polymer matrix – was five times diluted in tetrahydrofuran (THF) compared to the widely accepted cocktail composition [27].

As evident from the above, the bottleneck to the efficient mass production of membrane electrodes is the controlled deposition of the sensing membrane. The influence of the homogeneity of the deposited membrane on the standard potential reproducibility of the electrodes is not trivial. Gyurcsányi and Lindfors have demonstrated excellent standard potential reproducibility of perfluorinated alkanoate side chain functionalized poly(3,4-ethylenedioxythiophene) (PEDOT) hydrophobic membrane support before casting it with a potassium-selective membrane ($\pm$ 0.5 mV, $n = 6$). However, the standard potential reproducibility decreased to $\pm$ 3 mV after drop casting the membrane onto the hydrophobic support [28].

We present here an optimisation of the ion-selective membrane composition that allows for the precise, reproducible and fast deposition onto screen printed electrode arrays using an automated fluid dispenser that is aimed towards industrial production. The dry solute membrane content was not altered compared to the traditionally accepted composition. Instead, the solvents for the membrane preparation were optimized. In this manner, the required overall number of membrane deposition steps were reduced. The amount, morphology and precision of the depositions were probed by a colorimetric absorbance method [29]. Finally, a novel experimental setup based on time-resolved impedance spectroscopy was designed to directly track the membrane drying process as a function of different solvents used for membrane preparation.

2. Materials and methods

2.1. Equipment and methods

Potassium chloride ($\geq$ 99.5 %, KCl), sodium chloride ($\geq$ 99.5 %, NaCl), magnesium chloride ($\geq$ 97 %, MgCl$_2$), calcium chloride ($\geq$ 96 %), tetradodecylammonium tetrakis(4-chlorophenyl)borate (Selectophore™, ETH 500), potassium tetrakis(4-chlorophenyl)borate ($\geq$ 99.5 %, KTpClPB), bis(2-ethylhexyl) sebacate ($\geq$ 97.0 %, DOS), valinomycin (Selectophore™, K-ionophore(I)), tetrahydrofuran ($\geq$ 99.5 %, Selectophore™, THF), and cyclohexanone ($\geq$ 99.5 %, Selectophore™) were purchased from Sigma Aldrich. Nile Red was obtained from Fluka.

Screen printed electrode arrays on paper substrates were donated by Eaglenos Sciences, Inc., Nanjing, China and consisted of seven carbon-based working electrodes and a silver/silver chloride reference electrode, each electrode having a working area radius, $r = 1.00$ mm and distance between the electrodes, $d = 2.50$ mm (Fig. 1).

For colorimetric absorbance mapping, a blank polymeric membrane cocktail containing 33 mg PVC, 66 mg DOS, and 0.10 mg Nile Red in 1 mL solvent carrier was prepared. The membrane cocktail was spotted onto photographic paper using an automated dispensing system (Nordson E3 EFD, Ohio, USA) and dried at room temperature. The paper was found not to absorb the spotted membrane cocktail. The image data of the spotted membranes was obtained using a Canosan 9000f Mark II flatbed scanner. If needed the pictures were processed with Image J and further analyzed as described in Section 3.1.

The molar extinction coefficient (ε) of Nile Red in the membrane cocktail was estimated according to Beer's law. First, 1 µL of the cocktail (33 mg/mL PVC, 66 mg/mL DOS, and 0.10 mg/mL Nile Red) was drop cast onto the photo paper; the area of the spots and the colorimetric absorbance were determined after droplet drying. From the known wet volume and area, wet droplet thickness was calculated and used for the estimation of ε_{WET} (18,500 M^{-1} cm^{-1}). For ε_{DRY} estimation, the same membrane cocktail was diluted 10 times; 500 µL of this cocktail was poured into a 2.9-cm-diameter glass ring affixed on a PET sheet and dried. The dry membrane thickness of 50.33 µm was determined using an optical microscope KERN OBE134 (Fig. S1). Upon recording the absorbance spectra using a spectrophotometer, Shimadzu UV-1280, the ε_{DRY} of 19,665 M^{-1} cm^{-1} was determined.

Impedance measurements were performed with a PGSTAT302 (Metrohm Autolab, B.V., Utrecht, The Netherlands) controlled by Nova 2.1 software. A two-electrode configuration consisting of identical screen-printed carbon electrodes was used. The measurements were performed using the drying polymeric membrane (33 mg/mL PVC, 66 mg/mL DOS, 0.45 mg/mL KTpClPB and 0.5 mg/mL ETH 500) as the ion-conducting medium (Fig. 1B). The alternating potential of 10 mV was applied at a frequency scan from 100,000 to 10,000 Hz. Using a time-resolved program, the impedance (Z) at 10,000 Hz was plotted as a function of time.

For potentiometric measurements the potassium-selective membrane cocktail was prepared by weighing 33 mg PVC, 66 mg DOS, and
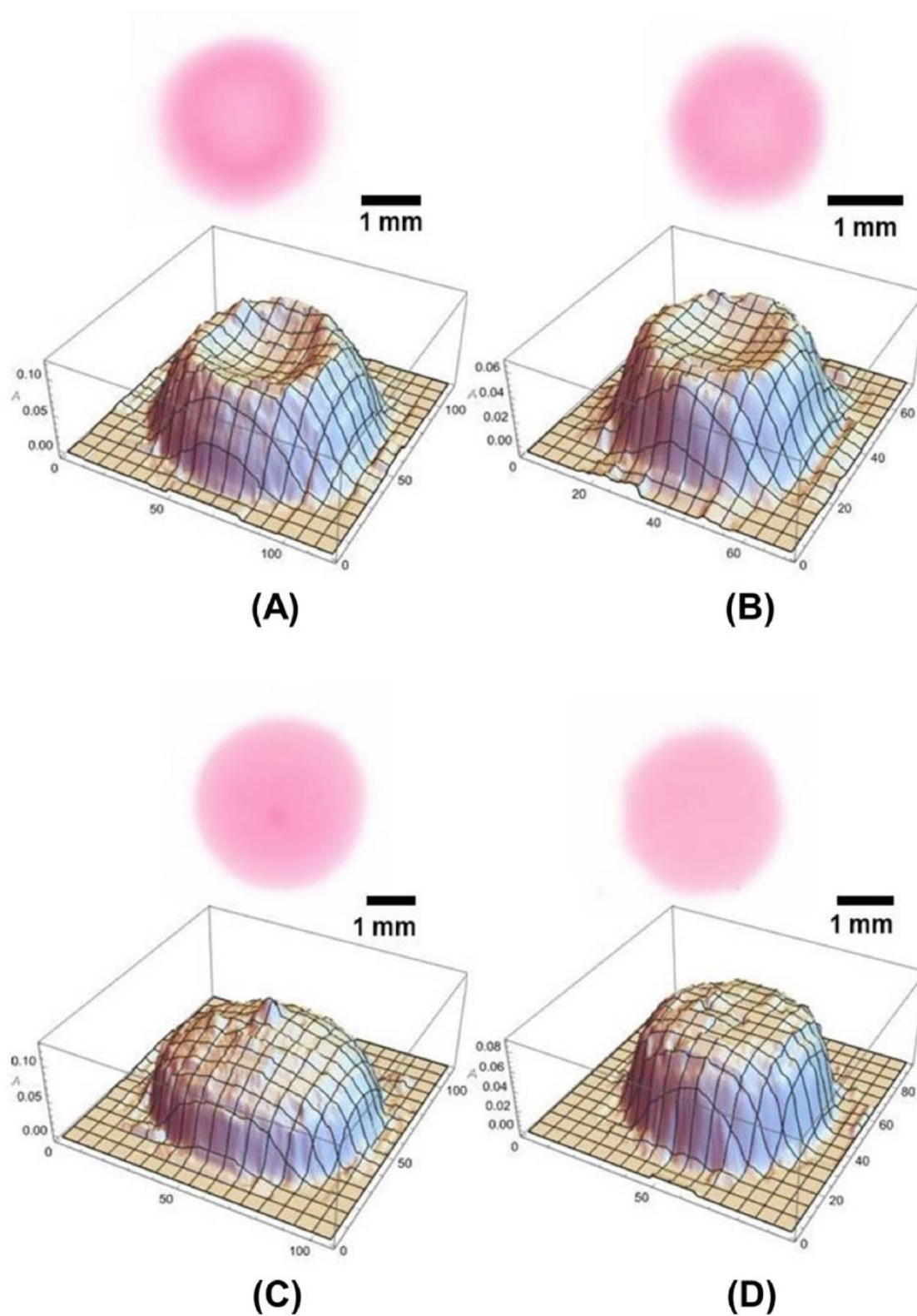
Fig. 2. Photographs and 3D plots of absorbance values for the spotted membrane prepared in **(A)** 90 vol% cyclohexanone, 10 vol% THF; **(B)** 75 vol% cyclohexanone, 25 vol% THF; **(C)** 60 vol% cyclohexanone, 40 vol% THF; and **(D)** 50 vol% cyclohexanone, 50 vol% THF.
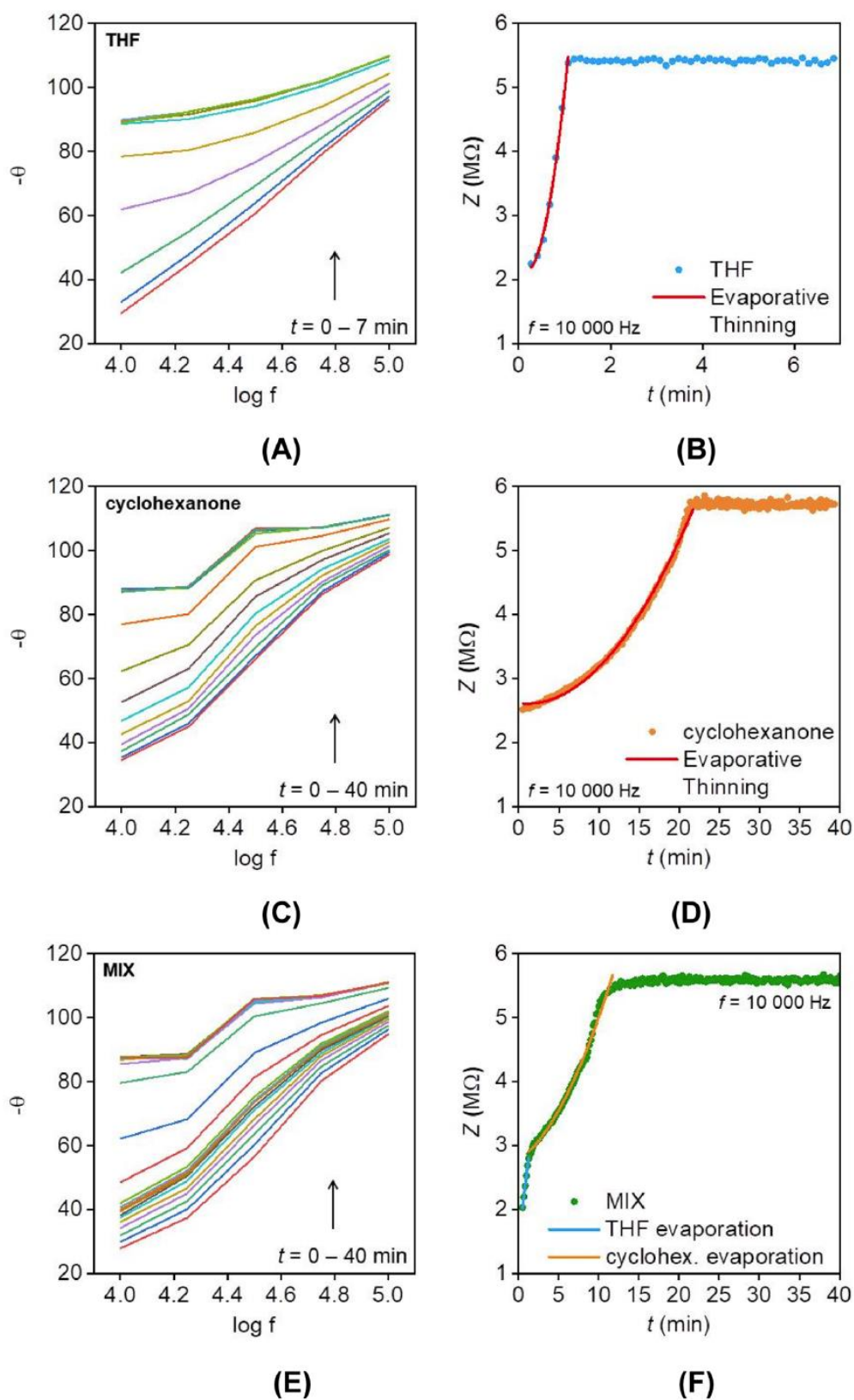
135

Fig. 3. Phase angle as a function of frequency and impedance profiles for the membranes prepared in **(A,B)** THF; **(C,D)** cyclohexanone; **(E,F)** 1:1 mixture of THF and cyclohexanone.

0.25 mg KTpClPB and 1.11 mg valinomycin into 1 mL THF:cyclohexanone (1:1) and vortexing the cocktail for 20 min. The membrane cocktails were spotted onto the screen-printed electrodes using the automated dispensing system and tested the following day.

Potentiometric measurements were performed in a flow cell built inhouse using a high impedance input 16-channel EMF monitor (Lawson Laboratories, Inc., Malvern, PA) to record the signal against screen printed silver/silver chloride as reference electrode embedded in a separate channel. The electrode calibrations were performed in KCl solutions with a constant ionic background of 10 mM NaCl. For selectivity tests, the separate solutions method (SSM) was used. The response of potassium-selective electrodes was compared to the response to Mg^{2+}, Ca^{2+} and Na^+ in the concentration range 10^{-4}–10^{-2} M of each salt. The selectivity coefficients were calculated using Eq. (1):

$$\log K_{IJ}^{pot} = \frac{z_I F(E_J - E_I)}{2.303RT} + \log\left(\frac{a_I}{a_J^{z_I/z_J}}\right) \tag{1}$$

where K_{IJ}^{pot} is the potentiometric selectivity coefficient, z_I (z_J) is the valency of ion I (J), R is the gas constant, E_I (E_J) is the measured potential and a_I (a_J) the activity of ion I (J).

All electrochemical measurements were carried out in a Faraday cage to prevent unwanted noise.

3. Results and discussion

3.1. Optimization of the membrane solvent carrier composition

Previously reported scalable fabrication procedures of miniaturized membrane electrodes utilize diluted ion-selective membranes, thus requiring multiple deposition steps to produce membranes having sufficient thicknesses to withstand the intended usage [14,26]. In this work, we overcome this challenge by optimizing the membrane solvent carrier composition without diluting the traditionally accepted membrane cocktail. The utility of THF in automated membrane deposition to the electrode surface is hindered by its low boiling point [29,30]. THF can be replaced with less volatile solvents (entirely or to some degree with miscible solvents) – such as cyclohexanone [14,31–33], which allows for better manipulation of membrane formulations and prevents separation of the membrane phase at the tip of the dispenser.

Four membrane cocktails were prepared in the following solvent mixtures: (1) 90 vol% cyclohexanone, 10 vol% THF; (2) 75 vol% cyclohexanone, 25 vol% THF; (3) 60 vol% cyclohexanone, 40 vol% THF; (4) 50 vol% cyclohexanone, 50 vol% THF. The membranes were spotted onto photographic paper using the automated fluid dispenser, with the same deposition parameters, including pressure to the dispenser syringe and the duration of applied pressure. Colorimetric absorbance data of the dried specimens was used to create three-dimensional plots giving information on the thickness uniformity of the spotted membranes. The absorbance of the image data was analyzed from the RGB information of the picture in Mathematica software [34] to obtain the corresponding colorimetric absorbance values and three-dimensional maps of the dye distribution. For an image taken by the digital camera, the data is corrected by a factor γ to make it appear more natural to human eye. The detected absorbance is described with:

$$A_{R,G,B} = \gamma \bullet \log\frac{I_{0,camera}}{I_{camera}} = -\gamma \bullet \log\frac{R, G, B}{R_{ref}, G_{ref}, B_{ref}} \tag{2}$$

$A_{R,G,B}$ is the colorimetric absorbance value in either the red, green, or blue channel; R,G,B is the corresponding RGB value for the signal and reference pixel in each channel obtained by the flatbed scanner. I_{camera} is the relative light intensity of the pixel normalized to a value between 0 and 1; $I_{0,camera}$ is the light output of a reference blank pixel.

As can be seen from the 3D absorbance plots in Fig. 2A,B, the dried specimens prepared with 90 and 75 vol% of cyclohexanone show a pronounced structure inhomogeneity. Most of the dye particles

accumulated at the periphery of the drop, forming a "coffee-ring" deposit. Such structure inhomogeneity follows from the capillary flow within the droplet during evaporation: the drop edge is pinned to the substrate and the solvent flows from the centre towards the edge of the drop. Increasing the volume of THF at the expense of cyclohexanone, the "coffee-ring" surface relief diminishes (Fig. 2C, D) owing to the differences in viscosities, surface tensions and boiling points of the respective solvents. As THF evaporates first, a surface tension gradient develops across the droplet, resulting in the appearance of the inward Marangoni flow that counteracts the capillary flow [35]. At equal volume ratios of the two solvents a controlled surface morphology and uniform thickness were obtained, indicating the most promising solvent composition for automated membrane spotting.

The extinction coefficients of the wet and dry membrane were determined from absorbance measurements, as explained in the Experimental section. Using ε_{WET}, the volume of a single spotted droplet was estimated to be $V \approx 0.20$ µL. The thicknesses of the wet deposits (initial thicknesses), l_i, of the 4 membrane compositions were (1) 36.3 µm, (2) 54.0 µm, (3) 61.5 µm, and (4) 50.5 µm. ε_{DRY} was used to determine the final thicknesses, l_f (1) 11.6 µm, (2) 17.2 µm, (3) 19.6 µm and (4) 16.1 µm.

3.2. Time-resolved impedance measurements

To characterize the influence of the solvent carrier composition on drying of the ion-selective membrane, a novel experimental setup was designed. Membrane cocktails containing PVC:DOS (1:2) and ETH500, and KTpClPB were prepared in pure THF, pure cyclohexanone and THF: cyclohexanone (1:1 by volume), indicated as MIX in the further text. The cocktails were drop cast onto two adjacent screen-printed electrodes (Fig. 1B), to mimic the methods for accurate conductivity measurements of small-volume samples [36–38]. 1 µL of the membrane cocktail was cast on each of the two neighbouring electrodes. The drops spread during wetting of the substrate and connected in the middle (Fig. 1B). In this manner the deposited membrane made an electrical connection between the two electrodes. The polymeric membrane consists of a volatile solvent (THF or a mixture of THF and cyclohexanone), non-volatile membrane solvent – plasticizer, DOS and a non-volatile solute (PVC, ETH 500, KTpClPB). As the solvent evaporation process imposes a change in the membrane composition and structure, the membrane impedance changes significantly with time.

Solvent evaporation is assumed to happen solely by means of diffusion and is predicted with a Fickian diffusion model [39]. Evaporative thinning profiles during polymeric membrane drying were here investigated using time-resolved impedance spectroscopy: a series of high-frequency short-time impedance measurements were recorded at distinct consecutive time intervals. The impedance measurements were started at the time of membrane casting, as the solvent removal starts at the same moment. Fig. 3A, C and E show the phase angle as a function of frequency during the evaporative drying of the membranes prepared in THF, cyclohexanone, and solvent mixture, respectively. At $t = 0$ (wet membrane) the phase angle strongly depends on the frequency of the sine excitation. At the highest frequency the phase angle approaches 90°, indicating capacitive behaviour, and falls to a minimum value as the frequency of the sine excitation falls.

As the membrane dries, the frequency dependence of phase angle becomes less pronounced and the membrane takes on a purely capacitive behaviour. Wet and dry membrane thicknesses were estimated from absorbance measurements as described in the Experimental section. The estimated wet membrane thicknesses were: 155.5±15.3 µm, 142.5±13.0 µm, and 91.5±9.0 µm, for a membrane prepared in THF, cyclohexanone, and solvent mixture, respectively. Dry membrane thicknesses were: 34.8±4.4 µm (THF), 37.3±4.4 µm (cyclohexanone), and 31.3±7.3 µm (solvent mixture).

Fig. 3B, D and F show the impedance profiles consisting of two parts: (i) the impedance gradient that reflects evaporative thinning of the
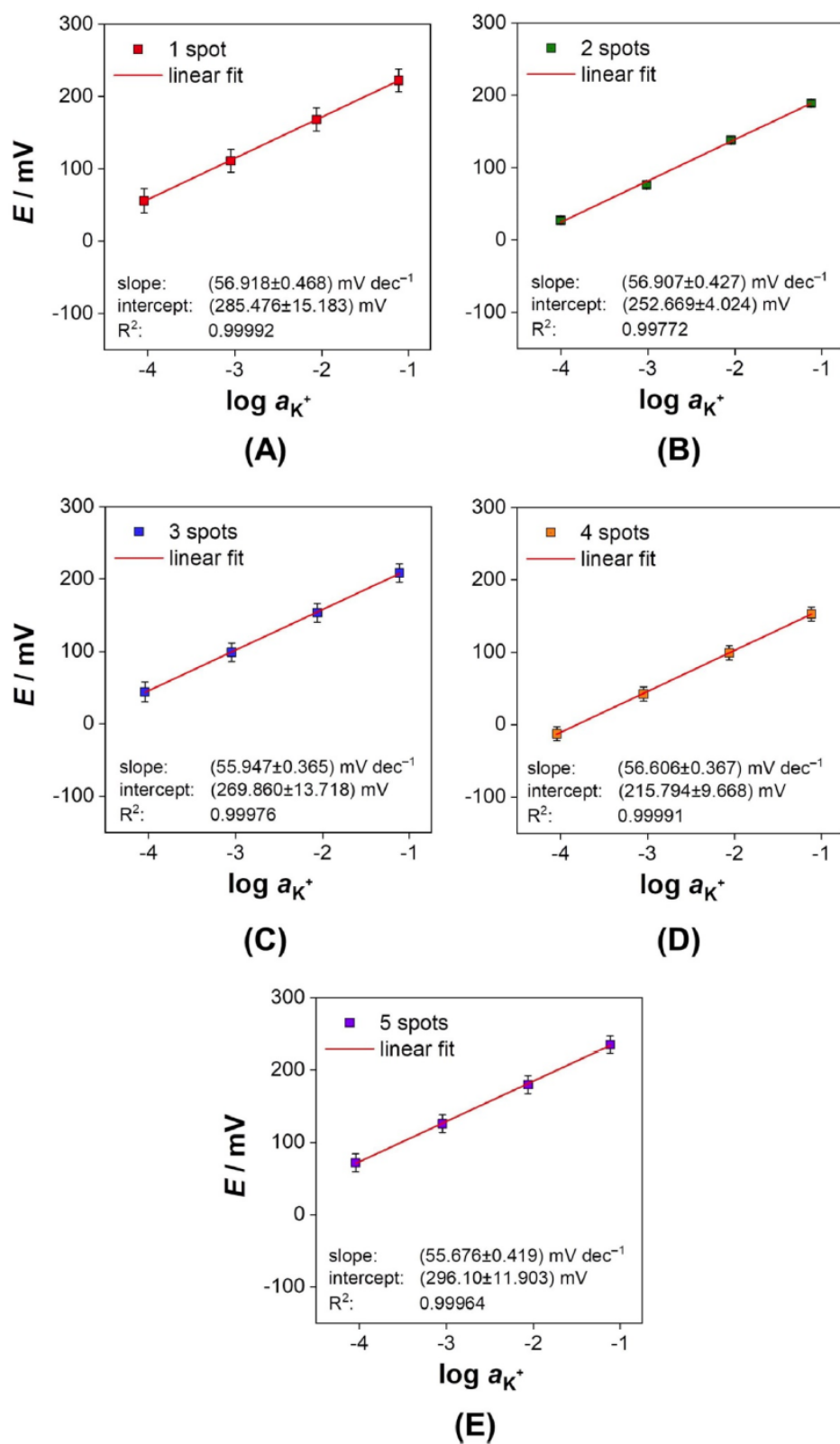
Fig. 4. The calibration plot of the electrode arrays modified with a potassium-selective membrane.

membrane; (ii) a constant maximum value. The starting membrane impedance at the moment, $t = 0$ s was 2.09±0.18 MΩ (THF) 2.65±0.05 MΩ (cyclohexanone), and 1.98±0.83 M (mixture).

The impedance changes due to evaporative thinning of membranes prepared with single solvents, Fig. 3B and D, were fitted to a second order polynomial (Table S1), describing the mass transfer in mixtures consisting of long poly(vinyl chloride) chains mixed with small solvent molecules (THF, cyclohexanone and DOS). The rate of diffusion within the polymeric solution is controlled by the free-volume within the polymeric mixture [40,41]. Based on this model, the total volume of the polymeric mixture consists of the actual volume occupied by the components of the mixture and surrounding them is the free-volume space. This free-volume consists of the solvent and is further expanded by the addition of the low-volatile plasticizer DOS [42]. The plasticizer does not evaporate during the experiment, but rather provides an excess of free-volume to the polymer. The significant difference in the two profiles arises from the difference in solvent volatility (THF vs. cyclohexanone). According to the free-volume theory, as the free volume diminishes due to solvent evaporation, the solvent diffusivity diminishes as well [43].

In contrast to typical drying curves of unplasticized polymeric solutions, where the solvent evaporation is the quickest at the beginning and slows down gradually [44], a slower increase in impedance is observed initially since the decrease in diffusivity of the lipophilic salts is countered by an increase in their concentration. Additionally, in case of both single solvents, the impedance sharply transitions to a plateau that indicates complete dryness of the membrane. Such sharp transitions have been previously observed, specifically in the case of diluted polymeric solutions, where the viscosity does not increase enough to hinder transportation of the solvent molecules to the evaporation surface and the evaporation rate remains constant [45,46]. In our case, as the plasticizer occupies roughly double the volume of the polymer, the evaporation of the last remaining solvent does not significantly alter solvent diffusion and the drying progresses is rapid. Furthermore, since conductivity does not increase linearly with concentration at high lipophilic salt concentration [47], a decrease in the rate of impedance increase is not expected. A membrane prepared with THF reaches the maximum impedance value of 5.14±0.27 MΩ already within 1 min. An impedance plateau at 5.89±0.19 MΩ is reached after 23.2 min for a membrane prepared with cyclohexanone.

The time-resolved impedance measurement of a ternary mixture containing THF and cyclohexanone at equal volume ratios is given in Fig. 3E, F. The evaporative impedance time profile consists of two parts, each fitted with its own second order polynomial (Table S2) for THF evaporation and cyclohexanone evaporation. Compared to membrane cocktails prepared in single solvents, the volume of each solvent is halved. As THF rapidly evaporates the free-volume diminishes and the polymeric chains rearrange. Thus, the diffusivity of the remaining solvent is significantly lowered [48]. The properties of the resulting film are governed by the less volatile solvent, cyclohexanone ($T_b = 156$ °C) [49], as confirmed by the strong similarity in the frequency dependence of the phase angle during the evaporative drying (Fig. 3C and E). The impedance plateau at 5.60±0.01 MΩ is reached within 11.5 min. This is in agreement with the drying time of the membrane containing only cyclohexanone (double volume).

3.3. Spotted membrane volume optimization

The polymeric membrane cocktail containing equal volume ratios of THF and cyclohexanone was used for automated spotting of screen printed electrode arrays. The potassium-selective membrane was spotted onto working electrodes in one, two, three, four and five repetitions, with one spot having a volume of 0.20 μL (as determined in Section 3.1). After drying, the membrane thickness of 16±1 μm was estimated based on absorbance measurements (single spot, $n = 5$). The electrodes were then examined with a camera to assure that the spotted membranes do not overlap and that the electrode working area is

Table 1
Experimental (biased) selectivity coefficient values for the potassium selective electrode arrays prepared with 2 spots of the valinomycin containing membrane.

Ion (J)	Slope (mV)	E_J^0 (mV)	$\log K_{K,J}^{pot}$
K$^+$	57.9	258.8	0
Na$^+$	14.3	− 64.2	− 4.05
Ca^{2+}	6.3	− 79.6	− 4.92
Mg^{2+}	− 8.3	− 108.9	− 5.02

completely covered with the membrane. The electrodes were embodied in a flow cell and calibrated in solutions of KCl with a constant ionic background of 10 mM NaCl. To mimic mass-fabricated single use sensors, the electrode arrays were not conditioned before the measurements. The potentiometric response was already quite stable upon first contact with aqueous solution. Fig. 4 shows the calibration plots for the devices prepared with different number of spots. Already with a single spot, an adequate potentiometric response is obtained within a clinically relevant potassium concentration range. Even though thinner membranes have been successfully used in open circuit potentiometry [50–52], herein we did not employ an intermediate layer of solid-contact material for the sake of simplifying the electrode modification towards mass production and evaluating purely the membrane properties. For routine applications such as clinical diagnostics, a single point calibration will however still be necessary. The inter-electrode reproducibility, as expressed as the standard deviation of E^0 values, improved from ±15.183 mV/dec to ±4.024 mV/dec after depositing a second spot of the potassium-selective membrane. Hence, the electrodes prepared with two spots were used to obtain the selectivity coefficients using the separate solutions method (SSM) [53]. The potentiometric response to K-ions was compared to the one obtained with clinically relevant interferents, Na$^+$, Ca^{2+} and Mg^{2+}, in the concentration range from 10^{-4} to 10^{-2} M, see Fig. S4. The selectivity coefficients are comparable to those previously reported with valinomycin-based potentiometric probes [54] (Table 1).

3.4. Conclusions

Presented here is the optimisation of membrane solvent carrier composition aimed at decreasing the production steps of the solid-contact ion-selective electrodes. It was shown that a 1:1 mixture of THF and cyclohexanone gives membranes with uniform deposits without coffee-ring structures. The influence of the solvent carrier composition to the evaporative drying of the deposited membranes was investigated using time-resolved impedance measurements. It was shown that THF evaporates first, within a minute of membrane casting, followed by cyclohexanone evaporation. As THF fully evaporates, the free-volume within the membrane significantly reduces, thus lowering the evaporation rate of cyclohexanone.

Using the automatized fluid dispenser, membranes prepared in the solvent mixture were spotted onto screen-printed electrodes. With only a single spot of potassium-selective membrane (total volume of 0.2 μL) a desired potentiometric response was obtained. The modification of one sensor array using the automated fluid dispenser takes less than a minute and complete membrane drying is achieved in less than 30 min. These results present a promising path towards rapid mass production of robust potentiometric sensor arrays.

CRediT authorship contribution statement

Ayian Speck: Methodology, Investigation. **Sara Krivacic:** Writing – original draft, Methodology, Investigation, Formal analysis, Conceptualization. **Eric Bakker:** Writing – review & editing, Supervision, Resources, Project administration, Methodology, Funding acquisition, Conceptualization. **Petar Kassal:** Writing – review & editing, Writing – original draft, Supervision, Funding acquisition, Formal analysis.

Declaration of Competing Interest

Eric Bakker is a scientific advisor for Eaglenos Sciences. No other interests are declared by the authors.

Acknowledgements

Appendix A. Supporting information

Supplementary data associated with this article can be found in the online version at doi:10.1016/j.snb.2024.136759.

Data availability

Data will be made available on request.

References

[1] K. Beaver, A. Dantanarayana, S.D. Minteer, Materials approaches for improving electrochemical sensor performance, JPC B 125 (2021) 11820–11834, https://doi.org/10.1021/acs.jpcb.1c07063.

[2] P. Bühlmann, E. Pretsch, E. Bakker, Carrier-based ion-selective electrodes and bulk optodes. 2. Ionophores for potentiometric and optical sensors, Chem. Rev. 98 (1998) 1593–1688, https://doi.org/10.1021/cr970113+.

[3] M.R. Huang, X.G. Li, Highly sensing and transducing materials for potentiometric ion sensors with versatile applicability, Prog. Mater. Sci. 125 (2022), https://doi.org/10.1016/j.pmatsci.2021.100885.

[4] M. Cuartero, E. Bakker, Environmental water analysis with membrane electrodes, Curr. Opin. Electrochem. 3 (2017) 97–105, https://doi.org/10.1016/j.coelec.2017.06.010.

[5] S.G. Li, H.Y. Zhang, M. Zhu, Z.J. Kuang, X. Li, F. Xu, et al., Electrochemical biosensors for whole blood analysis: recent progress, challenges, and future perspectives, Chem. Rev. 123 (2023) 7953–8039, https://doi.org/10.1021/acs.chemrev.1c00759.

[6] J.B. Hu, A. Stein, P. Bühlmann, Rational design of all-solid-state ion-selective electrodes and reference electrodes, TrAC Trends Anal. Chem. 76 (2016) 102–114, https://doi.org/10.1016/j.trac.2015.11.004.

[7] J. Bobacka, Conducting polymer-based solid-state ion-selective electrodes, Electroanalysis 18 (2006) 7–18, https://doi.org/10.1002/elan.200503384.

[8] T.J. Yin, W. Qin, Applications of nanomaterials in potentiometric sensors, TrAC Trends Anal. Chem. 51 (2013) 79–86, https://doi.org/10.1016/j.trac.2013.06.009.

[9] W.J. Lan, X.U. Zou, M.M. Hamedi, J.B. Hu, C. Parolo, E.J. Maxwell, et al., Paper-based potentiometric ion sensing, Anal. Chem. 86 (2014) 9548–9553, https://doi.org/10.1021/ac5018088.

[10] S.S.M. Hassan, A.H. Kamel, M.A. Fathy, All-solid-state paper-based potentiometric combined sensor modified with reduced graphene oxide (rGO) and molecularly imprinted polymer for monitoring losartan drug in pharmaceuticals and biological samples, Talanta 253 (2023), https://doi.org/10.1016/j.talanta.2022.123907.

[11] B. Mandjoukov, T. Lindfors, Planar, low-cost, flexible, and fully laminated graphene paper pseudo-reference and potassium-selective electrodes, Sens. Actuators B Chem. 403 (2024), https://doi.org/10.1016/j.snb.2023.135190.

[12] J.W. Ding, B.W. Li, L.X. Chen, W. Qin, A three-dimensional origami paper-based device for potentiometric biosensing, Angew. Chem. Int. Ed. 55 (2016) 13033–13037, https://doi.org/10.1002/anie.201606268.

[13] P. Sjöberg, A. Määttänen, U. Vanamo, M. Novell, P. Ihalainen, F.J. Andrade, et al., Paper-based potentiometric ion sensors constructed on ink-jet printed gold electrodes, Sens. Actuators B Chem. 224 (2016) 325–332, https://doi.org/10.1016/j.snb.2015.10.051.

[14] N. Ruecha, O. Chailapakul, K. Suzuki, D. Citterio, Fully inkjet-printed paper-based potentiometric ion-sensing devices, Anal. Chem. 89 (2017) 10608–10616, https://doi.org/10.1021/acs.analchem.7b03177.

[15] Y.Z. Shao, Y.B. Ying, J.F. Ping, Recent advances in solid-contact ion-selective electrodes: functional materials, transduction mechanisms, and development trends, Chem. Soc. Rev. 49 (2020) 4405–4465, https://doi.org/10.1039/c9cs00587k.

[16] W. Gao, S. Emaminejad, H.Y.Y. Nyein, S. Challa, K.V. Chen, A. Peck, et al., Fully integrated wearable sensor arrays for multiplexed in situ perspiration analysis, Nature 529 (2016) 509, https://doi.org/10.1038/nature16521.

[17] A. Lupu, A. Valsesia, F. Bretagnol, P. Colpo, F. Rossi, Development of a potentiometric biosensor based on nanostructured surface for lactate determination, Sens. Actuators B Chem. 127 (2007) 606–612, https://doi.org/10.1016/j.snb.2007.05.020.

[18] R.R. Suresh, M. Lakshmanakumar, J. Jayalatha, K.S. Rajan, S. Sethuraman, U. M. Krishnan, et al., Fabrication of screen-printed electrodes: opportunities and challenges, J. Mater. Sci. 56 (2021) 8951–9006, https://doi.org/10.1007/s10853-020-05499-1.

[19] L. Nayak, S. Mohanty, S.K. Nayak, A. Ramadoss, A review on inkjet printing of nanoparticle inks for flexible electronics, J. Mater. Chem. C 7 (2019) 8771–8795, https://doi.org/10.1039/c9tc01630a.

[20] A. Määttänen, U. Vanamo, P. Ihalainen, P. Pulkkinen, H. Tenhu, J. Bobacka, et al., A low-cost paper-based inkjet-printed platform for electrochemical analyses, Sens. Actuators B Chem. 177 (2013) 153–162, https://doi.org/10.1016/j.snb.2012.10.113.

[21] E. Bilbao, S. Kapadia, V. Riechert, J. Amalvy, F.N. Molinari, M.M. Escobar, et al., Functional aqueous-based polyaniline inkjet inks for fully printed high-performance pH-sensitive electrodes, Sens. Actuators B Chem. 346 (2021), https://doi.org/10.1016/j.snb.2021.130558.

[22] A.H. Kamel, N.H. Ashmawy, T.A. Youssef, M. Elnakib, H. Abd El-Naby, H.S.M. Abd-Rabboh, Screen-printed electrochemical sensors for label-free potentiometric and impedimetric detection of human serum albumin, Electroanalysis 35 (2023), https://doi.org/10.1002/elan.202200436.

[23] K.Y. Chen, A. Biswas, S.H. Cai, J.Y. Huang, J. Andrews, Inkjet printed potentiometric sensors for nitrate detection directly in soil enabled by a hydrophilic passivation layer, Adv. Mater. Technol. (2024), https://doi.org/10.1002/admt.202301140.

[24] S. Krivacic, M. Zubak, D. Vrsaljko, P. Kassal, Application of intense pulsed light in the development of poly(vinyl butyral)-based all-solid-state Ag/AgCl reference electrodes, Electroanalysis 36 (2024), https://doi.org/10.1002/elan.202300368.

[25] S. Krivačić, Ž. Boček, M. Zubak, V. Kojić, P. Kassal, Flexible ammonium ion-selective electrode based on inkjet-printed graphene solid contact, Talanta (2024) (In press).

[26] M.A. Ali, X.R. Wang, Y.C. Chen, Y.Y. Jiao, N.K. Mahal, S. Moru, et al., Continuous monitoring of soil nitrate using a miniature sensor with poly(3-octyl-thiophene) and molybdenum disulfide nanocomposite, ACS Appl. Mater. Interfaces 11 (2019) 29195–29206, https://doi.org/10.1021/acsami.9b07120.

[27] E. Bakker, P. Buhlmann, E. Pretsch, Carrier-based ion-selective electrodes and bulk optodes. 1. General characteristics, Chem. Rev. 97 (1997) 3083–3132, https://doi.org/10.1021/cr940394a.

[28] S. Papp, M. Bojtár, R.E. Gyurcsányi, T. Lindfors, Potential reproducibility of potassium-selective electrodes having perfluorinated alkanoate side chain functionalized poly(3,4-ethylenedioxythiophene) as a hydrophobic solid contact, Anal. Chem. 91 (2019) 9111–9118, https://doi.org/10.1021/acs.analchem.9b01587.

[29] U. Schaller, U.E. Spichiger, W. Simon, Novel magnesium ion-selective microelectrodes based on a neutral carrier, Eur. J. Appl. Physiol. 423 (1993) 338–342, https://doi.org/10.1007/bf00374414.

[30] R. Bernasconi, M.Costa Angeli, F. Mantica, D. Carniani, L. Magagnin, SU-8 inkjet patterning for microfabrication, Polymer 185 (2019) 121933, https://doi.org/10.1016/j.polymer.2019.121933.

[31] R.W. Cattrall, P. Chin-Poh, Coated wire ion selective electrode for the determination of iron(III), Anal. Chem. 47 (1975) 93–95, https://doi.org/10.1021/ac60351a045.

[32] B.D. Pendley, E. Lindner, A chronoamperometric method to estimate ionophore loss from ion-selective electrode membranes, Anal. Chem. 71 (1999) 3673–3676, https://doi.org/10.1021/ac990137b.

[33] M. Rostampour, B. Bailey, C. Autrey, K. Ferrer, B. Vantoorenburg, P.K. Patel, et al., Single-step integration of poly(3-octylthiophene) and single-walled carbon nanotubes for highly reproducible paper-based ion-selective electrodes, Anal. Chem. 93 (2021) 1271–1276, https://doi.org/10.1021/acs.analchem.0c04506.

[34] Y. Soda, K.J. Robinson, T.J. Cherubini, E. Bakker, Colorimetric absorbance mapping and quantitation on paper-based analytical devices, LOC 20 (2020) 1441–1448, https://doi.org/10.1039/d0lc00028k.

[35] H. Hu, R.G. Larson, Marangoni effect reverses coffee-ring depositions, JPC B 110 (2006) 7090–7094, https://doi.org/10.1021/jp0609232.

[36] P. Linderholm, A. Bertsch, P. Renaud, Resistivity probing of multi-layered tissue phantoms using microelectrodes, Physiol. Meas. 25 (2004) 645–658, https://doi.org/10.1088/0967-3334/25/3/005.

[37] E. Ravagli, M. Crescentini, M. Tartagni, S. Severi, Non-invasive measurement of electrical conductivity of liquids in biocompatible polymeric lines for hemodialysis applications, Sens. Actuators A Phys. 261 (2017) 252–260, https://doi.org/10.1016/j.sna.2017.04.034.

[38] W.C. Wang, W.C. Li, B.Y. Liu, L. Wang, K. Li, Y. Wang, et al., Temperature dependence of dielectric properties of blood at 10 Hz to 100 MHz, Front. Physiol. 13 (2022), https://doi.org/10.3389/fphys.2022.1053233.

[39] D. Vesely, Diffusion of liquids in polymers, Int. Mater. Rev. 53 (2008) 299–315, https://doi.org/10.1179/174328008x324602.

[40] P. Neogi, Diffusion in Polymers, Marcel Dekker, New York, 1996.

[41] J.L. Duda, Molecular diffusion in polymeric systems, Pure Appl. Chem. 57 (1985) 1681–1690, https://doi.org/10.1351/pac198557111681.

[42] M. Beltrán Marcilla, Mechanisms of plasticizers action, in: Handbook of Plasticizers, Elsevier, Amsterdam, The Netherlands, 2017.

140

[43] L. Masaro, X.X. Zhu, Physical models of diffusion for polymer solutions, gels and solids, Prog. Polym. Sci. 24 (1999) 731–775, https://doi.org/10.1016/S0079-6700(99)00016-7.

[44] S.P. Velaga, D. Nikjoo, P.R. Vuddanda, Experimental studies and modeling of the drying kinetics of multicomponent polymer films, AAPS Pharm. Sci. Tech. 19 (2018) 425–435, https://doi.org/10.1208/s12249-017-0836-8.

[45] L. Song, Study of Ordered Macroporous Polymer Films by Templating Breath Figures (PhD Thesis), Georgia Institute of Technology, 2005.

[46] V. Sharma, L.L. Song, R.L. Jones, M.S. Barrow, R. Williams, M. Srinivasarao, Effect of solvent choice on breath-figure-templated assembly of "holey" polymer films, Epl 91 (2010), https://doi.org/10.1209/0295-5075/91/38001.

[47] A. Singh, P.S. Dhapola, S. Kumar, S. Konwar, P.K. Singh, A.M.M. Ali, et al., Highly conducting ionic liquid doped polymer electrolyte for energy storage applications, JS: AMD 7 (2022), https://doi.org/10.1016/j.jsamd.2022.100511.

[48] L. Lapčík, L. Valko, Kinetic study of dissolution of poly(vinyl chloride) in cyclohexanone, J. Polym. Sci. Part B: Polym. Phys. 9 (1971) 633–643, https://doi.org/10.1002/pol.1971.160090406.

[49] G.C. Wildman, S.J.R. Hsu, Effect of solvent balance on the surface properties of poly(vinyl chloride), J. Appl. Polym. Sci. 30 (1985) 4385–4408, https://doi.org/10.1002/app.1985.070301115.

[50] E. Zdrachek, E. Bakker, Electrochemically switchable polymeric membrane ion-selective electrodes, Anal. Chem. 90 (2018) 7591–7599, https://doi.org/10.1021/acs.analchem.8b01282.

[51] T. Forrest, E. Zdrachek, E. Bakker, Thin layer membrane systems as rapid development tool for potentiometric solid contact ion-selective electrodes, Electroanalysis 32 (2020) 799–804, https://doi.org/10.1002/elan.201900674.

[52] T.T. Han, A.V. Kalinichev, Z. Mousavi, K.N. Mikhelson, J. Bobacka, Anomalous potentiometric response of solid-contact ion-selective electrodes with thin-layer membranes, Sens. Actuators B Chem. 357 (2022), https://doi.org/10.1016/j.snb.2022.131416.

[53] E. Bakker, E. Pretsch, P. Bühlmann, Selectivity of potentiometric ion sensors, Anal. Chem. 72 (6) (2000) 1127–1133, https://doi.org/10.1021/ac991146n.

[54] Y. Umezawa, P. Bühlmann, K. Umezawa, K. Tohda, S. Amemiya, Potentiometric selectivity coefficients of ion-selective electrodes, Part I. Inorganic cations, Pure Appl. Chem. 72 (2000) 1851–2082, https://doi.org/10.1351/pac200072101851.

Sara Krivačić is a research assistant at the Faculty of Chemical Engineering and Technology, University of Zagreb, where she is currently pursuing her PhD in applied chemistry with Prof. Petar Kassal. The topic of her PhD research is using printed electronics technologies in the development of ion-selective membrane electrodes and reference electrodes. She has recently completed a 6-month research training as an Excellence scholarship holder at the University of Geneva, Faculty of Science, under the supervision of Professor Eric Bakker.

Ayian Speck obtained his BSc in biochemistry in 2019 and his MSc in chemistry in 2022 at the University of Geneva. His MSc thesis was done in the group of Prof. Eric Bakker, where he is currently working as a PhD student. He focuses on dynamic electrochemistry principles to realize new diagnostic sensing systems. His most recent work has been on a cost-efficient and mass-producible all-solid state reference electrode that is controlled electrochemically.

Petar Kassal is associate professor at the Department of General and Inorganic Chemistry, Faculty of Chemical Engineering and Technology, University of Zagreb. He obtained his PhD in 2015, working on mobile and wireless (bio)chemical sensors. His research encompasses electrochemical and optical sensor and biosensor development, electroanalysis, environmental chemistry, wearable sensors, smart bandages, and functional nanomaterials. His current research is focused on scalable (bio) chemical sensor fabrication technologies.

Eric Bakker is professor of Analytical Chemistry at the University of Geneva. He received his Ph.D. from ETH Zurich and spent 14 years in the U.S., first as postdoc at the University of Michigan, then as faculty member at Auburn University and at Purdue University. He then spent three years in Perth, Australia at Curtin University before moving to Geneva in 2010. His research is focused on chemical sensors, with a particular emphasis on ion-selective membranes. He has published over 400 papers that have been globally cited over 30,000 times.

7.6. Appendix VI – Supplementary information for Publication 3

Supplementary information for the publication:

Towards mass-production of ion-selective electrodes by spotting: Optimization of membrane composition and real-time tracking of membrane drying

Sara Krivačić[1,2], Ayian Speck[2], Petar Kassal[1], Eric Bakker[2]

[1] Faculty of Chemical Engineering and Technology, University of Zagreb, Trg Marka Marulića 19, 10000 Zagreb, Croatia

[2] Department of Inorganic and Analytical Chemistry, University of Geneva, Quai Ernest-Ansermet 30, 1221 Genève, Switzerland

Supplementary Information for:

Towards Mass-Production of Ion-selective Electrodes: Optimization of Membrane Composition and Real-Time Tracking of Membrane Drying

Sara Krivačić[a,b], Ayian Speck[a], Petar Kassal[b,*], Eric Bakker[a,*]

[a] Department of Inorganic and Analytical Chemistry, University of Geneva, Quai Ernest-Ansermet 30, 1221 Genève, Switzerland.

[b] University of Zagreb, Faculty of Chemical Engineering and Technology, Trg Marka Marulića 19, HR-10000 Zagreb, Croatia.

E-mail addresses: skrivacic@fkit.unizg.hr (S. Krivačić), Ayian.Speck@unige.ch (A. Speck), pkassal@fkit.unizg.hr (P. Kassal), Eric.Bakker@unige.ch (E. Bakker)

Correspondence: Petar Kassal: pkassal@fkit.unizg.hr, Eric Bakker: Eric.Bakker@unige.ch
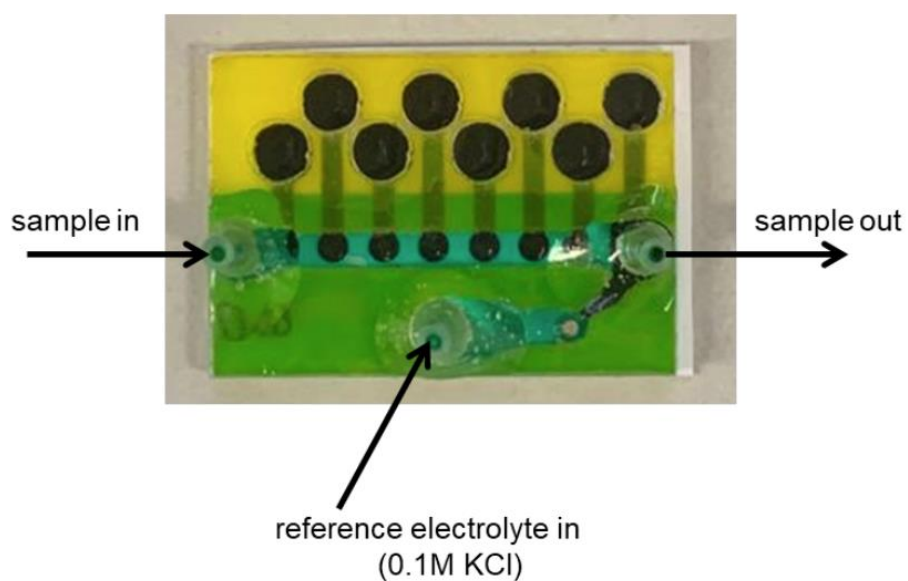
Figure S1. A photograph of the flow-through cell used for potentiometric measurements.
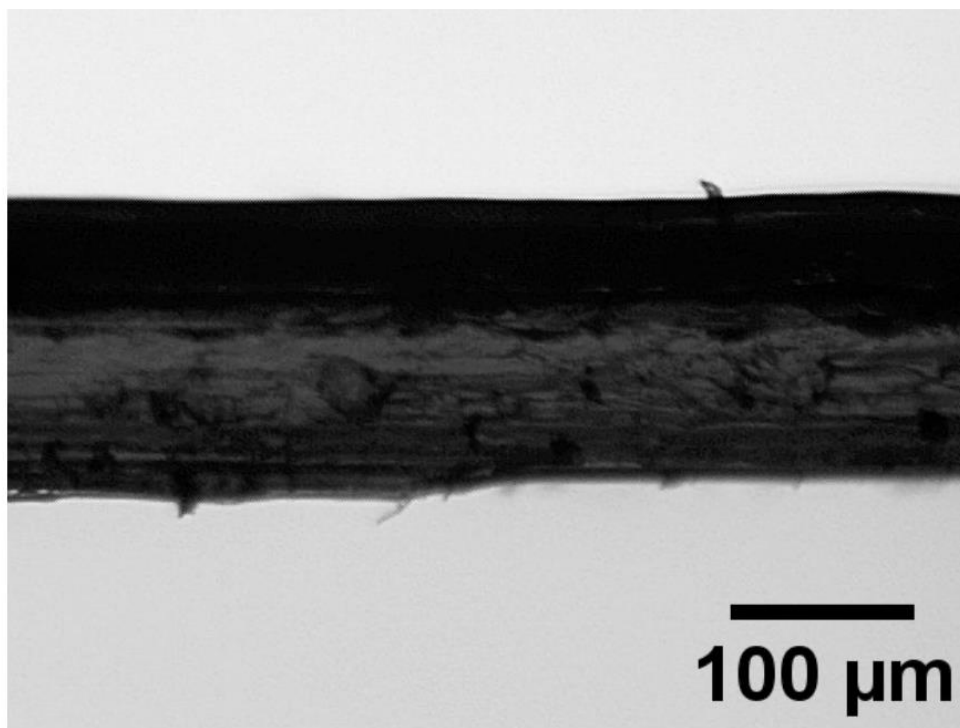
Figure S2. Cross-section of the Nile Red labelled membrane on a PET foil used for the determination of the thickness of the dry membrane, ε_{DRY}.
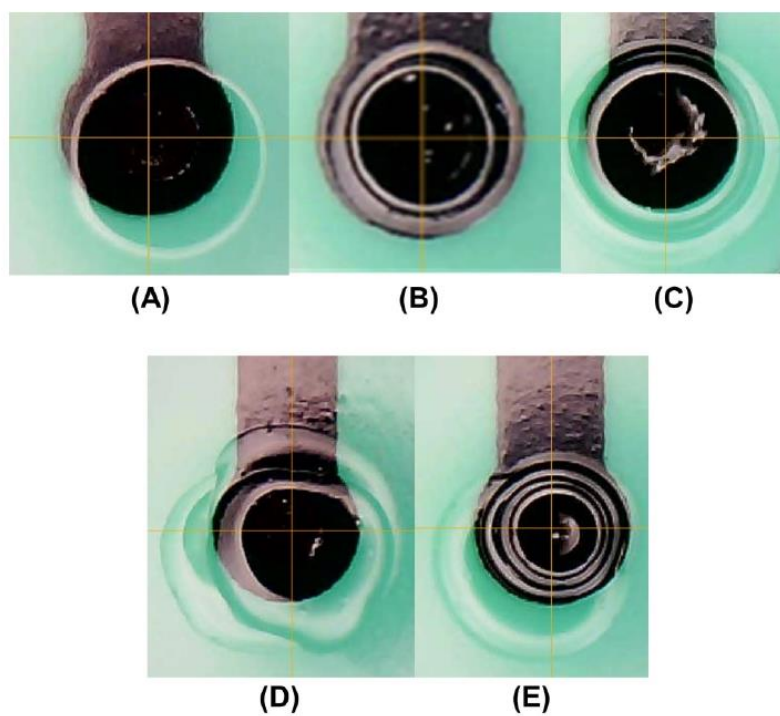
2

Figure S3. Photographs of the spotted membrane: **(A)** 1 spot, **(B)** 2 spots, **(C)** 3 spots, **(D)** 4 spots, **(E)** 5 spots.
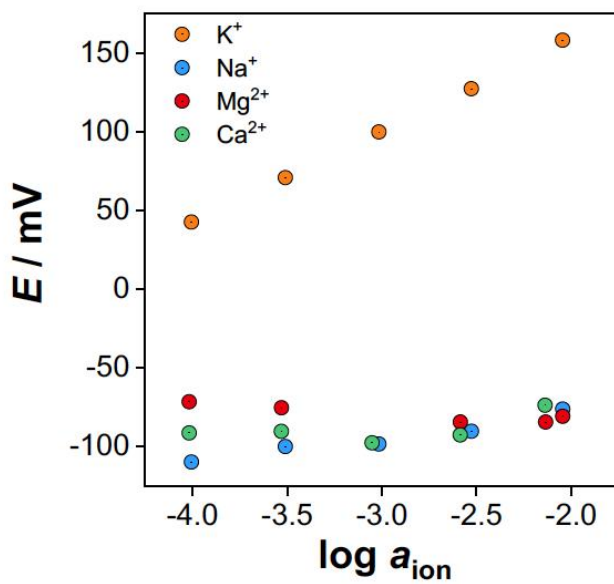
Figure S4. Electrode response towards potassium, sodium, magnesium and calcium ions.

3

Table S1. Fitting parameters for the evaporative thinning impedance measurements of the polymeric membranes prepared in THF and cyclohexanone. The standard deviations are given for three repeated measurements.

Equation	Z = Z(0) + B1*t + B2*t^2	
Solvent	THF	cyclohexanone
Z(0) / MΩ	2.09±0.18	2.66±0.05
B1 / s^{-1}	−0.888±0.396	0.027±0.001
B2 / s^{-2}	3.936±0.054	0.004±0.001
R2	0.9976	0.9900

Table S2. Fitting parameters for the evaporative thinning impedance measurements for the polymeric membranes prepared in a mixture of THF and cyclohexanone (1:1). The standard deviations are given for three repeated measurements.

Equation	Z = Z(0) + B1*t + B2*t^2	
Solvent	THF	cyclohexanone
Z(0) / MΩ	1.98±0.83	0.07±0.02
B1 / s^{-1}	1.19±0.24	0.013±0.00
B2 / s^{-2}	−0.21±0.003	0.992±0.002
R2	0.9790	0.8690

7.7. Appendix VII – Manuscript of Publication 4

Application of intense pulsed light in the development of poly(vinyl butyral)-based all-solid-state Ag/AgCl reference electrodes

Sara Krivačić[1], Marko Zubak[1], Domagoj Vrsaljko[1], Petar Kassal[1]

[1] Faculty of Chemical Engineering and Technology, University of Zagreb, Trg Marka Marulića 19, 10000 Zagreb, Croatia

RESEARCH ARTICLE

Application of intense pulsed light in the development of poly(vinyl butyral)-based all-solid-state Ag/AgCl reference electrodes

Sara Krivačić | **Marko Zubak** | **Domagoj Vrsaljko** (iD) | **Petar Kassal** (iD)

University of Zagreb, Faculty of
Chemical Engineering and Technology,
Zagreb, Croatia

Correspondence
Petar Kassal, University of Zagreb,
Faculty of Chemical Engineering and
Technology, Trg Marka Marulića 19,
HR-10000 Zagreb, Croatia.
Email: pkassal@fkit.unizg.hr

Funding information
Croatian Science Foundation, Grant/
Award Number: UIP-2020-02-9139,
DOK-2021-02-2362

Abstract

Intense pulsed light was investigated for partial photoreduction of AgCl in a poly(vinyl butyral) matrix to obtain a Ag/AgCl reference membrane. The membrane was deposited on both glassy carbon and inkjet-printed silver electrodes giving all-solid-state reference electrodes. Regardless of the electrode material, a sufficient potential stability was obtained in a broad concentration range of various salt solutions. Long-term potential stability was significantly improved with inkjet-printed silver electrical contacts. The electroanalytical performance of inkjet-printed electrodes was successfully demonstrated in potentiometric and amperometric systems.

KEYWORDS
all-solid-state reference electrode, flexible electrodes, inkjet-printed electrodes, intense pulsed light, potentiometry

1 | INTRODUCTION

Advanced insights into electroanalytical systems enabled the development of sensors for healthcare, environment and industrial processes monitoring [1,2]. Given this, manufacturing miniaturized devices has become a peculiar research topic aimed toward lower-cost and easy-to-use analytical solutions [3]. A reference electrode (RE) is an essential component of every electroanalytical protocol. An ideal reference electrode should provide an accurate, stable and reproducible potential, regardless of the sample composition, temperature, pH, redox or light activity [4–7]. Despite being universally adopted, conventional Ag|AgCl reference electrodes with liquid compartments come with convincing limitations concerning electrode miniaturization and maintenance, temperature usage, and unfit structure for wearables [8,9] or some point-of-care devices [10–13]. Miniaturising reference electrodes has been a focal research topic and can be summed up in eliminating burdensome glass electrode components filled with internal liquid junctions and replacing them with electrically transducing materials and polymer-based membranes [5,14]. This has resulted in a myriad of reference membranes based on a multitude of polymers and doping ions [15–19].

High throughput, cost-effective fabrication of sensing components is critical for the commercial viability of decentralized chemical sensing and biosensing [20]. Inkjet printing (IJP) has emerged as a powerful technology; it is digitally controlled, mask-less and non-contact, fast, low-cost, environmentally viable, and suitable for upscaling [21,22]. Hence, IJP has already been employed in the production of (flexible) miniaturized electrochemical systems [23–26]. However, these works usually employ quasi-reference electrodes, i.e. a layer of chemically or electrochemically formed silver chloride. The exact concentration of the silver chloride on the surface of such electrodes is never known with confidence, thus the potential of a quasi-reference electrode is likely to fluctuate due to the silver chloride dissolution [27–29].

Single junction-like solid-state reference electrodes are enabled by depositing a protective polymer-based membrane–within which a high Cl^- concentration is confined–over the AgCl layer. Inkjet printing has already

been employed in the development of such electrodes. Girault's group inkjet printed silver-ink electrodes on poly(ethylene terephthalate) (PET) substrates [30]. AgCl was formed by drop-casting a hypochlorite solution. A reference membrane was formulated by mixing KCl and tetradodecylammonium tetrakis(4-chlorophenyl)borate in commercially available polyacrylate inkjet ink and drop-cast onto the AgCl electrode.

Polyvinyl butyral (PVB) is an amphiphilic polymer consisting of a hydrophobic main chain and hydrophilic side chains [31], making it compatible with inorganic materials [32], soluble in polar organic solvents, but not in water [33], which is advantageous for its process-ability. A promising concept for decentralized sensing was given by Andrade's group, who formulated a PVB-based methanol solution with $AgNO_3$ and an excess of NaCl [34]. Upon the sonication of the mixture, AgCl was formed, and the membrane cocktail was exposed to a light bulb for 10 minutes, upon which a partial reduction of AgCl to Ag occurred. Variations of this approach using PVB have abundantly been used in the development of low-cost, flexible, paper-based and wearable sensors [35–38]. For example, Moya et.al. [39] have prepared a printable Cl^- saturated PVB-based membrane by diluting a 10 wt% PVB in anhydrous methanol in the mixture of xylene, diacetone alcohol, and butanol. The membrane was deposited over a printed AgCl electrode.

In this work, we evaluate the use of a PVB-based Ag/AgCl reference membrane, on flexible inkjet-printed electrodes. Since the membrane contains the Ag/AgCl system, it can be used on both silver and non-silver electrodes and the chemical chlorination step of a silver electrode can be omitted. We demonstrate this by coating with the membrane both a glassy carbon (GC) electrode and an inkjet-printed silver electrode and characterizing these solid-state reference electrodes. Furthermore, the partial photoreduction of AgCl in the membrane is for the first time caused by an intense pulsed light (IPL) system, which significantly reduces the reaction time, down to microseconds. IPL is a non-laser, high-intensity white light emitted from a xenon flash lamp. With processing times on the order of microseconds to milliseconds, it is highly compatible with inkjet printing and other high-throughput printed electronics fabrication technologies [40–42].

2 | EXPERIMENTAL

2.1 | Reagents

All chemicals used throughout this work were of ana-lytical grade, commercially available and were used as received. For the reference membrane preparation, anhydrous methanol and NaCl were purchased from Gram-Mol (Croatia), poly(vinyl butyral) (PVB) from Sigma Aldrich, (USA), and $AgNO_3$ was obtained from Alkaloid AD (North Macedonia).

Aqueous solutions for electrochemical character-izations were prepared with distilled water or deionized water (Millipore Milli-Q). $CaCl_2{\times}6H_2O$, KCl and $K_4[Fe(CN)_6]{\times}3H_2O$ were supplied from Kemika, Croatia; $K_3[Fe(CN)_6]$ from Merck, Germany: NaCl and $NaNO_3$ from Gram–Mol, Croatia. Universal buffer with pH in the range 2–12 (with increments of 2 pH units) was pre-pared by mixing HCl (30%, Merck, Germany), H_3PO_4 (85%, T.T.T., Croatia), citric acid monohydrate ($C_6H_8O_7{\times}H_2O$) and NaOH from Gram–Mol, Croatia, and H_3BO_3 from Acros Organics, Czechia.

2.2 | Electrode preparation

The glassy carbon disc electrode (GC, $A=0.283\ cm^2$) was polished with alumina of grain size 0.1 µm (Struers, Denmark) and sonicated for 10 min in Elma Transsonic T 460/H ultrasonic bath, Elma Schmidbauer GmbH, Germany.

The electrical contact patterns, with the working electrode area, $A=0.283\ cm^2$ were designed in Corel-DRAW Graphics Suite. Commercially available silver nanoparticle ink (JS−B25HV, NovaCentrix, USA) was inkjet printed on PET or polyimide (PI, Kapton, DuPont, Wilmington, NC, USA, $d=25$ µm) using a custom-made printer with a XP600 Epson print head. Subsequently, the printed electrodes (PE) were photonically annealed: PE were set 1 cm from the flash lamp (Xenon LH-912), of a Xenon X-1100 (Wilmington, NC, USA) IPL system and annealed with a single light pulse at 2500 V and 700 J.

2.3 | Reference membrane preparation

The reference membrane cocktail was prepared accord-ing to [34]. Briefly, a solution containing 10 wt% (395.5 mg) of PVB was formulated in 5 mL of methanol. The solution was homogenized in an ultrasonic bath (30 min, 50–60 Hz) and refrigerated at 5 °C to prevent solvent evaporation. Further on, 250 mg of NaCl and 250 mg of $AgNO_3$ were added to the previously prepared PVB solution. Upon repeating the homogenization step, a white suspension of AgCl is formed, with an excess of NaCl crystals at the bottom of the vial.

The obtained suspension was quantitatively trans-ferred to a petri dish and subjected to photonic

annealing ≈ 3 cm from the flash lamp of the IPL system. The photoreduction was concluded with a single light pulse of 100 J and 2000 V. Higher energies were also evaluated, but such reference membranes did not yield electrodes with stable responses. UV–Vis spectra of the reference membrane material were recorded on a Shimadzu UV-1280 spectrophotometer, after 400× dilution with ethanol.

The photonically reduced membrane cocktail was used right after the preparation: a total of 120 µL (4×30 µL, with drying in between) of the reference membrane cocktail was drop-cast on glassy carbon or inkjet-printed electrodes. The prepared electrodes were denoted as GC–RM (photonically reduced membrane cocktail drop-cast over GC-electrode) and PE–RM (photonically reduced membrane cocktail drop-cast over inkjet printed Ag-electrode). The entire fabrication process of the PE–RM and GC–RM is shown in Figure 1. Upon drop-casting the reference membrane (RM), the electrodes were dried overnight in dark conditions and conditioned in 3 M KCl for three hours before the electrochemical characterization.

2.4 | Electrode characterization

Dynamic potentiometric measurements were performed at room temperature using MA 5740 pH meter (Iskra, Slovenia) connected to a PC via a $4^{3/4}$ digit programmable multimeter HM8012 (Hambeg GmbH, Germany). All measurements were performed with the GC–RM or PE-RM connected as a working electrode (WE) and a commercial RE-5B Ag|AgCl|KCl (3 M) with 0.2 M NaNO$_3$ bridge electrolyte, both from ProSense, The Netherlands, as the reference electrode (RE).

The potential stability of prepared electrodes, GC–RM and PE–RM was studied over eight hours in an unstirred 10^{-2} M solution of KCl. Next, the electrodes' response was monitored in various solutions (KCl, NaCl, CaCl$_2$ and NaNO$_3$) of different concentrations (10^{-6}–10^{-2} M). The influence of solution pH was tested in universal buffer having pH values 2–12.

Electrochemical impedance spectroscopy (EIS) was performed using EG&G PAR Model 263 A Polarographic Analyser (Princeton, NJ, USA) connected to a frequency response detector (EG&G PAR Model 1025, Princeton, NJ, USA). The experiment was concluded at room temperature, in a three-electrode electrochemical cell filled with 10^{-1} M KCl solution; with GC–RM or PE–RM as a working electrode, Pt-electrode as a counter electrode and a commercial RE. The excitation potential ($E_{AC} = 5$ mV) was swept from 100 kHz to 100 mHz, at $E_{DC} = $ OCP.
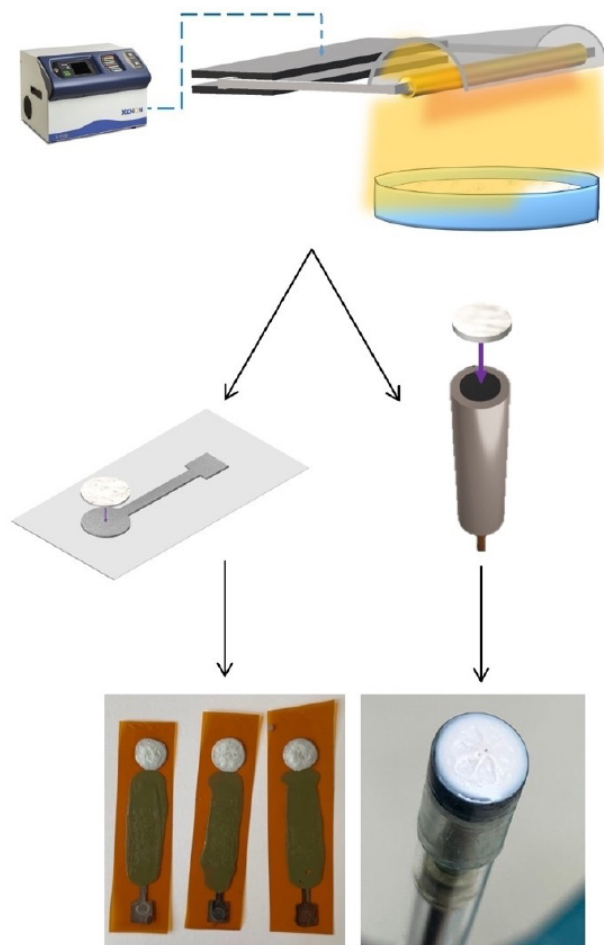

FIGURE 1 The schematic representation of solid-state reference electrode production.

Finally, the prepared electrodes were used as reference electrodes in two proof-of-concept experiments. First, the calibrations of commercially available sodium half-cell ion-selective electrode (DX223-NA, Mettler Toledo, USA) were performed at room temperature in unstirred NaCl solutions in the concentration range 10^{-6}–10^{-2} M. Finally, cyclic voltammetry (CV) measurements were performed using PalmSens4 potentiostat (PalmSens, Houten, the Netherlands) coupled to a personal computer. The CV measurements were performed in a solution consisting of a redox couple K$_3$[Fe(CN)$_6$]/K$_4$[Fe(CN)$_6$] (10 mM) in 10 mM KCl as a supporting electrolyte.

3 | RESULTS AND DISCUSSION

3.1 | Reference membrane preparation

For the reference membrane preparation, we followed the procedure proposed by Guinovart et.al. [34], which

suggests reducing the white colloidal AgCl to Ag^0 by exposing the membrane cocktail to a light bulb for about 10 min. We replaced this last step with the intense pulsed light (IPL) induced photoreduction. IPL is essentially a photonic technique and has already been employed for the reduction of various oxides in developing electrical circuits [43–46]. The growing interest in this technique is favoured by its potential for "in-line" coupling with the inkjet printing process, making it a promising economically viable mass-production protocol [47]. In this work, IPL was also used for photonic annealing of the silver nanoparticle ink during the fabrication of the silver IJP.

As hypothesized, IPL can be used for photoreduction of AgCl. Starting from low single-flash parameters (energies within hundreds of joules orders of magnitude), the colour change of the initially white colloid mixture is observed (Figure 2). At higher flashing energies, the mixture is heated, and a darker paste is obtained, indicating the formation and growth of silver nanoparticles (AgNPs) [32,48]. AgNP formation is corroborated by UV–Vis spectroscopy (Figure S1, Supporting Information).

During the initial screening, the RM cocktails prepared at three different IPL energies were drop cast on the GC-electrode and characterised in terms of potential stability against the change in Cl^- concentration by open circuit potentiometry (OCP) measurements in a narrow concentration range of 10^{-4}–10^{-2} M of KCl. At higher IPL energies, higher slopes ($> |8|$ mV/dec) were obtained, which indicates instability of the electrodes and

pronounced response to chloride ions due to a high degree of AgCl reduction to Ag^0. At low IPL parameters (100 J, 2000 V) the membrane cocktail is expected to consist of Ag–AgCl clusters in the PVB matrix. Mimicking the traditional Ag|AgCl reference electrodes, Ag–AgCl clusters are responsible for the non-polarizability of the electrode, while the high amount of chloride ions (from the excess of NaCl) in the membrane provides a constant phase boundary potential [34,49]. Reference membrane cocktails treated with IPL at 100 J, 2000 V (which are white, Figure 1) were thus used in all further experiments.

3.2 | Effect of conditioning time

Before potentiometric characterization, freshly prepared GC–RM and PE–RM electrodes were first placed in 3 M KCl and their potentiometric profile was tracked versus a conventional reference electrode at open-circuit conditions. As shown in Figure 3, upon initial contact with the conditioning solution, both electrodes show a pronounced potential drift which significantly reduces giving a stable value after around 40 min for a GC–RM and after only 3 min for a PE–RM electrode.

The reference electrodes' potential stabilization upon conditioning was probed by electrochemical impedance spectroscopy (EIS). The EIS measurements gave us
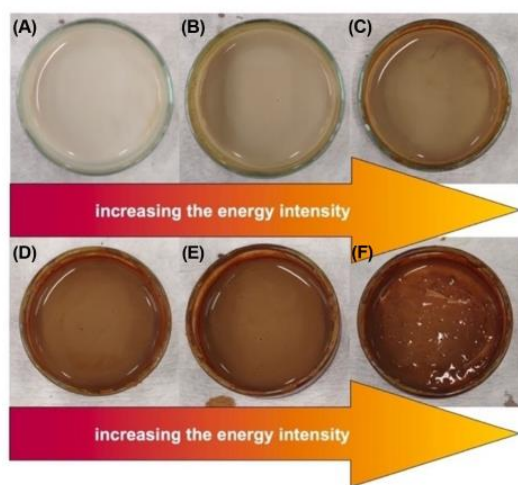

FIGURE 2 Changes in membrane colour with increasing intensity of IPL, demonstrating AgNP formation by IPL photoreduction: (A) without processing; (B) $U = 2500$ V, $E = 800$ J; (C) $U = 2500$ V, $E = 1400$ J; (D) $U = 3000$ V, $E = 1800$ J; (E) $U = 3000$ V, $E = 2000$ J; (F) $U = 3000$ V, $E = 2400$ J, the samples were treated with a single shot.
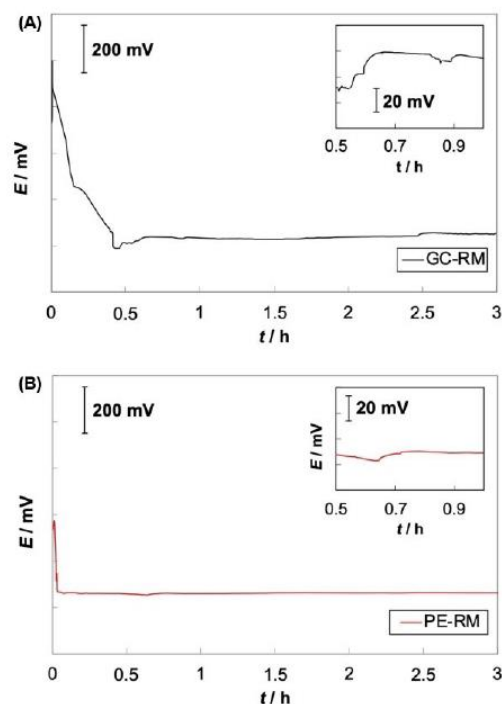

FIGURE 3 The potentiometric profile of (A) GC-RM and (B) PE–RM during three hours of conditioning in 3 M KCl.

151

useful insight into the surface changes on the RM-electrolyte interface during conditioning. Within the conditioning time, every 1 h the electrodes were switched to 10^{-1} M KCl and the EIS spectra were recorded (Figure 4).

Prominent changes in membrane resistance during the conditioning time are acquired in the case of GC–RM (Figure 4A). The EIS spectra before conditioning (blue dots) shows high impedance values, of 8.8 MΩ. A semi-circular impedance arc indicates a high charge transfer resistance of the membrane [50]. Already within the first hour, the impedance values show a dramatic decrease as the EIS response changes (Figure 4A, inset).

The Nyquist plot consists of a high-frequency small semi-circle followed by a straight line at intermediate and low frequencies. The high-frequency semi-circle, related to charge-transfer resistance, recedes during the conditioning, indicating ion diffusion into the membrane [51]. Concurrently,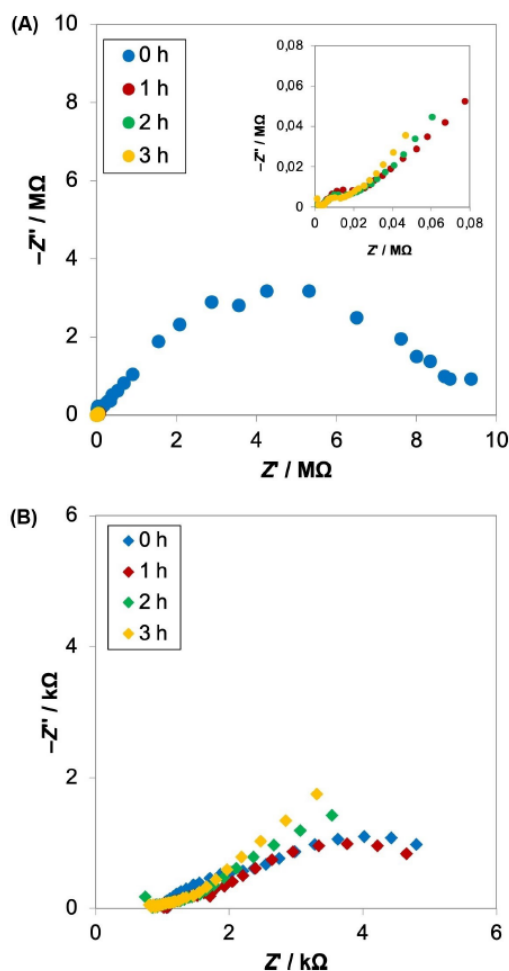 the slope of the low-frequency straight line increases with the duration of contact with the electrolyte and approaches unity, characteristic of a diffusion-controlled process. The depicted phenomena follow the well-known insights on polymeric membranes doped with ionic salts [30, 34]. "Inactive" reference membranes that do not contain ionic salts act as insulators and are not affected by water uptake from the sample [34, 52]. Conversely, adding salts to the membrane matrix is crucial to improving electrical contact with the sample solution, since the added salts induce a rapid uptake of a conditioning solution. Thereupon, morphological changes as indicated by nanochannel formation help to control the exchange of ions between the membrane and the conditioning solution, generating the electrical connection between the two phases [34, 39, 53]. As previously reported [34], changes on the molecular level in the PVB matrix are indicated by a steep increase in the intensity of the alcohol-stretching band due to the water percolation into the salt-containing membrane. High ionic activity in the membrane is favoured both by a large amount of AgCl and NaCl in the membrane matrix and PVB's intrinsically low glass transition temperature (T_g) [53]. The longer the conditioning time, the higher the rate of exchange of ions [54], as corroborated by the increase in the slope of the diffusion line [51]. In that way, the PVB matrix maintains the constant concentration of Cl^- ions at the reference membrane-sample interface, while simultaneously acting as a bridge between the electrolyte taken in by the membrane and the sample [34]. In doing so, as long as the Cl^- ions are within the polymeric membrane, the fabricated reference electrode resembles a single junction reference electrode [39].

The low-frequency capacitance, calculated using Equation (1), increased from 1.74 μF for the non-conditioned to 44.92 μF for the conditioned electrode.

$$C = 1/(2\pi f_{min}|Z_{im}|) \qquad (1)$$

Where C/F is the capacitance, f_{min}/Hz is the minimum frequency of the impedance measurement (100 mHz), and $|Z_{im}|$ is the absolute value of the imaginary component of the impedance at f_{min}.

Regarding the PE–RM (Figure 4B), much lower impedance values (on the order of kΩ) were obtained even within the first contact with the electrolyte. During the conditioning, the EIS spectra are dominated by a straight line, with a slope that increases with the contact time with the electrolyte, indicating a high ionic mobility within the membrane [55]. The low-frequency capacitance, which is related to diffusion processes within the membrane is 0.69 mF for PE–RM, as calculated using Equation (1). Since the membrane composition is the

FIGURE 4 The impedance spectra of (A) GC-RM and (B) PE-RM recorded in 10^{-1} M KCl during the three hours of conditioning in 3 M KCl.

same in case of both electrode types, the same morphological changes governed by the nanochannel formation are expected to occur. The double layer capacitance thus increases, capacitive reactance is reduced, and the EIS spectra resemble those characteristic of a diffusion-controlled electrode process. The initial improvement in overall electrical conductivity in the case of PE–RM points to an improved electrical contact between the PVB-based reference membrane and inkjet-printed Ag-electrode, compared to GC-electrode. Indeed, SEM images of the Ag electrode (Figure S2, Supporting Information) show a rough, coarse-grained structure of the electrode surface indicating a larger microscopic surface area than the smooth GC surface [56,57].

3.3 | Potentiometric measurements

The key requirement of a reliable reference electrode is to ensure proper potential stability regardless of the sample composition. Solid-state reference electrodes based on the Ag–AgCl reference pair tend to suffer from the interferences from chloride ions [27–29,39,49], hence a rigorous mid-term stability test was concluded with GC–RM and PE–RM by measuring drift in 10 mM KCl for 8 ho (Figure S3, Supporting Information). PE–RM retains a stable response throughout the initial test, with a drift value of -0.2464 mV/h. However, GC-RM exhibits a significant potential drop after 2 h within the solution. A leakage study [58] performed with the GC–RM demonstrated that this is not due to NaCl leakage from the membrane (Figure S4, Supporting Information). Instead, this can be attributed to partial delamination of the reference membrane from the GC electrode surface. Adhesion parameters between the RM and both electrode types were calculated from contact angle measurements (Table S1, Supporting Information). Although the calculated adhesion parameters (Table S2, Supporting Information) show us that the electrodes have very similar surface properties (and will in this respect have similar adhesion with the RM), the printed Ag electrode has a much rougher surface (Figure S2, Supporting Information) indicating that the RM can adhere much more strongly due to the interlocking with the Ag grains. Due to the RM delamination from the GC electrode surface, we conclude that the GC–RM configuration can be used for only short periods of time after stabilization (e.g. less than 1 h), which can be sufficient for short term and disposable electrochemical sensing. On the other hand, the PE–RM response is stable for a much longer time (more than 8 h).

Figure 5 depicts the results from the short-term stability tests that were concluded by measuring the OCP in several salts (KCl, NaCl, CaCl$_2$ and NaNO$_3$) within the concentration range 10^{-6}–10^{-2} M. For clarity purposes, the plots are offset by 50 mV, so that the potential profiles do not overlap. The slopes are given in Table 1. In all cases, the slope values were lower than 4 mV/dec, which indicates that the electrodes' response is not significantly affected by the sample composition or concentration. While the obtained values are not as good as some reported in the literature [34], the significant minimization of the photoreduction time with IPL (a total of 91 μs exposure) holds promise for quick large-scale fabrication of such reference electrodes.

The inter-electrode reproducibility of the printed electrodes can be expressed as standard deviation of E^0 and was found to be on average 3.9 mV, depending on the electrolyte. Measured in three electrolytes (NaCl, KCl, CaCl$_2$), the stdev of E^0 for n = 3 electrodes was in all cases less than 5.63 mV.

Another important factor regarding the reference electrode integrity is its insensitivity to pH fluctuations. Hence, we tested the electrodes' response in the prepared citrate buffer solutions within the pH range from 2 to 12. As depicted in Figure 6, both configurations show insignificant response fluctuations in the pH window from 2 to 10, with the slope values close to zero; -0.33 and -1.02 mV/decade for GC–RM and PE–RM, respectively.

3.4 | Electroanalytical performance of the inkjet printed electrode

We next evaluated whether the proposed membrane could ensure adequate potential stability to serve as a reference component of a potentiometric and voltammetric system. First, the calibration of a commercial sodium ion-selective electrode (Na-ISE) was performed, where the GC–RM and PE–RM were used as the reference electrode. Figure 7A shows the obtained calibration plot. A near-Nernstian slope (55.57 mV/pNa) was obtained for GC–RM and a Nernstian slope of 59.68 mV/pNa was obtained,

TABLE 1 Potentiometric characteristics for glassy carbon disc-electrode (GC-RM) and printed silver electrode (PE–RM) with PVB-based reference membrane.

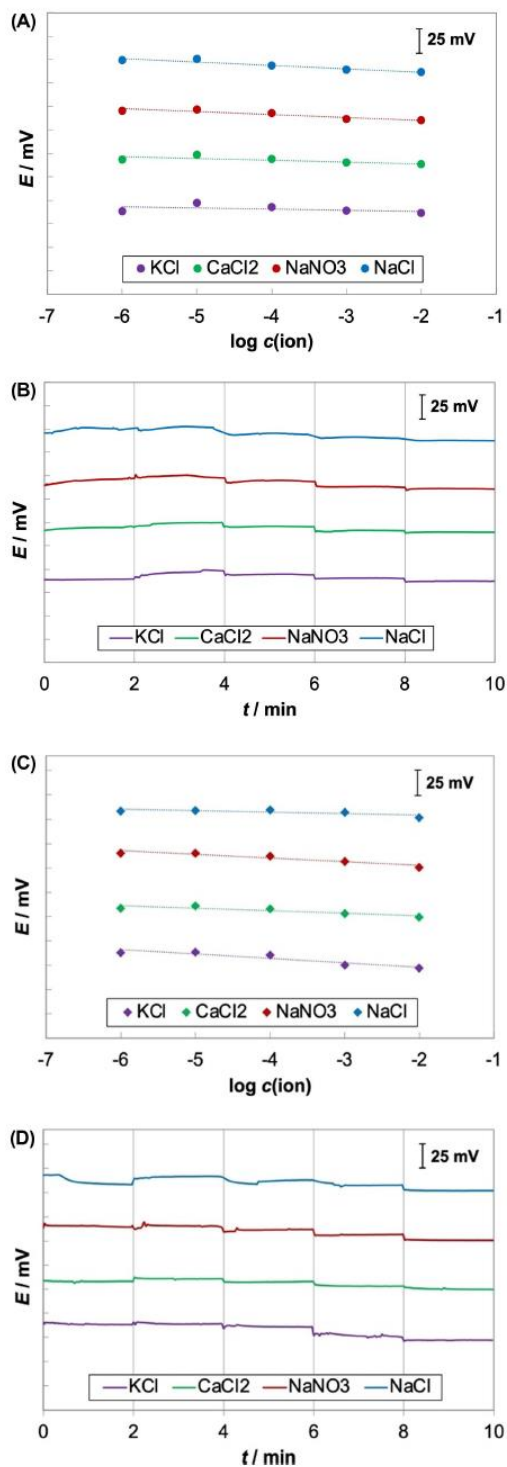| Aqueous solution	Linear region (GC-RM)	Linear region (PE-RM)	Slope (mV/log c) (GC-RM)	Slope (mV/log c) (PE-RM)
KCl	2–6	2–6	1.23	1.65
CaCl$_2$	2–6	2–6	1.84	2.57
NaNO$_3$	2–6	2–6	3.15	2.98
NaCl	2–6	2–6	3.59	3.25

FIGURE 5 The potentiometric response (E vs. t) for different electrolytes over a broad concentration range. For clarity purposes, plots are offset by 50 mV. (A, B) For GC–RM; and (C,D) for PE–RM.

which demonstrates that both solid-state electrodes can be used in potentiometric systems.

Cyclic voltammetry in 10 mM $[Fe(CN)_6]^{3-/4-}$ was performed with a glassy carbon working electrode against a
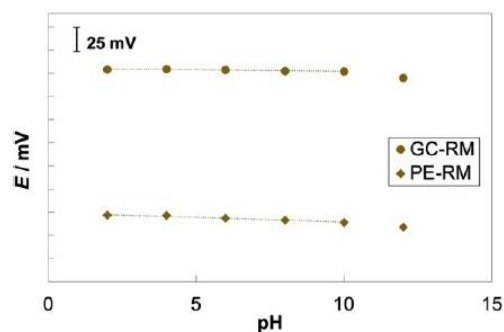

FIGURE 6 pH response of the two tested electrode configurations in a universal pH buffer solution.
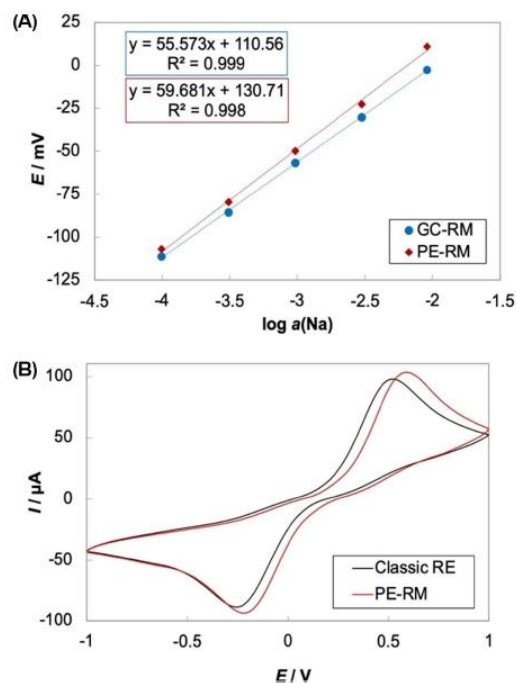

FIGURE 7 (A) Potentiometric response of the commercial Na-ISE against GC–RM and PE–RM; (B) The results of cyclic voltammetry experiments in 10 mM $[Fe(CN)_6]^{3-/4-}$.

commercial Ag|AgCl|KCl (3 M) with 0.2 M NaNO$_3$ bridge electrolyte and against the PE–RM reference electrode (Figure 7B). When using PE–RM as a reference, a small parallel shift occurs, due to the potential difference between PE–RM and the classic reference electrode of 92 mV [39]. The peak-to-peak separation potential (ΔE_p) was much higher compared to a theoretical value of 59.2 mV for a single electron process at 25 °C, due to an Ohmic drop between the working and reference electrode caused by low electrolyte conductivity [59]. Regardless of that, the difference in ΔE_p between the two measurements was less than 3 % RSD. The peak current values (I_p) of the studied redox system are described by the Randles–Ševčik equation which can be used to

calculate the geometric surface area of the working electrode (A) [59]. The geometric surface area was estimated to differ by less than 7 % RSD using the two reference electrodes.

4 | CONCLUSIONS

Presented here is the implementation of intense pulsed light in the production of a reference membrane for an all-solid-state reference electrode. The prepared reference membrane is based on a Ag/AgCl reference pair immobilized in a poly(vinyl butyral) membrane, making it compatible with different electrically conducting surfaces, including glassy carbon and flexible inkjet-printed silver electrodes. The surface changes on the reference membrane-electrolyte interface during conditioning were evaluated using electrochemical impedance spectroscopy, and favourable electrical contact between the RM and electrode surface was observed with inkjet-printed Ag-electrodes. This was confirmed by prolonged measurements in KCl, where a glassy-carbon electrode modified with the reference membrane started drifting after 2 h, while the inkjet-printed electrode showed superior potential stability, with a minor drift value of -0.2464 mV over 8 h. Regardless of the electrically conducting substrate, the electrodes have shown sufficient potential stability in a broad concentration range of various salt solutions (KCl, NaCl, $CaCl_2$ and $NaNO_3$), with the potential varying less than 4 mV per ten time increase of salt concentration. The electrochemical performances of inkjet-printed electrodes were successfully evaluated in potentiometric and amperometric systems. The presented results support the proposed protocol aimed towards lowering the electrode production steps and enabling rapid mass production of electrochemical sensor platforms.

CONFLICT OF INTEREST STATEMENT
The authors declare they have no conflict of interest.

DATA AVAILABILITY STATEMENT
The data that support the findings of this study are available from the corresponding author upon reasonable request.

ORCID
Domagoj Vrsaljko http://orcid.org/0000-0003-1383-5376
Petar Kassal http://orcid.org/0000-0001-7904-6439

REFERENCES
1. Y. R. Yang, W. Gao, *Chem. Soc. Rev.* **2019**, *48*, 1465–1491.
2. G. Lisak, *Environ. Pollut.* **2021**, *289*, 117882–117201.
3. Y. H. Cheong, L. Y. Ge, G. Lisak, *Anal. Chim. Acta* **2021**, *1162*, 338304–338127.
4. S. Blidi, K. Granholm, T. Sokalski, Z. Mousavi, A. Lewenstam, I. Leito, J. Bobacka, *Membranes* **2022**, *12*, 569–580.
5. J. B. Hu, K. T. Ho, X. U. Zou, W. H. Smyrl, A. Stein, P. Bühlmann, *Anal. Chem.* **2015**, *87*, 2981–2987.
6. U. Guth, F. Gerlach, M. Decker, W. Oelssner, W. Vonau, *J. Solid. State. Electrochem.* **2009**, *13*, 27–39.
7. B. K. Troudt, C. R. Rousseau, X. I. N. Dong, E. L. Anderson, P. Bühlmann, *Anal. Sci.* **2022**, *38*, 71–83.
8. M. Parrilla, M. Cuartero, G. A. Crespo, *Trac-Trends in Anal. Chem.* **2019**, *110*, 303–320.
9. Y. Lyu, S. Y. Gan, Y. Bao, L. J. Zhong, J. A. Xu, W. Wang, Z. B. Liu, Y. M. Ma, G. F. Yang, L. Niu, *Membranes* **2020**, *10*, 128–152.
10. S. K. Sailapu, C. Menon, *Adv. Sci.* **2022**, *9*, 2203690–2203713.
11. D. S. Macedo, M. Vepsäläinen, D. Acharya, C. D. Wood, D. C. Wen, L. Thomson, S. Peacock, T. Rodopoulos, C. F. Hogan, *Electrochim. Acta* **2021**, *368*, 137636–137645.
12. I. Shitanda, M. Komoda, Y. Hoshi, M. Itagaki, *Analyst* **2015**, *140*, 6481–6484.
13. Z. Mousavi, K. Granholm, T. Sokalski, A. Lewenstam, *Analyst* **2013**, *138*, 5216–5220.
14. Y. Z. Shao, Y. B. Ying, J. F. Ping, *Chem. Soc. Rev.* **2020**, *49*, 4405–4465.
15. F. X. Rius-Ruiz, A. Kisiel, A. Michalska, K. Maksymiuk, J. Riu, F. X. Rius, *Anal. Bioanal. Chem.* **2011**, *399*, 3613–3622.
16. R. C. Dawkins, D. C. Wen, J. N. Hart, M. Vepsäläinen, *Electrochim. Acta* **2021**, *393*, 139043–139053.
17. U. Mattinen, J. Bobacka, A. Lewenstam, *Electroanalysis* **2009**, *21*, 1955–1960.
18. Z. Mousavi, K. Granholm, T. Sokalski, A. Lewenstam, *Sens. Actuators B Chem.* **2015**, *207*, 895–899.
19. M. Sophocleous, J. K. Atkinson, *Sens. Actuator A Phys.* **2017**, *267*, 106–120.
20. M. Bariya, Z. Shahpar, H. Park, J. F. Sun, Y. Jung, W. Gao, H. Y. Y. Nyein, T. S. Liaw, L. C. Tai, Q. P. Ngo, M. H. Chao, Y. B. Zhao, M. Hettick, G. Cho, A. Javey, *ACS Nano* **2018**, *12*, 6978–6987.
21. A. Kamyshny, S. Magdassi, *Small* **2014**, *10*, 3515–3535.
22. A. Kamyshny, S. Magdassi, *Chem. Soc. Rev.* **2019**, *48*, 1712–1740.
23. K. Pokpas, N. Jahed, E. McDonald, P. Bezuidenhout, S. Smith, K. Land, E. Iwuoha, *Electroanalysis* **2020**, *32*, 3017–3031.
24. S. Papamatthaiou, U. Zupancic, C. Kalha, A. Regoutz, P. Estrela, D. Moschou, *Sci. Rep.* **2020**, *10*, 17152–17162.
25. A. Määttänen, U. Vanamo, P. Ihalainen, P. Pulkkinen, H. Tenhu, J. Bobacka, J. Peltonen, *Sens. Actuators B Chem.* **2013**, *177*, 153–162.
26. E. T. S. G. da Silva, S. Miserere, L. T. Kubota, A. Merkoçi, *Anal. Chem.* **2014**, *86*, 10531–10534.

27. H. S. Yang, S. K. Kang, C. A. Choi, H. Kim, D. H. Shin, Y. S. Kim, Y. T. Kim, *Lab Chip* **2004**, *4*, 42–46.

28. T. Y. Kim, S. A. Hong, S. Yang, *Sensors* **2015**, *15*, 6469–6482.

29. B. J. Polk, A. Stelzenmuller, G. Mijares, W. MacCrehan, M. Gaitan, *Sens. Actuators B Chem.* **2006**, *114*, 239–247.

30. A. Bananezhad, M. Jovic, L. F. Villalobos, K. V. Agrawal, M. R. Ganjali, H. H. Girault, *J. Electroanal. Chem.* **2019**, *847*, 113241–113264.

31. R. M. Zhang, J. W. Wang, M. J. Wang, Y. D. He, *J. Appl. Polym. Sci.* **2012**, *124*, 495–500.

32. K. V. Radha, V. Gopalakrishnan, A. Jayakumar, *Polymers* **2022**, *13*, 102–120.

33. Butvar Polyvinyl Resins, Properties and Uses, https://www.eastman.com/Literature_Center/A/ADDBVR3978.pdf.

34. T. Guinovart, G. A. Crespo, F. X. Rius, F. J. Andrade, *Anal. Chim. Acta* **2014**, *821*, 72–80.

35. A. M. Zamarayeva, N. A. D. Yamamoto, A. Toor, M. E. Payne, C. Woods, V. I. Pister, Y. Khan, J. W. Evans, A. C. Arias, *Apl. Mater.* **2020**, *8*, 100905–100916.

36. T. Guinovart, A. J. Bandodkar, J. R. Windmiller, F. J. Andrade, J. Wang, *Analyst* **2013**, *138*, 7031–7038.

37. A. J. Bandodkar, D. Molinnus, O. Mirza, T. Guinovart, J. R. Windmiller, G. Valdés-Ramírez, F. J. Andrade, M. J. Schöning, J. Wang, *Biosens. Bioelectron.* **2014**, *54*, 603–609.

38. W. Gao, S. Emaminejad, H. Y. Y. Nyein, S. Challa, K. V. Chen, A. Peck, H. M. Fahad, H. Ota, H. Shiraki, D. Kiriya, D. H. Lien, G. A. Brooks, R. W. Davis, A. Javey, *Nature* **2016**, *529*, 509–514.

39. A. Moya, R. Pol, A. Martínez-Cuadrado, R. Villa, G. Gabriel, M. Baeza, *Anal. Chem.* **2019**, *91*, 15539–15546.

40. H. S. Lim, S. J. Kim, H. W. Jang, J. A. Lim, *J. Mater. Chem. C* **2017**, *5*, 7142–7160.

41. M. Kralj, S. Krivacic, I. Ivanisevic, M. Zubak, A. Supina, M. Marcius, I. Halasz, P. Kassal, *Nanomaterials* **2022**, *12*, 2396–2411.

42. I. Ivanisevic, M. Kovacic, M. Zubak, A. Ressler, S. Krivacic, Z. Katancic, I. G. Pavlovic, P. Kassal, *Nanomaterials* **2022**, *12*, 4252–4275.

43. Y. R. Jang, S. J. Joo, J. H. Chu, H. J. Uhm, J. W. Park, C. H. Ryu, M. H. Yu, H. S. Kim, *Int. J. Precis. Eng. Manuf.–Green Technol.* **2021**, *8*, 327–363.

44. J. W. Park, C. J. Moon, Y. M. Ju, Y. R. Jang, S. S. Park, H. S. Kim, *Adv. Electron. Mater.* **2022**, *8*, 2101018–2101028.

45. Y. T. Hwang, H. S. Kim, *Int. J. Precis. Eng. Manuf. - Green Technol.* **2022**, *9*, 201–211.

46. M. Jha, R. Dharmadasa, G. L. Draper, A. Sherehiy, G. Sumana-sekera, D. Amos, T. Druffel, *Nanotechnology* **2015**, *26*, 175601–175611.

47. L. Rebohle, S. Prucnal, W. Skorupa, *Semicond. Sci. Technol.* **2016**, *31*, 103001–103039.

48. A. Chhatre, P. Solasa, S. Sakle, R. Thaokar, A. Mehra, *Colloid Surface A* **2012**, *404*, 83–92.

49. H. Suzuki, A. Hiratsuka, S. Sasaki, I. Karube, *Sens. Actuators B Chem.* **1998**, *46*, 104–113.

50. D. Stoica, P. J. Brewer, R. J. C. Brown, P. Fisicaro, *Electrochim. Acta* **2011**, *56*, 10009–10015.

51. J. Sun, Q. X. Wang, G. Luo, W. C. Meng, M. Cao, Y. Z. Li, M. D. Masterman-Smith, H. B. Yang, X. D. Sun, M. F. Lang, *J. Mater. Res. Technol.* **2020**, *9*, 13425–13433.

52. T. Lindfors, F. Sundfors, L. Höfler, R. E. Gyurcsányi, *Electroanalysis* **2009**, *21*, 1914–1922.

53. S. C. Park, H. J. Jeong, M. Heo, J. H. Shin, J. H. Ahn, *ACS Appl. Electron. Mater.* **2021**, *3*, 2580–2588.

54. S. Gopal, S. A. Agnihotry, V. D. Gupta, *Sol. Energy Mater. Sol. Cells* **1996**, *44*, 237–250.

55. F. X. Rius-Ruiz, D. Bejarano-Nosas, P. Blondeau, J. Riu, F. X. Rius, *Anal. Chem.* **2011**, *83*, 5783–5788.

56. S. Jafari, M. Dehghani, N. Nasirizadeh, H. R. Akrami, *Microchim. Acta* **2017**, *184*, 4459–4468.

57. Y. Yi, G. Weinberg, M. Prenzel, M. Greiner, S. Heumann, S. Becker, R. Schlögl, *Catal. Today* **2017**, *295*, 32–40.

58. D. Diamond, E. McEnroe, A. Lewenstam, *Electroanalysis* **1994**, *6*, 962–971.

59. N. Elgrishi, K. J. Rountree, B. D. McCarthy, E. S. Rountree, T. T. Eisenhart, J. L. Dempsey, *J. Chem. Educ.* **2018**, *95*, 197–206.

SUPPORTING INFORMATION

Additional supporting information can be found online in the Supporting Information section at the end of this article.

7.8. Appendix VI – Supplementary information for Publication 4

Supplementary information for the publication:

Application of intense pulsed light in the development of poly(vinyl butyral)-based all-solid-state Ag/AgCl reference electrodes

Sara Krivačić[1], Marko Zubak[1], Domagoj Vrsaljko[1], Petar Kassal[1]

[1] Faculty of Chemical Engineering and Technology, University of Zagreb, Trg Marka Marulića 19, 10000 Zagreb, Croatia

Application of intense pulsed light in the development of poly(vinyl butyral)-based all-solid-state Ag/AgCl reference electrodes

Sara Krivačić | Marko Zubak | Domagoj Vrsaljko | Petar Kassal

Application of Intense Pulsed Light in the Development of Poly(vinyl butyral)-based

All-solid-state Ag/AgCl Reference Electrodes

SUPPLEMENTARY DATA

Sara Krivačić, Marko Zubak, Domagoj Vrsaljko, Petar Kassal*

*pkassal@fkit.unizg.hr

University of Zagreb, Faculty of Chemical Engineering & Technology, Trg Marka Marulića
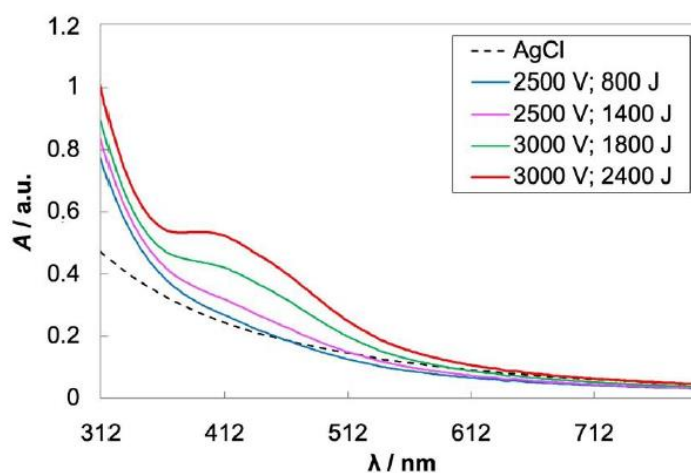
19, HR-10000 Zagreb, Croatia

Fig. S1. UV/Vis spectra of reference membrane material (diluted 400x in ethanol) upon

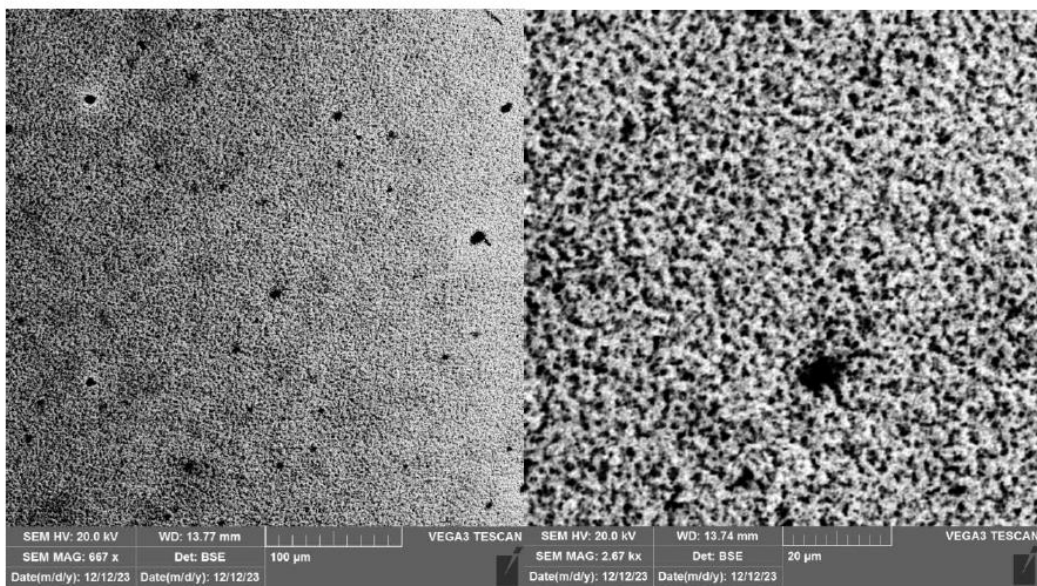different intensities of the IPL reduction.

Fig. S2. SEM micrographs of the Ag printed electrode surface at different magnifications.

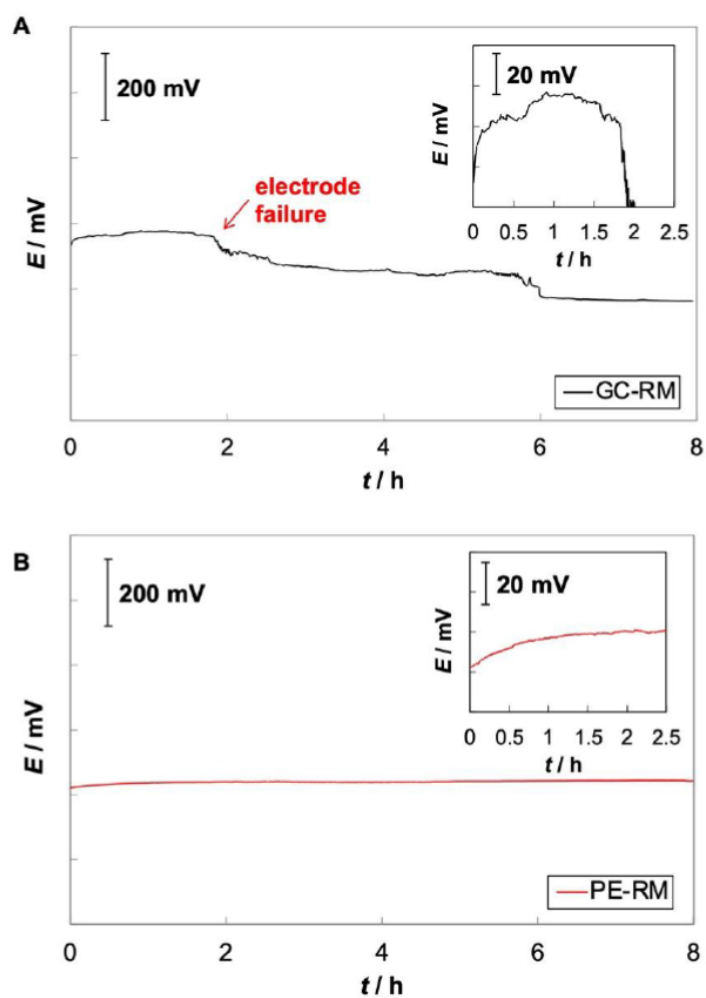Recorded with a A VEGA 3 Tescan scanning electron microscope.

Fig. S3. Drift measurements in 10 mM KCl with **(A)** GC-RM and **(B)** PE-RM. Before the measurements, both electrodes were conditioned in 3 M KCl for 3 hours.

Leakage study

The leakage study was carried out using a Thermo Scientific ORION STAR A112 Thermo conductometer and ORION 011050MD probe. The GC-RM was immersed in 100 ml of Mili-Q water together with the probe in a system sealed with parafilm. Apart from the initial increase in conductivity upon immersion (probably dissolution of surface NaCl), no significant changes or trends were observed over 4 hours. We thus conclude that salt leakage from the membrane is not significant.
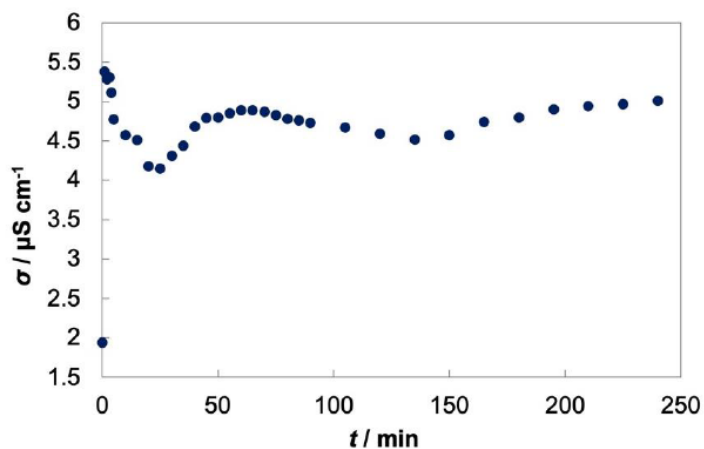

Fig. S4. Leakage study of the GC electrode: Conductivity of 100 mL of distilled water with immersed GC-RM over 4 hours.

Surface characterization

Surface investigations were carried out with a DataPhysics OCA 20 goniometer by measuring contact angles with three test liquids (water, formamide and diiodomethane) with known surface energy values [1]. Contact angle measurements are a valid method for determining the surface energy of solid materials [2]. For the contact angle measurements, sessile drops (2 µL) of test liquids were used: deionized water ($\lambda = 1.33$ µL cm^{-1}); formamide (p.a. 99.5 %, Fluka) and diiodomethane (p.a. 99 %, Aldrich), at 23 °C. The contact angle was determined 1 s after application of the drops. To ensure the reproducibility of the measurement data, average values were taken from at least three drops on different parts of the sample.

The surface energies of the RM and the two electrodes were calculated from the contact angle data using the Owens-Wendt method [3] (Equation 1), as well as interfacial surface energy (Equation 2), work of adhesion (Equation 3), coefficient of wetting (Equation 4):

$$\gamma_{AB}\,(1 + \cos\theta) = (\gamma_A^d\gamma_B^d)^{1/2} + (\gamma_A^p\gamma_B^p)^{1/2} \qquad (1)$$

$$\gamma_{AB} = \gamma_A + \gamma_B - 2\sqrt{\gamma_A^d\gamma_B^d} - 2\sqrt{\gamma_A^p\gamma_B^p} \qquad (2)$$

$$W_{AB} = \gamma_A + \gamma_B - \gamma_{AB} \qquad (3)$$

$$S_{AB} = \gamma_A - \gamma_B - \gamma_{AB} \qquad (4)$$

where γ^d is the dispersive and γ^p the polar component of the surface free energy ($\gamma = \gamma^d + \gamma^p$); γ_A and γ_B are the surface free energies of the two components, and θ is the contact angle.

Table S1. Surface free energy calculated by the Owens-Wendt model

	q (°)			OW (mJ m^{-2})		
	Water	Formamide	DIM	g	g^d	g^p
PVB	83.1 ± 1.3	70.2 ± 8.0	54.4 ± 6.5	32.7	28.5	4.2
RM	70.8 ± 1.9	63.6 ± 4.8	49.0 ± 4.5	38.5	29.8	8.8
GC electrode	78.3 ± 0.4	57.7 ± 1.9	43.6 ± 1.5	40.2	35.7	4.5
Ag electrode	83.2 ± 1.5	59.6 ± 1.1	31.3 ± 4.9	42.9	41.0	2.0

The results of determined total surface free energy (γ) as well as the dispersive and polar components of studied surfaces are shown in Table 1. Equations (2) to (4) were used to calculate the adhesion parameters (Table 2). The calculated adhesion parameters show us that the electrode surfaces have very similar material properties and in this respect will have a similar adhesion with the RM.

Table S2. Adhesion parameters of RM and two electrodes

A/B	g_{AB} (mJ m^{-2})	W_{AB} (mJ m^{-2})	S_{AB} (mJ m^{-2})
Ag/RM	3.3	78.2	1.1
GC/RM	1.0	77.8	0.7

REFERENCES

[1] J. Comyn, *J. Int. J. Adhes. Adhes.* **1992**, 12 (3), 145-149.

[2] S. Wu, Polymer Interface and Adhesion; Marcel Dekker: New York, 1982.

[3] D.K. Owens, R.C. Wendt, *J. Appl. Polymer. Sci.* **1969**, 13, 1741-1747.

8. BIOGRAPHY

Sara Krivačić was born on 28 June 1996 in Zagreb, Croatia. She completed her secondary education at XVI Gymnasium in 2015 and, in the same year, enrolled in the undergraduate study programme in Applied Chemistry at the University of Zagreb, Faculty of Chemical Engineering and Technology. She obtained her Bachelor's degree in 2018, defending a thesis entitled "*Determination of Hexacyanoferrate by Ion-Selective Solid-State Electrode*", prepared at the Department of General and Inorganic Chemistry under the supervision of Assoc. Prof. Stjepan Milardović, PhD. In the same year, she continued her education in the graduate study programme in Applied Chemistry at the same Faculty. During her graduate studies, she volunteered in the Laboratory for Functional Materials at the Division of Materials Chemistry, Ruđer Bošković Institute, where she worked under the mentorship of Ana Šantić, PhD. In 2020, she earned her Master's degree, having defended a thesis entitled "*Corrosion Resistance of Biomedical Titanium-Based Implant Materials*", conducted at the Department of Electrochemistry under the supervision of Assoc. Prof. Jozefina Katić, PhD. In 2021, she enrolled in the Postgraduate Doctoral Studies in Chemical Engineering and Applied Chemistry at the same institution, where she conducted her doctoral research under the supervision of Assoc. Prof. Petar Kassal, PhD. During her doctoral studies, she collaborated on three scientific research projects (UIP-2020-02-9139, IP-2024-05-4339, and Biomimetic Multifunctional Calcium Phosphate Coatings with Enhanced Anticorrosion Protection). She was actively involved in teaching activities at the Department of General and Inorganic Chemistry, assisting in laboratory courses and mentoring students. Over the course of her work, she supervised six master's theses and two bachelor's theses. In 2024, she was awarded the Outbound Mobility of Research Assistants (MOBDOK-2023) scholarship by the Croatian Science Foundation, which enabled her to spend six months as an Excellence Scholarship Fellow at the University of Geneva, Faculty of Science, Department of Inorganic and Analytical Chemistry, where she conducted research within the group of prof. Eric Bakker, PhD. Throughout her doctoral studies, she participated in thirteen scientific conferences and co-authored seven scientific papers published in journals indexed in the Web of Science (WoS) and Current Contents (CC) databases.

List of publications:

(7) **S. Krivačić**, A. Speck, P. Kassal, E. Bakker, Towards Mass-Production of Ion-selective Electrodes by Spotting: Optimization of Membrane Composition and Real-Time Tracking of Membrane Drying, Sensors and Actuators B: Chemical 423 (2025) 136759.

(6) **S. Krivačić**, Ž. Boček, M. Zubak, V. Kojić, P. Kassal, Flexible ammonium ion-selective electrode based on inkjet-printed graphene solid contact, Talanta 279 (2024) 126614.

(5) **S. Krivačić**, M. Zubak, D. Vrsaljko, P. Kassal, Application of intense pulsed light in the development of poly (vinyl butyral)-based all-solid-state Ag/AgCl reference electrodes, Electroanalysis 36, 5 (2024) e202300368.

(4) J. Katić, **S. Krivačić**, Ž. Petrović, D. Mikić, M. Marciuš, Titanium implant alloy modified by electrochemically deposited functional bioactive calcium phosphate coatings, Coatings 13, 3 (2023) 640.

(3) I. Ivanišević, M. Kovačić, A. Ressler, **S. Krivačić**, Z. Katančić, I Gudan Pavlović, P. Kassal, Amphiphilic silver nanoparticles for inkjet-printable conductive inks, Nanomaterials 12, 23 (2022) 4252.

(2) M. Kralj*, **S. Krivačić***, I. Ivanišević, M. Zubak, A. Supina, M. Marciuš, I. Halasz, P. Kassal, Conductive inks based on melamine intercalated graphene nanosheets for inkjet printed flexible electronics, Nanomaterials 12, 17 (2022) 2396.

(1) L. Pavić, **S. Krivačić**, M. Moguš Milanković, A. Šantić, Low potassium mobility in iron pyrophosphate glasses, Journal of Non-Crystalline Solids 535 (2020) 119969.